ELECTROCHEMICAL ANALYSIS OF PHOTOELECTRO-, ELECTRO-, AND THERMAL CATALYSIS TOWARDS MORE EFFICIENT HYDROGEN PEROXIDE PRODUCTION

BY

MATTHEW LOGAN KROMER

DISSERTATION

Submitted in partial fulfillment of the requirements
for the degree of Doctor of Philosophy in Chemistry
in the Graduate College of the
University of Illinois at Urbana-Champaign, 2020

Urbana, Illinois

Doctoral Committee:

Associate Professor Joaquín Rodríguez-López
Associate Professor David W. Flaherty
Professor Catherine J. Murphy
Professor Hong Yang

Abstract

Hydrogen peroxide is a chemical with growing industrial relevance but is plagued with high production costs. There are several compelling alternatives to produce H_2O_2, and most revolve around the 2-electron oxygen reduction reaction. There is a large amount of foundational research on the mechanisms and theoretical aspects of electrochemically reducing oxygen to form H_2O_2, but this production method remains to be implemented on the industrial scale due to a lack of effective catalysts. Explored here are alternative H_2O_2 production methods involving the 2-electron reduction of O_2. Specifically, photoelectrochemical, electrocatalytic, and thermal catalytic methods are investigated further to draw out necessary catalyst properties and design parameters for producing H_2O_2. Each catalytic system is analyzed under the lens of electrochemically detecting H_2O_2 that is catalytically produced. Electrochemical analysis of these catalytic systems provides the added advantage of being able to utilize high throughput screening techniques to quickly discover and test novel catalyst compositions. Optimal catalyst design parameters are identified for each H_2O_2 production method and these parameters can be assessed over several catalyst compositions through high throughput electrochemical screening. The research presented here acts as a basis for further improvements onto these already compelling H_2O_2 production methods.

Acknowledgements

I would like to acknowledge the staff in the SCS machine shop, particularly Mike "Hodge" Harlin and Dave Hire. Their help made my research possible and allowed me to perform technically difficult experimentation.

Towards his contributions to shaping me as a scientist and electrochemist, I would also like to acknowledge Professor Joaquín Rodríguez-López. Thank you for taking me into your lab and providing me with the guidance to become the scientist I am today. Also, the JRL lab members and other materials chemistry students were instrumental in my success in graduate school, whether it be from scientific discussions or just sharing memes and being friends.

I would also like to thank my committee members, Professor Catherine Murphy, Professor David Flaherty, and Professor Hong Yang for being with me and providing guidance throughout my graduate career. I am also extremely grateful towards Professor David Flaherty and Jason Adams for being incredible collaborators and working with Joaquín and me to produce some impactful research.

To my parents, thank you for your endless support and encouragement to achieve my goals. I would not be where I am today without you both. I would also like to thank Alex Bragg for forming and fostering the Urbana Boulders rock climbing community. It may seem minor, but the relationships I established in that group of people have gotten me through particularly rough patches and significantly bolstered my mental health throughout graduate school. Finally, I'd like to thank my older brother David for calling in and making me nervously laugh with good natured ribbing.

Dedicated to Dr. Paul Jasien and Dr. Michael Schmidt for igniting my passion for chemistry and to Dr. James Jancovich for encouraging me to pursue graduate studies.

Table of Contents

Chapter 1:

Alternative H_2O_2 production methods

1.1. Abstract

New, less expensive methods of producing hydrogen peroxide are required for it to be utilized as a green oxidant in the chemical industry. The most attractive alternatives to be discussed in more detail below are electrocatalytic, photocatalytic, and thermal catalytic production of H_2O_2. All of these methods involve reducing O_2 over a catalytic surface in some capacity and each present their own set of advantages to producing H_2O_2 at lower costs.

1.2. Hydrogen peroxide production for industrial applications

Hydrogen peroxide (H_2O_2) is a promising green oxidant that has several prospects in the chemical industry. Due the benign nature of its byproducts (H_2O, O_2), H_2O_2 is poised to supplant chlorinated oxidants which can produce chloroform, chlorinated hydrocarbons, or dioxins as byproducts.[1-3] Several industrial processes (pulp and paper bleaching, textile bleaching, wastewater treatment, synthesis of fine chemicals, etc.) utilize chlorinated oxidants which lead to the formation of several harmful byproducts such as chloroform, chlorinated hydrocarbons, or dioxins.[1,4-6] H_2O_2 is an environmentally benign alternative because the only byproducts from oxidations involving H_2O_2 is water and oxygen. Additionally, H_2O_2 has been shown to be useful for the selective oxidation of short chain alkanes (methane, ethane) to their mono-oxygenated counterparts (methanol, ethanol).[7,8] These innovative reactions can revolutionize methanol and ethanol production by replacing current inefficient processes[9,10] with more selective and efficient methods involving H_2O_2. However, despite the numerous chemical processes H_2O_2 can improve

upon, it is not implemented due to prohibitive costs. Therefore, a new production method must be adopted if H_2O_2 is to be utilized more frequently in the chemical industry.

H_2O_2 is currently produced on the industrial scale using the anthraquinone autoxidation method (AO), shown in Figure 1.1. The AO process produces H_2O_2 by reducing anthraquinone to a hydroquinone counterpart via H_2 treatment over a catalyst. When exposed to oxygen, this hydroquinone is oxidized back to the active anthraquinone species and produces H_2O_2 as a byproduct (Figure 1.1). There are three major factors that are intrinsic to this production method that lead to high costs of H_2O_2. These factors are separation/purification costs, costs of transporting H_2O_2, and overall efficiency of the process.[2] The H_2O_2 that is produced from the AO process needs to be separated from the anthraquinone and organic solvent that the reaction takes place in. These isolation and purification steps result in very complicated reactor designs that lead to much higher costs of production. In terms of scale of production, the AO process is only economically viable on very large scales (~2 x 10^5 tons H_2O_2 $year^{-1}$).[2] This leads to the centralization of the production of H_2O_2 because one plant produces ample H_2O_2 for any application. This then requires that the H_2O_2 is transported to whichever site where it is to be utilized, thus adding further costs due to specific regulations on transporting strong oxidants. The most economically feasible manner to transport H_2O_2 is to do so in a concentrated form (30 wt%) in stainless steel containers that need to be thoroughly cleaned with nitric acid to prevent any unwanted reactions between H_2O_2 and any impurities in the storage tank. Finally, the overall efficiency of the AO process is also fairly low which leads to more costs. Specifically, the reduction of the anthraquinone can lead to several different byproducts that are not the hydroquinone species. For instance, a hydroxyquinone species can form and the oxidation of this chemical does not lead to the formation of H_2O_2. All of these

byproducts must be converted back into the initial anthraquinone species, which leads to additional components in an already complicated reactor design.

There have been examples in recent years of emerging technologies that make H_2O_2 less costly to utilize. One technology that successfully circumvented the transportation costs associated to H_2O_2 is the BASF/Dow hydrogen peroxide propylene oxide (HPPO) plant.[11] At this plant, H_2O_2 made from the AO process is directly used as an oxidant to carry out the conversion of propylene to propylene oxide, a valuable polymer precursor chemical. However, while the process successfully removes transportation costs, it remains infeasible to implement on smaller scales. An ideal alternative to the AO process would be one that requires little to no separations, can be more easily implemented near or at the location in which the H_2O_2 will be used, and is highly selective toward producing H_2O_2.

1.3. Alternative H_2O_2 production methods

1.3.1. Photoelectrocatalysis

There have been reports of several alternatives to the AO process including photoelectrocatalysis, electrocatalysis, and direct synthesis. The literature on photoelectrochemical production of H_2O_2 typically involves a material that both absorbs light and carries out the conversion of O_2 to H_2O_2.[12-14] The most common example of photoelectrochemical production of H_2O_2 is through the use of TiO_2 nanoparticles that absorb light to form excited electron-hole pairs. The electrons are used to reduce O_2 to form H_2O_2 and the holes go to a sacrificial reagent added to solution (ethanol, Cu^+).[12,13] The biggest issues with this method are the relatively low yields of H_2O_2 and the fact that a sacrificial reagent must be added in order for the process to effectively produce H_2O_2 at all. There is also the question of stability of H_2O_2 that is

produced in the presence of the sacrificial reagent. Species such as ethanol and Cu^{+} are readily oxidized, and will likely oxidize in the presence of H_2O_2, thus adding another complication to this process of utilizing TiO_2 semiconducting nanoparticles. Also, the presence of such sacrificial reagents does not eliminate the requirement for separation and purification steps downstream in this production process, which makes it difficult for this approach to compete with the AO process.

In recent years, much more compelling reports of photoelectrochemical production of H_2O_2 have been published and involve using g-C_3N_4 components to absorb visible light to drive H_2O_2 production.[14] This report utilizes metal free catalysts in the form of graphitic carbon nitride and also is advantageous from a light absorbing perspective. Traditionally used n-type semiconducting nanoparticles such as TiO_2 have a band gap that limits their light absorption to the UV region of light, while the g-C_3N_4 catalysts can absorb well into the visible spectrum, as is demonstrated in the study. Visible light absorption of an H_2O_2 photocatalyst is an important characteristic when considering the bond stability of H_2O_2. It is well known that the O-O bond in peroxide species photodissociates in the presence of UV light. Therefore, it would be deleterious for a H_2O_2 photocatalyst to require UV light, when the same light source would inevitably degrade any H_2O_2 formed in this process. The biggest disadvantages to this production method are that the g-C_3N_4 still rely on sacrificial reagents and are also possess poor light conversion efficiencies. Due to the poor activity under illumination, this process produces a solution of H_2O_2 that is 30 μmol after 12 h of reaction time. This is extremely low when considering traditional industrial processes utilize concentrations of H_2O_2 at about 30 wt.%, or about 10 M. The utilization of photocatalysts to produce H_2O_2 would be most effective if the process could utilize more efficient light absorbers, but also remove the issue of H_2O_2 photodissociating in UV light.

1.3.2. Electrocatalytic reduction of O_2

A more common alternative H_2O_2 production method is the electrocatalytic reduction of O_2. The Dow process is an industrial H_2O_2 production method based on electrocatalysis and it involves the reduction of O_2 to form H_2O_2 at a carbon-based cathode while an anode half-cell carries out oxygen evolution.[15] This method generates a ~2.1% w/w H_2O_2 product with 95% current efficiency. The biggest limitation to this approach is the use of a resistive ionic membrane to separate the anode and cathode half cells, which leads to rather low production rates of H_2O_2. Additionally, the catalysts used are simple carbon-based materials with the intention of minimizing cost of the overall system. While generally selective toward H_2O_2, carbon-based catalysts typically display higher overpotentials toward ORR compared to other, more state-of-the-art catalysts. Decreasing the catalyst overpotentials while maintaining the cost effectiveness introduced by carbon-based catalysts would be of great interest.

In order to better understand how H_2O_2 is formed through ORR, knowledge of the mechanism is paramount. However, this topic has been one of great discussion for decades, and there is still no generally accepted rate determining mechanistic steps to how ORR occurs on an electrocatalytic surface. It is rather difficult to pin down one dominant mechanism that presides over ORR, as the Tafel slope for the reaction is both pH and potential dependent.[16] The Tafel slope for a given catalyst changes with pH and overpotential, which implies different rate determining steps in each scenario. Despite the lack of consensus on a detailed microkinetic model for ORR, it is generally accepted is that the mechanistic step that leads to H_2O formation instead of H_2O_2 formation involves splitting the O-O bond in O_2.[16-19] The most commonly discussed kinetic steps are shown below:

$$OOH^* + e^- + H_3O^+ \rightarrow OOH^{-*} + H_3O^+ \quad (1.1)$$

$$OOH^* + e^- + H_3O^+ \rightarrow OH^- + O^* + H_3O^+ \quad (1.2)$$

Where reaction 1.1 depicts the preservation of the O-O bond, ultimately leading to the formation of H_2O_2, and in reaction 1.2 the O-O bond is cleaved leading to the formation of H_2O. The selectivity for a given catalyst to carry out reaction 1 and form H_2O_2 is a thoroughly researched area in the electrocatalytic literature. Figure 1.2 shows the selectivity of commonly used catalyst materials to carry out H_2O_2 conversion. Metals like Au and Pd are generally referred as "good" H_2O_2 catalysts while materials like Pt are well-known to predominately carry out the 4-electron reduction of O_2. It has been shown through kinetic isotope effects that catalysts that form H_2O_2 tend to have rate determining steps involving proton-coupled transfer reactions.[20] Specifically, it is postulated that the electron transfer kinetics from the catalyst to O_2 must be slower than the proton transfer kinetics in order for H_2O_2 to form more preferentially than H_2O. These observations are both useful for guiding catalyst design for catalysts that demonstrate higher H_2O_2 yields. A catalyst that is selective towards H_2O_2 formation would therefore operate in a way that preserves the O-O bond and there are a number of methods in the electrocatalytic literature to achieving this goal.

The other methods employed to increase H_2O_2 selectivity is through the use of ensemble and electronic effects.[17,21-23] Ensemble effects refer to diluting active metals in a "sea" of relatively inactive metals. The rationale behind this is to limit the number of sites to which O_2 can bind, thus inhibiting the catalyst's ability to split the O-O bond and forcing it to only produce H_2O_2. Ensemble effects are a means of reducing chemical dissociation of OOH* to OH* and rely on the presence of relatively inactive metals that are stable across a large potential range and do not corrode into solution. Common candidates to fulfill the goals of ensemble effects are metals such as Au or Hg. Both of these metals display low catalytic activity toward ORR at low overpotentials, making them

an efficient diluent for more active metals such as Pt or Pd. Ensemble effects are also achievable without the utilization of metal atoms, as is shown with Co or Fe porphyrin species. These catalysts are selective towards H_2O_2 formation because the most catalytically active sites towards O_2 are the metal centers, which are far from each other in space due to the nitrogen and carbon-based ligands separating them. Although these catalysts are show high selectivity and reactivity towards H_2O_2 formation, they are plagued with poor stability as the N_4 ligands are prone to degradation from H_2O_2.

The other method by which researchers control H_2O_2 yield is through electronic effects. This refers to a thermodynamic phenomenon in which a metal active towards O_2 reduction is alloyed with an electron withdrawing metal. The aim of this approach is to control the binding energy of the O_2 active metal to prevent it from interacting with O_2 too strongly and splitting the O-O bond.[17] The electrocatalytic community typically refers to volcano plots showing the binding energy of OOH* and OH* to discuss this concept. It generally accepted that if an electrocatalyst binds the OOH* intermediate more strongly than the OH* intermediate, then the catalyst will be more selective toward H_2O_2 formation.[17] In the electrocatalytic H_2O_2 production literature, these ensemble and electronic effects are often employed, with some of the most efficient catalysts reported being PdAu, PdHg, and PtHg alloys.[17,21,24]

1.3.3. Direct Synthesis from O_2 and H_2

Among the most compelling alternatives to the AO process is the direct synthesis (DS) of H_2O_2 from elemental forms of hydrogen and oxygen. This process produces H_2O_2 in an aqueous solution with minimal use of separations and organic solvents.[2,3,25,26] The direct synthesis process has also been shown in an economic analysis to be more viable than the AO process on smaller scales of production.[3] Therefore, direct synthesis is a strong contender for supplanting the AO

process since it can be implemented on site and produces H_2O_2 with less energy and more economic efficiency. However, low H_2O_2 conversion efficiencies plague DS when the process is carried out in neutral conditions and the most effective catalysts utilize noble metals such as Pd and Au.[26]

New efficient and inexpensive catalysts must be utilized in order for DS to gain traction in the chemical industry. When considering the design of these catalysts, knowledge of the mechanism by which H_2O_2 is formed in DS is paramount. The topic of H_2O_2 formation mechanism in direct synthesis has received a great deal of attention over the years and there is still no one single mechanism that is generally agreed upon. The most predominantly suggested mechanism is based on Langmuir-Hinshelwood type kinetics in which H_2 and O_2 both bind to a catalyst, interact on the surface to form H_2O_2, and detach from said catalyst.[27-29] There are many detailed studies that perform kinetic analyses to determine how H_2O_2 formation rates depend on H_2 and O_2 concentrations. Other reports vary the type of reactors in which H_2O_2 is formed via direct synthesis and identify kinetically relevant steps in the reaction.[30] Despite this vast amount of research, it is difficult to say that all the performed experiments suggest the presence of this type of mechanism.

There has also been significant computational research done on direct synthesis to determine important catalytic factors that determine H_2O_2 yields.[31,32] Such studies have identified that the most kinetically relevant steps in direct synthesis are how the catalyst binds O_2 and how this binding affects the retention or splitting of the O-O bond. Such observations have been supported by the fact that alloying typical direct synthesis catalysts (e.g. Pd) with metals that withdraw electron density (e.g. Au) result in an increase in H_2O_2 selectivity. This is similar to the ensemble and electronic effects utilized in the electrocatalytic literature.

An alternative H_2O_2 formation mechanism that has been proposed in direct synthesis is that the H_2O_2 is formed through proton-coupled electron transfers (PCETs). This mechanism follows a Langmuir-Rideal type scheme in which the O_2 binds to the direct synthesis catalyst and interacts with protons in solution to form H_2O_2. Initial reports of this mechanism were rather incomplete because they proposed proton-coupled electron transfers because it was observed that a more oxidized Pd surface carried out H_2O_2 formation more rapidly.[33] Because of this, the authors proposed that H_2 does not bind at all. A more complete analysis of this mechanism was reported in recent years in which it was proposed that H_2O_2 is formed from O_2 in direct synthesis through a proton-coupled electron transfer, and the H_2 provides the chemical potential needed to drive this reaction.[34] In this study, aspects such as H_2/O_2 partial pressures, pH, and the type of solvent (protic or aprotic) were altered, and all results suggested the presence of a mechanism involving H_2 oxidation acting as the driving force for a PCET. For instance, it was observed that all H_2 formation rates were unmeasurable in aprotic solvents and in the absence of H_2. This suggests that protons are required for the PCET and the H_2 is required to provide the potential necessary to drive this reaction. From an electrochemical point of view, it can be stated that in direct synthesis, the catalyst is carrying out the hydrogen oxidation reaction (HOR) and 2-electron oxygen reduction reaction (ORR) in concert.[34] This proposed mechanism presents an interesting opportunity to capitalize upon the electrochemical literature to guide catalyst design in direct synthesis. For instance, based on this hypothesis, it should be possible to measure electrochemical kinetic parameters and correlate it to catalysts performing direct synthesis. Shown in Figure 1.3 is the effect of these electrochemical parameters. The rate constants, k^0, determine the overpotential range for the catalyst to carry out HOR and ORR. The amount of overlap between these two reactions should

be intimately related for a given catalyst's ability to carry out direct synthesis. Further research on this topic is discussed in depth in Chapter 4.

1.4. Figures

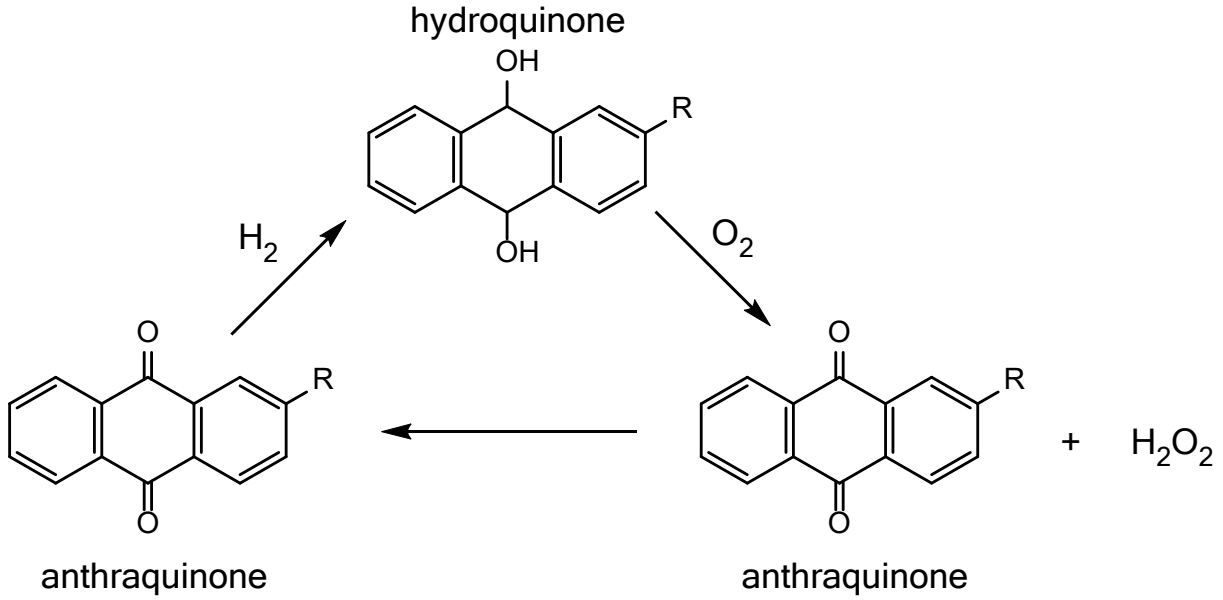

Figure 1.1 Schematic for the anthraquinone process of forming H_2O_2. Not shown here is the multitude of undesired hydroquinone and oxanthrone species that form upon exposing the anthraquinone to a reductive treatment (H_2). For each of these deleterious side products, there is a process required to reform the initial anthraquinone species to react again, which further increases the energy requirements of this process.

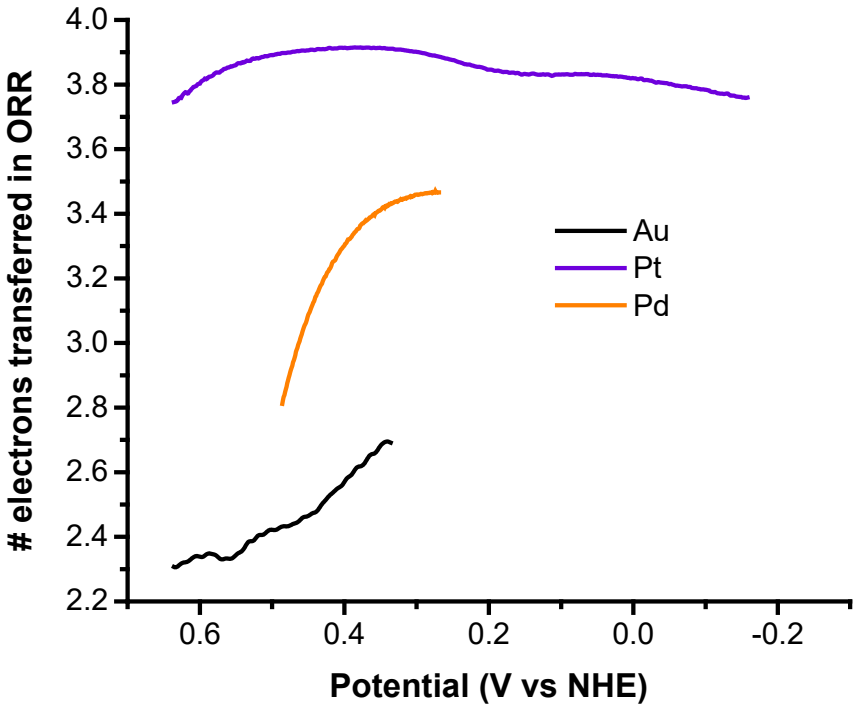

Figure 1.2 Plot of number of electrons transferred in ORR as a function of potential for various catalysts. The data shown here is specific to 0.1 M H_2SO_4 electrolyte. This analysis is especially important for catalysts like Pd because the H_2O_2 selectivity of Pd changes drastically as a function of overpotential. The methods by which these plots are generated are discussed in more detail in Chapter 2.

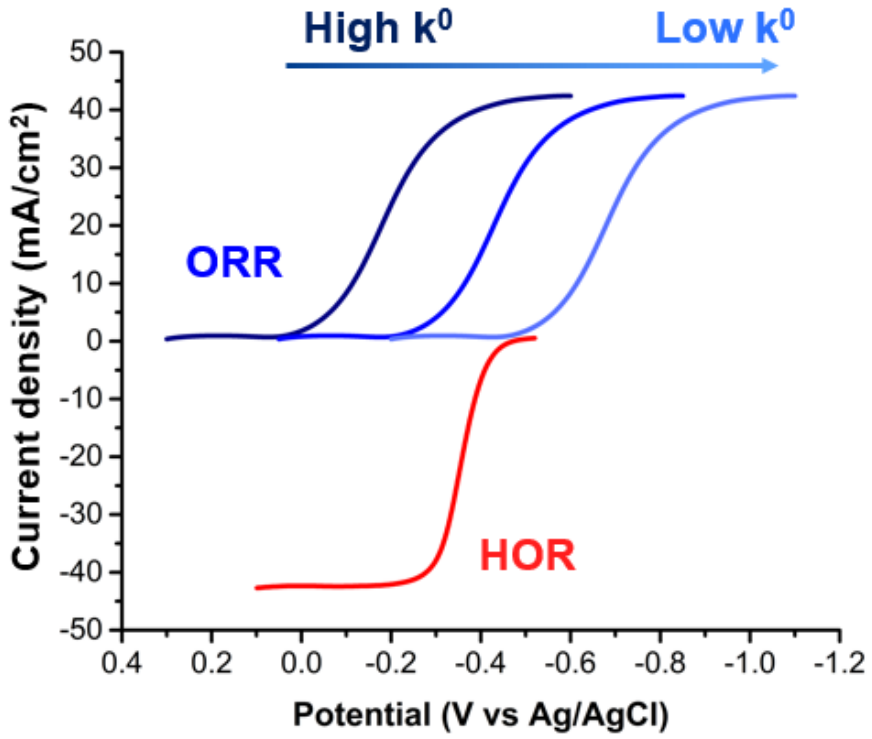

Figure 1.3 Shown here is the impact of electrochemical kinetics (k^0) on the overpotential for ORR. In this case, it would be advantageous for a catalyst to exhibit facile kinetics (dark blue ORR trace) in order to maximize overlap in activity for ORR and HOR.

1.5. References

(1) Goor, G.; Glenneberg, J.; Jacobi, S.: Hydrogen Peroxide. In *Ullmann's Encyclopedia of Industrial Chemistry*; Wiley-VCH Verlag GmbH & Co.: Veinheim, Germany 2007.

(2) Campos-Martin, J. M.; Blanco-Brieva, G.; Fierro, J. L. G. Hydrogen peroxide synthesis: An outlook beyond the anthraquinone process. *Angew. Chem. Int. Ed.* **2006**, *45*, 6962-6984.

(3) Garcia-Serna, J.; Moreno, T.; Biasi, P.; Cocero, M. J.; Mikkola, J. P.; Salmi, T. O. Engineering in direct synthesis of hydrogen peroxide: targets, reactors and guidelines for operational conditions. *Green Chem.* **2014**, *16*, 2320-2343.

(4) Sedlak, D. L.; von Gunten, U. The Chlorine Dilemma. *Science* **2011**, *331*, 42-43.

(5) Kosaka, K.; Yamada, H.; Shishida, K.; Echigo, S.; Minear, R. A.; Tsuno, H.; Matsui, S. Evaluation of the treatment performance of a multistage ozone/hydrogen peroxide process by decomposition by-products. *Water Res.* **2001**, *35*, 3587-3594.

(6) Ragnar, M.; Henriksson, G.; Lindström, M. E.; Wimby, M.; Blechschmidt, J.; Heinemann, S.: Pulp In *Ullmann's Encyclopedia of Industrial Chemistry*; Wiley-VCH, Ed.; Wiley-VCH: Veinheim, Germany, 2014.

(7) Hammond, C.; Forde, M. M.; Ab Rahim, M. H.; Thetford, A.; He, Q.; Jenkins, R. L.; Dimitratos, N.; Lopez-Sanchez, J. A.; Dummer, N. F.; Murphy, D. M.; Carley, A. F.; Taylor, S. H.; Willock, D. J.; Stangland, E. E.; Kang, J.; Hagen, H.; Kiely, C. J.; Hutchings, G. J. Direct Catalytic Conversion of Methane to Methanol in an Aqueous Medium by using Copper-Promoted Fe-ZSM-5. *Angew. Chem. Int. Ed.* **2012**, *51*, 5129-5133.

(8) Forde, M. M.; Armstrong, R. D.; Hammond, C.; He, Q.; Jenkins, R. L.; Kondrat, S. A.; Dimitratos, N.; Lopez-Sanchez, J. A.; Taylor, S. H.; Willock, D.; Kiely, C. J.; Hutchings,

G. J. Partial Oxidation of Ethane to Oxygenates Using Fe- and Cu-Containing ZSM-5. *J. Am. Chem. Soc.* **2013**, *135*, 11087-11099.

(9) Ott, J.; Gronemann, V.; Pontzen, F.; Fiedler, E.; Grossmann, G.; Kersebohm, D. B.; Weiss, G.; Witte, C.: Methanol. In *Ullmann's Encyclopedia of Industrial Chemistry*; Wiley-VCH Verlag GmbH & Co.: Veinheim, Germany, 2012.

(10) Kosaric, N.; Duvnjack, Z.; Farkas, A.; Sahm, H.; Bringer-Meyer, S.; Goebel, O.; Mayer, D.: Ethanol. In *Ullmann's Encyclopedia of Industrial Chemistry*; Wiley-VCH Verlag GmbH & Co.: Veinheim, Germany, 2011.

(11) Russo, V.; Tesser, R.; Santacesaria, E.; Di Serio, M. Chemical and Technical Aspects of Propene Oxide Production via Hydrogen Peroxide (HPPO Process). *Ind. Eng. Chem. Res.* **2013**, *52*, 1168-1178.

(12) Foster, N. S.; Noble, R. D.; Koval, C. A. Reversible Photoreductive Deposition and Oxidative Dissolution of Copper Ions in Titanium-Dioxide Aqueous Suspensions. *Environ. Sci. Technol.* **1993**, *27*, 350-356.

(13) Teranishi, M.; Naya, S.; Tada, H. In Situ Liquid Phase Synthesis of Hydrogen Peroxide from Molecular Oxygen Using Gold Nanoparticle-Loaded Titanium(IV) Dioxide Photocatalyst. *J. Am. Chem. Soc.* **2010**, *132*, 7850.

(14) Shiraishi, Y.; Kanazawa, S.; Kofuji, Y.; Sakamoto, H.; Ichikawa, S.; Tanaka, S.; Hirai, T. Sunlight-Driven Hydrogen Peroxide Production from Water and Molecular Oxygen by Metal-Free Photocatalysts. *Angew. Chem. Int. Ed.* **2014**, *53*, 13454-13459.

(15) Foller, P. C.; Bombard, R. T. Processes for the Production of Mixtures of Caustic Soda and Hydrogen-Peroxide via the Reduction of Oxygen. *J.Appl. Electrochem.* **1995**, *25*, 613-627.

(16) Holewinski, A.; Linic, S. Elementary Mechanisms in Electrocatalysis: Revisiting the ORR Tafel Slope. *J. Electrochem. Soc.* **2012**, *159*, H864-H870.

(17) Siahrostami, S.; Verdaguer-Casadevall, A.; Karamad, M.; Deiana, D.; Malacrida, P.; Wickman, B.; Escudero-Escribano, M.; Paoli, E. A.; Frydendal, R.; Hansen, T. W.; Chorkendorff, I.; Stephens, I. E. L.; Rossmeisl, J. Enabling direct H_2O_2 production through rational electrocatalyst design. *Nat. Mater.* **2013**, *12*, 1137-1143.

(18) Shinagawa, T.; Garcia-Esparza, A. T.; Takanabe, K. Insight on Tafel slopes from a microkinetic analysis of aqueous electrocatalysis for energy conversion. *Sci. Reports* **2015**, *5*.

(19) Fernandez, J. L.; Walsh, D. A.; Bard, A. J. Thermodynamic guidelines for the design of bimetallic catalysts for oxygen electroreduction and rapid screening by scanning electrochemical microscopy. M-Co (M : Pd, Ag, Au). *J. Am. Chem. Soc.* **2005**, *127*, 357-365.

(20) Tse, E. C. M.; Varnell, J. A.; Hoang, T. T. H.; Gewirth, A. A. Elucidating Proton Involvement in the Rate-Determining Step for Pt/Pd-Based and Non-Precious-Metal Oxygen Reduction Reaction Catalysts Using the Kinetic Isotope Effect. *J. Phys. Chem. Lett.* **2016**, *7*, 3542-3547.

(21) Ham, H. C.; Hwang, G. S.; Han, J.; Nam, S. W.; Lim, T. H. On the Role of Pd Ensembles in Selective H_2O_2 Formation on PdAu Alloys. *J. Phys. Chem. C* **2009**, *113*, 12943-12945.

(22) Jirkovsky, J. S.; Panas, I.; Ahlberg, E.; Halasa, M.; Romani, S.; Schiffrin, D. J. Single Atom Hot-Spots at Au-Pd Nanoalloys for Electrocatalytic H_2O_2 Production. *J. Am. Chem. Soc.* **2011**, *133*, 19432-19441.

(23) Sun, Y. Y.; Sinev, I.; Ju, W.; Bergmann, A.; Dresp, S.; Kuhl, S.; Spori, C.; Schmies, H.; Wang, H.; Bernsmeier, D.; Paul, B.; Schmack, R.; Kraehnert, R.; Roldan Cuenya, B.; Strasser, P. Efficient Electrochemical Hydrogen Peroxide Production from Molecular Oxygen on Nitrogen-Doped Mesoporous Carbon Catalysts. *ACS Catal.* **2018**, *8*, 2844-2856.

(24) Verdaguer-Casadevall, A.; Deiana, D.; Karamad, M.; Siahrostami, S.; Malacrida, P.; Hansen, T. W.; Rossmeisl, J.; Chorkendorff, I.; Stephens, I. E. L. Trends in the Electrochemical Synthesis of H_2O_2: Enhancing Activity and Selectivity by Electrocatalytic Site Engineering. *Nano Lett.* **2014**, *14*, 1603-1608.

(25) Crole, D. A.; Freakley, S. J.; Edwards, J. K.; Hutchings, G. J. Direct synthesis of hydrogen peroxide in water at ambient temperature. *Proc. Math. Phys. Eng. Sci.* **2016**, *472*.

(26) Samanta, C. Direct synthesis of hydrogen peroxide from hydrogen and oxygen: An overview of recent developments in the process. *Appl. Catal. A* **2008**, *350*, 133-149.

(27) Edwin, N. N.; Edwards, J. K.; Carley, A. F.; Lopez-Sanchez, J. A.; Moulijn, J. A.; Herzing, A. A.; Kiely, C. J.; Hutchings, G. J. The role of the support in achieving high selectivity in the direct formation of hydrogen peroxide. *Green Chem.* **2008**, *10*, 1162-1169.

(28) Ford, D. C.; Nilekar, A. U.; Xu, Y.; Mavrikakis, M. Partial and complete reduction of O-2 by hydrogen on transition metal surfaces. *Surface Sci.* **2010**, *604*, 1565-1575.

(29) Rankin, R. B.; Greeley, J. Trends in Selective Hydrogen Peroxide Production on Transition Metal Surfaces from First Principles. *ACS Catal.* **2012**, *2*, 2664-2672.

(30) Voloshin, Y.; Halder, R.; Lawal, A. Kinetics of hydrogen peroxide synthesis by direct combination of H_2 and O_2 in a microreactor. *Catal.* **2007**, *125*, 40-47.

(31) Deguchi, T.; Iwamoto, M. Catalytic Properties of Surface Sites on Pd Clusters for Direct H_2O_2 Synthesis from H_2 and O_2: A DFT Study. *J. Phys. Chem. C* **2013**, *117*, 18540-18548.

(32) Grabow, L. C.; Hvolbaek, B.; Falsig, H.; Norskov, J. K. Search Directions for Direct H_2O_2 Synthesis Catalysts Starting from Au-12 Nanoclusters. *Top. Catal.* **2012**, *55*, 336-344.

(33) Abate, S.; Centi, G.; Melada, S.; Perathoner, S.; Pinna, F.; Strukul, G. Preparation, p erformances and reaction mechanism for the synthesis of H_2O_2 from H_2 and O_2 based on palladium membranes. *Catal.* **2005**, *104*, 323-328.

(34) Wilson, N. M.; Flaherty, D. W. Mechanism for the Direct Synthesis of H_2O_2 on Pd Clusters: Heterolytic Reaction Pathways at the Liquid-Solid Interface. *J. Am. Chem. Soc.* **2016**, *138*, 574-586.

Chapter 2:

Electroanalytical methods for H_2O_2 detection: Quantifying kinetics for ORR and electrochemical detection of H_2O_2

2.1. Abstract

Detailed here is the analytical aspects that act as a foundation for studies performed in future chapters. Because each of the alternative H_2O_2 production methods of interest all involve the electrochemical reduction of O_2, the kinetics of each type of catalyst were quantified with similar electrochemical methods. Additionally, in each of the alternative H_2O_2 production methods of interest, the H_2O_2 is detected electrochemically as this method enables *in situ* and quantitative detection that is not possible with other methods. The electrochemical detection of H_2O_2 is described in experimentally relevant setups such as scanning electrochemical microscopy and rotating disk electrode methods.

2.2. Electrochemical quantification of ORR kinetics

2.2.1. Rotating disk electrode methods

Rotating disk electrode (RDE) methods are a commonly employed electroanalytical technique for quantifying relevant kinetic parameters. RDE methods involve rotating a bulk electrode fixed to a rotating shaft to generate a specific flow profile in which electroactive species is brought to the electrode surface in a controlled manner. As is shown in Figure 2.1, this results in a peak in current due to a growing diffusion layer that is commonly observed in quiescent solutions. In RDE, kinetic parameters are quantifiable through a Koutecky-Levich analysis. For systems displaying fast electron transfer kinetics, the current-potential profile in this setup behaves according to Butler-Volmer kinetics similar to quiescent systems at low overpotentials. However,

upon reaching higher overpotentials to where the electrode reaches a mass transfer limit, which is described with the Levich equation.[1]

$$i_{lim} = 0.62nFAD_o^{2/3}\nu^{-1/6}C_o^*\omega^{1/2} \quad (2.1)$$

Where i is current, n is number of electrons, F is Faraday's constant, A is geometric area of electrode, D_o is the diffusion coefficient, ν is the kinematic viscosity of the liquid in which the electrode is being rotated, C_o^* is the concentration of electroactive species in the bulk solution, and ω is the rotation rate of the electrode. This expression predicts a linear increase in limiting current with $\omega^{-1/2}$. This relation begins to break down at very high rotation rates for systems with rather sluggish electron transfer kinetics because the electrochemical reaction becomes limited by electron transfer kinetics rather than mass transfer. Despite the rotation rate and mass transfer to the electrode increasing, the transfer of the electron into or out of the electroactive molecule is too slow, and the current becomes limited by this phenomenon. For systems with rather sluggish kinetics, one can perform a Koutecky-Levich analysis[1,2] (Figure 2.2B) to acquire kinetic parameters associated with the electron transfer. The underlying assumption for the Koutecky-Levich analysis is that if the rotation rate affects the current at steady state (mass-transfer limited), then it likely affects the current at all potentials. This would result in an offset in current at every potential that takes the form shown below:

$$\frac{1}{i} = \frac{1}{i_L} + \frac{1}{i_k} \quad (2.2)$$

Where i_L is the current contributed from a typical Levich response, and i_K represents the current that flows in the absence of mass transfer effects. Alternatively, i_k can be defined as the current that would flow if the rotating electrode was able to maintain the bulk concentration of

electroactive species at the surface of the electrode (i.e. rotating infinitely fast). For electrochemical systems with fast electron transfer kinetics, a plot of i^{-1} vs. $\omega^{-1/2}$ will approach the origin in the limit of infinite rotation rate. This is because the electron transfer is occurring sufficiently fast and the system is able to maintain the bulk concentration of electroactive species at the surface of the electrode. However, if the system displayed sluggish electron transfer kinetics, as is the case for ORR, a plot of i^{-1} vs. $\omega^{-1/2}$ will have a non-zero intercept. Such a result is due to the fact that as the rotation rate approaches infinity, the system will be limited by the sluggish electron transfer kinetics. This current offset is referred to as i_k and takes the following form:

$$i_k = nFAk_fC_o^* \tag{2.3}$$

This k_f value is a potential dependent parameter (as defined by Butler-Volmer kinetics). The potential independent standard rate constant, k^0, can be quantified using k_f using the Butler-Volmer expression shown below:

$$k_f = k^0 e^{-\alpha f(E-E^0)} \quad \text{or} \quad \ln(k_f) = -\alpha f(E - E^0) + \ln(k^0) \tag{2.4}$$

By acquiring this k_f value at a variety of potentials and plotting it vs. $E\text{-}E^0$ for ORR, it is possible to derive k^0 and α. For the context of ORR electrocatalysts, these parameters are important to quantify as they represent a useful metric for the overall facility of a given catalyst's ability to transfer electrons to O_2. It is worthwhile to note that an electrochemical system must exhibit rather sluggish kinetics in order for this type of analysis to be possible. In systems with faster kinetics, the intercept in a Koutecky-Levich plot (i^{-1} vs. $\omega^{-1/2}$) will approach the origin, thus erroneously predicting infinitely fast kinetics for the system.

2.2.2. Scanning electrochemical microscopy

Relevant kinetic parameters (k^0 and α) are also able to be quantified through scanning electrochemical microscopy (SECM). SECM is a scanning probe technique that involves scanning an ultramicroelectrode (UME) over a substrate of interest.[3] Through the feedback mode of this technique, one can quantify kinetic parameters. If the UME used in SECM is positioned over a conductive surface, the UME can experience positive feedback. For instance, if the UME is carrying out the reaction $O + e^- \rightarrow R$, and the conductive substrate is biased to carry out the oxidation of species R, the current of the UME will increase. The nature of this increase will be dependent on the substrate's ability to perform the reverse reaction. Figure 2.3 shows example feedback responses for a UME over a substrate with different kinetics for performing positive feedback. Using established theory,[4] these approach curves can be fit to acquire relevant kinetics parameters. The advantage of this technique over RDE is that SECM can probe much faster kinetics and is not limited to sluggish kinetic parameters like RDE. Specifically, RDE is unable to quantify rate constants (k^0) values that exceed ~10^{-3} cm/s. A Koutecky-Levich analysis typically overestimates electron transfer rates for a system with facile (>10^{-2} cm/s) kinetics. Because SECM is able to probe much faster kinetics, and is able to efficiently quantify rate constants on the order of 10 cm/s. The biggest reason for this difference is because of mechanical limitations in RDE. In order to probe fast kinetics, the electrode must be rotated extremely fast to the RPM values that are not achievable with modern rotary motors. Of interest in this work is the ability of SECM to quantify the reactivity of a catalyst to perform oxygen reduction.

2.3. Electrochemical detection of H_2O_2

2.3.1. Electrochemical sensors for H_2O_2

There are a multitude of methods by which H_2O_2 can be detected in experiments involving these alternative production methods. Historically, spectroscopic methods such as UV-vis and electron paramagnetic resonance (EPR) have been the most commonly employed.[5-7] In the research detailed here and in future chapters, H_2O_2 is always detected electrochemically. This has an advantage over other techniques in that the H_2O_2 can be detected *in-situ* while other methods of detection require that the solution containing H_2O_2 is transferred to some spectroscopic setup to be detected. The electrochemical detection of H_2O_2 has been studied on several different electrode materials such as Pt, Prussian blue, and others.[8-12] In all the experiments here, Pt was used to detect H_2O_2 because it is stable in many different conditions and the most applicable as a H_2O_2 sensor. Other materials such as Prussian blue have been shown to be much more sensitive to changes in H_2O_2 concentrations, but this material is only stable in very acidic solutions, as the iron in Prussian blue preferentially binds to hydroxide ions.[9] This causes the Prussian blue to dissolve very quickly in higher pH's, thus making Prussian blue unsuitable for anything but acidic solutions

The detection of H_2O_2 on Pt can be carried out either through oxidation or reduction of the H_2O_2. In the literature, the oxidation of H_2O_2 on Pt is much more well researched than the reduction.[10,13] The oxidation of H_2O_2 on Pt is generally accepted to be mediated through a surface oxide on the Pt.[10] The oxidation of H_2O_2 on Pt is very interesting in that it takes place in potential regions of oxide growth on Pt. It has been observed that cyclic voltammograms of Pt in a solution with H_2O_2 result in a shift of the onset potential for H_2O_2 oxidation to lower overpotentials on the return scan.[10] This is because as the potential is scanned positive initially, a Pt oxide forms, and on the return sweep, this oxide causes the oxidation of H_2O_2 to be more favorable. Interestingly,

the mechanism for H_2O_2 oxidation on Pt is assumed to not involve a direct electron transfer to the H_2O_2 from Pt, as is evidenced by the shift of H_2O_2 oxidation to lower overpotentials after forming Pt oxide. It is assumed that the H_2O_2 reduces Pt oxides and it is the reformation of the Pt oxide that gives rise to an anodic signal. Additionally, the optimal potential to detect H_2O_2 has also been extensively addressed in the literature. An optimal potential to detect H_2O_2 is one that re-oxidizes surfaces sites rapidly as H_2O_2 reduces them (>0.8 V vs. Ag/AgCl at pH ~7). Shown in Figure 2.3 is a calibration curve for the detection of H_2O_2 on Pt in neutral solution. As is shown by the curve, the detection of H_2O_2 on a Pt UME is very linear over a very large concentration range. This enables the approximate quantification of H_2O_2 concentration as it is detected. The concentration acquired from this calibration curve is merely an approximation because the electrochemical detection of H_2O_2 is always near the surface of a catalyst producing it. Therefore, the volume of space occupied by the H_2O_2 is much smaller than bulk values, and the actual concentration of H_2O_2 being produced is quite small. The concentrations presented in the calibration curve are all experimentally relevant, as the most concentrated H_2O_2 solutions formed reach ~10 mM.[14-17] Ultimately, it is the ease of fabrication and the vast amount of foundational research of H_2O_2 oxidation on Pt that makes this sensor particularly useful for the experiments presented here.

2.4. Quantification of H_2O_2 selectivity via generation-collection methods

2.4.1. Rotating ring disk electrode methods

The most commonly reported electrochemical detection of H_2O_2 is with rotating ring disk electrode (RRDE) methods.[2,18,19] This technique leverages the flow profile established in a rotating disk electrode experimental setup and utilizes a ring outside of the disk to detect products formed at the ring. For H_2O_2 detection, a Pt ring is the most commonly used material and is held at relevant

biases discussed above. For oxygen reduction studies, the electrocatalytic literature utilizes the following equations to quantify H_2O_2 selectivity:

$$n = \frac{4*i_G}{i_G+(\frac{i_C}{CE})} \tag{2.5}$$

$$\%\ H_2O_2 = \frac{4-n}{2} * 100 \tag{2.6}$$

i_G = generator current
i_C = collector current
CE = collection efficiency

Where the generator current is the current of the disk, and collector current is that of the ring. It is important to note that these expressions are exclusive to ORR, as the maximum number of electrons than can result from equation 2.5 is 4 (for the formation of H_2O) and the minimum value is 2 (for H_2O_2). The collection efficiency is defined by the geometry of the system and can be theoretically quantified with the following equation:[1]

$$CE_{theoretical} = 1 - \sigma_{OD}^2 + \sigma_B^{\frac{2}{3}} - G(\sigma_C) - \sigma_B^{\frac{2}{3}} G(\sigma_A) + \sigma_{OD}^2 G(\sigma_C \sigma_{OD}^3) \tag{2.7}$$

$$G_{(x)} = \frac{1}{4} + \left(\frac{\sqrt{3}}{4\pi}\right) \ln\left[\frac{\left(x^{\frac{1}{3}}+1\right)^3}{x+1}\right] + \left(\frac{3}{2\pi}\right) \arctan\left[\frac{2x^{\frac{1}{3}}-1}{\sqrt{3}}\right] \tag{2.8}$$

$$\sigma_A = \sigma_{ID}^3 - 1 \tag{2.9}$$

$$\sigma_B = \sigma_{OD}^3 - \sigma_{ID}^3 \tag{2.10}$$

$$\sigma_C = \frac{\sigma_A}{\sigma_B} \tag{2.11}$$

$$\sigma_{OD} = \frac{OD_{ring}}{OD_{disk}} \tag{2.12}$$

$$\sigma_{ID} = \frac{ID_{ring}}{OD_{disk}} \quad (2.13)$$

x = distance away from electrode

OD = outer diameter

ID = inner diameter

Equation 2.7 can be interpreted to roughly state that the collection efficiency in RRDE increases as the distance between ring and disk, $(ID_{ring} - OD_{disk})$, decreases and as the surface area of the ring, $\pi\left[\left(\frac{OD_{ring}}{2}\right)^2 - \left(\frac{ID_{ring}}{2}\right)^2\right]$, approaches that of the disk. Typically, the collection efficiency is assessed empirically through a generation-collection experiment involving a simple redox mediator, such as ferrocene or ferricyanide (Figure 2.4). Through these well-established methods, it is possible to quantify the selectivity of a given catalyst to produce H_2O_2 as a function of overpotential towards ORR.

2.4.2. Scanning electrochemical microscopy

Detection of H_2O_2 produced from ORR is also achievable in a scanning electrochemical microscopy (SECM) setup. The UME can be biased to detect products formed at the substrate, much like the ring electrode in RRDE methods. SECM has the added analytical advantage of resolving electrochemical activity with spatial resolution. The substrate generation/tip collection mode (SG/TC) of SECM has been employed in many studies of ORR and has been shown to be an effective method to detect and quantify H_2O_2 production over various catalytic surfaces.[13,20-23] A schematic of an SECM generation-collection experiment and a typical data set is shown in Figure 2.5. The measurement is intrinsically at steady because of the hemispherical diffusion profile at the UME, so no external convention (like in RRDE) is required. Equations 2.1 and 2.2 are also applicable in the case of SECM for determining H_2O_2 selectivity as a function of

overpotential. The major difference between SECM and RRDE methods is that the collection efficiency in SECM is generally much higher,[20] because distances between generator and collector are on the micron length scale, which is not attainable in RRDE. SECM also possesses the added analytical advantage of being able to resolve intermediates that exist on much smaller time scales. The effects of relevant SECM parameters (r_g, L, probe size, and substrate size) on the signal collected in a SG/TC experiment has been well researched and simulated.[20]

2.5. Figures

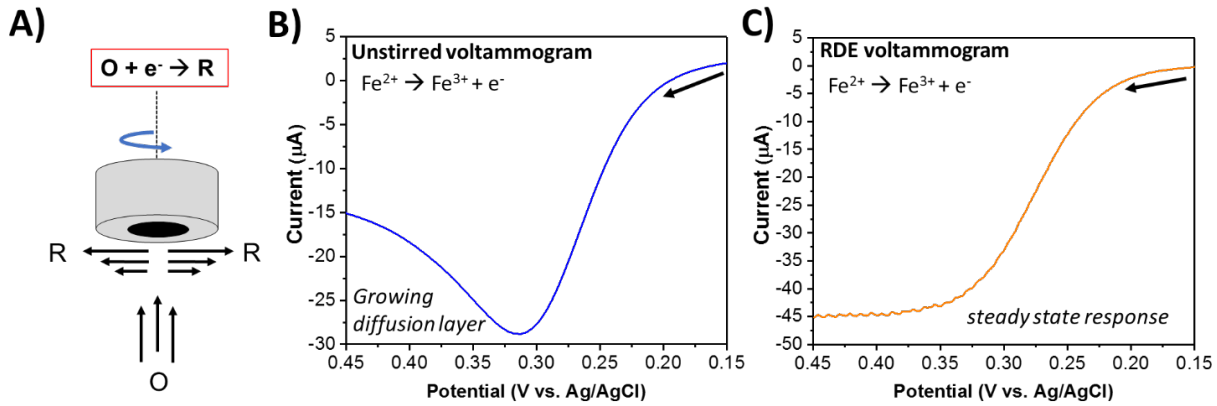

Figure 2.1 A) General schematic for the flow profile in RDE methods. Electroactive species are brought toward the surface of the electrode where electrons are transferred. The rate of mass transfer of species O to the electrode increases with rotation rate, ω. B and C) show how the voltammogram response differs between unstirred voltammetry and RDE methods. Because unreacted electroactive species is constantly brought to the electrode, there is no observed decay in current which is typically due to a growing depletion layer outward from the electrode.

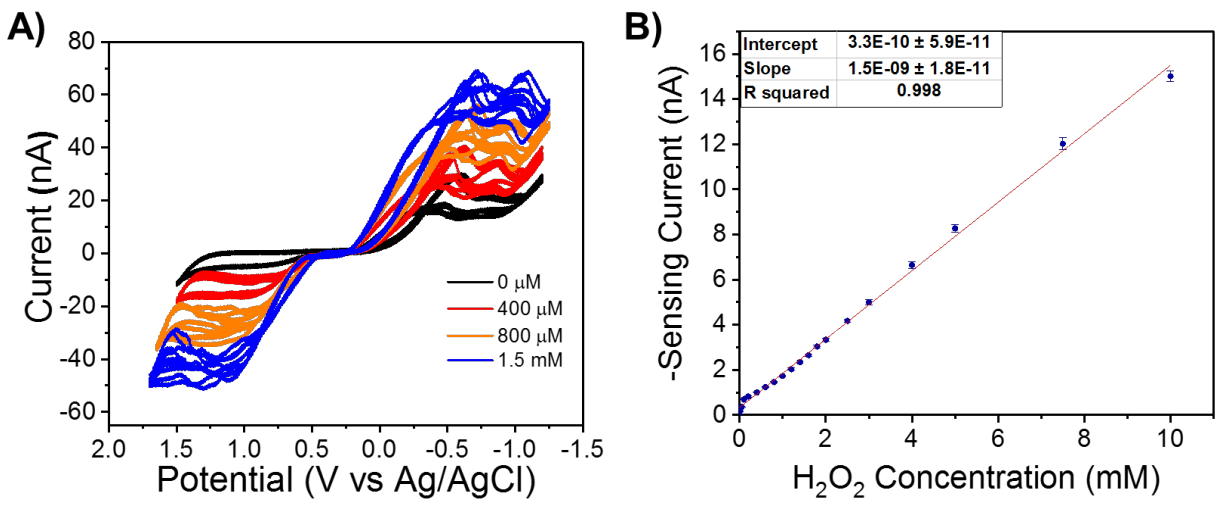

Figure 2.2 A) Shown here is a cyclic voltammogram of Pt in 0.1 M $NaClO_4$ with varying concentrations of H_2O_2 present. Both the reduction and oxidation of H_2O_2 can be carried out by Pt, but the reduction signal overlaps with O_2, making it not as selective of a measurement. The oxidation of H_2O_2 on Pt does involve Pt oxide, and the signal of Pt oxide formation is minimal with appropriate probe pre-treatments (holding at an oxidative potential). B) Calibration curve for Pt oxidizing H_2O_2 which displays the ability for Pt to act as a quantitative H_2O_2 sensor.

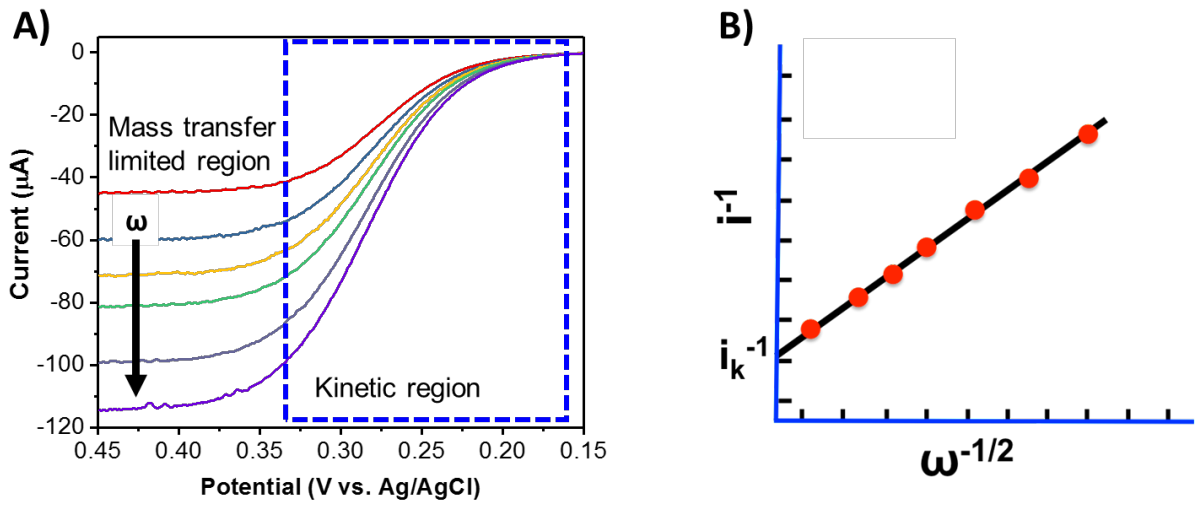

Figure 2.3 A) This is a typical data set for an RDE experiment. Shown here is the oxidation of Fe^{2+} to Fe^{3+} at an RDE with various rotation rates. B) Data points from the kinetic region (blue box in (A)) are collected for each rotation rate at a specific potential (i.e. 0.30 V vs. Ag/AgCl). These data points are plotted as shown in (B) for a Koutecky-Levich analysis. This process is repeated for a range of potentials in the kinetic region, and the intercept acquired from each line is related to a forward rate constant, k_f. A plot of $\ln(k_f)$ vs. $E\text{-}E^0$ (equation 2.4 in text) allows the quantification of k^0 and α of the system.

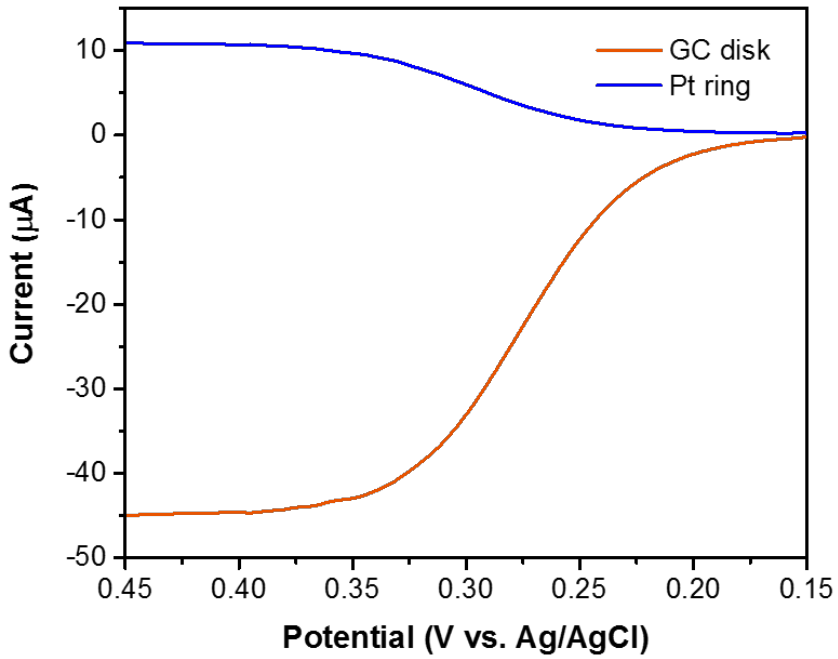

Figure 2.4 Shown here is a generation-collection experiment for an $Fe^{2+/3+}$ system performed with RRDE. This is an empirical method commonly used for determining true collection efficiency. For the geometry of this particular RRDE setup, the theoretical collection efficiency is predicted to be 25%. Displayed in the data above is a collection efficiency of ~24%.

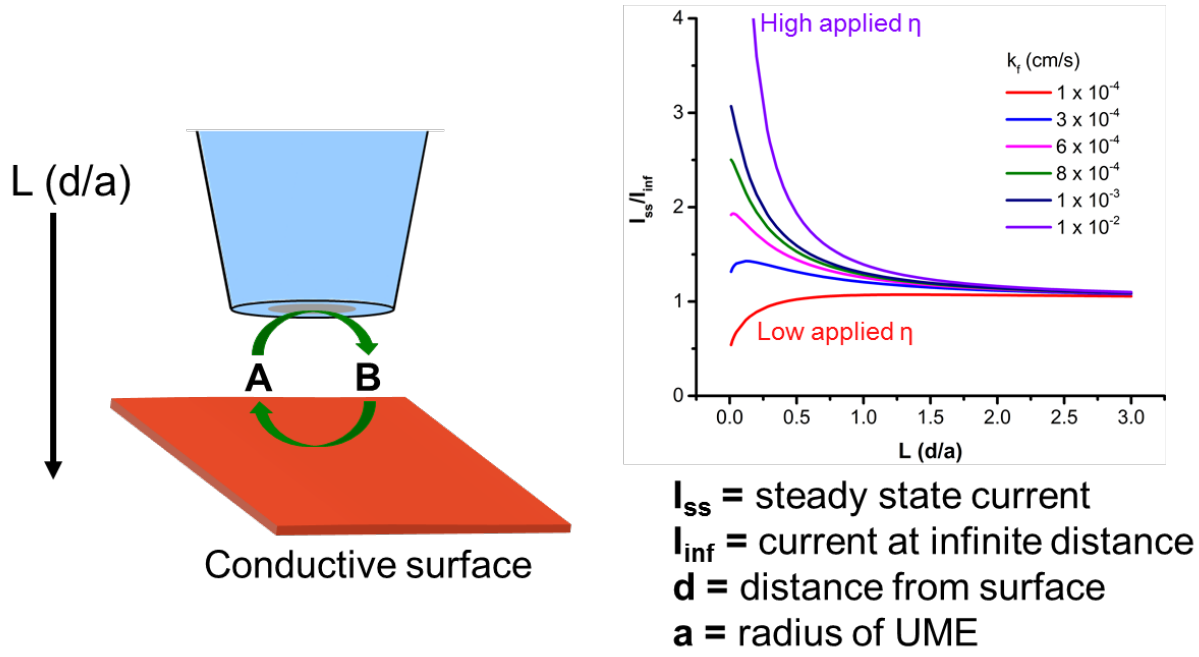

Figure 2.5 Shown here are positive feedback approach curves for SECM. The degree of observed positive feedback will depend on the relative activation of the substrate. Curves collected while the substrate is biased at high overpotentials (η) will display high level of positive feedback and vice versa for low overpotentials. The data plotted above can be utilized to acquire k^0 and α.

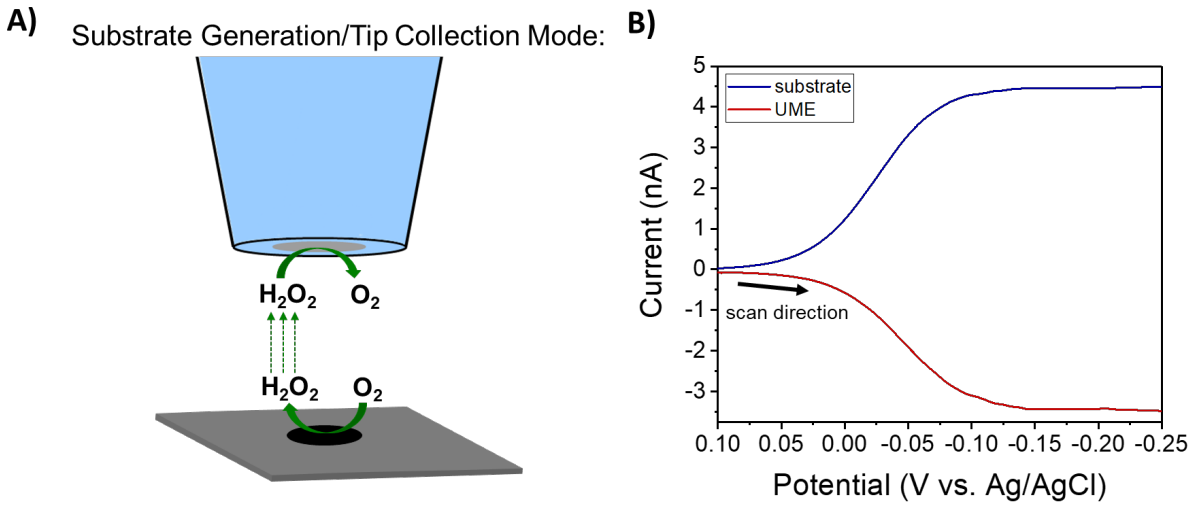

Figure 2.6 A) Schematic for the SG/TC mode of SECM in which H_2O_2 is produced by an electrocatalyst and subsequently oxidized by a Pt UME. B) Typical data set for the collection of H_2O_2 by a UME in an SECM experiment. Note that the UME is held at a constant potential to detect H_2O_2 and is not swept like the substrate.

2.6. References

(1) Bard, A. J.; Faulkner, L. R.: Chapter 9. Electrochemical Methods: Fundamentals and Applications 2nd Edition. John Wiley & Sons Inc.: New York, 2001; pp 331-367.

(2) Maruyama, J.; Inaba, M.; Ogumi, Z. Rotating ring-disk electrode study on the cathodic oxygen reduction at Nafion®-coated gold electrodes. *J. Electroanal. Chem.* **1998**, *458*, 175-182.

(3) Rodríguez-López, J.; Zoski, C. G.; Bard, A. J.: Chapter 16. SECM applications to electrocatalysis and photocatalysis and surface interrogation. In *Scanning Electrochemical Microscopy*; Bard, A. J., Mirkin, M. V., Eds.; CRC Press, 2012; pp 525-568.

(4) Lefrou, C.; Cornut, R. Analytical Expressions for Quantitative Scanning Electrochemical Microscopy (SECM). *Chemphyschem* **2010**, *11*, 547-556.

(5) He, W. W.; Zhou, Y. T.; Wamer, W. G.; Boudreau, M. D.; Yin, J. J. Mechanisms of the pH dependent generation of hydroxyl radicals and oxygen induced by Ag nanoparticles. *Biomater.* **2012**, *33*, 7547-7555.

(6) Fukuzumi, S.; Yamada, Y.; Karlin, K. D. Hydrogen peroxide as a sustainable energy carrier: Electrocatalytic production of hydrogen peroxide and the fuel cell. *Electrochim. Acta* **2012**, *82*, 493-511.

(7) Chen, W.; Chen, J.; Feng, Y. B.; Hong, L.; Chen, Q. Y.; Wu, L. F.; Lin, X. H.; Xia, X. H. Peroxidase-like activity of water-soluble cupric oxide nanoparticles and its analytical application for detection of hydrogen peroxide and glucose. *Analyst* **2012**, *137*, 1706-1712.

(8) Tao, Y.; Ju, E. G.; Ren, J. S.; Qu, X. G. Polypyrrole nanoparticles as promising enzyme mimics for sensitive hydrogen peroxide detection. *Chem. Comm.* **2014**, *50*, 3030-3032.

(9) Karyakin, A. A. Prussian Blue and its analogues: Electrochemistry and analytical applications. *Electroanalysis* **2001**, *13*, 813-819.

(10) Hall, S. B.; Khudaish, E. A.; Hart, A. L. Electrochemical oxidation of hydrogen peroxide at platinum electrodes. Part 1. An adsorption-controlled mechanism. *Electrochim. Acta* **1998**, *43*, 579-588.

(11) Hall, S. B.; Khudaish, E. A.; Hart, A. L. Electrochemical oxidation of hydrogen peroxide at platinum electrodes. Part II: effect of potential. *Electrochim. Acta* **1998**, *43*, 2015-2024.

(12) Chen, W.; Cai, S.; Ren, Q. Q.; Wen, W.; Zhao, Y. D. Recent advances in electrochemical sensing for hydrogen peroxide: a review. *Analyst* **2012**, *137*, 49-58.

(13) Mezour, M. A.; Cornut, R.; Hussien, E. M.; Morin, M.; Mauzeroll, J. Detection of Hydrogen Peroxide Produced during the Oxygen Reduction Reaction at Self-Assembled Thiol-Porphyrin Monolayers on Gold using SECM and Nanoelectrodes. *Langmuir* **2010**, *26*, 13000-13006.

(14) Voloshin, Y.; Halder, R.; Lawal, A. Kinetics of hydrogen peroxide synthesis by direct combination of H_2 and O_2 in a microreactor. *Catal. Today* **2007**, *125*, 40-47.

(15) Wilson, N. M.; Flaherty, D. W. Mechanism for the Direct Synthesis of H_2O_2 on Pd Clusters: Heterolytic Reaction Pathways at the Liquid-Solid Interface. *J. Am. Chem. Soc.* **2016**, *138*, 574-586.

(16) Wilson, N. M.; Schroder, J.; Priyadarshini, P.; Bregante, D. T.; Kunz, S.; Flaherty, D. W. Direct synthesis of H_2O_2 on PdZn nanoparticles: The impact of electronic modifications and heterogeneity of active sites. *J. Catal.* **2018**, *368*, 261-274.

(17) Siahrostami, S.; Verdaguer-Casadevall, A.; Karamad, M.; Deiana, D.; Malacrida, P.; Wickman, B.; Escudero-Escribano, M.; Paoli, E. A.; Frydendal, R.; Hansen, T. W.;

Chorkendorff, I.; Stephens, I. E. L.; Rossmeisl, J. Enabling direct H_2O_2 production through rational electrocatalyst design. *Nat. Mater.* **2013**, *12*, 1137-1143.

(18) Anastasijevic, N. A.; Vesovic, V.; Adzic, R. R. Determinatino of the Kinetic-arameters of the Oxygen Reduction Reaction Using the Rotating-Ring-Disk Electrode. 1. Theory. *J. Electroanal. Chem.* **1987**, *229*, 305-316.

(19) Paulus, U. A.; Schmidt, T. J.; Gasteiger, H. A.; Behm, R. J. Oxygen reduction on a high-surface area Pt/Vulcan carbon catalyst: a thin-film rotating ring-disk electrode study. *J. Electroanal. Chem.* **2001**, *495*, 134-145.

(20) Sanchez-Sanchez, C. M.; Rodiriguez-Lopez, J.; Bard, A. J. Scanning electrochemical microscopy. 60. Quantitative calibration of the SECM substrate generation/tip collection mode and its use for the study of the oxygen reduction mechanism. *Anal. Chem.* **2008**, *80*, 3254-3260.

(21) Sanchez-Sanchez, C. M.; Bard, A. J. Hydrogen Peroxide Production in the Oxygen Reduction Reaction at Different Electrocatalysts as Quantified by Scanning Electrochemical Microscopy. *Anal. Chem.* **2009**, *81*, 8094-8100.

(22) Fernandez, J. L.; Walsh, D. A.; Bard, A. J. Thermodynamic guidelines for the design of bimetallic catalysts for oxygen electroreduction and rapid screening by scanning electrochemical microscopy. M-Co (M : Pd, Ag, Au). *J. Am. Chem. Soc.* **2005**, *127*, 357-365.

(23) Fernandez, J. L.; Mano, N.; Heller, A.; Bard, A. J. Optimization of "wired" enzyme O_2-electroreduction catalyst compositions by scanning electrochemical microscopy. *Angew. Chem. Int. Ed.* **2004**, *43*, 6355-6357.

Chapter 3:

Evaluating the impact of catalyst selection and semiconductor band edge on the photoelectrochemical production of H_2O_2 via a real-time *in situ* probe

The research described in this chapter is part of the unpublished publication submitted and under review titled "Evaluating the impact of catalyst selection and semiconductor band edge on the photoelectrochemical production of H_2O_2 via a real-time in situ probe," by Matthew L. Kromer, Burton H. Simpson, and Joaquín Rodríguez-López. Burton H. Simpson provided useful discussion on experimental design and data interpretation. All other electrochemical experiments and simulations were performed and designed by Matthew L. Kromer and overseen by Joaquín Rodríguez-López.

3.1. Abstract

Generating H_2O_2 through the use of photoelectrochemical cells (PECs) is attractive for integrating renewable energies into the production of this environmentally-friendly chemical oxidant. Here, a PEC is fabricated for producing H_2O_2, establish an effective analytical platform for studying this device, and determine optimal catalysts to use. Specifically, scanning electrochemical microscopy (SECM) is utilized as an analytical technique to measure H_2O_2 production *in-situ* from a PEC and study a variety of electrocatalysts and photocatalysts. The effects of materials properties such as photoanode band edge and H_2O_2 electrocatalyst selectivity are probed here to determine ideal catalytic properties for an optimal H_2O_2 PEC. This work successfully incorporated SECM as an H_2O_2 detection method into a 2-electrode PEC, and it also demonstrates the potential to streamline the discovery of new materials for implementation into a high efficiency H_2O_2 PEC.

3.2. Introduction

Hydrogen peroxide (H_2O_2) is a green oxidant that replaces environmentally harmful chlorinated oxidants[1] in industrial processes such as paper and pulp bleaching and the selective oxidation of alkenes to fine chemicals.[2-4] However, chlorinated oxidants such as Cl_2 or ClO_2 are less expensive to produce and are therefore more prevalent in the chemical industry.[5] The higher production costs of H_2O_2 originate from the anthraquinone autoxidation (AO) process, which involves several isolation and purification steps.[2,3] For H_2O_2 to become an economically feasible substitute for chlorinated oxidants, a more effective, and environmentally benign method potentially using renewable inputs is highly desirable.

Electrochemical production of H_2O_2 is a compelling alternative as it would provide a means of decentralizing H_2O_2 production.[6] A small scale photovoltaic driven electrolyzer (PV-E) or photoelectrochemical cell (PEC) would enable on-site production of H_2O_2 from renewable resources and furthermore eliminate transportation of H_2O_2. The PV-E and PEC approaches have been recently compared toward their economic viability to produce H_2.[7] This analysis suggests that a PEC is more economically viable than a PV-E without any support from grid electricity.[7]

Previous work demonstrating the photocatalytic production of H_2O_2 involves utilizing a single material as both the light absorber and H_2O_2 catalyst. In some cases, H_2O_2 is produced photocatalytically on semiconducting nanoparticles (e.g. TiO_2) in which the photogenerated electrons are used to reduce O_2 to H_2O_2 and photogenerated holes go to some sacrificial regent (e.g. Cu^+, ethanol) in solution.[8-10] Other methods to produce H_2O_2 photocatalytically involve the utilization of g-C_3N_4 photocatalysts that absorb light to become free radical species that react with O_2 to form H_2O_2.[11]

Here, the production of H_2O_2 is explored using a PEC configuration that optimizes the characteristics of photoanode and electrocatalyst half-cells, which has not been extensively reported in the literature. The photoanode uses energy from light to oxidize water and the electrocatalyst subsequently reduces O_2 via the $2e^-$ pathway to form H_2O_2. This PEC configuration is potentially more beneficial because it removes the requirements for a single material to be both an effective light absorber and a H_2O_2 producing catalyst. This configuration also removes the requirements of a sacrificial reagent to scavenge photogenerated holes, which is a common component to other reports on photoelectrochemically produced H_2O_2.[8-10] Additionally, it is crucial to consider the conduction band edge of the photocatalysts used in this two half-cell configuration. A significant research effort in the design of PECs focuses on producing H_2, and the photoanode in those cases would ideally produce photocurrent at potentials that lie negative of the hydrogen evolution reaction. For an H_2O_2 PEC, the onset potential for photocurrent should not be excessively negative because this could result in the H_2O_2 electrocatalyst becoming activated toward H_2 evolution or change its selectivity from a predominant $2e^-$ pathway to the $4e^-$ pathway (Figure 3.1).[14,15,22] The simplest circumvention to this issue it to utilize photoanode materials with a conduction band edge that is positive in energy relative to the hydrogen evolution reaction but sufficiently negative to activate the $2e^-$ oxygen reduction pathway to form H_2O_2.

For proof of concept, various photocatalyst/electrocatalyst combinations were analyzed here to determine optimal characteristics of materials to be used in an H_2O_2 PEC. The photoanodes of interest were strontium titanate ($SrTiO_3$/STO) and Ti-doped hematite (α-Fe_2O_3), and the H_2O_2 production electrocatalysts were silver (Ag), gold (Au), and a palladium gold alloy (PdAu). These provided a useful range of variability to determine ideal characteristics of materials for use in an

H_2O_2 PEC. Furthermore, a suitable method of screening materials is demonstrated in this work to streamline the process of identifying optimal electrocatalysts for producing H_2O_2.

Owing to its ability to quantify H_2O_2 produced at the surface of electrocatalysts, scanning electrochemical microscopy (SECM)[14-16] was chosen to monitor the impact of materials and PEC operational conditions on H_2O_2 generation. The substrate generation/tip collection mode (SG/TC) of SECM was used here to collect any H_2O_2 produced at the surface of the electrocatalysts. Traditional methods for detecting products formed from a PEC involve detecting gaseous H_2 and O_2.[12,13] In order to study H_2O_2 production in real time and with versatility to address the impact of operation conditions of the PEC, SECM acts as an ideal technique that detects H_2O_2 produced *in situ* from the electrocatalyst while the PEC is operating in a 2-electrode configuration.

3.3. Materials and methods

3.3.1. Reagents

Sulfuric acid (H_2SO_4, Sigma Aldrich, 99+%), sodium hydroxide (NaOH, pellets Sigma Aldrich, 97+%), sodium perchlorate ($NaClO_4$, Sigma Aldrich, 98+%), iron (III) chloride ($FeCl_3$ anhydrous, Fisher Scientific), titanium butoxide (Sigma Aldrich, 97%), hydrochloric acid (HCl, Macron, 37.2 wt.%)

3.3.2. Preparation of photoanode and electrocatalyst materials

The Ti-doped hematite was prepared per previous reports, which involved mixing and annealing (550^{o}C) $FeCl_3$ and titanium butoxide in sequential layers on fluorine doped tin oxide (FTO, Delta Technologies, 25 x 25 x 1.3 mm, $R_s \leq 14$ Ω).[17] The STO was procured via MTI Corporation, in a slide with dimensions 10x10x1 mm, and 1 side polished. For the fabrication of Au electrocatalysts, Au was coated onto a silicon wafer by electron beam evaporation (Temescal

FC-2000) to be 100 nm thick with a 5 nm thick Ti adhesion layer. The evaporation rate was 0.1 – 0.2 Å/s. The Ag electrocatalyst was prepared via sputter coating (AJA Orion 3) of a 100 nm thick layer of Ag on a Si wafer. The PdAu alloys were sputter coated (Emitech K575) at ~2.5 Å/s to yield a 10 nm thick layer onto a Si wafer.

3.3.3. H_2O_2 detection

The SG/TC mode of SECM was utilized to detect H_2O_2 produced by the H_2O_2 electrocatalysts while in a 2-electrode PEC configuration with the photoanode. The setup for these measurements is shown in Figure 3.2. A Pt UME probe (radius=12.5 μm) was positioned over the H_2O_2 electrocatalyst surface and was held at a suitable potential (1.2 V vs. NHE) to oxidize any H_2O_2 being produced. All SECM measurements were carried out in a custom-made 2 mL Teflon cell and with a CHI920D workstation (CH Instruments). The H_2O_2 electrocatalyst half-cell was connected to the photoanode half-cell through a Keithley 2400 Source Meter and the lamp used for illumination was a 6258 Oriel Xe lamp.

3.4. Results and discussion

3.4.1. Characterization of H_2O_2 electrocatalysts

The catalyst materials were selected because each is expected to produce H_2O_2 at different overpotentials. It is for this reason that a control SG/TC experiment was performed on the electrocatalyst half-cell of the PEC (Figure 3.3). The potential of the various substrates was scanned while the Pt UME was held at a constant potential suitable to oxidize any H_2O_2 produced. As is shown in Figure 3.3, the chosen electrocatalysts produced H_2O_2 in different potential ranges, with PdAu being the optimal H_2O_2 producing electrocatalyst of the three since H_2O_2 was produced with the lowest overpotentials. These control experiments also allow for the H_2O_2 selectivities to

be quantified using established theory.[14] The Au electrocatalyst was determined to be ~80% selective, PdAu was ~75% selective, and Ag was ~35% selective. These electrocatalysts could be used for multiple experiments, but for replicate measurements, a freshly deposited film of the respective electrocatalyst was used.

3.4.2. Characterization of photoanodes

Figure 3.4 shows the impact of band edge position and bandgap on the photoelectrochemical activity of hematite and STO. The large difference in reactivity toward water oxidation between the two can be attributed in part to the difference in conduction band edges of the two materials. The conduction band edge for STO lies more negative than the potential for hydrogen evolution, while the conduction band edge of hematite lies positive of it (Figure 3.1).[18,19] This information is important to consider for a H_2O_2 PEC because, from a thermodynamic standpoint, the STO is expected to activate the electrocatalysts toward H_2 evolution while hematite should only be able to activate the desired $2e^-$ reduction of oxygen at no applied bias.

3.4.3. Collection of H_2O_2 with SECM/PEC platform

Having performed initial characterizations of each of the catalysts of interest here, they were then assembled into a functioning PEC shown in Figure 3.2. In order to detect H_2O_2 produced from this PEC, the UV-lamp was modulated to expose the photoanode to 20 s of illumination followed by 20 s of darkness. If the Pt UME was held at potentials to oxidize any H_2O_2, then an increase in anodic signal at the Pt UME was observed during the period of illumination. The bias between the hematite and the electrocatalyst was subsequently increased in 50 or 100 mV increments, leading to greater activation of the photocatalyst and the H_2O_2 electrocatalyst.

Increasing the applied bias in this manner resulted in an increase in the amount of anodic current detected at the Pt UME.

Figure 3.5A shows the chronoamperometry of the Pt UME when positioned over a PdAu substrate that is activated by hematite. When the hematite is under illumination, the collection current of the Pt UME becomes more anodic due to the oxidation of H_2O_2 produced by the ORR at PdAu. Alternatively, the PdAu could be producing H_2, which would also be detected since the Pt UME is held at a highly oxidizing potential. To verify that the substrate was producing H_2O_2 and not H_2, oxygen concentration in solution was altered by either saturating the solution with O_2 or Ar. As is shown in Figure 3.5B, it was observed that the intensity of the signal increased in the presence of O_2 saturation and decreased in the absence of O_2. Another way to confirm that the substrate is producing H_2O_2 is to note that the amount of collection current in the chronoamperometry goes down as applied bias increases. This is due to the PdAu becoming more activated toward the $4e^-$ reduction of O_2 rather than the $2e^-$ reduction. Such behavior is expected from the initial control experiments performed with each of the electrocatalysts (Figure 3.3). Each catalyst exhibited a potential region in which H_2O_2 production decreased.

At a bias of 1.8 V, a large increase in anodic current was observed when the hematite was illuminated, which may seem like the formation of H_2O_2 is once again the predominant reaction occurring at the PdAu electrocatalyst. However, upon removing O_2 from the solution, it was observed that the amount of collection current did not decrease. This suggests that the catalyst no longer produces H_2O_2, but instead H_2, which is expected when a large bias is applied.

The same chronoamperometry data was collected for the silver and gold electrocatalysts (Figure 3.9). The three different electrocatalysts are compared with plots of collection current vs. applied bias in Figure 3.6. These results showed that the peak for H_2O_2 production occurs around

200 mV of applied bias for PdAu, 500 mV for Au, and 600 mV for Ag (Figure 3.6). The potential difference between the peaks for the various electrocatalysts agrees with the initial characterization of the electrocatalysts (Figure 3.3). Also, in the case of PdAu, roughly 50% of the peak current is achieved in the absence of bias, thus suggesting the appropriate conditions for the chemical splitting of water into O_2 and H_2O_2.

When using STO as the photoanode instead of hematite, it was observed that the electrocatalysts were activated to predominantly carry out hydrogen evolution. This was evident from the larger collection currents were much larger than those observed in the initial control experiments (Figure 3.3) and showed no dependence on the concentration of O_2 in solution (Figure 3.8). Thus, this highlights the necessity for the photoanode material to possess an appropriate band edge position so that the electrocatalyst is not activated to carry out undesirable reactions such as H_2 production or the $4e^-$ pathway for O_2 reduction.

3.4.4. Assessing efficiencies of H_2O_2 PEC

Since the PdAu catalyst produced H_2O_2 at the lowest biases, further characterization of the H_2O_2 PEC was done using PdAu as the electrocatalyst. In the previous experiments, the hematite was only exposed to light for a maximum of 20 seconds, and, at some biases, the H_2O_2 electrocatalyst was unable to reach steady state production on those time scales. Thus, H_2O_2 production was activated for 5 minutes to achieve a steady state collection. Chronoamperometry data for these experiments can be seen in Figure 3.10. Using the steady state current at the Pt UME and the collection efficiency, it is possible to acquire the selectivity of the PdAu catalyst toward H_2O_2 production. The collection efficiency was calculated using simulation of SG/TC SECM with COMSOL Multiphysics 4.4, and information about the model can be found in the supplemental

information (Figure 3.11). For PdAu, the selectivity toward H_2O_2 evolution was calculated to be $77.9 \pm 6.6\%$.

The efficiency of the overall H_2O_2 PEC can easily be improved by using well studied techniques to improve visible light utilization and light conversion efficiency at the photoanode.[20-22] An advantage of this analytical platform for studying H_2O_2 PECs is it can be used to rapidly assess multiple catalyst materials to determine which electrocatalysts are the most effective. Rather than testing a single electrocatalyst at a time, an array of various catalyst compositions can be screened when in this 2-electrode PEC configuration. Shown in Figure 3.7 is an example of this screening process. A catalyst array was fabricated by using a small pipette filled with $(NH_4)_2[PdCl_6]$ to make spots on a glassy carbon substrate. This was then annealed at 550^0C under H_2 to reduce the Pd precursor to Pd^0. This substrate with patterned Pd spots was then used as the electrocatalyst in the PEC. Using SECM imaging, each spot can be imaged at different applied biases to determine how much H_2O_2 is being produced. Previous work in this field has established the thermodynamic and kinetic considerations necessary for predicting which bimetallic catalysts would be selective for the $2e^-$ reduction of oxygen.[22-24] The screening of electrocatalyst arrays is also a well-researched application of SECM,[25-28] and the combination of the two for this purpose would be particularly effective. This type of analytical screening can be utilized to determine electrocatalyst efficiency and longevity of several electrocatalyst compositions in a single setup.

3.5. Conclusions

Shown here is the successful incorporation of SECM into a 2-electrode PEC to measure H_2O_2 produced. It was demonstrated that the electrocatalyst selectivity could be acquired using this SECM platform for detecting H_2O_2. There is room for optimization of the materials used, and, to this end, it was also shown how this experimental setup can be used to streamline the process

of discovering state of the art photoanodes and electrocatalysts to be used in an H_2O_2 PEC. Such endeavors will reveal new electrocatalysts that do not lose appreciable activity over time, produce H_2O_2 with greater efficiencies, and reduce O_2 at lower overpotentials than the ones studied in this work. The results shown here indicate that H_2O_2 production is possible at no applied bias, but the optimal rate of formation was at about 200 mV of applied bias. Discovering new materials will enable the production of H_2O_2 from a PEC without having to apply bias to achieve the optimal rate of production. The pursuits of fabricating a highly efficient H_2O_2 PEC will act as a means to supplant the prevalent use of harmful chlorinated oxidants in the chemical industry and using the approach to catalyst discovery discussed here will provide insights toward understanding oxygen reduction catalysts for producing H_2O_2.

3.6. Figures

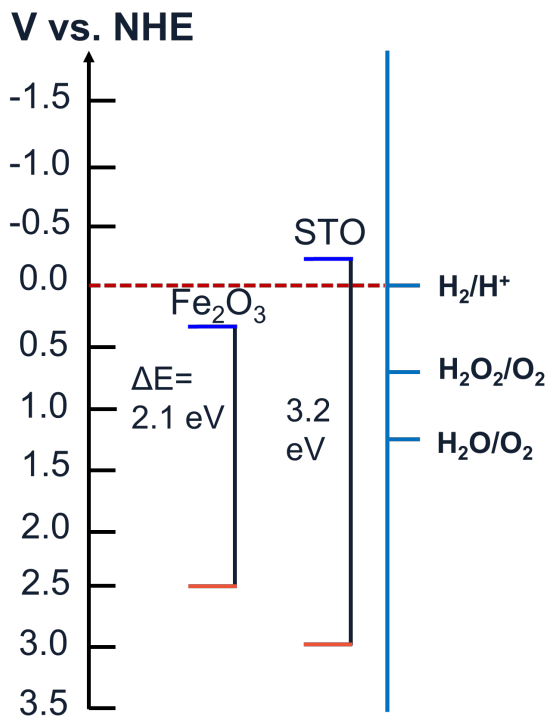

Figure 3.1 Semiconductor band alignment diagram for strontium titanate and hematite compared to the potentials vs. NHE of oxygen reduction and hydrogen evolution processes.

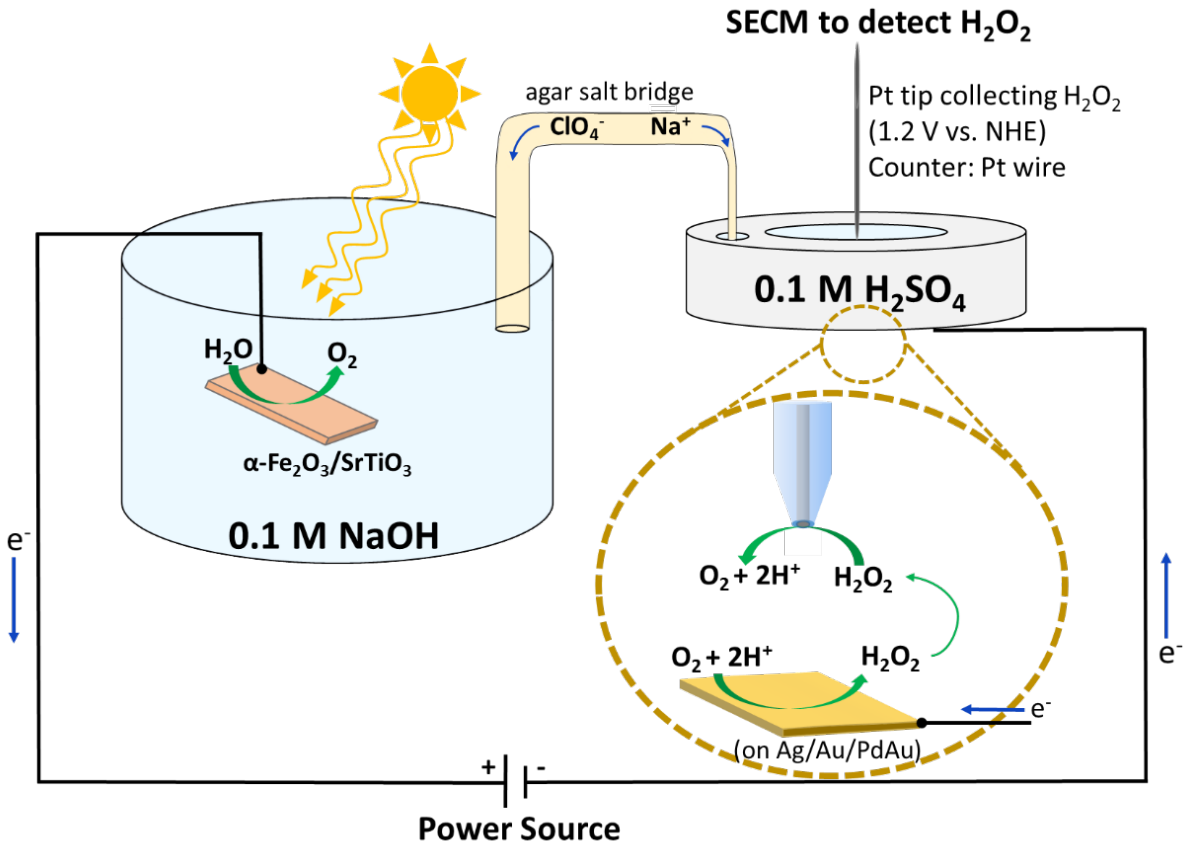

Figure 3.2 Experimental setup for incorporating SECM into a photoelectrochemical cell.

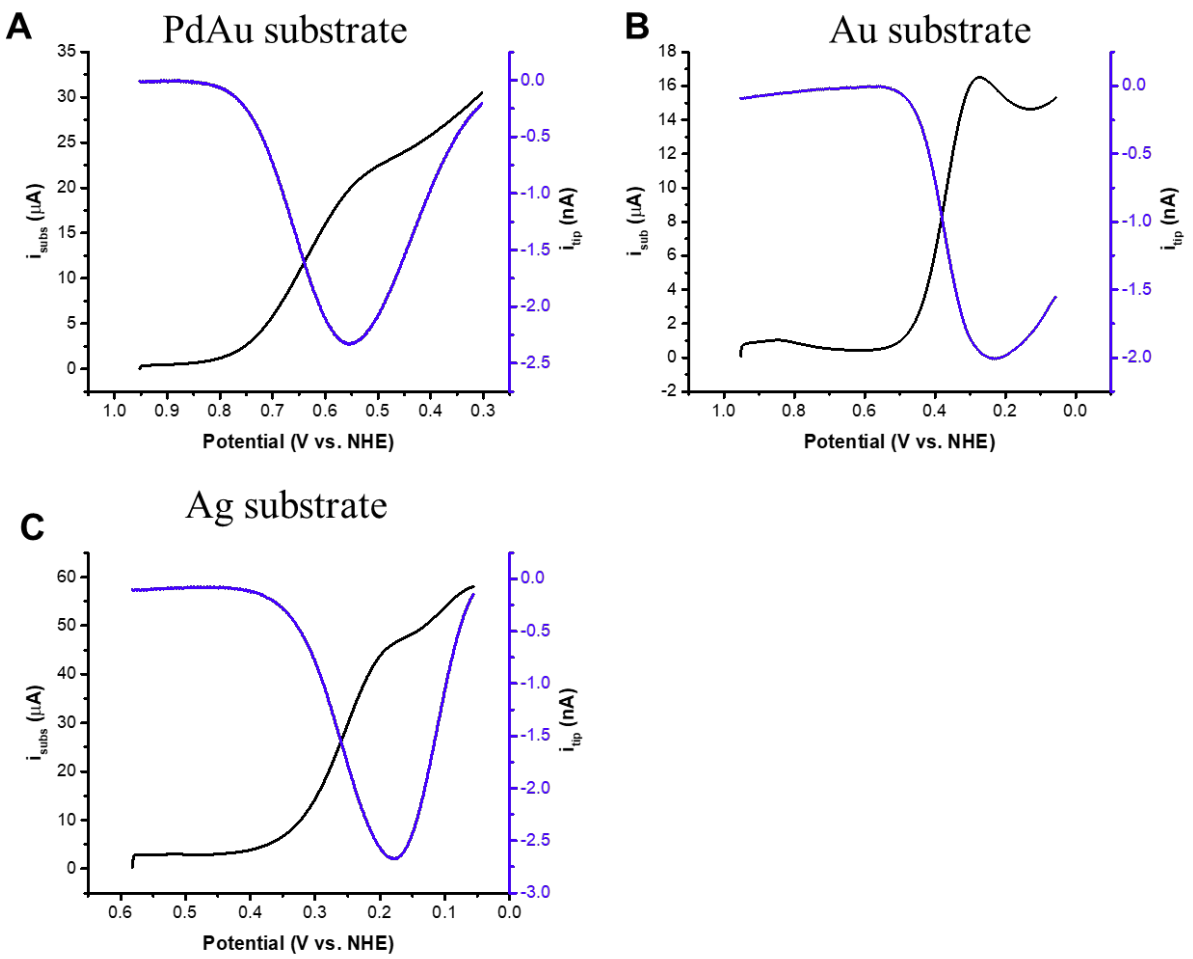

Figure 3.3 Control SG/TC SECM measurements in 0.1 M H_2SO_4 of the potential ranges in which the catalysts produce H_2O_2. Electrocatalysts all had the same exposed area of 0.2 cm^2 and a Pt UME with radius of 12.5 μm was held at 1.0 V vs. Ag/AgCl (1.2 V vs. NHE) to collect H_2O_2 produced at electrocatalyst surface.

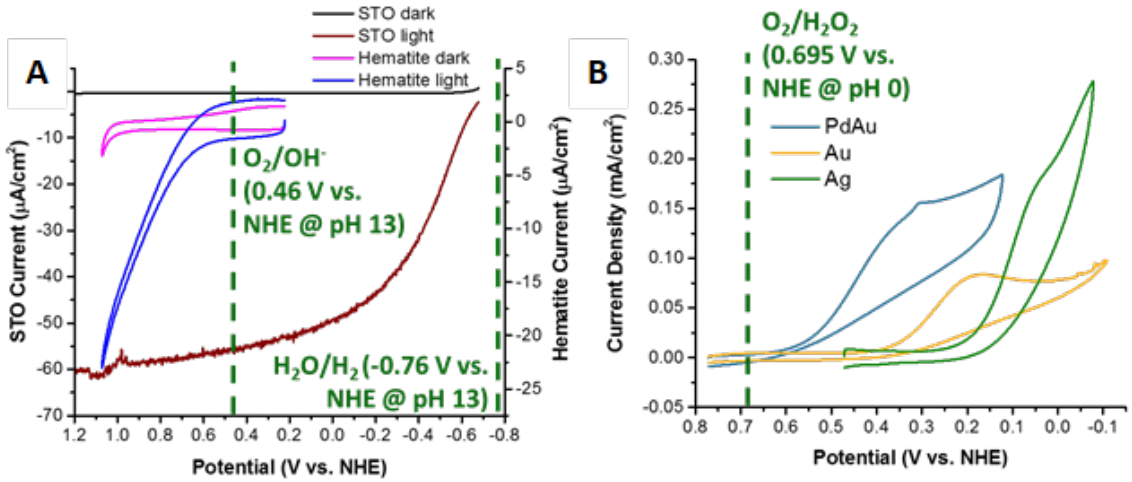

Figure 3.4 Shown in (A) are cyclic voltammograms of hematite and STO under illumination (0.1 M NaOH), depicting the large difference in reactivity between the two. In (B) are the cyclic voltammograms for the various electrocatalysts (0.1 M H_2SO_4) which produce H_2O_2 near the photocurrent onset potential for hematite.

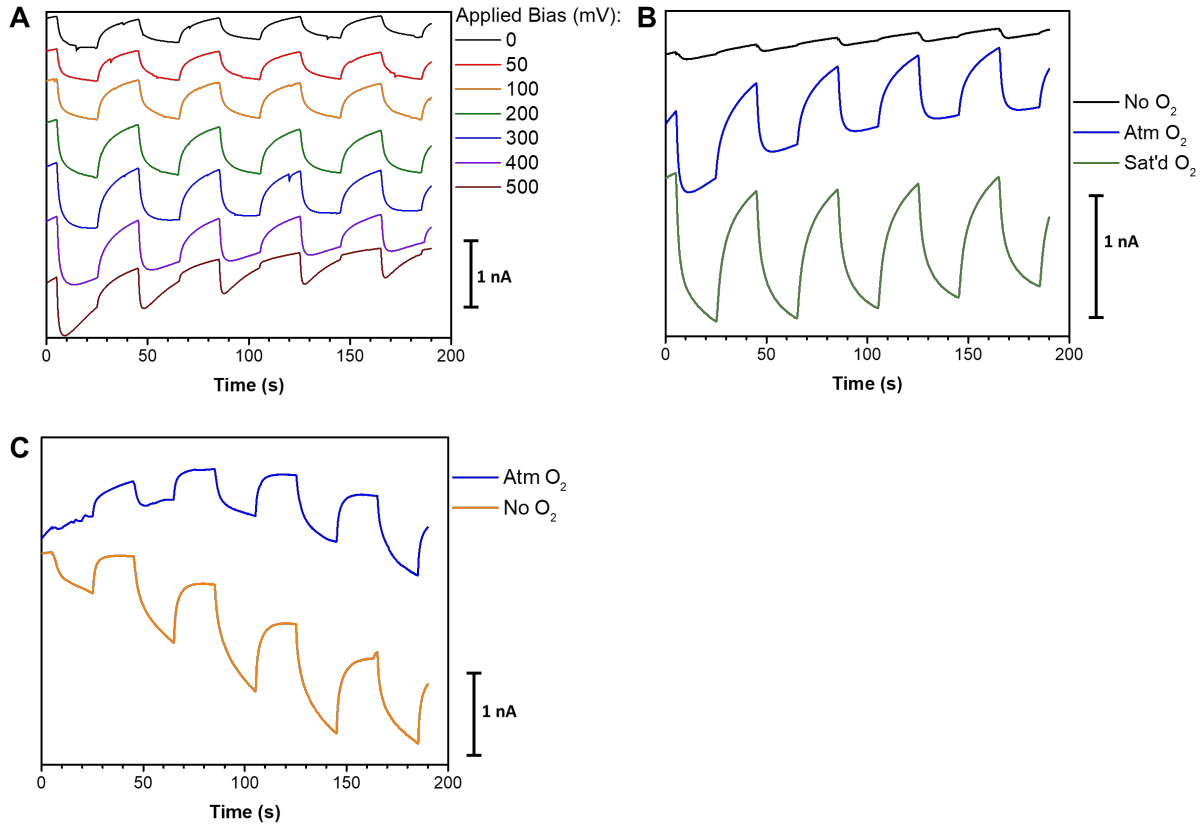

Figure 3.5 A) Chronoamperometry at the Pt UME while the hematite is being exposed to chopped light. The substrate being used for this set of data is PdAu. B and C) Oxygen dependence studies showing effect of O_2 concentration at 0.2 V bias (B) and 1.8 V (C) bias.

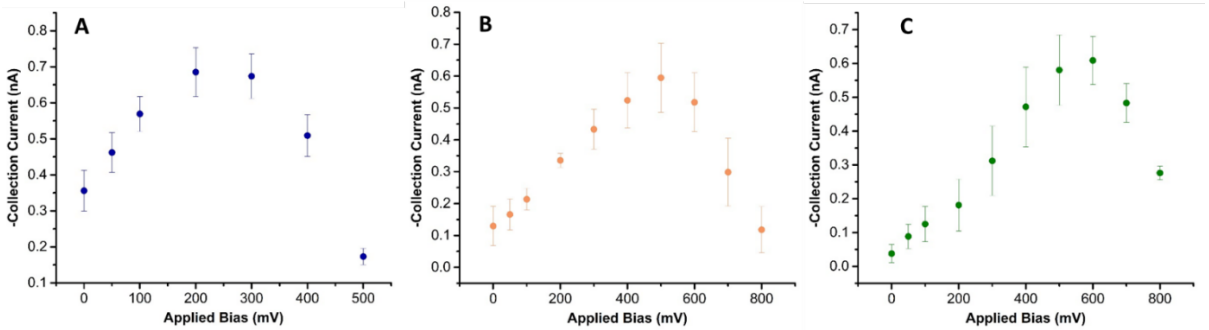

Figure 3.6 Depicted here are plots of collection current (collecting H_2O_2) vs. bias for PdAu (A), Au (B), and Ag (C). Each plot is an average of three trials per electrocatalyst.

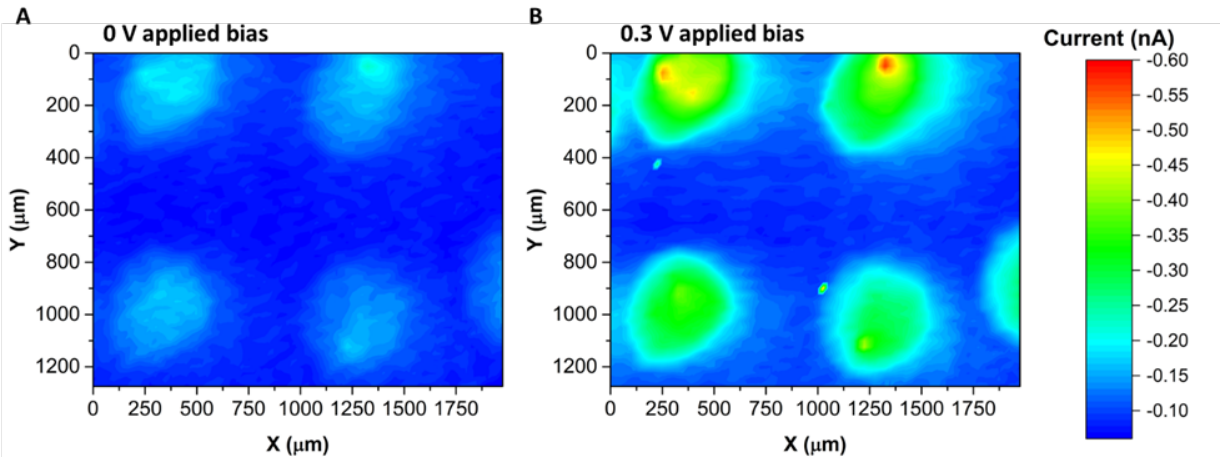

Figure 3.7 PEC/SECM image in which the electrocatalyst is an array of Pd spots that are activated to H_2O_2 production from a hematite photoanode. New electrocatalysts can be discovered by fabricating arrays similar to this one with variations in elements and compositions between spots.

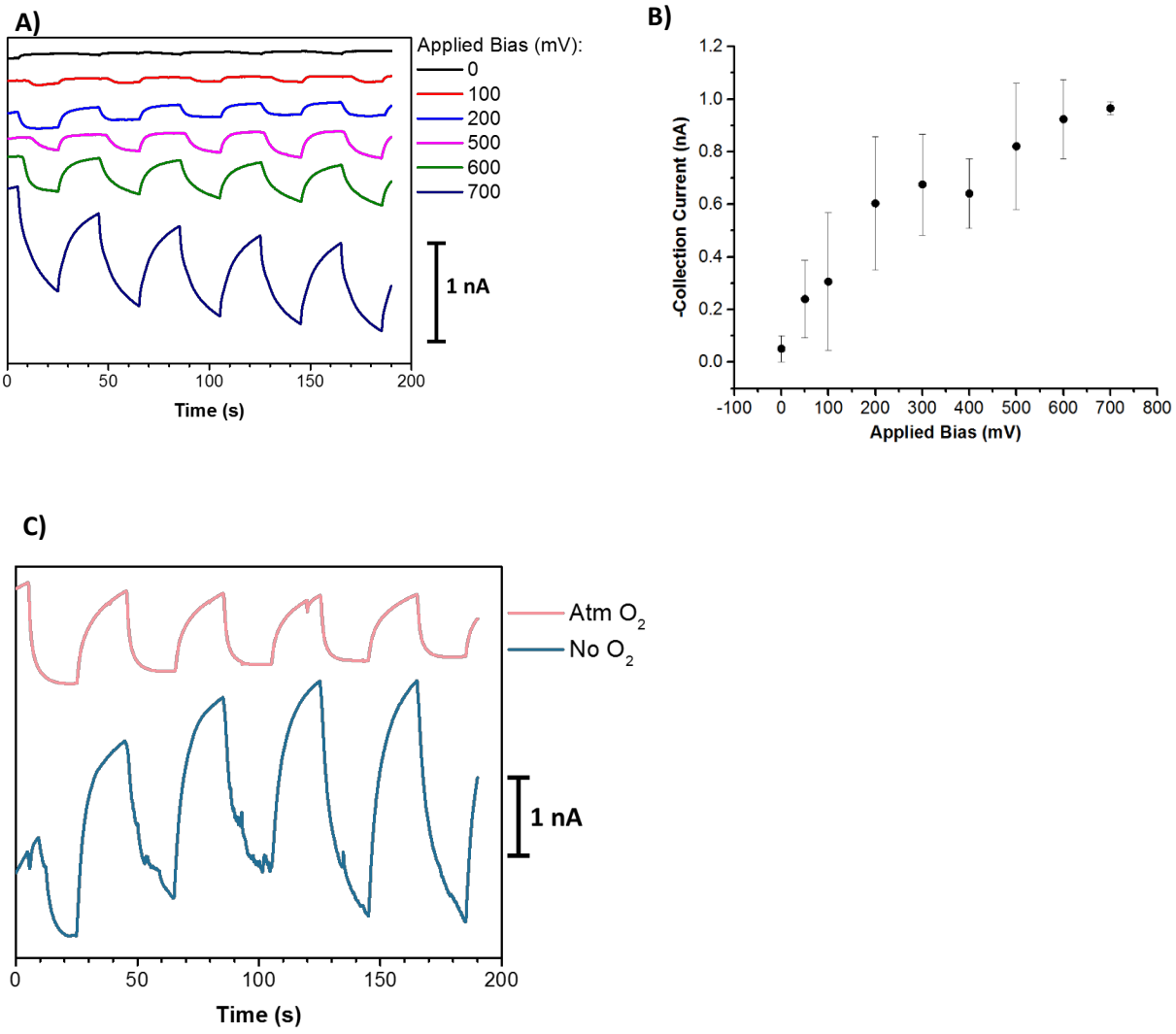

Figure 3.8 A) Shown here are chronoamperometry collection experiments carried out with STO in the photoanode half-call and PdAu in H_2O_2 producing half-cell. B) Collection currents from the experiment performed in (A) show that as bias is increased, the collection current also increases, and does not ever form a peak with increasing applied bias. C) Shown here are O_2 dependence experiments which strongly suggest that the species being collected is H_2 and not H_2O_2. It can therefore be stated that STO activates the PdAu beyond the 2-electron reduction of oxygen and only activates it toward hydrogen reduction.

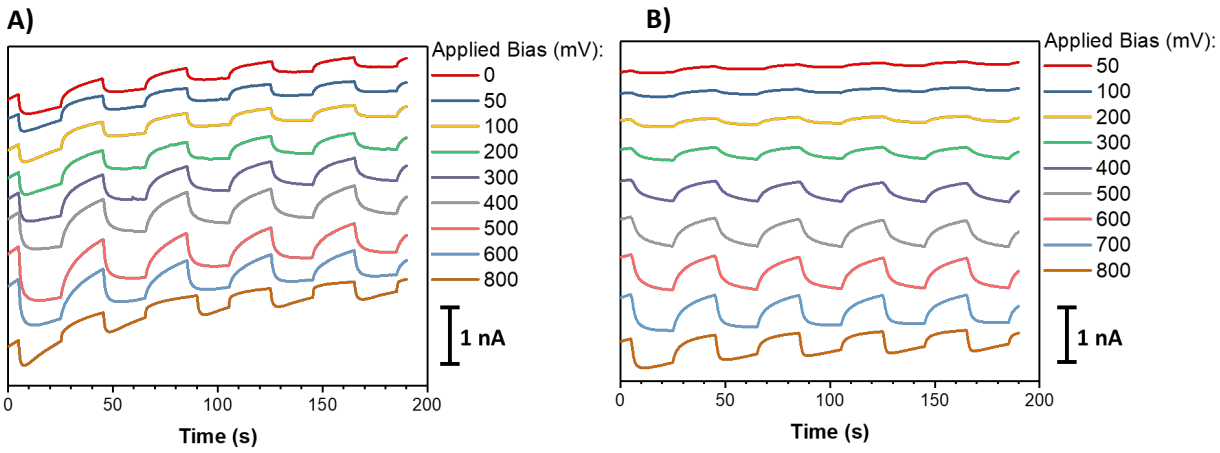

Figure 3.9 Above are chronoamperometry collection experiments carried out with Fe_2O_3 and Au (A) and Ag (B). These data were collected in the same setup as is shown in Figure 3.2. These experiments were used to generate Figure 3.6B and C.

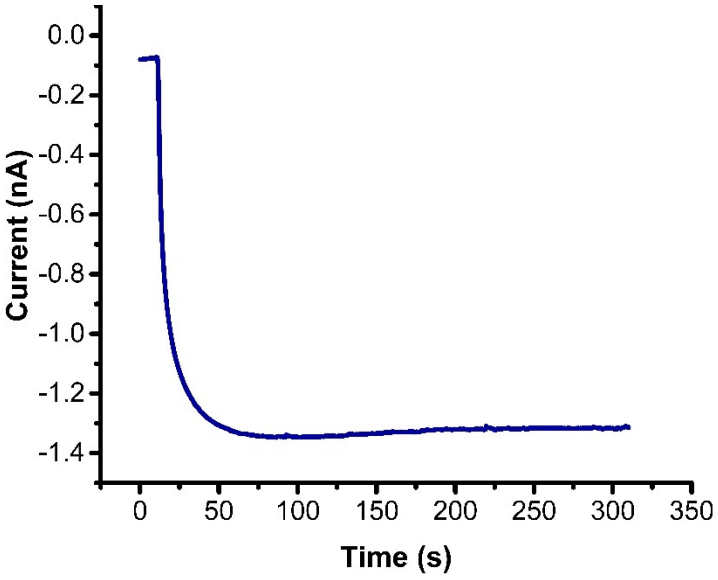

Figure 3.10 Shown above are chronoamperometry data in which the Fe_2O_3 was illuminated for 5 minutes. This was to measure a steady state collection to then determine the current density and selectivity at which the substrate was producing H_2O_2.

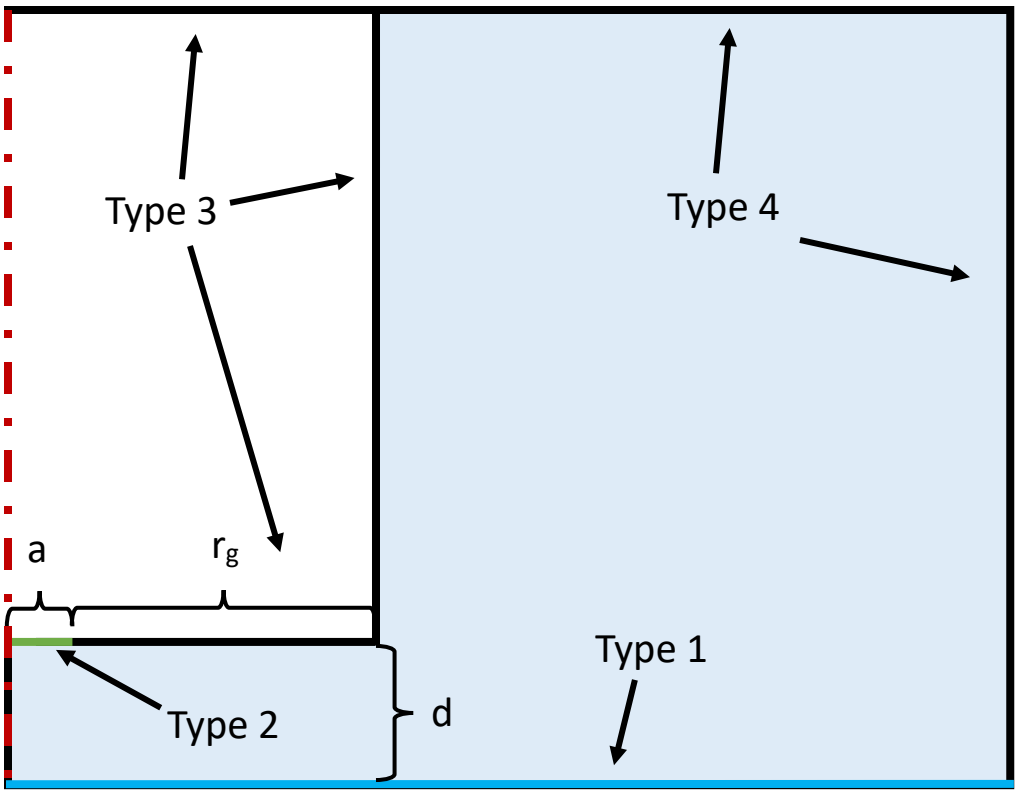

Figure 3.11 Above are the geometries and boundary conditions used for the COMSOL simulation for the SECM collection experiments. Type 1 boundaries correspond to the electrocatalyst producing H_2O_2, type 2 correspond to the Pt UME oxidizing H_2O_2 at steady state ($C_{H2O2} = 0$), and type 3 are no flux boundaries representing the insulating glass on the SECM tip electrode. By setting a flux of H_2O_2 being produced from the substrate with a type 1 boundary, it is possible to determine the flux necessary to measure the same amount of collection current that was observed during the longer time scale collection experiments shown in Figure 3.10. The flux at the type 1 boundary corresponds only to H_2O_2 production and does not consider other processes that may be happening ($4e^-$ ORR). During the experiment, the current flowing through the Keithley voltage source can be recorded and compared to the current calculated from the flux in the simulation. Ideally, the values would be identical, but the current measured with the Keithley is always higher than the simulated current because the electrocatalysts are not 100% selective to carry out the $2e^-$ reduction of oxygen. Therefore, by dividing the current calculated at the substrate by the current flow through the voltage source, the selectivity of the electrocatalyst can be determined.

3.7. References

(1) Sedlak, D. L.; von Gunten, U. The Chlorine Dilemma. *Science* **2011**, *331*, 42-43.

(2) Goor, G.; Glenneberg, J.; Jacobi, S.: Hydrogen Peroxide. In *Ullmann's Encyclopedia of Industrial Chemistry*; Wiley-VCH Verlag GmbH & Co.: Veinheim, Germany 2007.

(3) Eul, W.; Moeller, A.; Steiner, N.: Hydrogen Peroxide. In *Kirk-Othmer Encyclopedia of Chemical Technology*; John Wiley & Sons, Inc., 2001.

(4) Clerici, M. G.; Bellussi, G.; Romano, U. Synthesis of Propylene-Oxide from Propylene a nd Hydrogen-Peroxide Catalyzed by Titanium Silicate. *J. Catal.* **1991**, *129*, 159-167.

(5) Ragnar, M.; Henriksson, G.; Lindström, M. E.; Wimby, M.; Blechschmidt, J.; Heinemann, S.: Pulp In *Ullmann's Encyclopedia of Industrial Chemistry*; Wiley-VCH, Ed.; Wiley-VCH: Veinheim, Germany, 2014.

(6) Chen, Z. H.; Chen, S. C.; Siahrostami, S.; Chakthranont, P.; Hahn, C.; Nordlund, D.; Dimosthenis, S.; Norskov, J. K.; Bao, Z. N.; Jaramillo, T. F. Development of a reactor with carbon catalysts for modular-scale, low-cost electrochemical generation of H_2O_2. *React. Chem. Eng.* **2017**, *2*, 239-245.

(7) Shaner, M. R.; Atwater, H. A.; Lewis, N. S.; McFarland, E. W. A comparative technoeconomic analysis of renewable hydrogen production using solar energy. *Energ. Environ. Sci.* **2016**, *9*, 2354-2371.

(8) Tsukamoto, D.; Shiro, A.; Shiraishi, Y.; Sugano, Y.; Ichikawa, S.; Tanaka, S.; Hirai, T. Photocatalytic H_2O_2 Production from Ethanol/O_2 System Using TiO_2 Loaded with Au-Ag Bimetallic Alloy Nanoparticles. *ACS Cat.* **2012**, *2*, 599-603.

(9) Teranishi, M.; Naya, S.; Tada, H. In Situ Liquid Phase Synthesis of Hydrogen Peroxide from Molecular Oxygen Using Gold Nanoparticle-Loaded Titanium(IV) Dioxide Photocatalyst. *J. Am. Chem. Soc.* **2010**, *132*, 7850.

(10) Foster, N. S.; Noble, R. D.; Koval, C. A. Reversible Photoreductive Deposition and Oxidative Dissolution of Copper Ions in Titanium-Dioxide Aqueous Suspensions. *Environ. Sci. Technol.* **1993**, *27*, 350-356.

(11) Shiraishi, Y.; Kanazawa, S.; Kofuji, Y.; Sakamoto, H.; Ichikawa, S.; Tanaka, S.; Hirai, T. Sunlight-Driven Hydrogen Peroxide Production from Water and Molecular Oxygen by Metal-Free Photocatalysts. *Angew. Chem. Int. Ed.* **2014**, *53*, 13454-13459.

(12) Luo, J. S.; Im, J. H.; Mayer, M. T.; Schreier, M.; Nazeeruddin, M. K.; Park, N. G.; Tilley, S. D.; Fan, H. J.; Gratzel, M. Water photolysis at 12.3% efficiency via perovskite photovoltaics and Earth-abundant catalysts. *Science* **2014**, *345*, 1593-1596.

(13) Chen, Z.; Dinh, H. N.; Miller, E.: *Photoelectrochemical Water Splitting*; 1 ed.; Springer-Verlag New York, 2013. pp. 10-11

(14) Sanchez-Sanchez, C. M.; Rodiriguez-Lopez, J.; Bard, A. J. Scanning electrochemical microscopy. 60. Quantitative calibration of the SECM substrate generation/tip collection mode and its use for the study of the oxygen reduction mechanism. *Anal. Chem.* **2008**, *80*, 3254-3260.

(15) Sanchez-Sanchez, C. M.; Bard, A. J. Hydrogen Peroxide Production in the Oxygen Reduction Reaction at Different Electrocatalysts as Quantified by Scanning Electrochemical Microscopy. *Anal. Chem.* **2009**, *81*, 8094-8100.

(16) Mezour, M. A.; Cornut, R.; Hussien, E. M.; Morin, M.; Mauzeroll, J. Detection of Hydrogen Peroxide Produced during the Oxygen Reduction Reaction at Self-Assembled

Thiol- Porphyrin Monolayers on Gold using SECM and Nanoelectrodes. *Langmuir* **2010**, *26*, 13000-13006.

(17) Wang, G. M.; Ling, Y. C.; Wheeler, D. A.; George, K. E. N.; Horsley, K.; Heske, C.; Zhang, J. Z.; Li, Y. Facile Synthesis of Highly Photoactive alpha-Fe_2O_3-Based Films for Water Oxidation. *Nano Lett.* **2011**, *11*, 3503-3509.

(18) Gratzel, M. Photoelectrochemical cells. *Nature* **2001**, *414*, 338-344.

(19) Xu, Y.; Schoonen, M. A. A. The absolute energy positions of conduction and valence bands of selected semiconducting minerals. *Am. Mineral.* **2000**, *85*, 543-556.

(20) Roske, C. W.; Popczun, E. J.; Seger, B.; Read, C. G.; Pedersen, T.; Hansen, O.; Vesborg, P. C. K.; Brunschwig, B. S.; Schaak, R. E.; Chorkendorff, I.; Gray, H. B.; Lewis, N. S. Comparison of the Performance of CoP-Coated and Pt-Coated Radial Junction n(+)p-Silicon Microwire-Array Photocathodes for the Sunlight-Driven Reduction of Water to H_2(g). *J. Phys. Chem. Lett.* **2015**, *6*, 1679-1683.

(21) Sivula, K.; Le Formal, F.; Gratzel, M. Solar Water Splitting: Progress Using Hematite (alpha-Fe_2O_3) Photoelectrodes. *Chemsuschem* **2011**, *4*, 432-449.

(22) Siahrostami, S.; Verdaguer-Casadevall, A.; Karamad, M.; Deiana, D.; Malacrida, P.; Wickman, B.; Escudero-Escribano, M.; Paoli, E. A.; Frydendal, R.; Hansen, T. W.; Chorkendorff, I.; Stephens, I. E. L.; Rossmeisl, J. Enabling direct H_2O_2 production through rational electrocatalyst design. *Nat. Mater.* **2013**, *12*, 1137-1143.

(23) Ham, H. C.; Hwang, G. S.; Han, J.; Nam, S. W.; Lim, T. H. On the Role of Pd Ensembles in Selective H_2O_2 Formation on PdAu Alloys. *J. Phys. Chem. C* **2009**, *113*, 12943-12945.

(24) Gao, F.; Goodman, D. W. Pd-Au bimetallic catalysts: understanding alloy effects from planar models and (supported) nanoparticles. *Chem. Soc. Rev.* **2012**, *41*, 8009-8020.

(25) Zoski, C. G.; Simjee, N.; Guenat, O.; Koudelka-Hep, M. Addressable microelectrode arrays: Characterization by imaging with scanning electrochemical microscopy. *Anal. Chem.* **2004**, *76*, 62-72.

(26) Fernandez, J. L.; Mano, N.; Heller, A.; Bard, A. J. Optimization of "wired" enzyme O_2-electroreduction catalyst compositions by scanning electrochemical microscopy. *Angew. Chem. Int. Ed.* **2004**, *43*, 6355-6357.

(27) Fernandez, J. L.; Walsh, D. A.; Bard, A. J. Thermodynamic guidelines for the design of bimetallic catalysts for oxygen electroreduction and rapid screening by scanning electrochemical microscopy. M-Co (M : Pd, Ag, Au). *J. Am. Chem. Soc.* **2005**, *127*, 357-365.

(28) Fernandez, J. L.; White, J. M.; Sun, Y. M.; Tang, W. J.; Henkelman, G.; Bard, A. J. Characterization and theory of electrocatalysts based on scanning electrochemical microscopy screening methods. *Langmuir* **2006**, *22*, 10426-10431.

Chapter 4:

Relating electro- and thermal catalysis to enable high throughput catalyst discovery for direct synthesis of hydrogen peroxide

The research described in this chapter are part of the unpublished publication prepared for submission by Matthew L. Kromer, Jason S. Adams, Joaquín Rodríguez-López, and David W. Flaherty, "Unifying Concepts in Electro- and Thermal Catalysis towards Hydrogen Peroxide Production." All catalyst syntheses and thermal catalytic measurements were performed by Jason Adams and overseen by David W. Flaherty. The electrochemical experiments and simulations were performed and designed by Matthew L. Kromer and overseen by Joaquín Rodríguez-López.

4.1. Abstract

Here, the relationship between electrocatalysis and thermal catalysis is explored in the context of the reduction of O_2 to form H_2O_2 and H_2O on metal nanoparticle catalysts, which are known within their respective fields as the direct synthesis of H_2O_2 and the oxygen reduction reaction (ORR). Mechanistic similarities between these reactions in aqueous systems suggest that the rates and selectivities should be similar for a given metal nanoparticle catalyst when the thermodynamic forces driving these reactions are equivalent (i.e., at equal electrochemical potentials, $\bar{\mu}_i$). This hypothesis is examined using quantitative methods from the electro- and thermal catalysis. Electrochemical kinetic parameters (e.g., k^0 and α) were measured on a series of twelve monometallic and bimetallic nanoparticles supported on porous carbons using Koutecky-Levich and Butler-Volmer analyses and fit to a theoretical model. This model was based upon Butler-Volmer kinetics and treated each catalyst as a short-circuited electrochemical cell. This model assumed that hydrogen oxidation reaction (HOR) and ORR were occurring at equal rates,

which lead to a prediction of a defined cell potential given a pressure of H_2 and O_2. The predictions this model makes appear to agree closely with measured values for the potential of each type of nanoparticle catalyst during thermal catalytic O_2 reduction at elevated pressures of H_2 and O_2 reactants (50 – 400 kPa). This agreement demonstrates that electrocatalytic processes (e.g., proton-electron transfer, heterolytic hydrogen oxidation) occur during the direct synthesis of H_2O_2, which has been proposed to be a thermal catalytic reaction mediated by homolytic elementary steps. Steady-state rates and selectivities for H_2O_2 formation were determined in both thermal catalytic and electrocatalytic systems, and at equivalent electrochemical potentials for H_2 ($\bar{\mu}_{H2}$), the thermal and electrocatalytic performance correlate strongly across the full series of catalysts and potentials examined. The mechanistic insight and quantitative relationships provided design principles for improved catalysts with greater yield of H_2O_2 under both thermal or electrocatalytic conditions, which are validated by comparisons between PdAu and PtAu nanoparticle catalysts. These findings demonstrate the role of electrochemical processes during the direct synthesis of H_2O_2, provide a quantitative experimental foundation for relating thermal and electrocatalytic reactions, and give guiding principles to engineer nanoparticle catalysts for greater productivity of H_2O_2.

4.2. Introduction

Interest and motivation to produce H_2O_2 has grown significantly in recent years, because this oxidant can supersede the use of chlorine in selective oxidations, disinfection, and bleaching and thereby reduce the formation of environmentally impactful chlorinated wastes.[1-4] While traditionally formed by anthraquinone autooxidation chemistry, two emerging methods for H_2O_2 production are the thermal catalytic direct synthesis reaction ($H_2 + O_2 \rightarrow H_2O_2$) and the electrocatalytic two electron oxygen reduction reaction ($2H^+ + 2e^- + O_2 \rightarrow H_2O_2$). Both of these reactions can be catalyzed by metal nanoparticles in aqueous solutions at neutral or acidic

conditions (pH ≤ 7).[5,6] Although the mechanism of the oxygen reduction reaction (ORR) is known to involve heterolytic processes such as proton-coupled electron transfers,[7] the mechanism of the thermal catalytic direct synthesis reaction has been debated in the heterogenous catalysis community, which has yet to reach a clear consensus. The most frequently proposed mechanism for thermal catalytic H_2O_2 formation involves chemisorption of H_2 and O_2 to a metal surface, dissociation of H_2, and the sequential addition of H*-atoms to O_2* by homolytic reactions that do not directly involve the solvent.[8-10] Recently, Wilson et al. proposed that H_2O_2 forms on metal surfaces by the reduction of O_2* by solvent-mediated proton-coupled electron transfer, and H_2 gas provides the required chemical potential for reduction but also H^+ and e^- by heterolytic oxidation on the same nanoparticle that binds O_2*.[11] From an electrochemical perspective, the proposed mechanism for thermal catalytic H_2O_2 can be restated as a single metal nanoparticle co-catalyzing the hydrogen oxidation reaction (HOR) and two electron oxygen reduction reaction (ORR) simultaneously and, therefore, acting as a short-circuited hydrogen fuel cell.

Figure 4.1 shows the system of elementary steps for the proposed mechanism for thermal catalytic O_2 reduction to H_2O_2 and H_2O (adapted from [2016 Wilson et. al, 2020 Adams et al.]) and emphasizes the strong mechanistic connection between the direct synthesis reaction and the broadly accepted mechanisms for the HOR and the ORR. The similarities of these reaction mechanisms imply that a given catalyst (e.g., a metal nanoparticle supported on porous carbon) should provide identical rates and selectivities for the formation of H_2O_2 and H_2O in thermal catalytic and electrocatalytic reactors provided that systems operate at equivalent electrochemical potentials of the reactants ($\bar{\mu}_i$), which is defined as:

$$\bar{\mu}_i = \mu_i + z_i F \phi \tag{4.1}$$

where μ_i is the chemical potential of species i (kJ mol^{-1}), z is the charge on that same species, F is Faraday's constant (96.4 kC mol^{-1}), and ϕ is the local potential (V or J C^{-1}). The chemical potential takes the well-known form:

$$\mu_i = \left(\frac{\partial G}{\partial n_i}\right)_{T,P,n_j} = \mu_i{}^0 + RT \cdot \ln(a_i) \tag{4.2}$$

where G represents the Gibbs free energy of the system, $\mu_i{}^0$ is the standard state chemical potential of species *i*, *R* is the universal gas constant, and *T* is temperature (K), and a_i is the thermodynamic activity of species *i*. During electrocatalytic ORR, investigators most commonly manipulate $\bar{\mu}_i$ by changes to ϕ (also denoted as E in the electrocatalytic community) in order to determine reaction barriers and kinetically relevant steps on a given catalyst. On the other hand, practitioners of thermal catalysis (e.g., direct synthesis) typically vary $\bar{\mu}_i$ via changes to the temperature of the reactor to determine activation energies or by altering the activities of reactants (i.e., concentrations) to probe the kinetic relevance of different steps. Therefore, a given value of the electrochemical potential can be obtained by an infinite number of combinations of ϕ, *T*, and a_i, which provides a bridge between measurements made within the disciplines.

Our interdisciplinary investigation of the reduction of O_2 to H_2O_2 or H_2O is motivated by several reasons. First, the relative simplicity of this reaction network (two reactants and two products) provides an opportunity to compare steady-state catalytic selectivities in addition to rates using accessible analytical methods. Second, electrochemists have studied the ORR for decades, and the vast amount of understanding and research could be used to inform understanding of the direct synthesis of H_2O_2 as well as to propose catalyst for this reaction. Third, electrochemists have developed a high-throughput catalyst synthesis and screening methods that could be used to

accelerate the discovery of new catalysts for H_2O_2 production in thermal or electrocatalytic reactors.[12]

Here the relation between electrocatalysis and thermal catalysis is explored through the formation of H_2O_2. In order to relate electrocatalysis and thermal catalysis, electrochemical kinetic measurements were performed on a library of twelve catalysts. From these measurements, electrochemical kinetic parameters k^0 and α were quantified and were then input into a theoretical model. This model was based entirely on electrochemical kinetic theory and assumed a thermal catalytic nanoparticle behaves as a short-circuited electrochemical cell that performs HOR and ORR at equal rates. This resulted in a relation between potential and hydrogen partial pressure assuming H_2O_2 was formed according to the mechanism shown in Figure 4.1. This model was utilized to predict how the electrochemical potential would change as a function of H_2 pressure, and these predictions were directly measured for each catalyst to assess its accuracy.

4.3. Experimental methods

4.3.1. Chemicals

Sodium perchlorate ($NaClO_4$, Sigma Aldrich, 98+%), palladium (II) nitrate ($Pd(NO_3)_2$, Sigma Aldrich), tetraamine platinum (II) nitrate ($(NH_3)_4[Pt(NO_3)_2]$, Sigma Aldrich), gold (III) chloride, ($HAuCl_4$, Sigma Aldrich), Cobalt Nitrate ($Co(NO_3)_2$, Sigma Aldrich), Zinc Nitrate ($Zn(NO_3)_2$), Nickel Nitrate ($Ni(NO_3)_2$), Copper Nitrate ($Cu(NO_3)_2$), Ammonium Hydroxide (0.5 M, 300 mL, Macron 6665).

4.3.2. Catalyst preparation

Catalysts were prepared via either a modified incipient wetness impregnation methodology (Pd, PdNi, PdZn, PdCu, PdCo, Pt, PtCo, PdPt, Au) or an electroless deposition methodology

(PdAu, $PtAu_{60}$, $PtAu_{15}$, $PtAu_5$) using activated carbon (Vulcan XC-72, pellets, Cabot Corporation), as a support.

Catalysts prepared by modified incipient wetness were synthesized by first dissolving the respective nitrate solutions into a 3 vol% aqueous NH_4OH solution. This solution was then added drop wise over the untreated carbon support and allowed to dry at 333 K over-night. The dried samples were then reduced in a 20% H_2/He mixture at 973 K for 4 hours in a quartz tube furnace. Once cooled, the resulting catalyst was passivated by ambient air. However, Au catalysts were instead prepared by first adding $HAuCl_4$ dropwise to the carbon support followed by washing with a 3 vol% aqueous NH_4OH solution, since $Au(OH)_3$ would precipitate out of the basic solution. The resulting Au precursor on carbon was then reduced in a 20% H_2/He mixture at 393 K for 4 hours in a quartz tube furnace.

Catalysts prepared by electroless deposition were synthesized from the Au-XC-72 materials described above. The Au-XC-72 was added to a solution of DI H_2O and was stirred at 500 RPM in spinner flask while blanketing the solution with a 20% H_2/He mixture. After saturating for 30 minutes, a solution of either $Pd(NO_3)_2$ or $(NH_3)_4Pt(NO_3)_2$ was added gradually to the catalyst slurry. Afterwards, the solution was heated to 50°C and held at a constant temperature for 3 hours and then cooled back to room temperature. The resulting slurry was then vacuum filtered at 298K until dry.

4.3.3. Steady-state reaction rate measurements

All steady-state H_2O_2 and H_2O formation rates were measured in a continuous-flow trickle bed reactor system described in past work[27]. In this system, 150-1000 mg of catalyst was loaded into the center of a jacketed stainless-steel reactor (26 cm length, 1 cm inner diameter) and the catalyst was supported by glass wool and glass rods. Temperature was controlled across the reactor

by flowing a 50/50 (v/v) mixture of ethylene glycol (>99.8%, Fisher Scientific E178) and DI water from a recirculating chiller (Cole-Parmer Polystat). H_2 and O_2 compositions in the reactor were controlled by flowing certified gas mixtures (25% H_2/N_2 and 5% O_2/N_2 or 5% H_2/N_2 and 21% O_2/N_2, Airgas) through digital mass-flow controllers (Bronkhorst F-211CV) (DANGER! Pressurized H_2/O_2 mixtures are explosive if one of two of the components rise above 5% composition). Before contacting the catalyst, this gas mixture was premixed with either DI water (> 17.8 MΩ) or methanol (>99.8%, Macron 3016) and delivered by an HPLC pump (SSI LS class). The pressure of the resultant gas-liquid mixture was maintained in the reactor by a back-pressure regulator (Equilibar LF series) and controlled by an electronic pressure regulator (Equilibar GP1). The reactor effluent was passed through a gas-liquid separator (GLS) where the gas fraction was analyzed by a gas chromatograph (Agilent 7890B, thermal conductivity detector, Ar reference) equipped with a capillary column (Vici, Molecular Sieve 5Å, 30 m x 0.53 mm x 20 μm). The liquid fraction was drained from the GLS every 10 minutes by an electronic valve (Banjo LEV025PL) and pulled into an electronic two-position 10 port valve (Vici EPC10W). This 10-port valve would inject 1 cm^3 from the liquid fraction and 1 cm^3 of a colorimetric titrant (12 mM neocuproine [>99%, Sigma-Aldrich 121908], 8.3 mM $CuSO_4$ [>98.6%, Fisher Scientific C493], 25/75 (v/v) ethanol/DI water mixture [>99.9%, Decon Laboratories 2701]) into test tubes held in an automated fraction collector (Biorad 2110). Each tube was analyzed by a UV-VIS spectrophotometer (Spectronic 20 Genesys) at a wavelength of 454 nm to measure the H_2O_2 concentration using a corresponding calibration curve. All experiments were conducted at a liquid flow rate of 35 cm^3 min^{-1} to avoid external mass transfer limitations.

All time-on-stream plug flow data reported in this study represent directly measured rates and selectivities. For pressure dependence and activation enthalpy measurements in organic-

containing solvents, data were corrected over time using a model for exponential site deactivation reported elsewhere. In these measurements, the reactor was brought back to the initial conditions then corrected after the measurement to minimize artifacts stemming from this deactivation.

4.3.4. Rotating disk electrode (RDE) measurements

The RDE measurements were carried out on a CHI 760 potentiostat (CH Instruments) and were performed with a Pine ASR electrode rotator (Pine Research) using a 5.0 mm glassy carbon disk insert with a Pt ring assembly (OD=7.50 mm, ID=6.50 mm). Levich and Koutecky-Levich analyses were performed on each of the catalysts in order to acquire electrochemical kinetic parameters. More information on these analyses can be found in Chapter 2 of this dissertation. All RDE experiments were carried out in 0.1 M $NaClO_4$ supporting electrolyte with a Ag/AgCl reference (CH Instruments). To modify the rotating disk electrode, the carbon-supported catalysts were suspended in a solution of 5.0 mg catalyst, 1.0 mL of Millipore water (Elga, 18 MΩ), and 0.6 mL of ethanol. 10.0 µL of this slurry was drop cast onto the 5.0 mm glassy carbon disk and dried with an infrared lamp. Once dry, 5.0 µL of 1 wt% Nafion® was drop cast on the top of the modified electrode to prevent detachment of the catalyst during measurements.

4.3.5. Pressurized electrochemical potential measurements

Danger! Mixing H_2 and O_2 must be done in controlled environments to prevent explosive mixtures from forming. To avoid explosive mixtures, never exceed 5% composition for the gas not in excess. For instance, if H_2 is at 20% composition, O_2 should never exceed 5%. These measurements were carried out in a custom-built stainless-steel electrochemical cell with a custom-built gas manifold to sparge the liquid phase with a gas stream with known pressures of H_2 and O_2 gas (state ranges of pressured in kPa). More rigorous details on the pressurized cell dimensions and fabrication can be found in the supplemental information. All pressurized cell

measurements were carried out with a Ag/AgCl reference electrode, catalyst modified glassy carbon electrode, and a carbon rod counter electrode (if pressurized voltammetry was being performed). A glassy carbon electrode (BASi 3.0 mm diameter) was modified by drop casting 5.0 μL of a catalyst slurry (recipe above) onto the electrode surface. The catalyst was then coated with 1.0 μL of a 1 wt% Nafion® solution to prevent catalyst loss. The measurements were carried out in Millipore water with no supporting electrolyte. A supporting electrolyte consisting of 0.1 M $NaClO_4$ was used in the pressurized cell only in the case of pressurized voltammetry to minimize solution resistance. For these measurements, the potential at zero current was constantly monitored as a function of time. The pressurized cell was brought to pressures of 60, 200, 300, and 400 kPa of H_2 while O_2 was held constant at 60 kPa. The cell was held at each of these pressures for about 30 minutes to 1 hour, and the last 5 minutes of each time period was averaged to yield a single data point for the pressure of H_2 the cell was held at.

4.4. Relating electrochemical potential to H_2 and O_2 pressures

As stated earlier, equation 4.1 dictates that the electrochemical potential should be intimately related to a_i, T, and ϕ (or E). Here it was decided to relate E and a_{H2}. A typical thermal catalytic experiment involves measuring reaction rates as a specific reactant is changed. In the case of H_2O_2 direct synthesis, previous studies show a notable change in reaction rate as H_2 partial pressures are increased over a very large range.[11] Because of the relationship between electrochemical potential and activity of H_2, it should be possible to measure changes in potential on a catalyst surface as the pressure of H_2 is altered. In order to elucidate the potential of a catalyst at these elevated pressures, a custom-built electrochemical cell that enclosed a three-electrode cell into a pressurized container was utilized. This experimental setup was utilized because thermal catalytic kinetic analyses involve measuring reaction rates at pressures of H_2 that lie well above

atmospheric pressure. The relative pressures of H_2 and O_2 were controlled to measure the potential of a given catalyst at pressures up to 400 kPa of H_2. A typical data set for these measurements is shown in Figure 4.2A for a PdAu catalyst. As the pressure of H_2 increases, the potential of the catalyst is subsequently shifted to more negative values, which agrees with qualitative expectations. Since H_2 is a well-known reducing agent, one would expect a subsequent shift in potential towards more reducing potentials as P_{H2} is increased.

Having acquired this experimental relation between potential and P_{H2}, is was of interest to determine if this potential vs. H_2 relationship could be fit to theory based on electrocatalysis. The most simplistic method by which potential and pressure can be related is through the Nernst equation:

$$E_{eq} = E^{0\prime} - \frac{RT}{nF}\ln\left(\frac{a_R}{a_O}\right) \text{ or } E_{eq} = E^{0\prime} - \frac{59.2\text{ mV}}{n}\log\left(\frac{a_R}{a_O}\right) \quad (4.3)$$

Where E is the equilibrium potential, $E^{0'}$ is the formal potential (where activity is considered), R is the gas constant, T is temperature (298 K), n is the number of electron transferred in the reaction (2 for HOR and 2 to 4 for ORR), F is Faraday's constant, and a_R and a_O are the activities of reduced and oxidized species, respectively, which can be related to partial pressures of gaseous reactants. In the case of HOR and ORR, the oxidized species would be H^+ and O_2 and the reduced species would be H_2 and H_2O_2, respectively. This Nernst equation is simply another form of equation 4.1 and is arrived at by substituting in equation 4.2 in for μ_i and rewriting ϕ as E.[13] This equation is entirely derived from thermodynamic considerations and assumes that all reactions of interest are occurring at their thermodynamically defined barriers. This theory was more thoroughly treated by using the Nernst equation to make a prediction of potential at a defined H_2 partial pressure. This prediction for a range of H_2 pressures is shown in Figure 4.2B. Of the catalysts in this plot, all displayed a change in potential that was consistent to what a Nernstian response would predict.

However, the catalysts plotted here (and all catalysts not plotted) were rather far much more positive than the potentials defined by the Nernst equation. The Pt catalyst showed a dependence of potential on H_2 pressure closest to what the Nernst equation would predict, and the PdZn showed the furthest deviation from this prediction. The catalyst behavior shown here is reasonable because HOR and ORR are multi-step electrochemical reactions that typically occur beyond their thermodynamically defined barriers.[14-16] Although Pt based catalysts are commonly reported to carry out HOR and HER with very little overpotential, contaminated Pt, or Pt with surface adsorbates, can exhibit higher overpotentials to carry out these transformations.[17] The Pt based catalysts used here are all supported on carbon, and it is therefore likely that the surface of our Pt catalysts contains some amount of adsorbates or contaminants, which provides a explains why a normally ideal catalyst for HOR is underperforming. Based on the data shown in Figure 4.2B, the Nernst equation unsuitable to define a thermal catalytic system, and a current-potential relationship that includes reaction kinetics must be utilized.

Because our catalysts did not follow simple Nernstian response, Butler-Volmer kinetics were utilized to better fit the potentials that were measured on the catalyst library. For electrochemical reactions, kinetic expressions are derived from Arrhenius expressions and rate constants are written in the following form:

$$O + e^- \underset{k_b}{\overset{k_f}{\rightleftharpoons}} R$$

$$k_f = k^0 e^{\frac{-\alpha F(E-E^0)}{RT}} \quad \text{and} \quad k_b = k^0 e^{\frac{(1-\alpha)F(E-E^0)}{RT}} \tag{4.4}$$

Where k_f is a rate constant for reductions (cathodic currents) and k_b is a rate constant for oxidations (anodic currents). The Arrhenius expressions here are separated into potential independent and

potential dependent components. The component that is not potential dependent is referred to as k^0 or the standard rate constant. This value signifies how quickly the electron transfer is being carried out at equilibrium (no applied potential) and is a general measure for the kinetic facility of a given electron transfer. A high k^0 value results in relatively small overpotentials, and a small k^0 value (kinetically hindered electron transfers) leads to higher overpotentials to carry out the electron transfer. The activation barrier, E_a, is referred to as $-\alpha F(E-E^0)$, where α is a transfer coefficient ($0<\alpha<1$) which describes the symmetry of the energy barrier and strongly impacts how the electron transfer rate changes as potential is applied to the system. For a simple one electron transfer, an α above 0.5 describes a reaction in which the products (or the reduction of species O) are favored and vice versa for an α below 0.5. For a system like ORR or HOR, the transfer coefficient is much more complicated because there are several electron transfers and mechanistic steps. A transfer coefficient measured for these systems is more of a transfer parameter that is more dependent on the rate determining steps rather than if the products or reactants are favored. An expression for current (or reaction rate) can be formulated from the expressions above to result in the following expression for reaction rate (v):

$$v_{TOT} = v_f - v_b = k_f[C_O] - k_b[C_R] \tag{4.5}$$

Where C_O is the concentration of oxidized species and C_R is the concentration of reduced species. An expression for current (amperes/second) is achieved by setting the expression above equal to the flux of material to the electrode, or $\frac{i}{nFA}$. These electrochemical kinetic expressions are more realistic and applicable to our system because unlike the Nernst equation, they take into account more sluggish kinetics that lead to higher kinetic barriers to carry out an electron transfer. It is for this reason that Butler-Volmer kinetics were used to act as a link between potential and H_2

pressure. For the purposes of fitting our potential vs. H_2 data, it is postulated that the rate of ORR and HOR are equal:

$$v_{ORR} = v_{HOR} \quad \text{or} \quad k_{f,ORR}[O_2] = k_{b,HOR}[H_2] \tag{4.6}$$

Equation 4.6 assumes that a given direct synthesis catalyst operates at potentials in which k_b for ORR (H_2O oxidation) and k_f for HOR (HER) are negligible. This is a very realistic assumption for ORR since that reaction is very electrochemically (thermodynamically) irreversible. Equation 4.6 can be expanded and multiplied by nFA (to make it in terms of current rather than flux) to take the following form:

$$i_{ORR} = i_{HOR} \quad \text{or}$$

$$n_{ORR}FAk^0e^{\frac{-\alpha F(E-E^0)}{RT}}[O_2] = n_{HOR}FAk^0e^{\frac{\beta F(E-E^0)}{RT}}[H_2] \tag{4.7}$$

Where i is current and α/β are potential dependent parameters (acquired experimentally) that change based on the rate determining step.[18] To input concentrations into equation 4.7, the Henry's law constants for O_2 or H_2 in water were multiplied by the partial pressure of O_2 or H_2. Using Equation 4.7, it is possible to relate concentrations of H_2 and O_2 to potential, E, and provides a useful model to fit our pressurized cell potential measurements.

This model was utilized to predict what potential a given catalyst would be operating at when exposed to direct synthesis conditions. Values for k^0 and α/β determined for each of the catalysts using standard rotating disk electrode methods (Table A.1) and a discussion on that analysis is included in Chapter 2. Then, Equation 4.7 was used to generate plots of log i vs. E for HOR and ORR (Figure 4.3A). The predicted potential from this model was acquired from the intersection points in the curves for HOR and ORR, as this represents where the two reactions are occurring at an equal rate (Equation 4.6). Because the kinetics of each of the catalysts were

different, this model is able to take these discrepancies into account and give a more accurate prediction for an equivalent potential at a given H_2 pressure.

This approach to fitting the measured pressurized potentials does not make any assumptions about the mechanism or microkinetic model for either the HOR and ORR mechanisms. Instead it only reports apparent rate constants (i.e., values of k^0 and α) and the functional form of currents predicted from a reaction with the specific values measured for k^0 and α. As depicted in Figure 4.3A, an increase in the H_2 pressure should lead to a negative displacement of the Tafel plot crossing point on the potential axis. This is consistent with the expectation of a higher H_2 concentration providing a more reducing environment. The validity of this model was extensively tested by measuring the potentials of a library of catalysts as a function of H_2 pressure. The measured potentials are compared to the potentials predicted from our model in Figure 4.3B. This plot shows a strong correlation between these two quantities, suggesting that electrocatalysis and thermal catalysis are intimately related. The data shown in Figure 4.3B also demonstrates a predictable change in potential that is consistent with electrochemical theory. For this thermal catalytic system, an ideal Nernstian response as well as Butler-Volmer kinetics both predict that as H_2 concentration (partial pressure) increases, then the potential should shift to more negative values. It also reasonable to assume that the potential of a given catalyst carrying out ORR and HOR will lie closer to the thermodynamic potential of HOR, which agrees with the findings in Figure 4.3B. For all of the catalysts, the overpotential required to carry out HOR was smaller than what was required for ORR. Therefore, for the two reaction to be carried out at an equal rate, the potential the catalyst would have to operate at must lie at higher overpotentials for ORR than for HOR. This result is consistent with findings in the electrocatalytic literature, where electron transfers involving H_2 are always more facile than those involving the activation of O_2. The Tafel

plots used to predict operating potentials for the catalysts can also be used to form general predictions for rates of H_2O_2 production as well. The catalysts that exhibited the fastest HOR kinetics resulted in an intersection point in the theoretical Tafel plots at increasingly negative values. This intersection point represents the point at which ORR and HOR are occurring at equal rates, and as it shifts negative this magnitude of current also increases dramatically. Therefore, a catalyst with a more negative intersection point in its corresponding Tafel plots for HOR and ORR is predicted to also possess a relatively higher turnover rate for oxygen reduction in a thermal catalytic system. However, this may not translate directly to higher H_2O_2 turnover rates, as catalyst selectivity is also an important parameter. For instance, of the catalysts studied here, Pt possessed the most negative intersection point and consequently is predicted to reduce oxygen at the highest rates in direct synthesis. Pt also exhibits poor selectivity to the 2-electron reduction of oxygen and therefore predominately forms the undesired product, H_2O, from the reduction of oxygen. Nonetheless, this model is still an effective prediction tool for catalyst performance because it can assess a given catalysts O_2 turnover rates relative to other catalysts of interest.

4.5. Comparing catalyst performance between thermal and electrocatalysis

Based on the potential measurements acquired in the pressurized cell, each of the catalysts exhibited a change in ~100 mV going from 60 kPa H_2 to 400 kPa. It is well researched in the field of ORR electrocatalysis that this magnitude of difference in potential can result in a substantial change in H_2O_2 selectivity.[19] If a thermal catalytic process is carried out via an electrochemical mechanism, then the changes in electrocatalytic selectivity as a function of potential should correlate to equal changes in thermal catalytic selectivity as a function of H_2 pressure. Prior to making this comparison between electrocatalytic and thermal catalytic selectivity, thermal catalytic steady-state rate measurements were conducted on the library of carbon-supported

catalysts to determine whether these materials followed a similar mechanistic behavior. Figure 4.4 shows the rate of thermal catalytic H_2O_2 formation as a function of H_2 pressure for each material used in this study. On each catalyst, rates increased in proportion with H_2 pressure (<100 kPa, 60 kPa O_2, 298K) before reaching a constant value at the greatest pressures (150 kPa – 400 kPa H_2, 60 kPa O_2, 298K). The results from these experiments showed a very consistent response to increasing H_2 pressure among all the catalysts, which suggests that a single mechanism predominates in all cases.

To compare the H_2O_2 selectivity between electro and thermal catalysis, the catalyst selectivity was determined in both electrocatalysis (via rotating ring-disk electrode methods, Figure A.15-5.27) and thermal catalysis, using a neocuproine titration and gas chromatography downstream from the trickle-bed reactor. In thermal catalysis, selectivity is determined as a function of H_2 pressure (a_{H2} in equation 4.1) and in electrocatalysis, selectivity is determined as a function of potential (ϕ in equation 4.1). The relation between electrochemical potential and H_2 pressure (Figure 4.3B) was used to guide the direct comparison between thermal and electrochemical selectivity yielding the parity plot shown in Figure 4.5. These comparisons show a strong correlation between thermal and electrocatalysis, where poor catalysts (PdCu, PdPt, Pt, etc.) were poor for both methods and vice versa for exceptional H_2O_2-forming catalysts ($PtAu_{15}$, Pd_4Ni_3, $PtAu_5$, etc.). These results show very clearly the correlation between electro and thermal catalysis and strongly suggest the existence of an electrochemical mechanism in the direct synthesis of H_2O_2.

Nonetheless, Figure 4.5 also shows several materials that behave as outliers. It is hypothesized that these discrepancies are consistent with a Pd to PdH_x phase transition. Similar phase transitions were reported on TiO_2 supported Pd nanoparticles at similar ratios of H_2 to O_2

gas (~2:1), in which Operando EXAFS measurements elucidated the nanoparticle phase under reaction conditions. Similar Pd-PdH_x transitions are also reported for Pd materials operating at increasingly negative electrical potentials. Additionally, the data shown in Figure 4.4 support our hypothesis that a phase transition occurs under operational conditions, as described above to explain H_2O_2 selectivity values. The rates in the intermediate pressure ranges (60-150 kPa) are unreported, as many Pd materials showed highly metastable behavior and took 4-10 hours to reach a true steady-state.

4.6. Qualitative thermal catalytic rate predictions

The relation between electro- and thermal catalysis established in the previous section was tested by performing a more detailed analysis on the Au/Vulcan, $PdAu_{60}$/Vulcan, and $PtAu_{60}$/Vulcan catalysts (Figure 4.6). Shown in Figure 4.6A is rotating ring disk electrode methods used to electrochemically quantify H_2O_2 selectivity of the catalysts as a function of potential. In Figure 4.6B are rotating disk voltammograms for each of the catalysts performing hydrogen oxidation. It is clear from these experiments, that Au was not at all active towards HOR, and $PdAu_{60}$ and $PtAu_{60}$ were both clearly active towards this process. According to these analyses, all three of these catalysts displayed similar selectivities toward H_2O_2 production but all carry out HOR with notably different activity (Figure 4.6B). Based on the differences toward HOR activity, these electrochemical measurements predict that the reactivity of the catalyst should decrease in the order $PtAu_{60}$/Vulcan> $PdAu_{60}$/Vulcan>Au/Vulcan when producing H_2O_2 in direct synthesis. The $PtAu_{60}$ was able to carry out HOR at ~150 mV less overpotential compared to $PdAu_{60}$. This difference in activation barrier inevitably results in an overlap of HOR and ORR at higher rates, which should make $PtAu_{60}$ the most effective thermal catalyst of the three shown here. In fact, the Au/Vulcan should not produce any H_2O_2 in direct synthesis since it is largely inactive toward

HOR, and this effect has been observed reproducibly in the literature.[5] Thermal catalytic rates of H_2O_2 formation on $PtAu_{60}$ and $PdAu_{60}$ were measured, and it was observed that normalized turnover rates were nearly double for $PtAu_{60}$ at all pressures of H_2 compared to the rates on $PdAu_{60}$. The data shown in Figure 4.6C validates our prediction that $PtAu_{60}$/Vulcan should be a more effective direct synthesis catalyst than $PdAu_{60}$/Vulcan. After assessing these catalysts toward their ability to produce H_2O_2 in direct synthesis, it is apparent that there is a link between the electrochemical observations and thermal catalytic performance. Of course, it is well known in the direct synthesis community that an ideal catalyst should effectively activate hydrogen, and the results discussed here clearly show the reason for that design rule. The predictive nature of electrochemical measurements toward thermal catalysis ultimately enables decades of electrocatalytic research on HOR and ORR to be used as a guide for catalyst design for direct synthesis. Both the selectivity and relative H_2O_2 production rate of a thermal catalyst can be effectively predicted through simple electrochemical measurements.

4.7. Future work and outlook

This work sought out to show the intimate relationship between electrocatalysis and thermal catalysis, and the implications of the findings here are far reaching in the catalytic community. Hydrogen peroxide was a large topic of interest in this work, and one of its most promising applications is the selective oxidation for the production of fine chemicals.[3,4] Additionally, there is also growing amount of research dealing with the conversion of CO_2 into useful chemicals,[20,21]. The methodology outlined here will undoubtedly be useful to these other thermal systems to the ends of identifying optimal catalyst materials and reaction conditions for higher rates of transformation and selectivities.

The connections between thermal and electrocatalysis that are established by this work create new opportunities for using electrochemical methods to discover new heterogeneous catalysts. The model presented here requires the input of electrochemical kinetic parameters and accurately predict an operating potential or change in potential when the catalyst is exposed to conditions used in thermal catalysis. The predictive nature of this model can be further extended to determine effective catalysts for thermal catalysis by performing simple electrochemical measurements. This is beneficial from a catalyst discovery standpoint because the field of electrocatalysis has a large foundation of research on rapidly screening catalysts. The results of these screening procedures can now be applied to thermal catalytic systems as well. There is a large volume of work toward utilizing combinatorial methodologies for screening the electrochemistry of various catalysts and reactions, such as those based on scanning electrochemical microscopy (SECM) to the ends of rapidly screening electrocatalysts.[12,22-24] The advantages of SECM based methods is that very small amounts catalyst materials and solvent is required to perform these high-throughput measurements. Catalyst screening via thermal catalytic methods is less attractive due to the large quantities of both catalyst material and solvents that are required for such studies.

4.8. Conclusions

Shown here is a comparative H_2O_2 direct synthesis and electrocatalytic study that lays the groundwork for correlating electrocatalytic and thermal catalytic processes aimed toward optimizing the production of useful products for use in the chemical industry. Electrocatalysts and thermal catalysts were compared by measuring how H_2 partial pressure affects the open circuit potential of each of the catalysts studied. This relation enabled the H_2O_2 selectivities to be compared between the two different methods. Comparing a vast amount of catalysts has shown

that a strong correlation between catalyst performance between electrocatalysis and thermal catalysis. Furthermore, this correlation was assessed with Au, PdAu, and PtAu catalysts and demonstrated the importance for a thermal catalyst to be able to oxidize hydrogen effectively in addition to being selective toward H_2O_2 formation. The results reported here can be used to further our understanding of direct synthesis catalysts and ultimately enable the discovery of a new catalyst that is both low cost and high selective toward producing H_2O_2 for industrial applications. The results reported here are applicable not only to catalyst design, but also to reaction cell design. By proving that the formation of H_2O_2 via direct synthesis occurs through a controlled electron transfer between H_2 and O_2, a more optimal cell can be designed where the two reactants are separated to maximize their respective concentrations and H_2O_2 conversion rates. The implications of this work extend far beyond the scope of H_2O_2 formation and are also applicable to numerous other thermal processes involving redox chemistry.

4.9. Acknowledgments

This work was supported by funding from the Energy and Biosciences Institute and Shell. This work was carried out in part in the Materials Research Laboratory Central Research Facilities, University of Illinois.

4.10. Figures

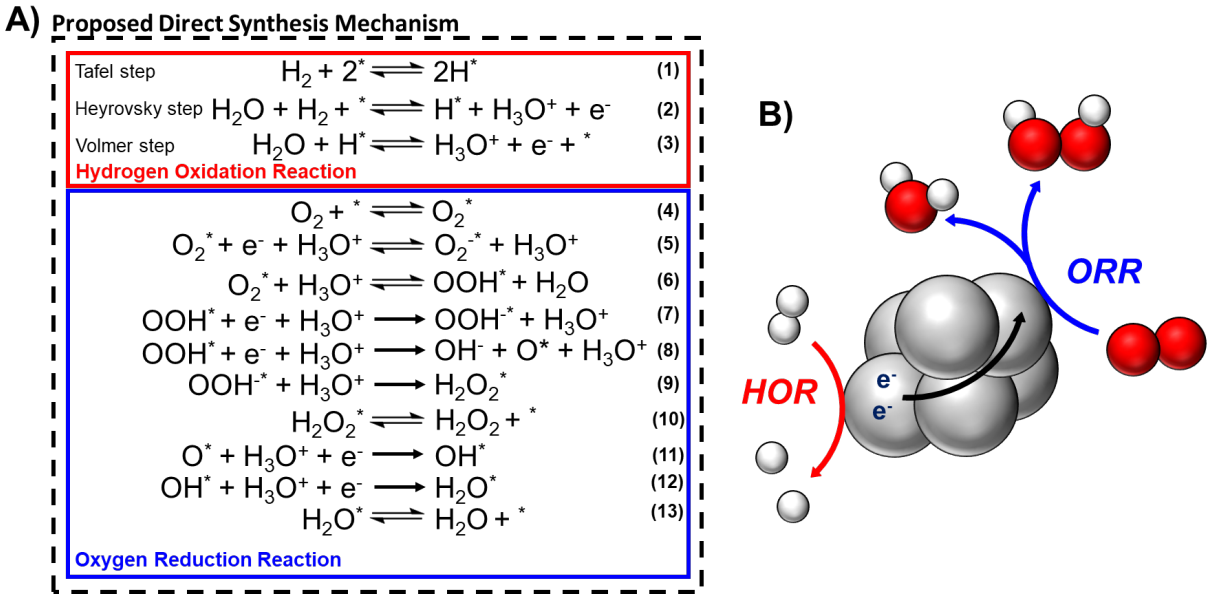

Figure 4.1 A) A schematic showing the mechanistic steps for hydrogen oxidation and oxygen reduction that have been proposed by the electrocatalytic literature and recent direct synthesis studies. B) Pictorial representation of the proposed mechanism for direct synthesis where HOR and ORR occur in concert on a catalyst surface.

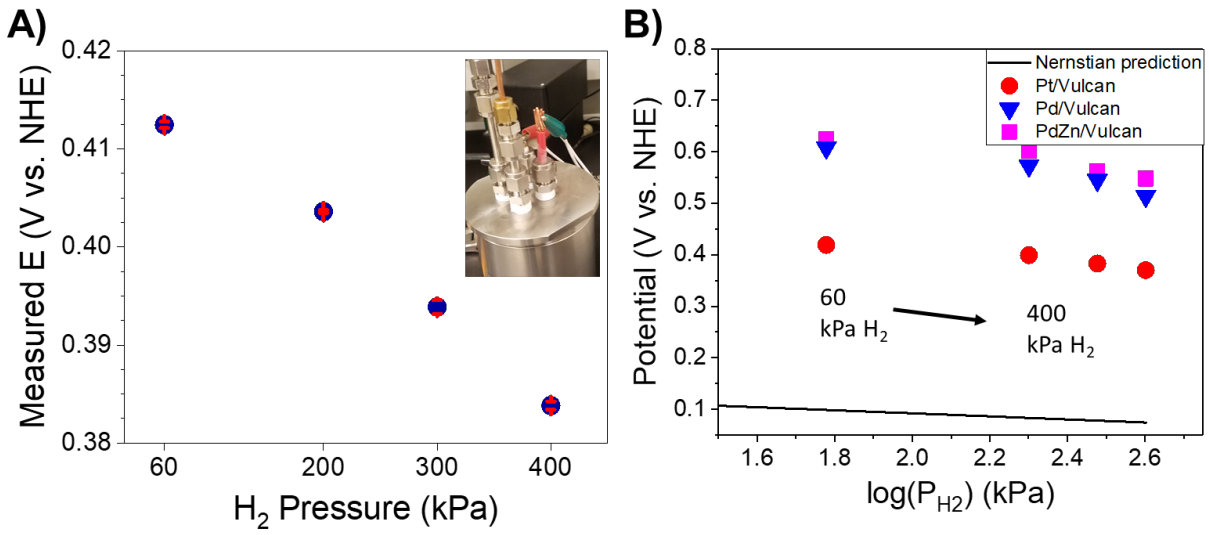

Figure 4.2 A) Example data set collected with the pressurized electrochemical cell for a PdAu catalyst. The negative shifts in potential as P_{H2} increased shown here were observed in all of the catalyst studied. In (B) is an attempt to fit the data using the Nernst equation. This analysis shows that electrochemical theory derived entirely from thermodynamics is clearly not suitable to describe the catalytic system of interest here.

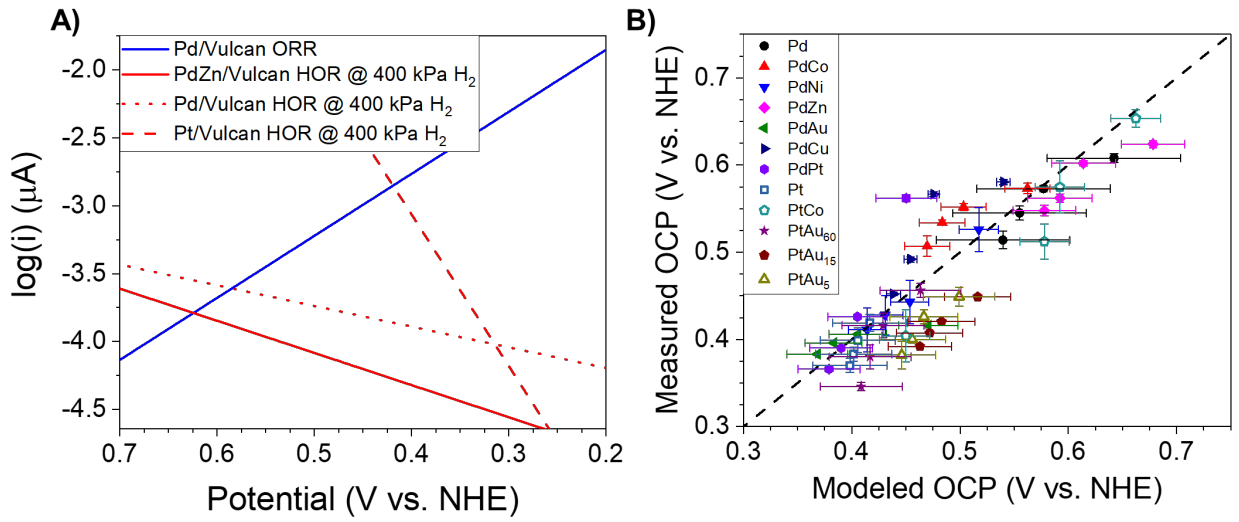

Figure 4.3 A) Theoretical Tafel plots generated from kinetics measured with rotating disk electrode methods. The intersection points between HOR and ORR from these plots were used to determine a predicted potential at which the catalyst would be operating at a given pressure of H_2 and O_2. B) Parity plot of predicted and measured OCPs based on the Butler-Volmer theory presented in part A. This plot demonstrates the accuracy of this model and that electrocatalyst and thermal catalysis are intimately related in the case of direct synthesis.

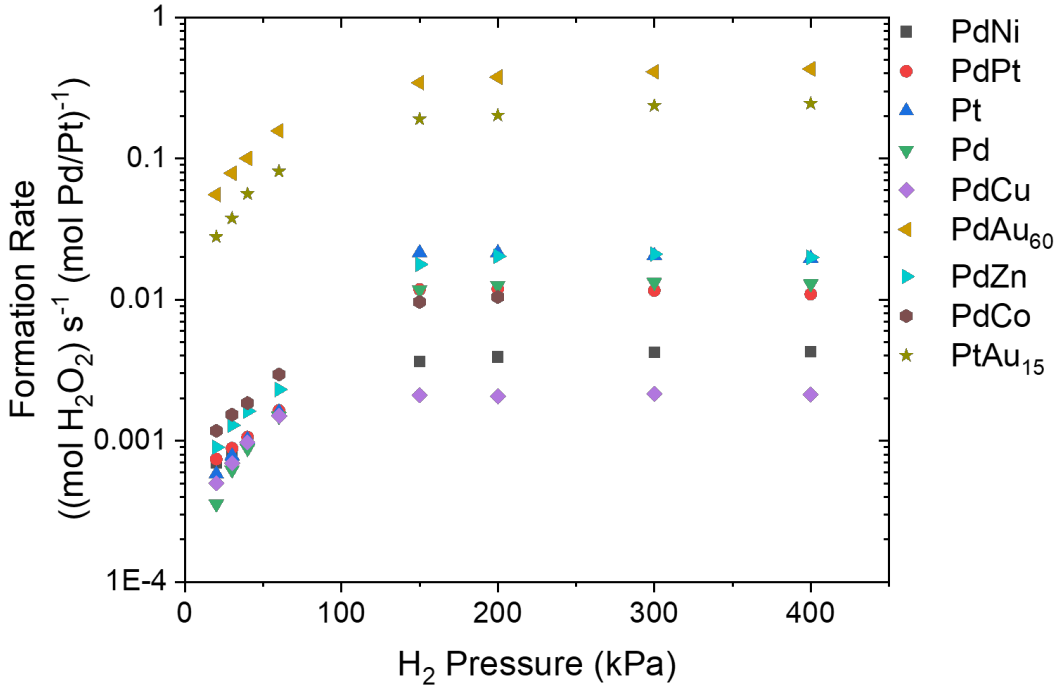

Figure 4.4 H_2O_2 formation as a function of H_2 partial pressure for each of the catalysts. The similarity in H_2 dependence of all the catalysts is strongly indicative that one mechanism is driving the formation of H_2O_2 in every case.

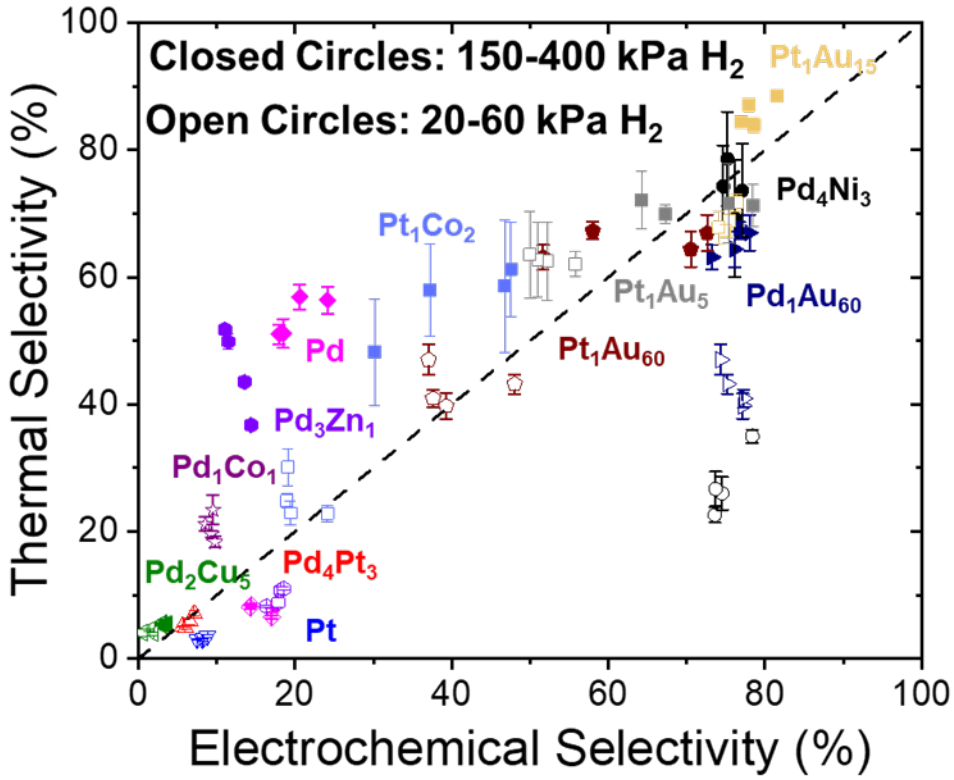

Figure 4.5 Parity plot of electrocatalytic and thermal catalytic selectivity toward H_2O_2 production. Electrocatalytic selectivity was determined with rotating ring disk electrode (RRDE) methods in 0.1 M $NaClO_4$. Thermal catalytic selectivity was determined by dividing H_2O_2 produced (determined by neocuproine titration) by H_2 that the catalyst converted (determined by gas chromatography).

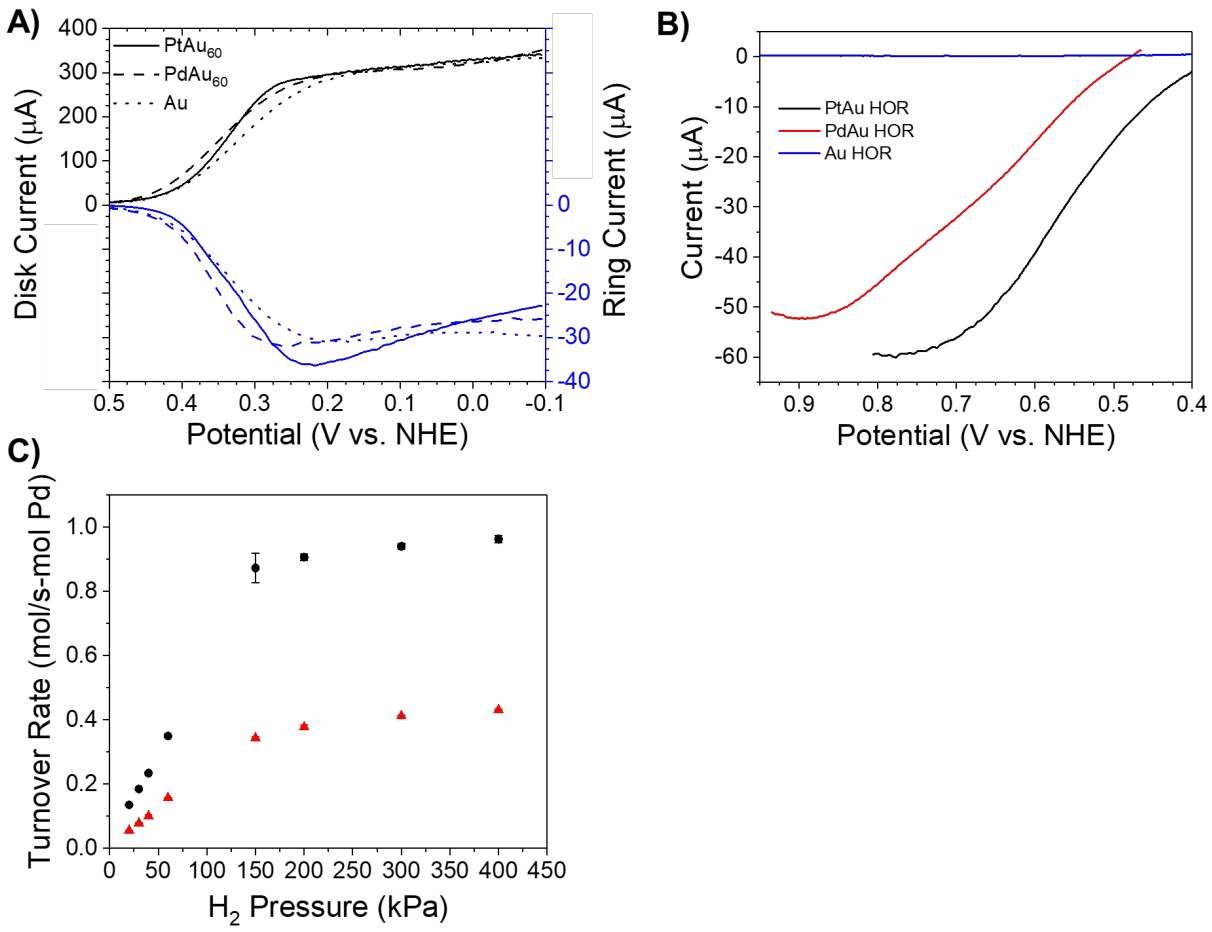

Figure 4.6 A) Comparison between Au, PdAu, and PtAu towards electrochemical H_2O_2 production showing that all produce H_2O_2 with equivalent selectivity. B) Comparison between the same catalysts towards HOR reactivity which shows a very clear trend where Au<PdAu<PtAu. C) Comparison of direct synthesis turnover rates where H_2O_2 cannot be measured from Au, and PtAu produces H_2O_2 at roughly twice the rate. The Butler-Volmer kinetic model detailed in Section 4.4 predicts that $PtAu_{60}$ should produce H_2O_2 in direct synthesis roughly 4 times as fast as $PdAu_{60}$. This slight overestimation is most likely due to a lack of knowledge of active surface species that are affecting the kinetics of H_2O_2 formation for each of these catalysts. Regardless, these data successfully illustrate the predictive power of electrochemical methods toward catalyst design of direct synthesis catalysts.

4.11. Raw Electrochemical Data

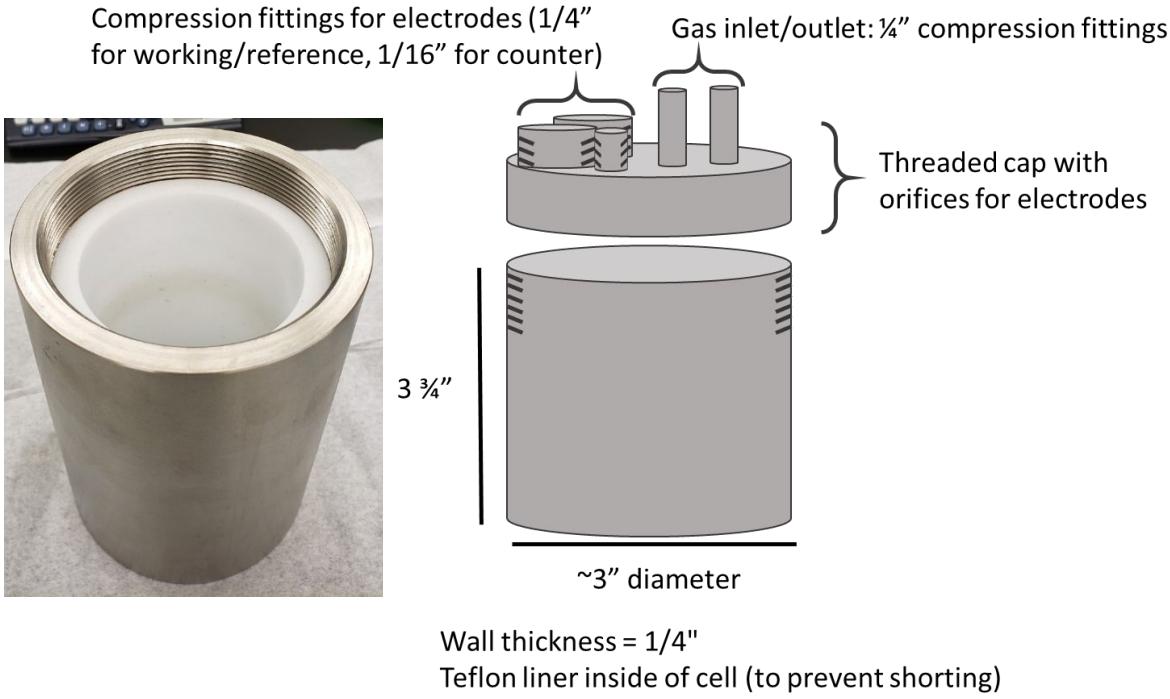

Supplementary Figure 4.1 Above are the dimensions and pictures for the pressurized cell design. The working electrode was a 3.0 mm diameter BASi glassy carbon electrode, the reference electrode was a CH Instruments Ag/AgCl electrode, and the counter electrode was a carbon rod connected to a 1/16" stainless steel wire. Below is are pictures of the cap with and without electrodes. The cyclic voltammogram is a control experiment with 0.5 mM ferrocenemethanol in 0.1 M KNO_3 to ensure that voltammetry is achievable at high pressures.

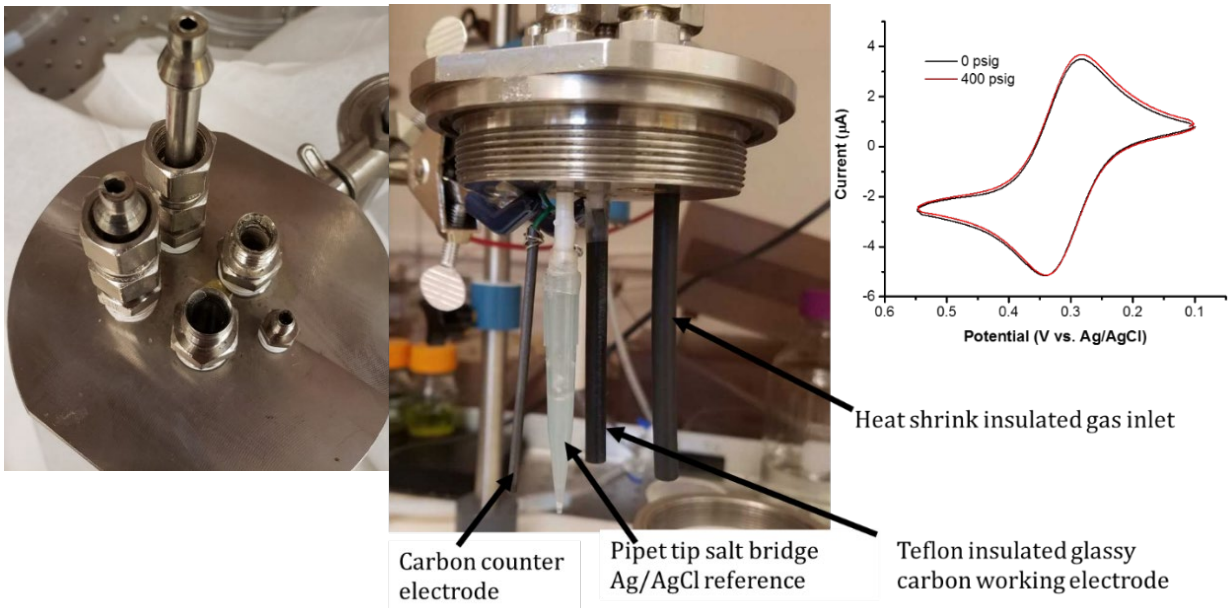

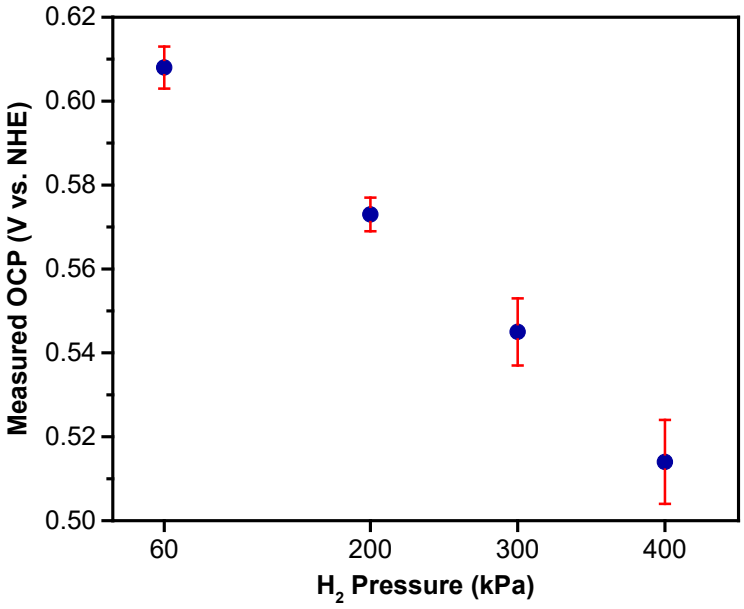

Supplementary Figure 4.2 Pressurized OCP measurements for Pd/Vulcan. Potentials were measured at various H_2 pressures with a constant O_2 pressure of 60 kPa.

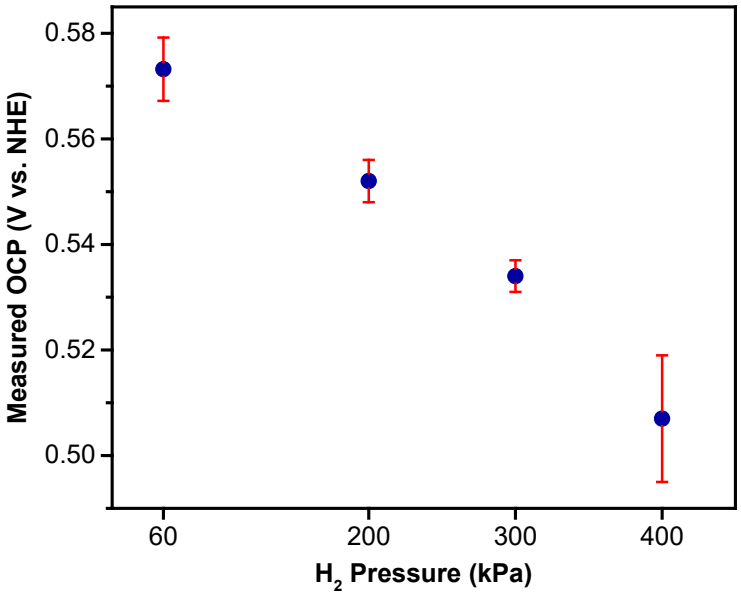

Supplementary Figure 4.3 Pressurized OCP measurements for PdCo/Vulcan with water as a solvent. Glassy carbon working electrode was modified with 5 µL of a catalyst slurry (5 mg catalyst, 1 mL water, 0.6 mL ethanol) and 1 µL of 0.5 wt% Nafion solution. Potentials were measured at various H_2 pressures with a constant O_2 pressure of 60 kPa.

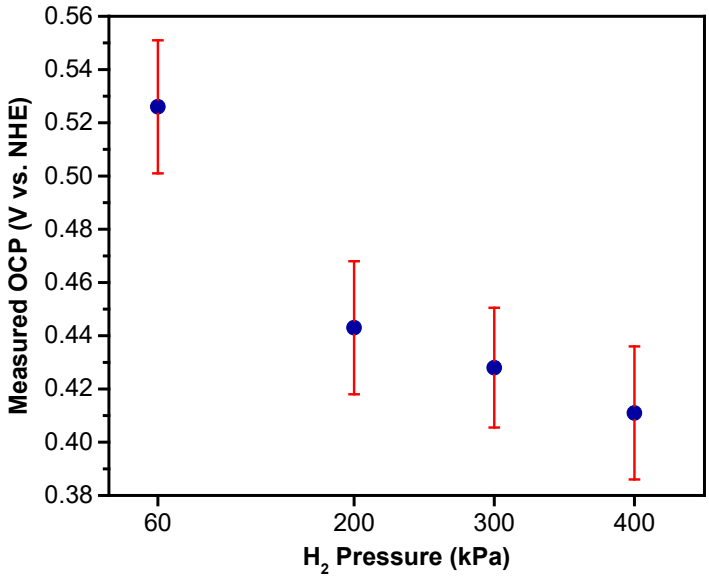

Supplementary Figure 4.4 Pressurized OCP measurements for PdNi/Vulcan with water as a solvent. Glassy carbon working electrode was modified with 5 µL of a catalyst slurry (5 mg catalyst, 1 mL water, 0.6 mL ethanol) and 1 µL of 0.5 wt% Nafion solution. Potentials were measured at various H_2 pressures with a constant O_2 pressure of 60 kPa.

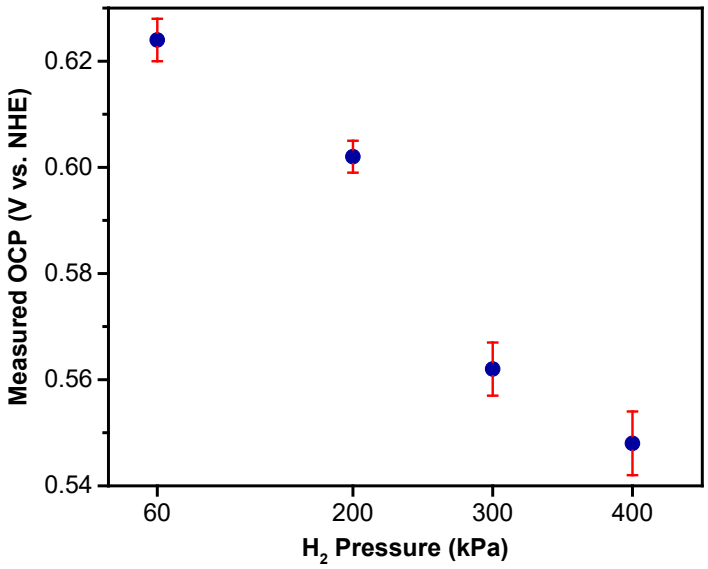

Supplementary Figure 4.5 Pressurized OCP measurements for PdZn/Vulcan with water as a solvent. Glassy carbon working electrode was modified with 5 µL of a catalyst slurry (5 mg catalyst, 1 mL water, 0.6 mL ethanol) and 1 µL of 0.5 wt% Nafion solution. Potentials were measured at various H_2 pressures with a constant O_2 pressure of 60 kPa.

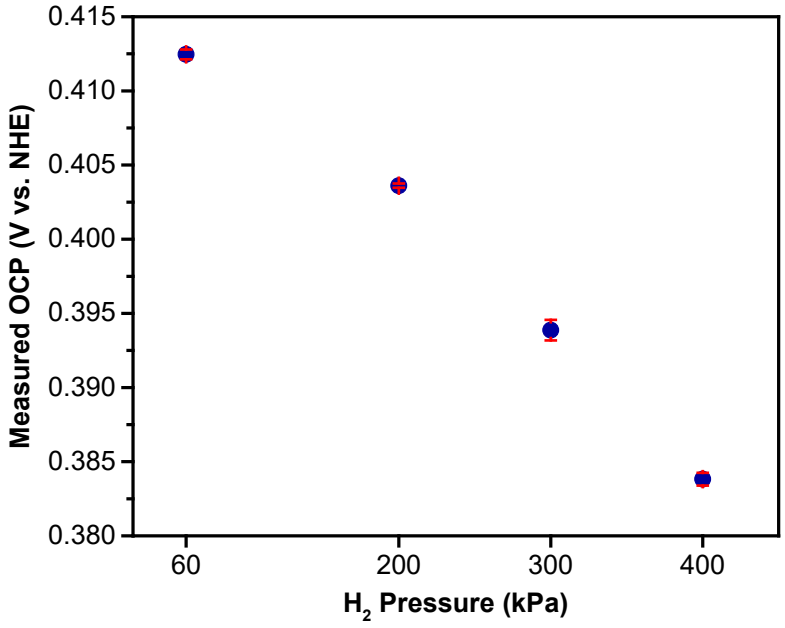

Supplementary Figure 4.6 Pressurized OCP measurements for $PdAu_{60}$/Vulcan with water as a solvent. Glassy carbon working electrode was modified with 5 µL of a catalyst slurry (5 mg catalyst, 1 mL water, 0.6 mL ethanol) and 1 µL of 0.5 wt% Nafion solution. Potentials were measured at various H_2 pressures with a constant O_2 pressure of 60 kPa.

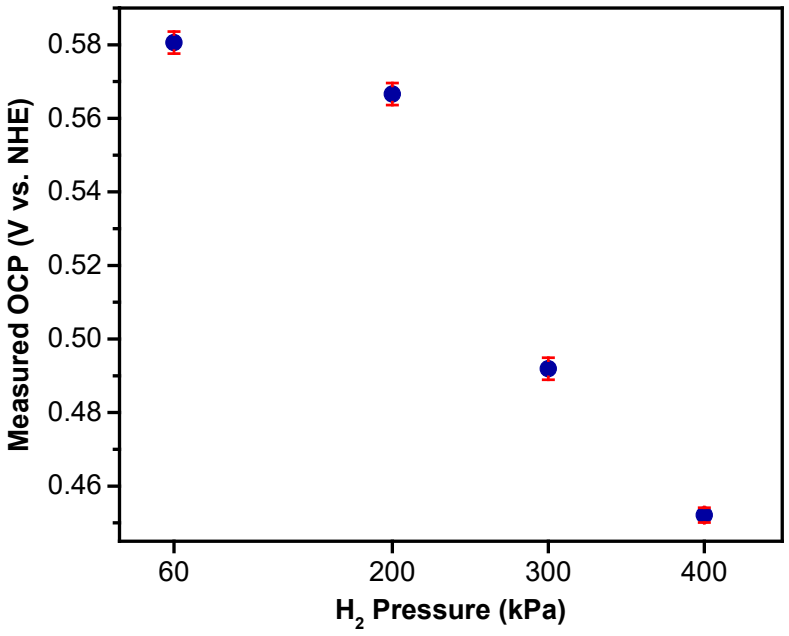

Supplementary Figure 4.7 Pressurized OCP measurements for PdCu/Vulcan with water as a solvent. Glassy carbon working electrode was modified with 5 µL of a catalyst slurry (5 mg catalyst, 1 mL water, 0.6 mL ethanol) and 1 µL of 0.5 wt% Nafion solution. Potentials were measured at various H_2 pressures with a constant O_2 pressure of 60 kPa.

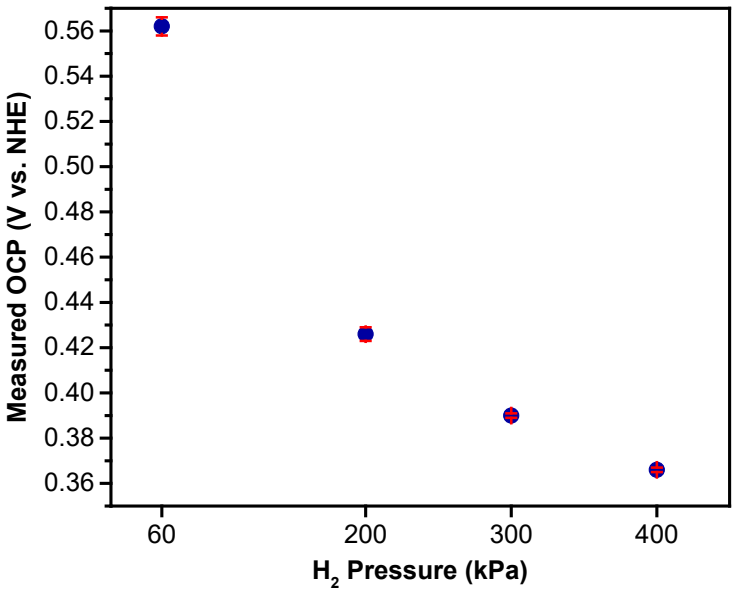

Supplementary Figure 4.8 Pressurized OCP measurements for PdPt/Vulcan with water as a solvent. Glassy carbon working electrode was modified with 5 µL of a catalyst slurry (5 mg catalyst, 1 mL water, 0.6 mL ethanol) and 1 µL of 0.5 wt% Nafion solution. Potentials were measured at various H_2 pressures with a constant O_2 pressure of 60 kPa.

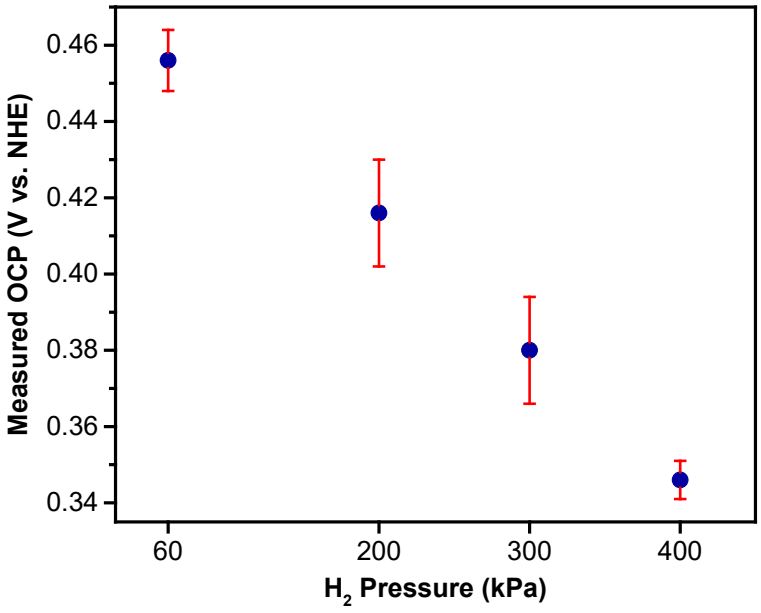

Supplementary Figure 4.9 Pressurized OCP measurements for $PtAu_{60}$/Vulcan with water as a solvent. Glassy carbon working electrode was modified with 5 µL of a catalyst slurry (5 mg catalyst, 1 mL water, 0.6 mL ethanol) and 1 µL of 0.5 wt% Nafion solution. Potentials were measured at various H_2 pressures with a constant O_2 pressure of 60 kPa.

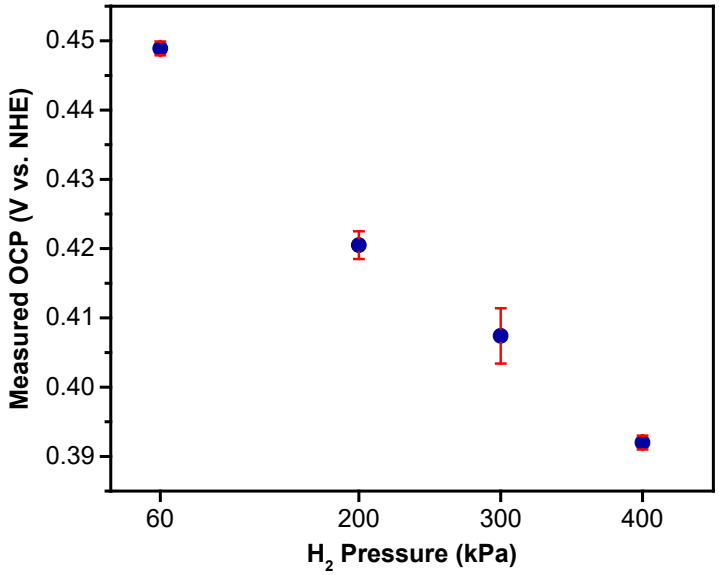

Supplementary Figure 4.10 Pressurized OCP measurements for $PtAu_{15}$/Vulcan with water as a solvent. Glassy carbon working electrode was modified with 5 µL of a catalyst slurry (5 mg catalyst, 1 mL water, 0.6 mL ethanol) and 1 µL of 0.5 wt% Nafion solution. Potentials were measured at various H_2 pressures with a constant O_2 pressure of 60 kPa.

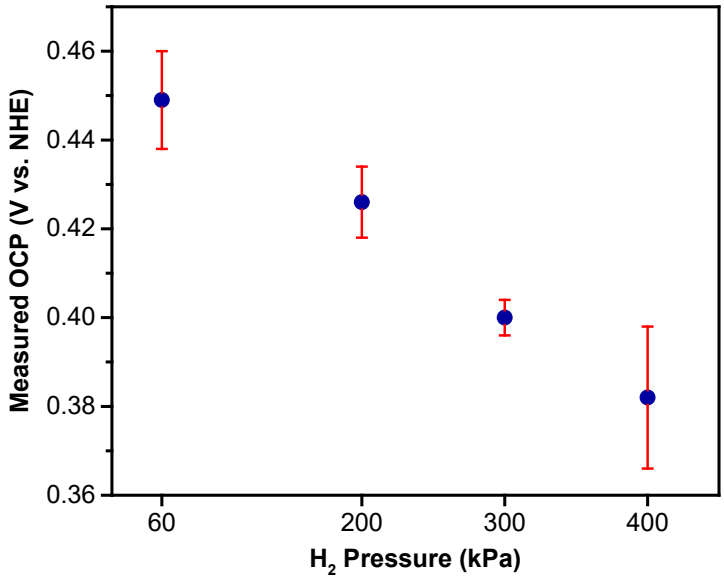

Supplementary Figure 4.11 Pressurized OCP measurements for $PtAu_5$/Vulcan with water as a solvent. Glassy carbon working electrode was modified with 5 µL of a catalyst slurry (5 mg catalyst, 1 mL water, 0.6 mL ethanol) and 1 µL of 0.5 wt% Nafion solution. Potentials were measured at various H_2 pressures with a constant O_2 pressure of 60 kPa.

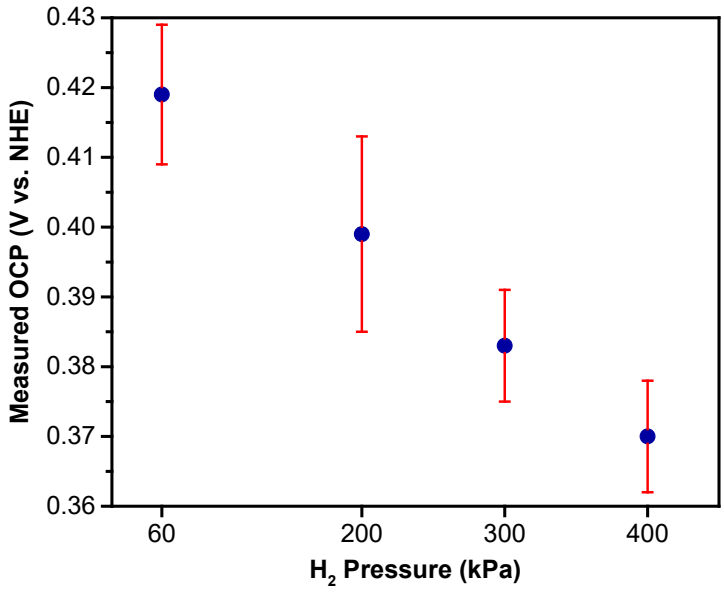

Supplementary Figure 4.12 Pressurized OCP measurements for Pt/Vulcan with water as a solvent. Glassy carbon working electrode was modified with 5 µL of a catalyst slurry (5 mg catalyst, 1 mL water, 0.6 mL ethanol) and 1 µL of 0.5 wt% Nafion solution. Potentials were measured at various H_2 pressures with a constant O_2 pressure of 60 kPa.

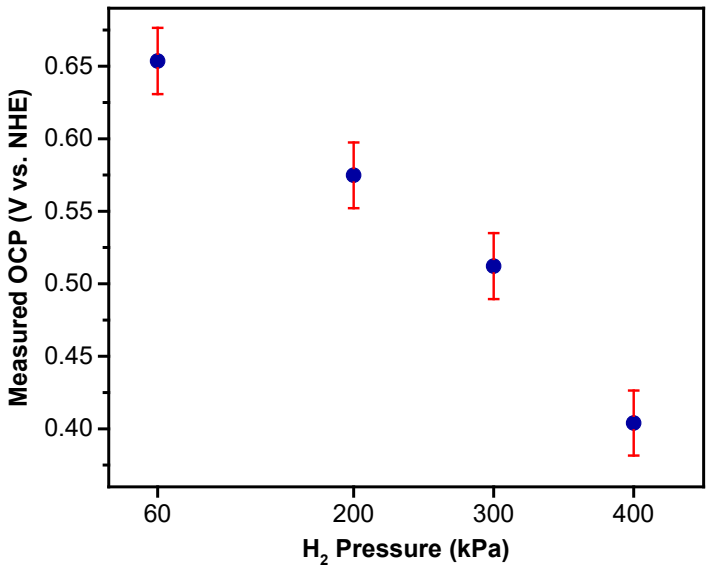

Supplementary Figure 4.13 Pressurized OCP measurements for PtCo/Vulcan with water as a solvent. Glassy carbon working electrode was modified with 5 µL of a catalyst slurry (5 mg catalyst, 1 mL water, 0.6 mL ethanol) and 1 µL of 0.5 wt% Nafion solution. Potentials were measured at various H_2 pressures with a constant O_2 pressure of 60 kPa.

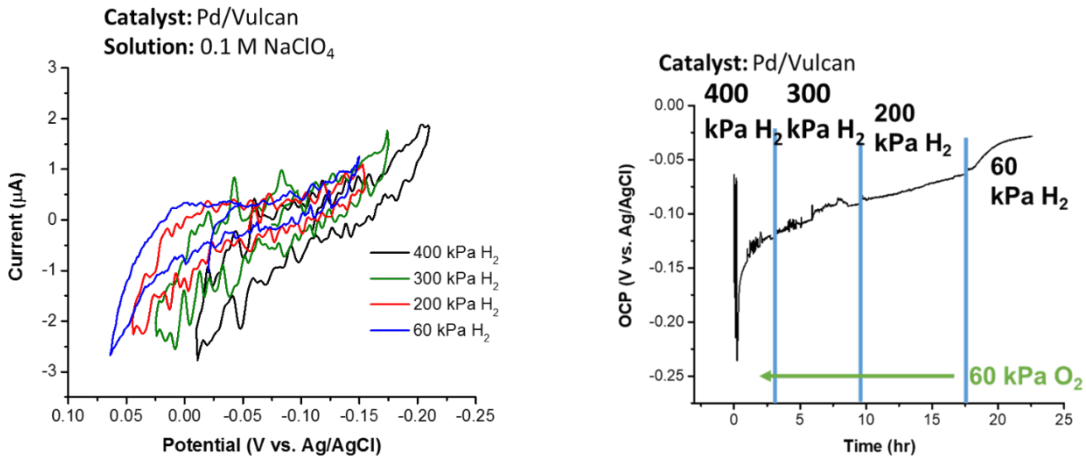

Supplementary Figure 4.14 Pressurized amperometric experiments on Pd/Vulcan in which a cyclic voltammogram was acquired at each H_2 pressure achieved during the OCP measurements. The potential range of the voltammograms agrees well with the potential range of the OCP measurements, which supports the validity of these measurements.

Materials	ORR k^0 (cm/s)	ORR α	HOR k^0 (cm/s)	HOR β
Pd	$2.8 \times 10^{-4} \pm 1.3 \times 10^{-4}$	0.27 ± 0.03	$1.1 \times 10^{-4} \pm 0.4 \times 10^{-4}$	0.91 ± 0.01
PdZn	$3.3 \times 10^{-4} \pm 0.9 \times 10^{-4}$	0.24 ± 0.05	$2.8 \times 10^{-5} \pm 0.4 \times 10^{-5}$	0.86 ± 0.01
Pt	$2.5 \times 10^{-4} \pm 1.9 \times 10^{-4}$	0.28 ± 0.05	$1.0 \times 10^{-5} \pm 2.5 \times 10^{-6}$	0.34 ± 0.03
PtCo	$4.3 \times 10^{-4} \pm 2.6 \times 10^{-4}$	0.30 ± 0.06	$4.1 \times 10^{-6} \pm 9.0 \times 10^{-7}$	0.25 ± 0.02
PdCo	$2.9 \times 10^{-4} \pm 0.5 \times 10^{-4}$	0.24 ± 0.04	$6.2 \times 10^{-5} \pm 2.0 \times 10^{-5}$	0.82 ± 0.01
PdPt	$4.1 \times 10^{-4} \pm 2.4 \times 10^{-4}$	0.32 ± 0.08	$2.0 \times 10^{-6} \pm 1.0 \times 10^{-6}$	0.23 ± 0.06
PdNi	$4.7 \times 10^{-4} \pm 6.0 \times 10^{-5}$	0.21 ± 0.05	$1.1 \times 10^{-4} \pm 0.4 \times 10^{-4}$	0.88 ± 0.02
PdCu	$2.4 \times 10^{-4} \pm 0.2 \times 10^{-4}$	0.21 ± 0.02	$2.7 \times 10^{-5} \pm 0.6 \times 10^{-5}$	0.82± 0.02
Pd_1Au_{60}	$4.3 \times 10^{-5} \pm 1.7 \times 10^{-5}$	0.37 ± 0.04	$3.3 \times 10^{-5} \pm 0.5 \times 10^{-5}$	0.93 ± 0.01
Au	$3.1 \times 10^{-5} \pm 0.5 \times 10^{-5}$	0.37 ± 0.01	(too slow to measure w/ RDE)	--
Pt_1Au_{60}	$2.0 \times 10^{-5} \pm 0.4 \times 10^{-5}$	0.36 ± 0.02	$4.1 \times 10^{-5} \pm 2.8 \times 10^{-5}$	0.72 ± 0.05
Pt_1Au_{15}	$1.6 \times 10^{-5} \pm 0.8 \times 10^{-5}$	0.41 ± 0.03	$1.2 \times 10^{-5} \pm 3.0 \times 10^{-6}$	0.73 ± 0.02
Pt_1Au_5	$2.2 \times 10^{-5} \pm 0.4 \times 10^{-5}$	0.46 ± 0.02	$7.6 \times 10^{-5} \pm 4.3 \times 10^{-5}$	0.77 ± 0.08

Supplementary Table 4.1 Average k^0 and alpha values (ORR and HOR) for each of the catalysts of interest. Each measurement is an average of triplicate analyses.

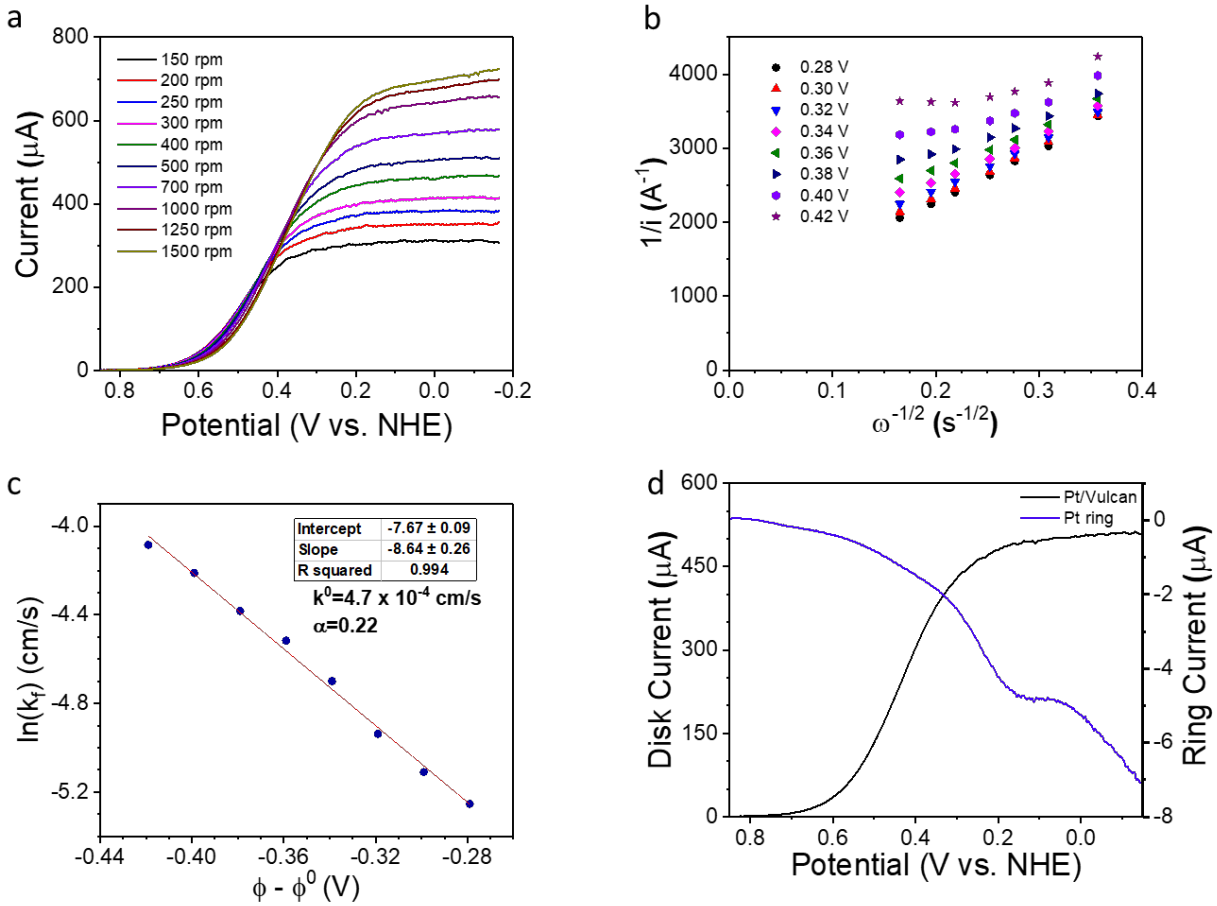

Supplementary Figure 4.15 R(R)DE, Koutecky-Levich, and Butler-Volmer analyses for Pt/Vulcan ORR. These analyses were carried out in O_2 saturated 0.1 M $NaClO_4$. All catalysts were adhered to the RDE by dispensing 10 μL of a catalyst slurry (5 mg catalyst, 1 mL water, 0.6 mL ethanol) onto the disk and adding 5 μL of 0.5 wt.% Nafion to prevent desorption.

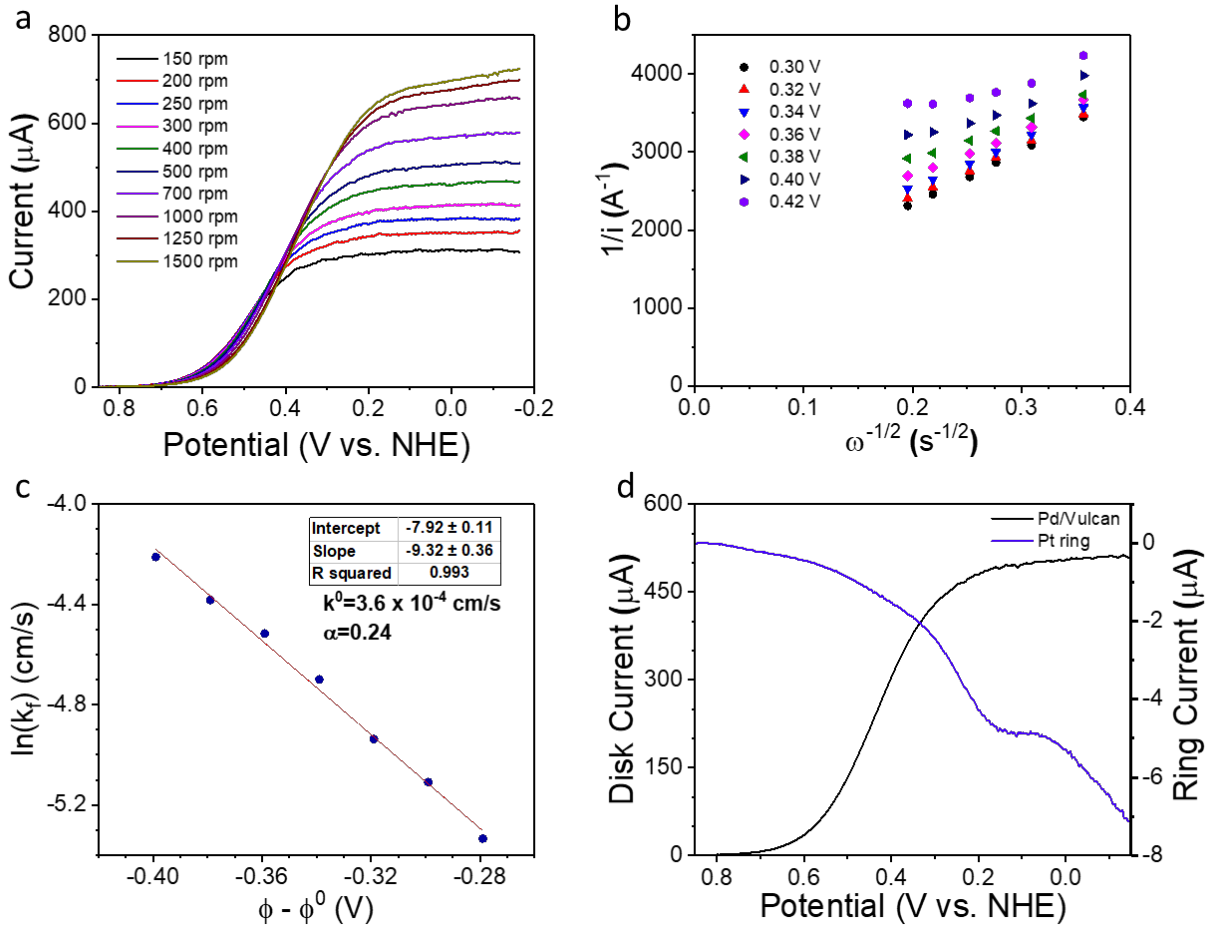

Supplementary Figure 4.16 R(R)DE, Koutecky-Levich, and Butler-Volmer analyses for Pd/Vulcan ORR. These analyses were carried out in O_2 saturated 0.1 M $NaClO_4$.

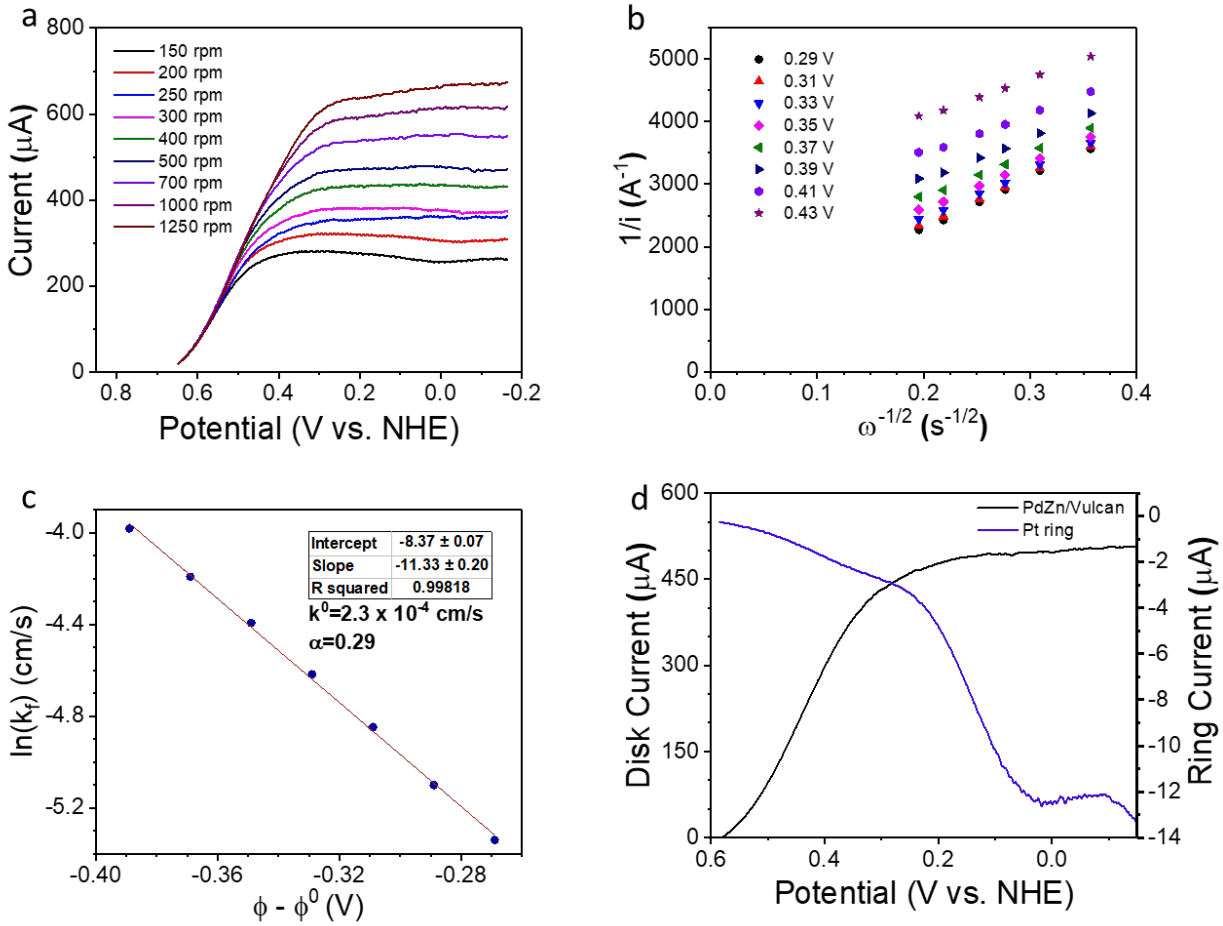

Supplementary Figure 4.17 R(R)DE, Koutecky-Levich, and Butler-Volmer analyses for PdZn/Vulcan ORR. These analyses were carried out in O_2 saturated 0.1 M $NaClO_4$.

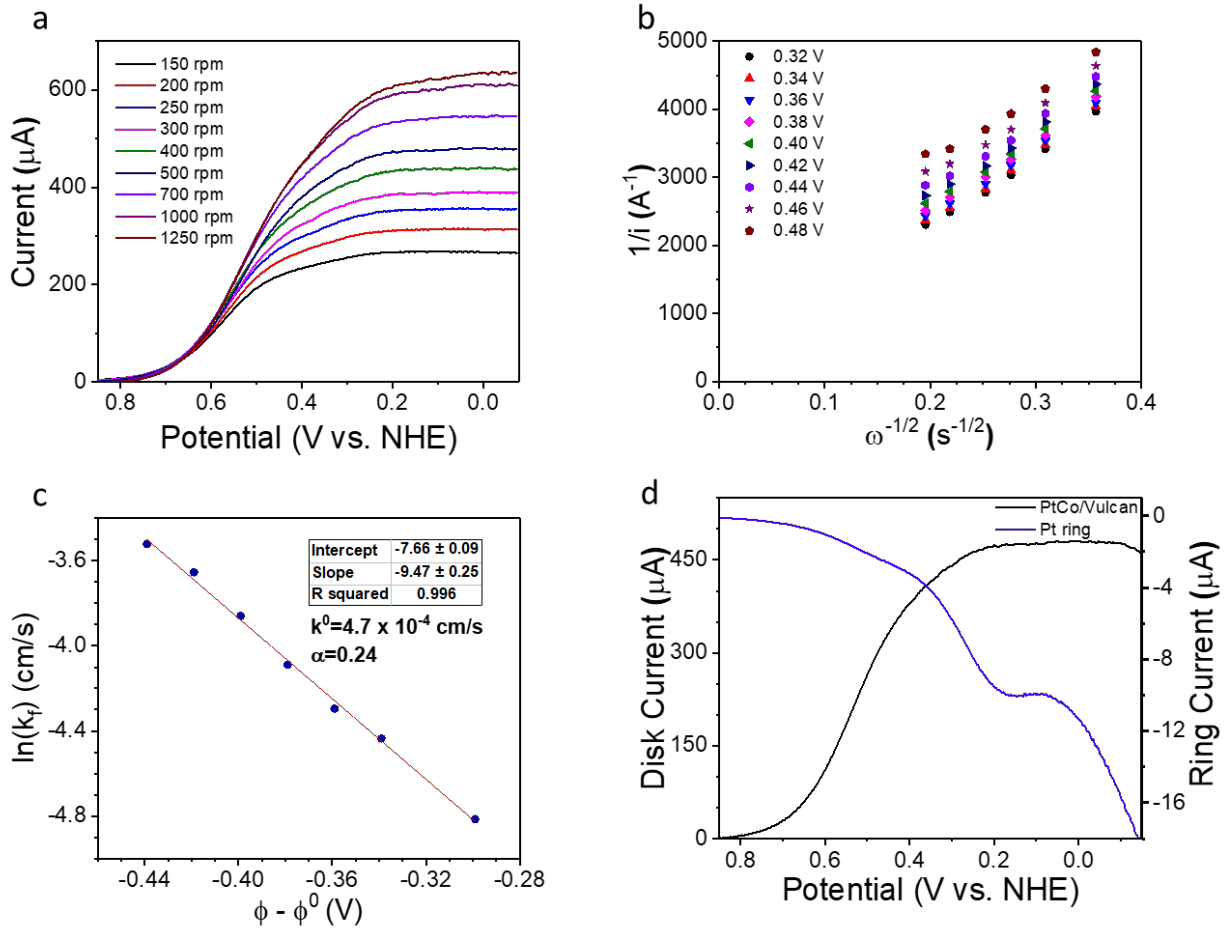

Supplementary Figure 4.18 R(R)DE, Koutecky-Levich, and Butler-Volmer analyses for PtCo/Vulcan ORR. These analyses were carried out in O_2 saturated 0.1 M $NaClO_4$.

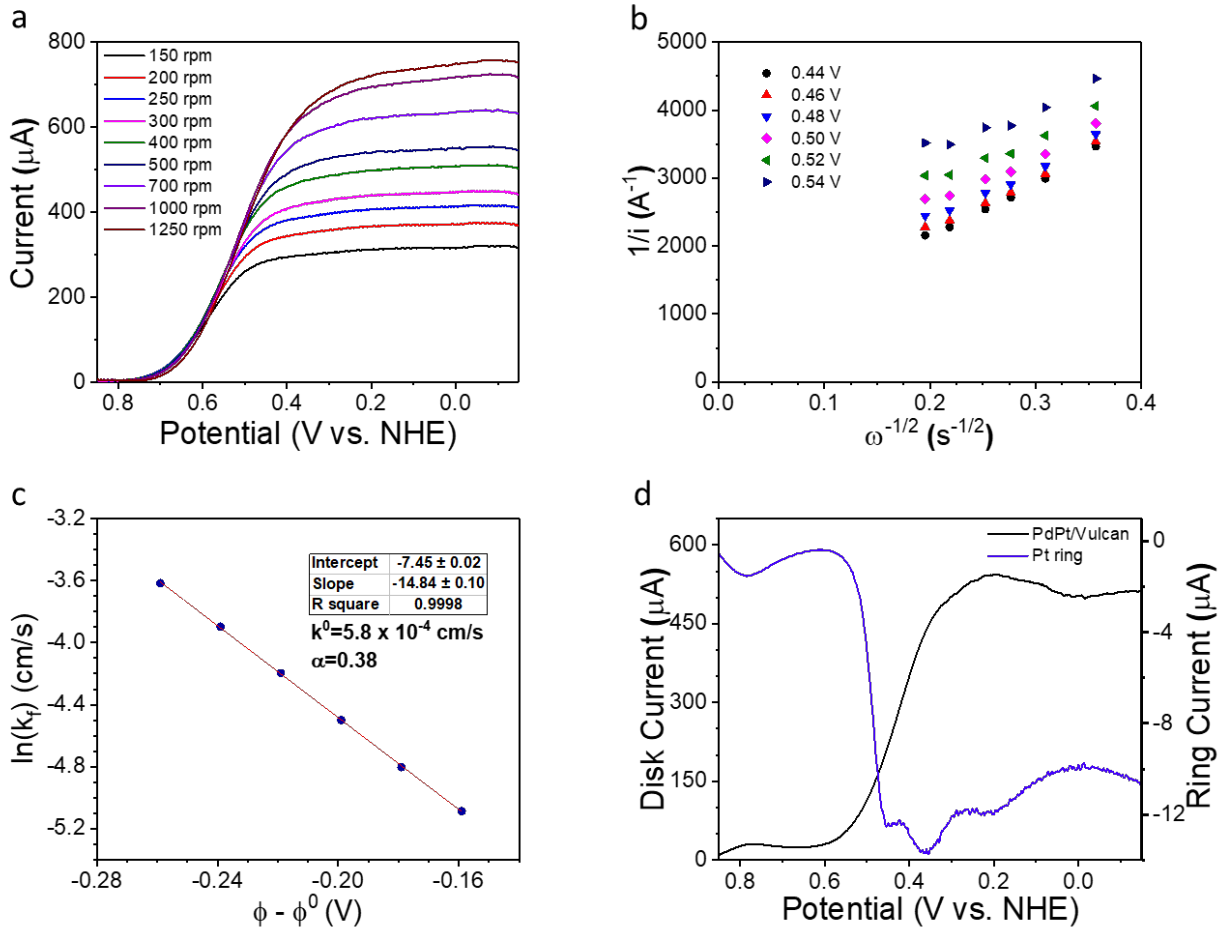

Supplementary Figure 4.19 R(R)DE, Koutecky-Levich, and Butler-Volmer analyses for PdPt/Vulcan ORR. These analyses were carried out in O_2 saturated 0.1 M $NaClO_4$.

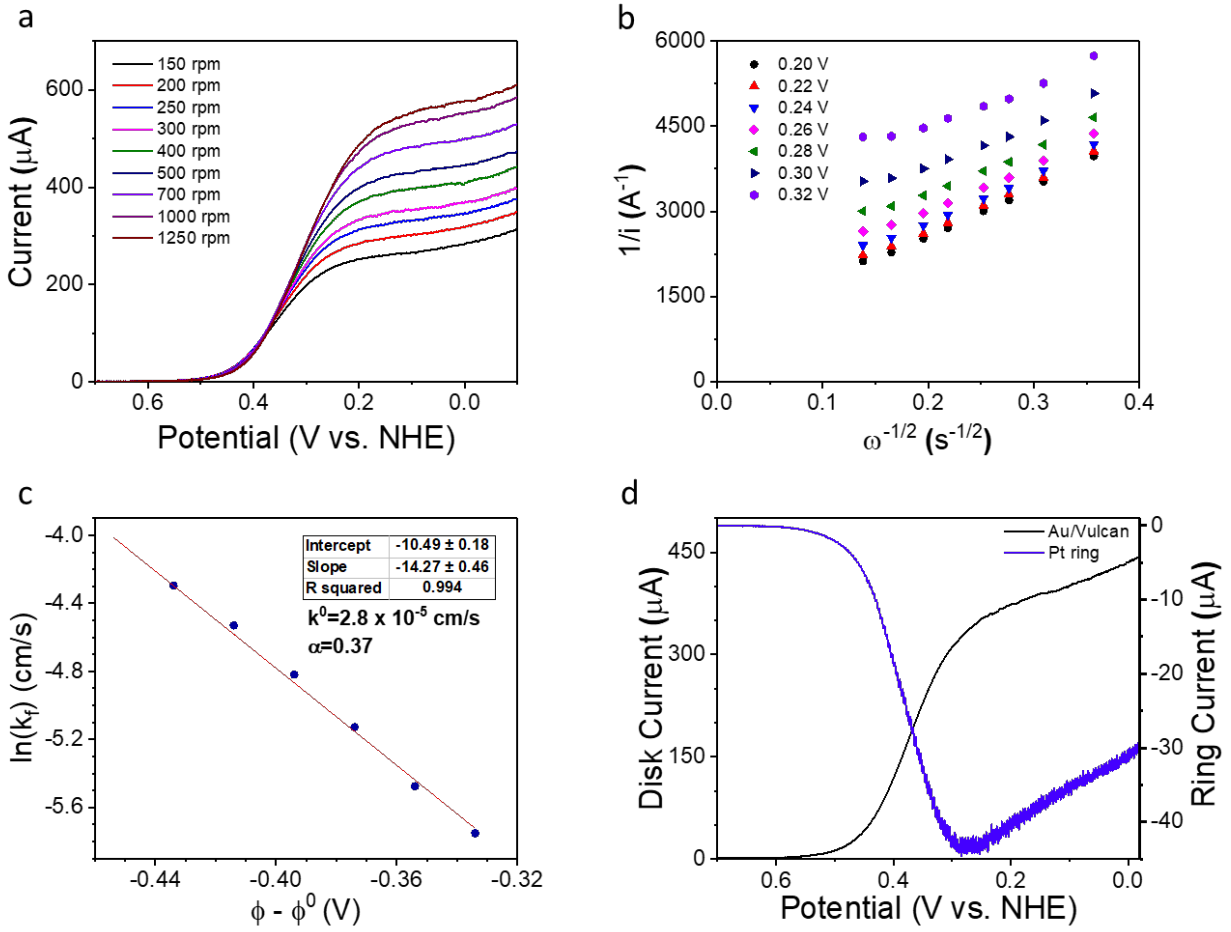

Supplementary Figure 4.20 R(R)DE, Koutecky-Levich, and Butler-Volmer analyses for Au/Vulcan ORR. These analyses were carried out in O_2 saturated 0.1 M $NaClO_4$.

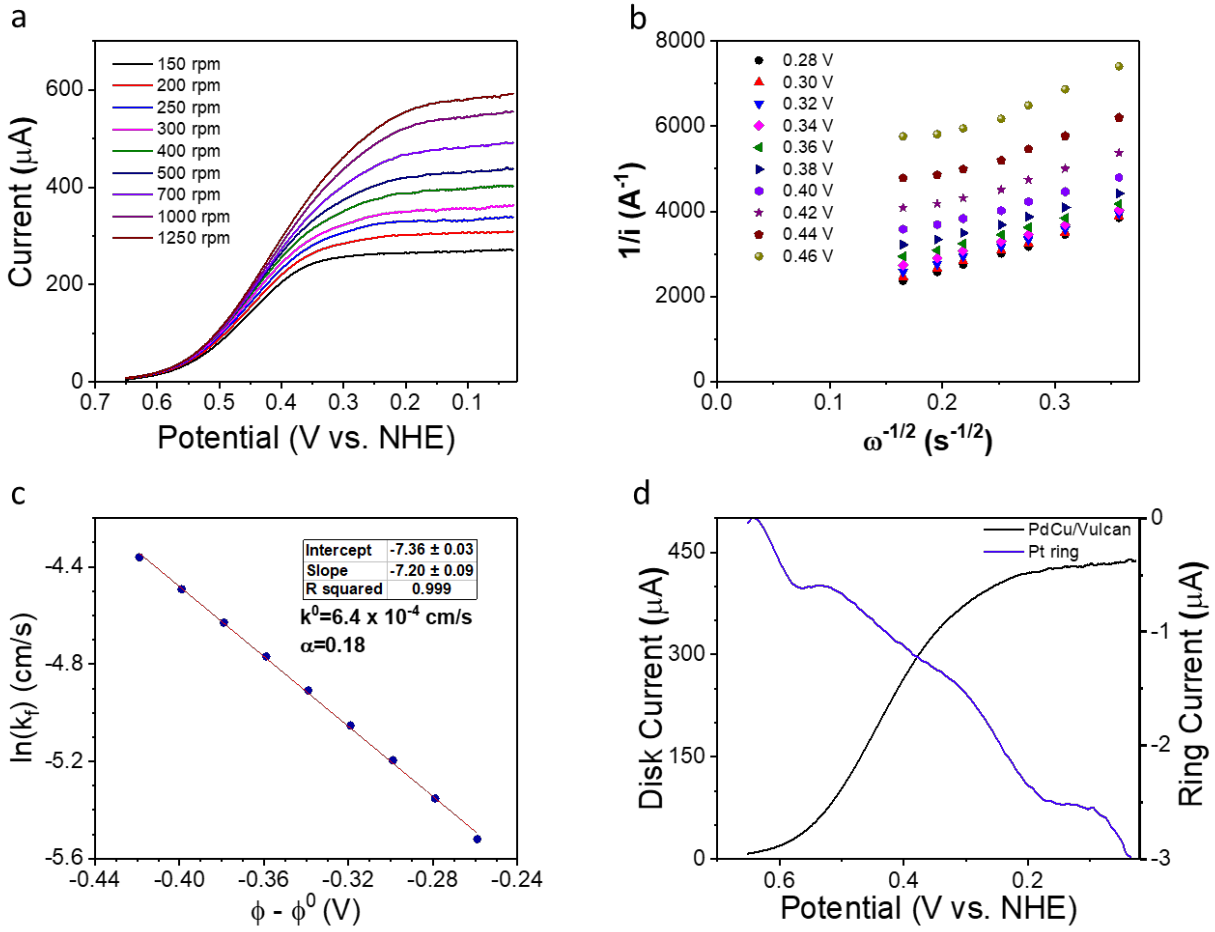

Supplementary Figure 4.21 R(R)DE, Koutecky-Levich, and Butler-Volmer analyses for PdCu/Vulcan ORR. These analyses were carried out in O_2 saturated 0.1 M $NaClO_4$.

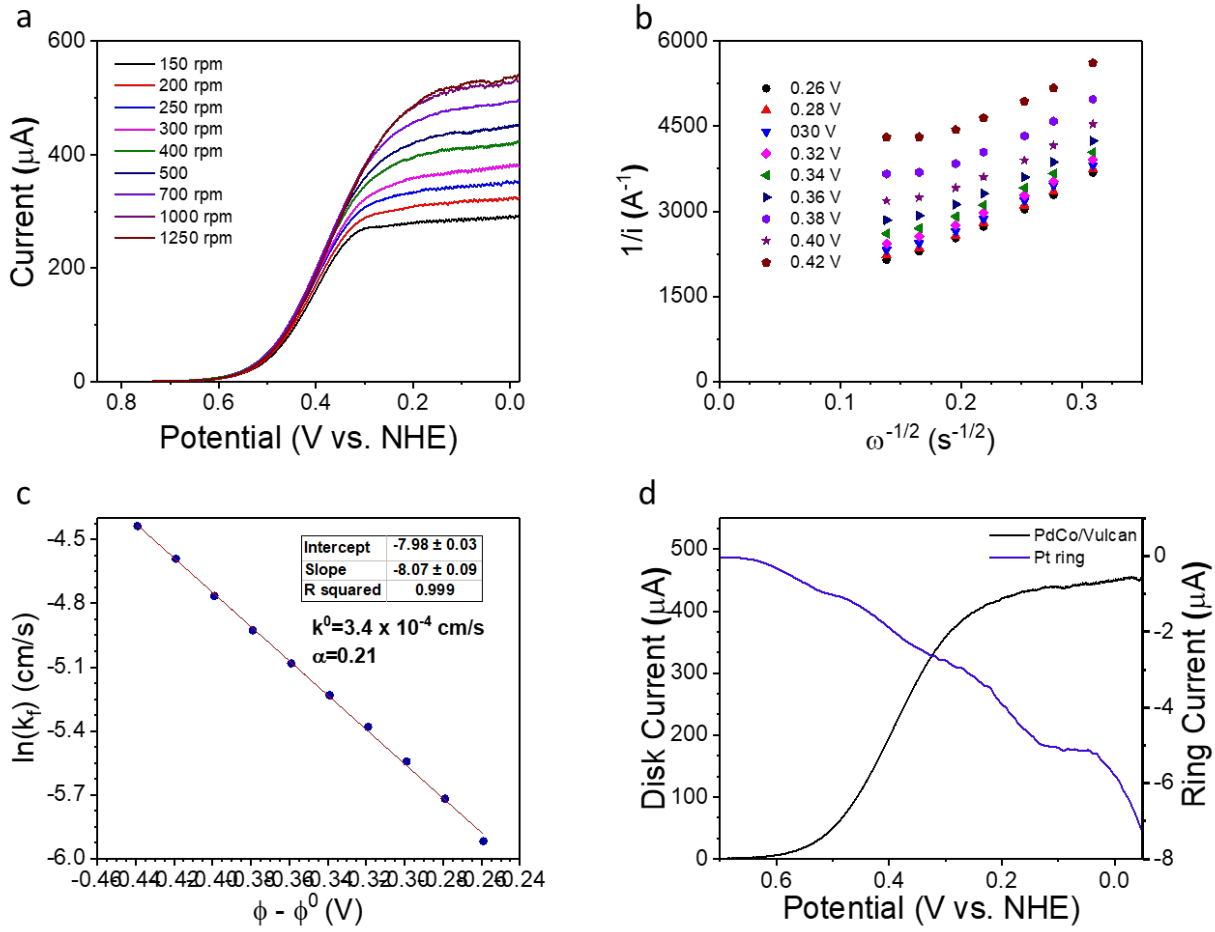

Supplementary Figure 4.22 R(R)DE, Koutecky-Levich, and Butler-Volmer analyses for PdCo/Vulcan ORR. These analyses were carried out in O_2 saturated 0.1 M $NaClO_4$.

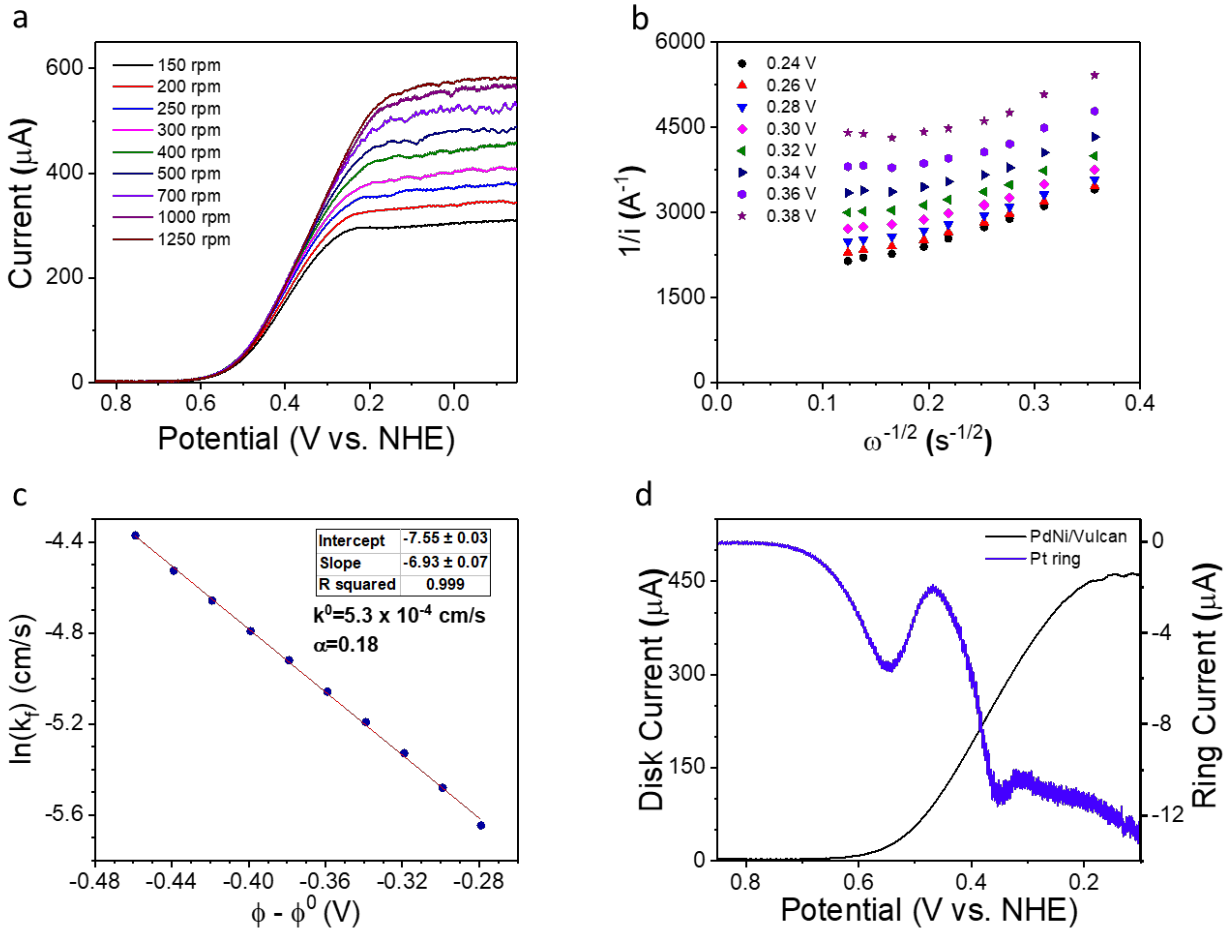

Supplementary Figure 4.23 R(R)DE, Koutecky-Levich, and Butler-Volmer analyses for PdNi/Vulcan ORR. These analyses were carried out in O_2 saturated 0.1 M $NaClO_4$.

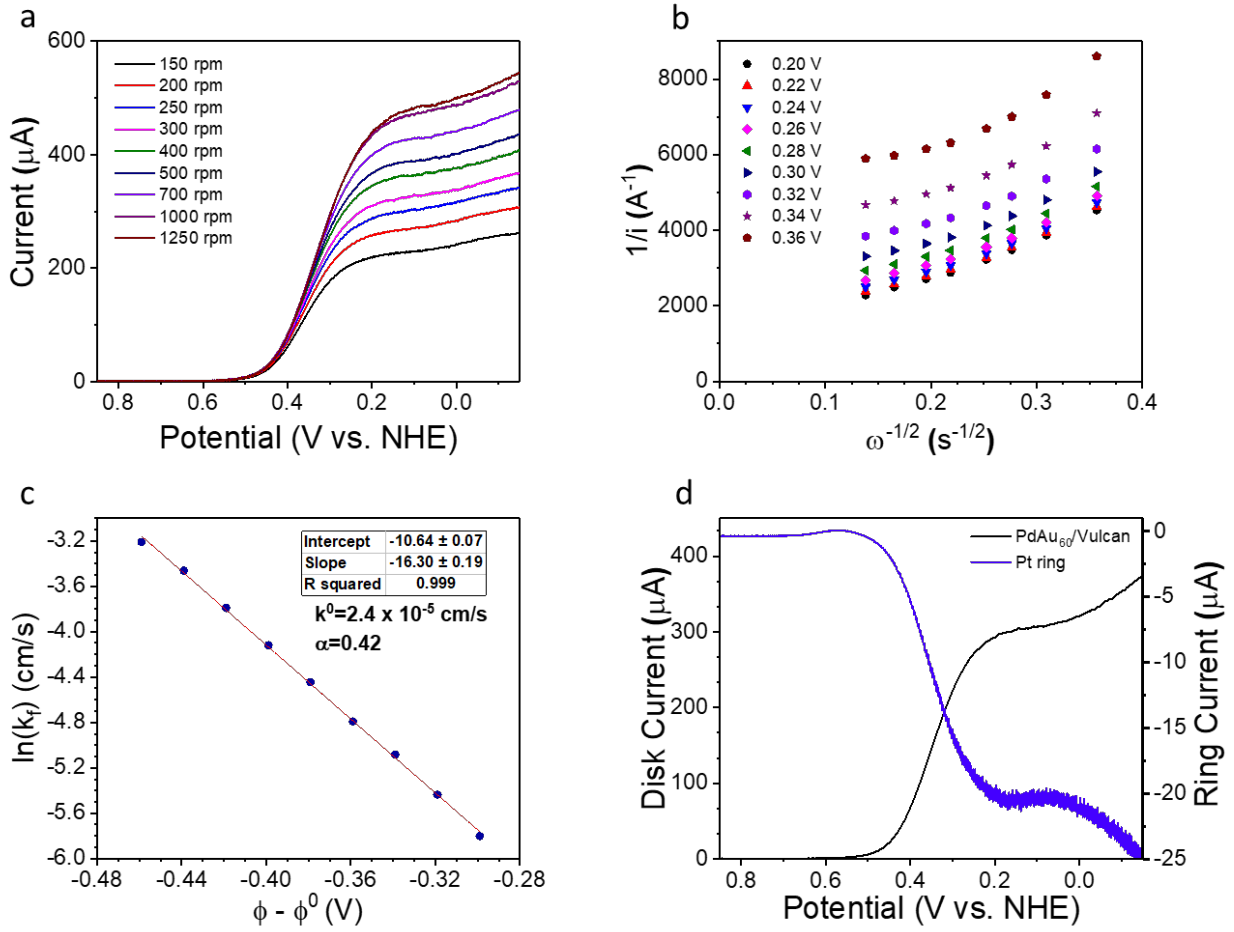

Supplementary Figure 4.24 R(R)DE, Koutecky-Levich, and Butler-Volmer analyses for $PdAu_{60}$/Vulcan ORR. These analyses were carried out in O_2 saturated 0.1 M $NaClO_4$.

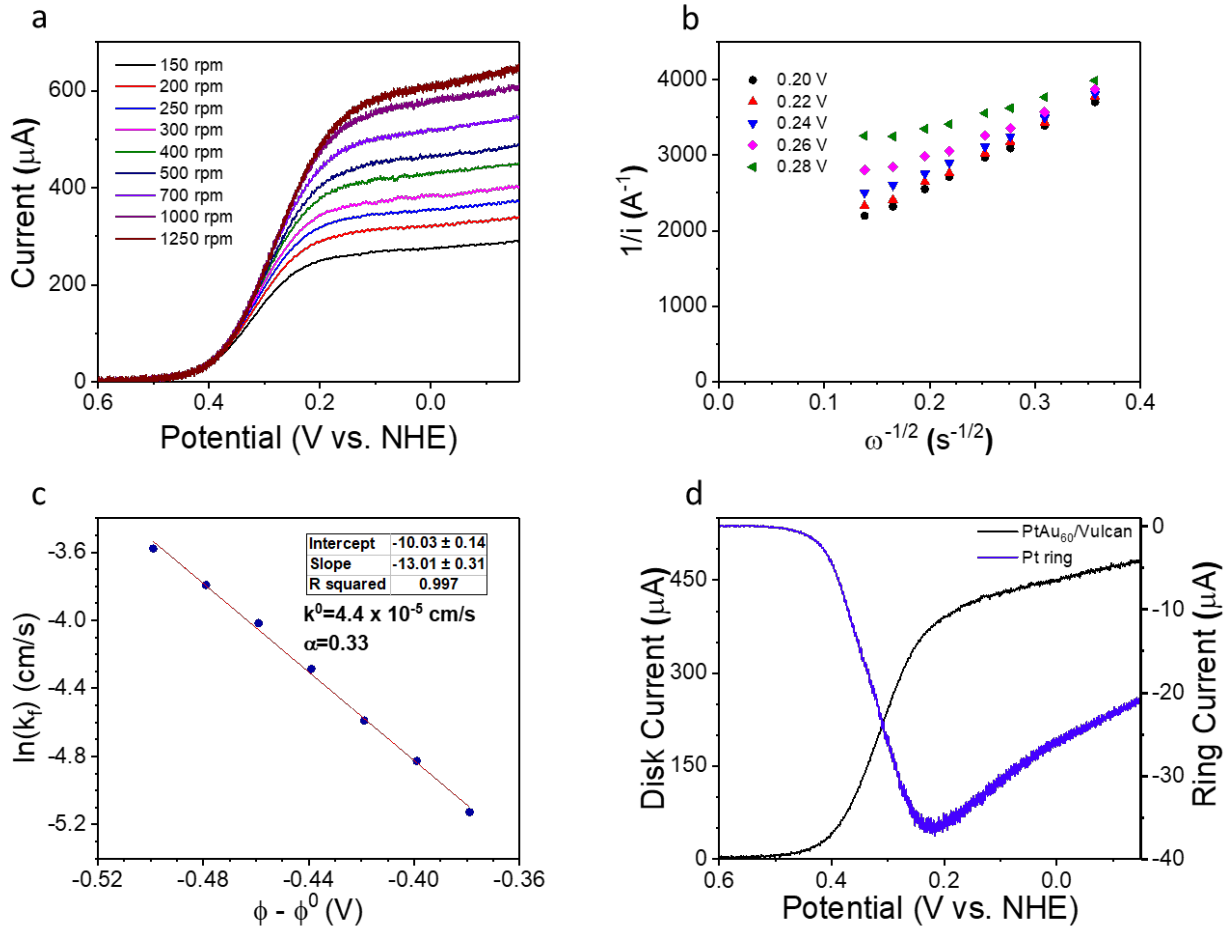

Supplementary Figure 4.25 R(R)DE, Koutecky-Levich, and Butler-Volmer analyses for $PtAu_{60}$/Vulcan ORR. These analyses were carried out in O_2 saturated 0.1 M $NaClO_4$.

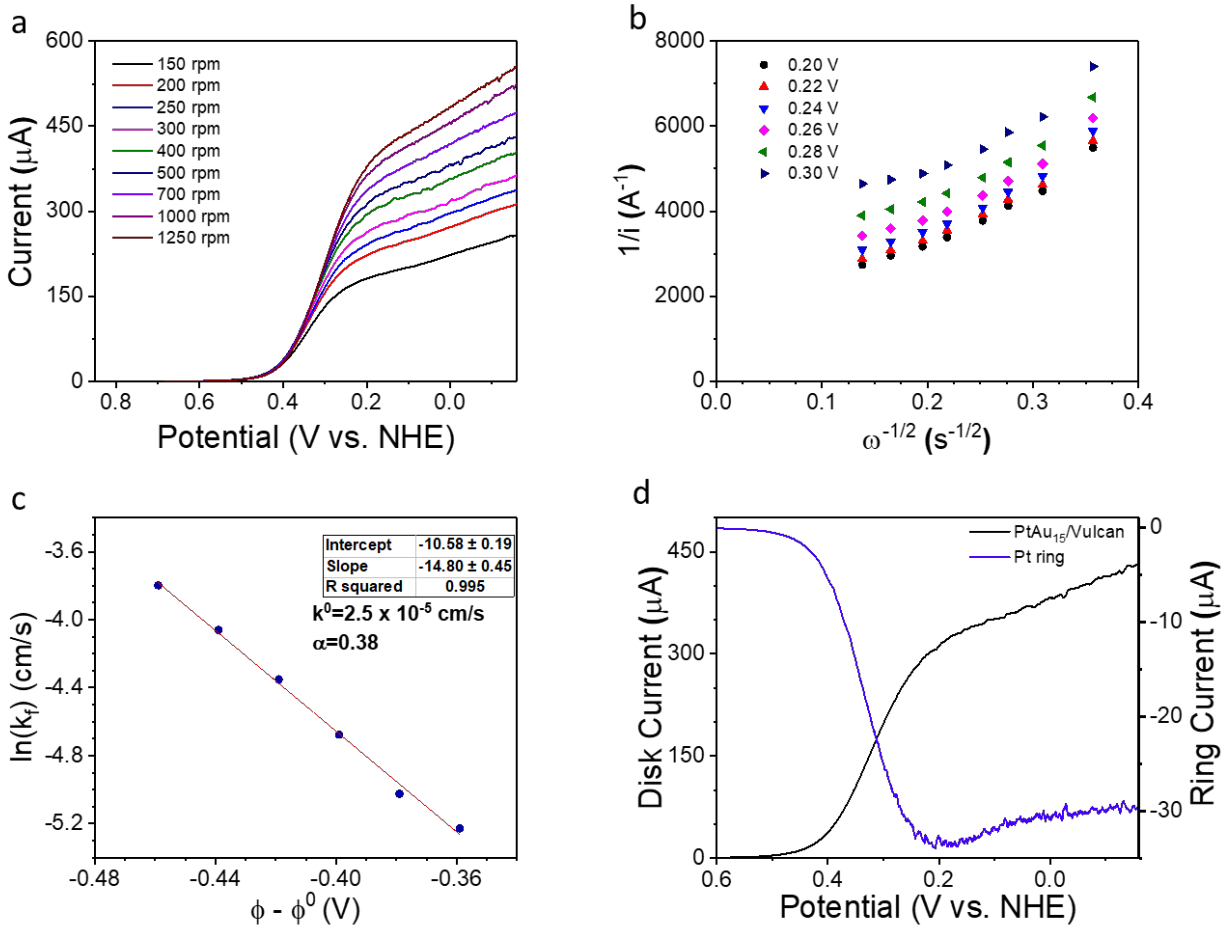

Supplementary Figure 4.26 R(R)DE, Koutecky-Levich, and Butler-Volmer analyses for $PtAu_{15}$/Vulcan ORR. These analyses were carried out in O_2 saturated 0.1 M $NaClO_4$.

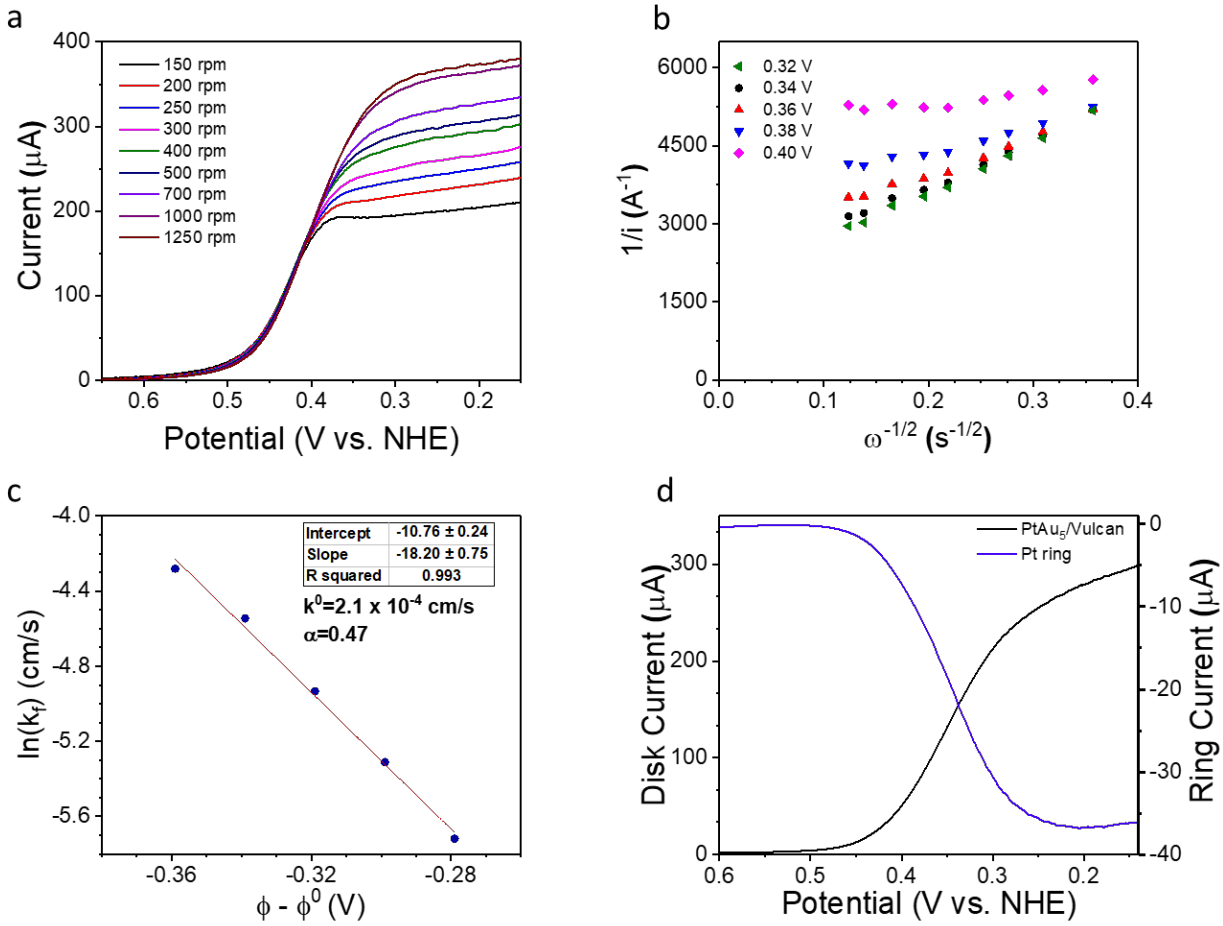

Supplementary Figure 4.27 RDE, Koutecky-Levich, and Butler-Volmer analyses for $PtAu_5$/Vulcan. These analyses were carried out in O_2 saturated 0.1 M $NaClO_4$.

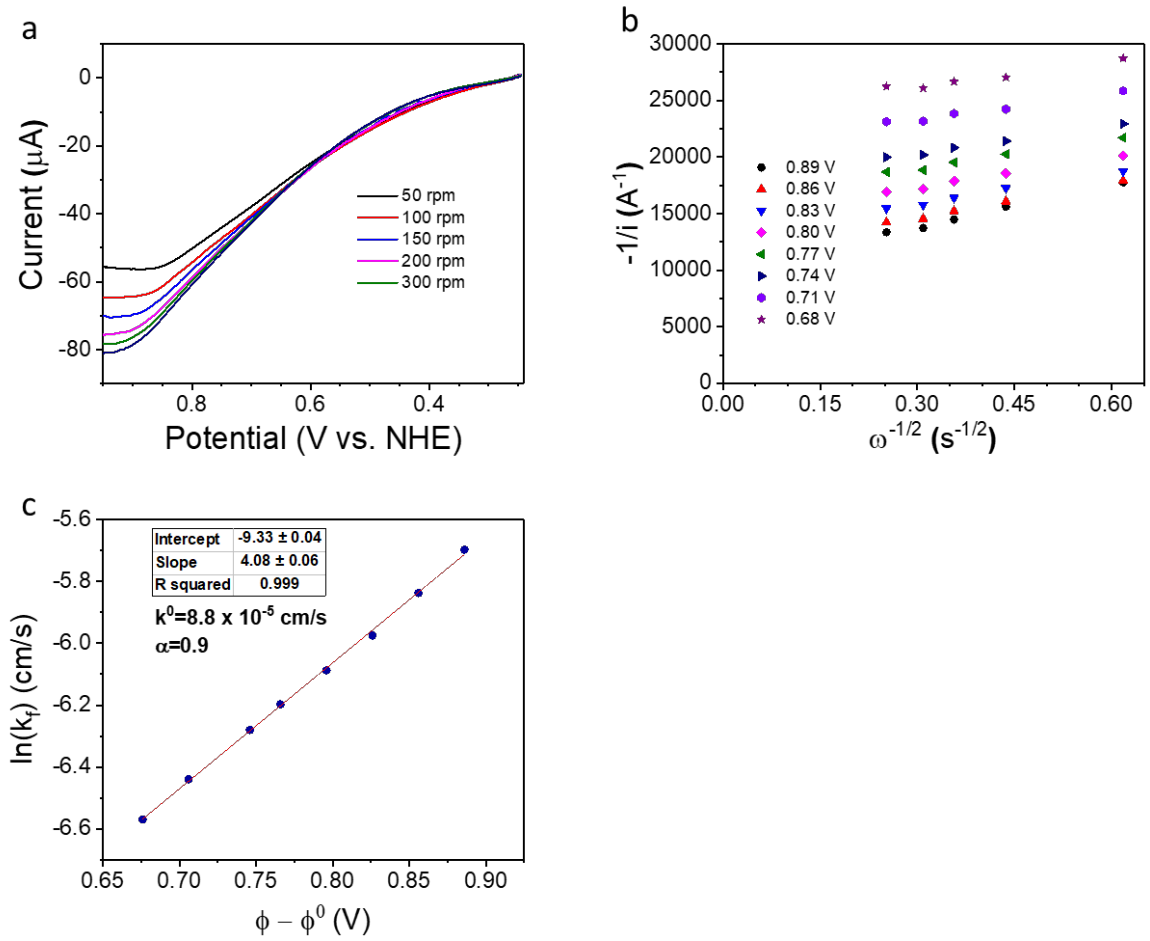

Supplementary Figure 4.28 RDE, Koutecky-Levich, and Butler-Volmer analyses for Pd/Vulcan HOR. These analyses were carried out in H_2 saturated 0.1 M $NaClO_4$.

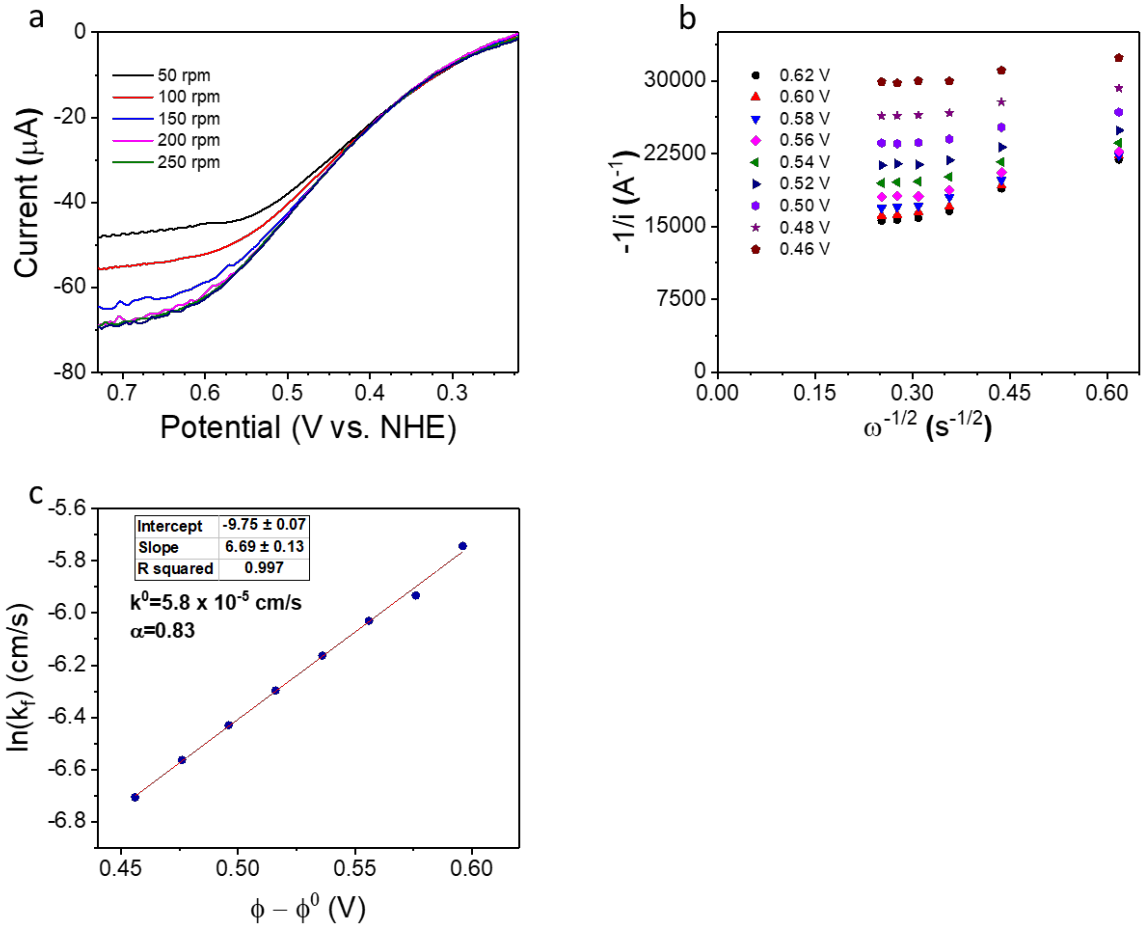

Supplementary Figure 4.29 RDE, Koutecky-Levich, and Butler-Volmer analyses for PdCo/Vulcan HOR. These analyses were carried out in H_2 saturated 0.1 M $NaClO_4$.

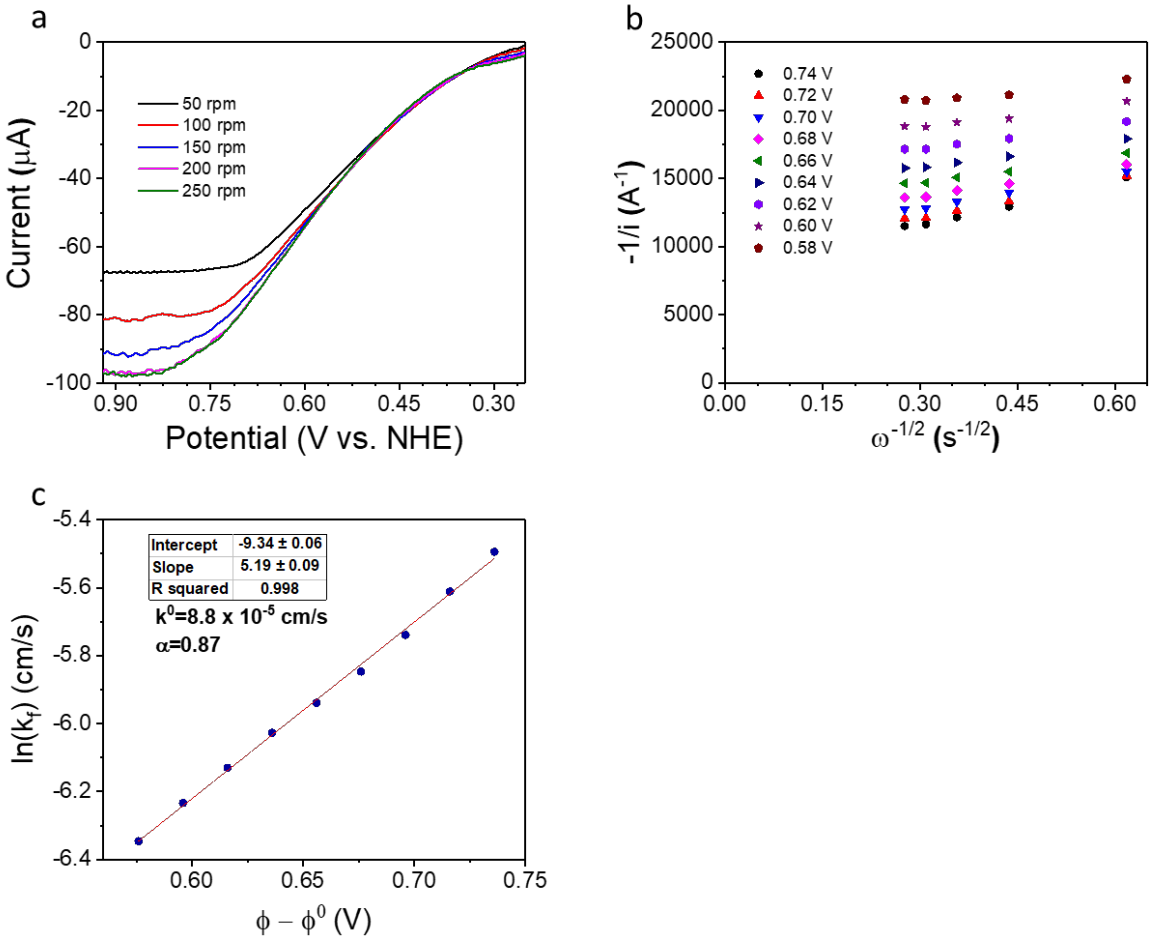

Supplementary Figure 4.30 RDE, Koutecky-Levich, and Butler-Volmer analyses for PdNi/Vulcan HOR. These analyses were carried out in H_2 saturated 0.1 M $NaClO_4$.

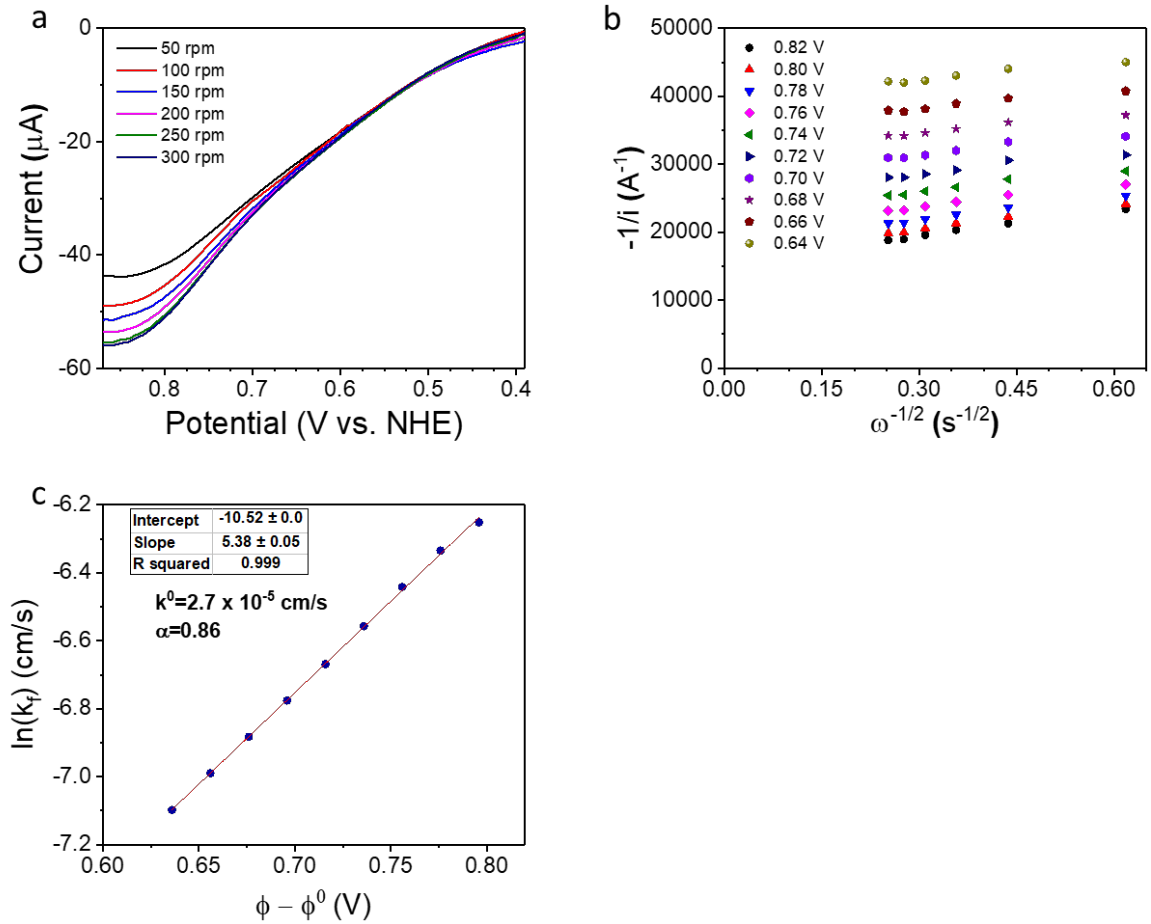

Supplementary Figure 4.31 RDE, Koutecky-Levich, and Butler-Volmer analyses for PdZn/Vulcan HOR. These analyses were carried out in H_2 saturated 0.1 M $NaClO_4$.

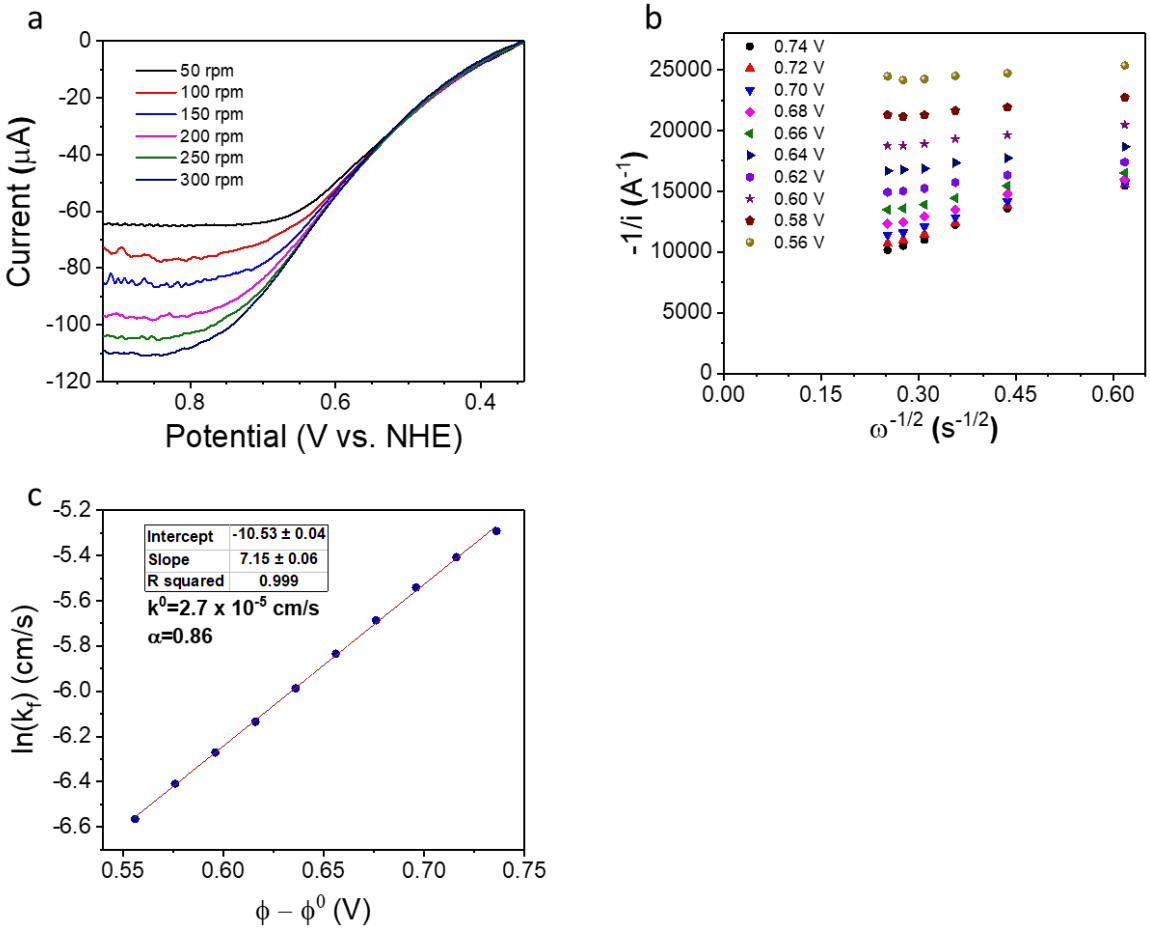

Supplementary Figure 4.32 RDE, Koutecky-Levich, and Butler-Volmer analyses for PdCu/Vulcan HOR. These analyses were carried out in H_2 saturated 0.1 M $NaClO_4$.

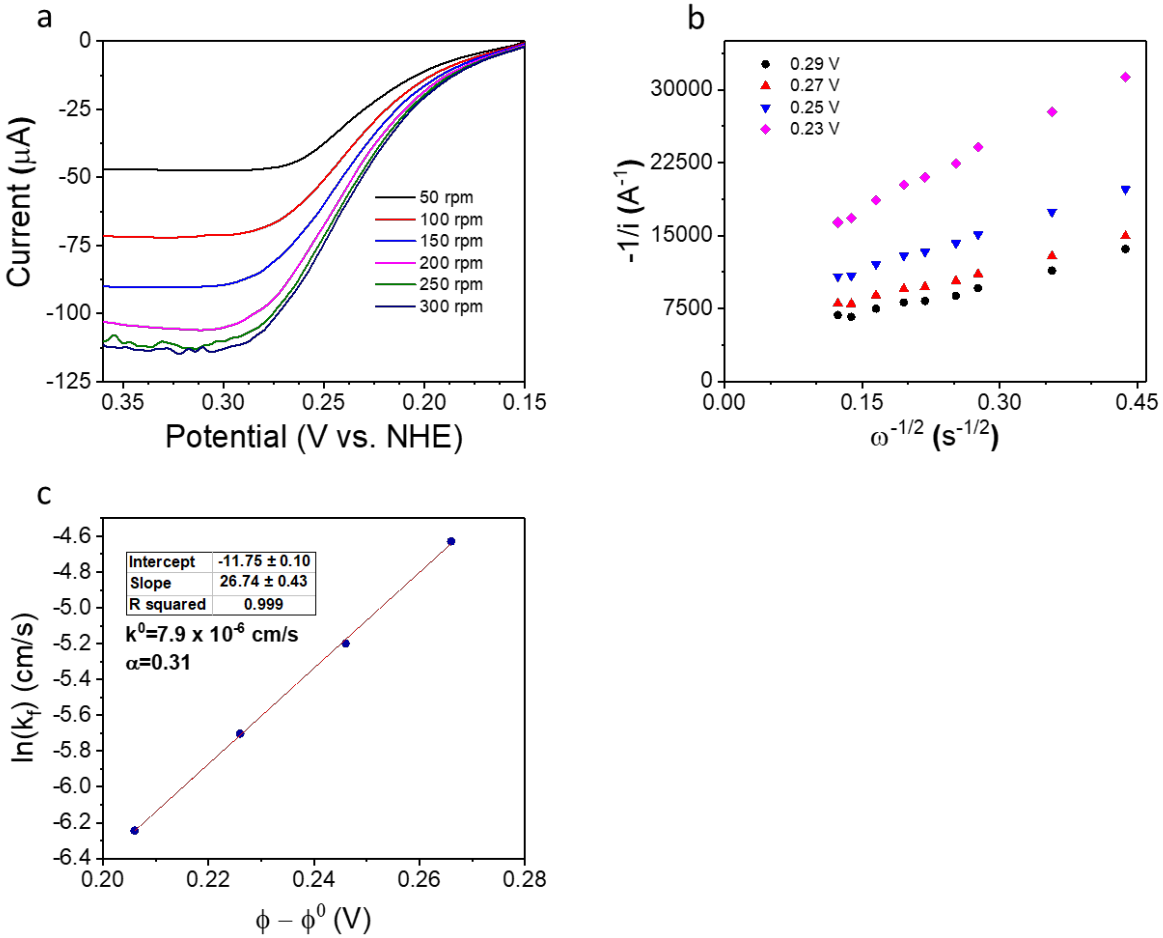

Supplementary Figure 4.33 RDE, Koutecky-Levich, and Butler-Volmer analyses for Pt/Vulcan HOR. These analyses were carried out in H_2 saturated 0.1 M $NaClO_4$.

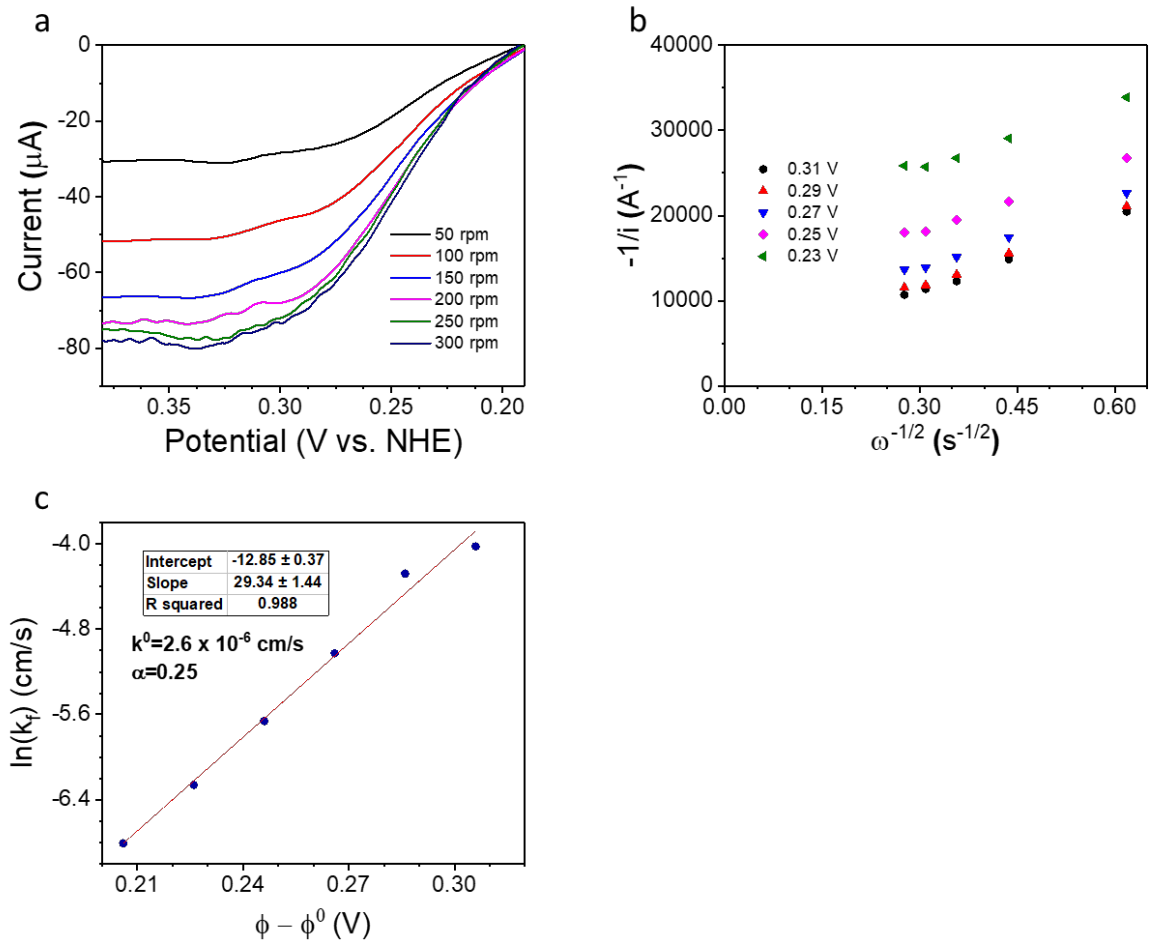

Supplementary Figure 4.34 R(R)DE, Koutecky-Levich, and Butler-Volmer analyses for PdPt/Vulcan HOR. These analyses were carried out in H_2 saturated 0.1 M $NaClO_4$.

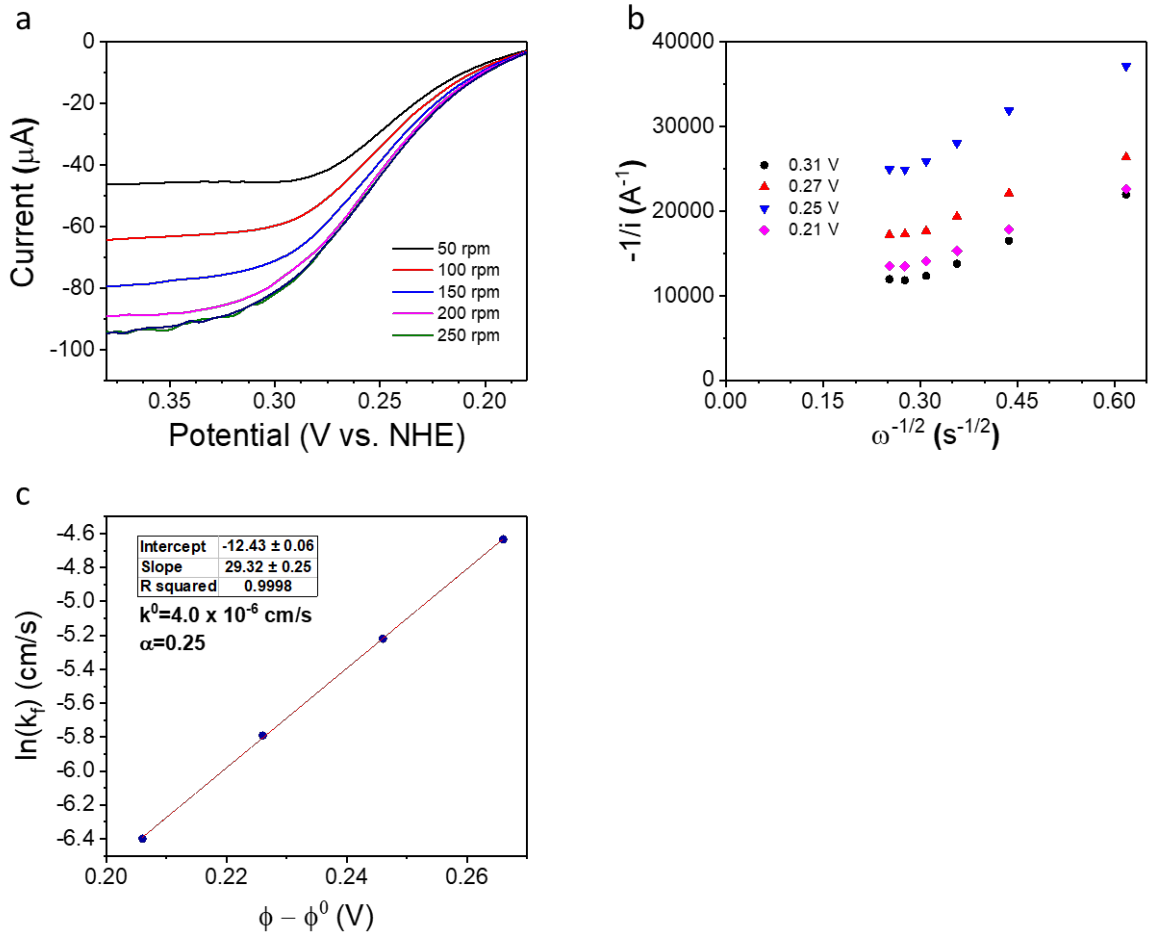

Supplementary Figure 4.35 R(R)DE, Koutecky-Levich, and Butler-Volmer analyses for PtCo/Vulcan HOR. These analyses were carried out in H_2 saturated 0.1 M $NaClO_4$.

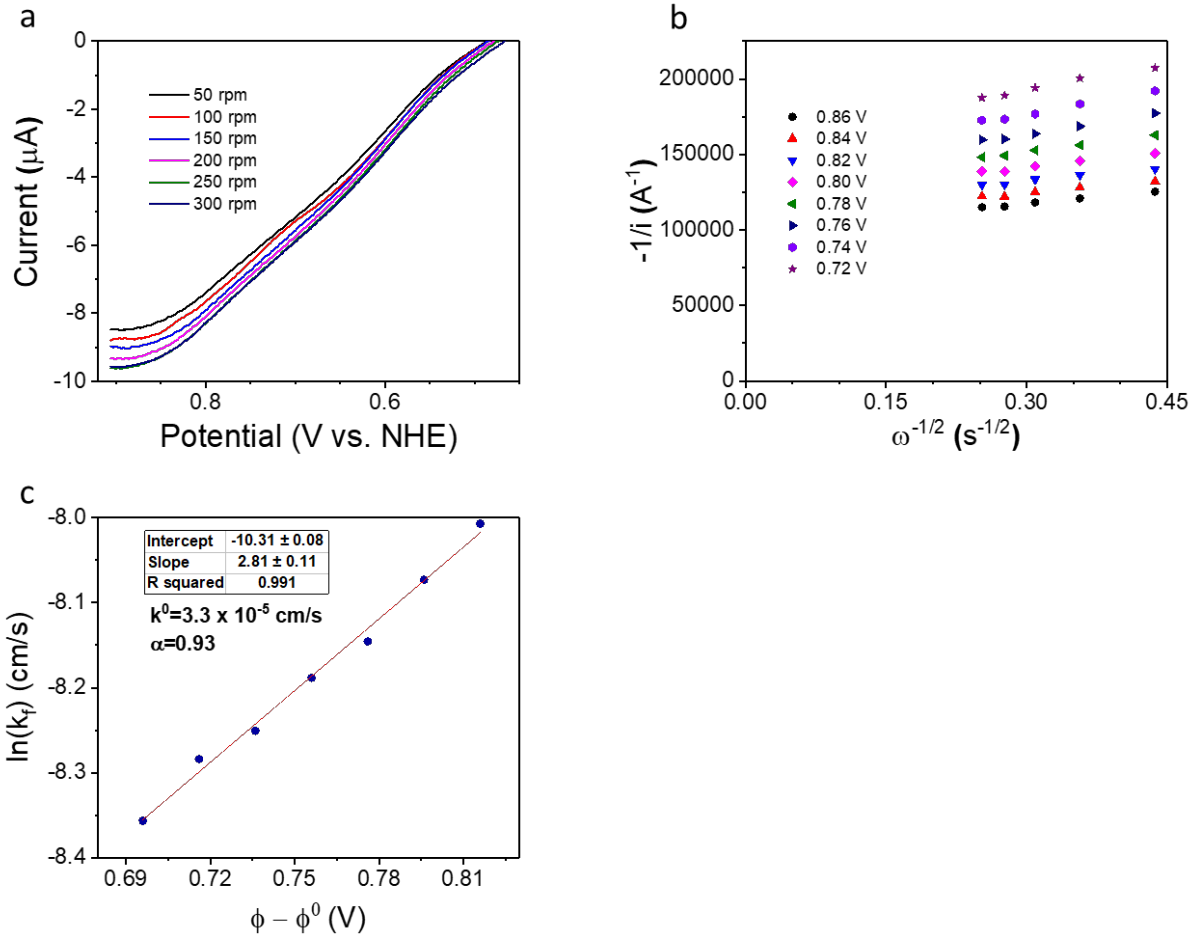

Supplementary Figure 4.36 R(R)DE, Koutecky-Levich, and Butler-Volmer analyses for $PdAu_{60}$/Vulcan HOR. These analyses were carried out in H_2 saturated 0.1 M $NaClO_4$.

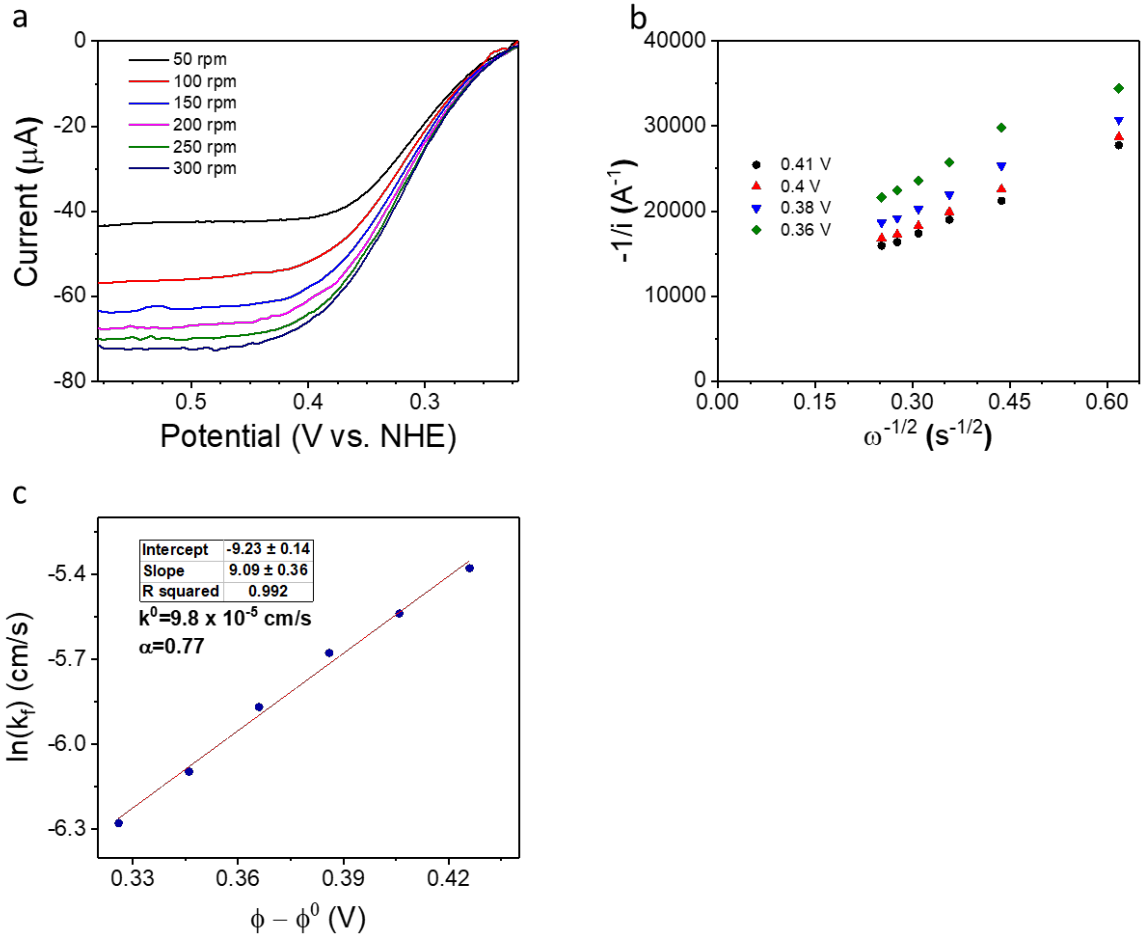

Supplementary Figure 4.37 RDE, Koutecky-Levich, and Butler-Volmer analyses for $PtAu_{60}$/Vulcan HOR. These analyses were carried out in H_2 saturated 0.1 M $NaClO_4$.

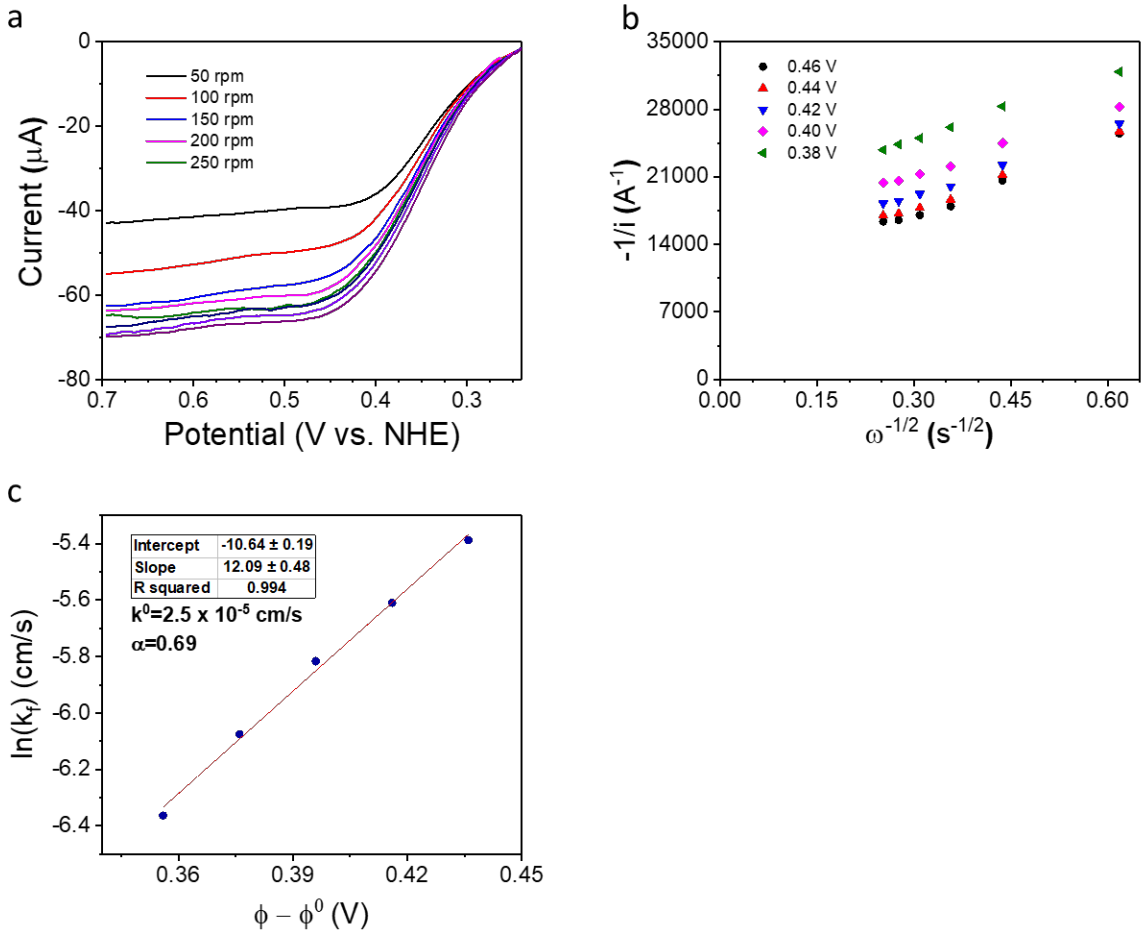

Supplementary Figure 4.38 RDE, Koutecky-Levich, and Butler-Volmer analyses for $PtAu_{15}$/Vulcan HOR. These analyses were carried out in H_2 saturated 0.1 M $NaClO_4$.

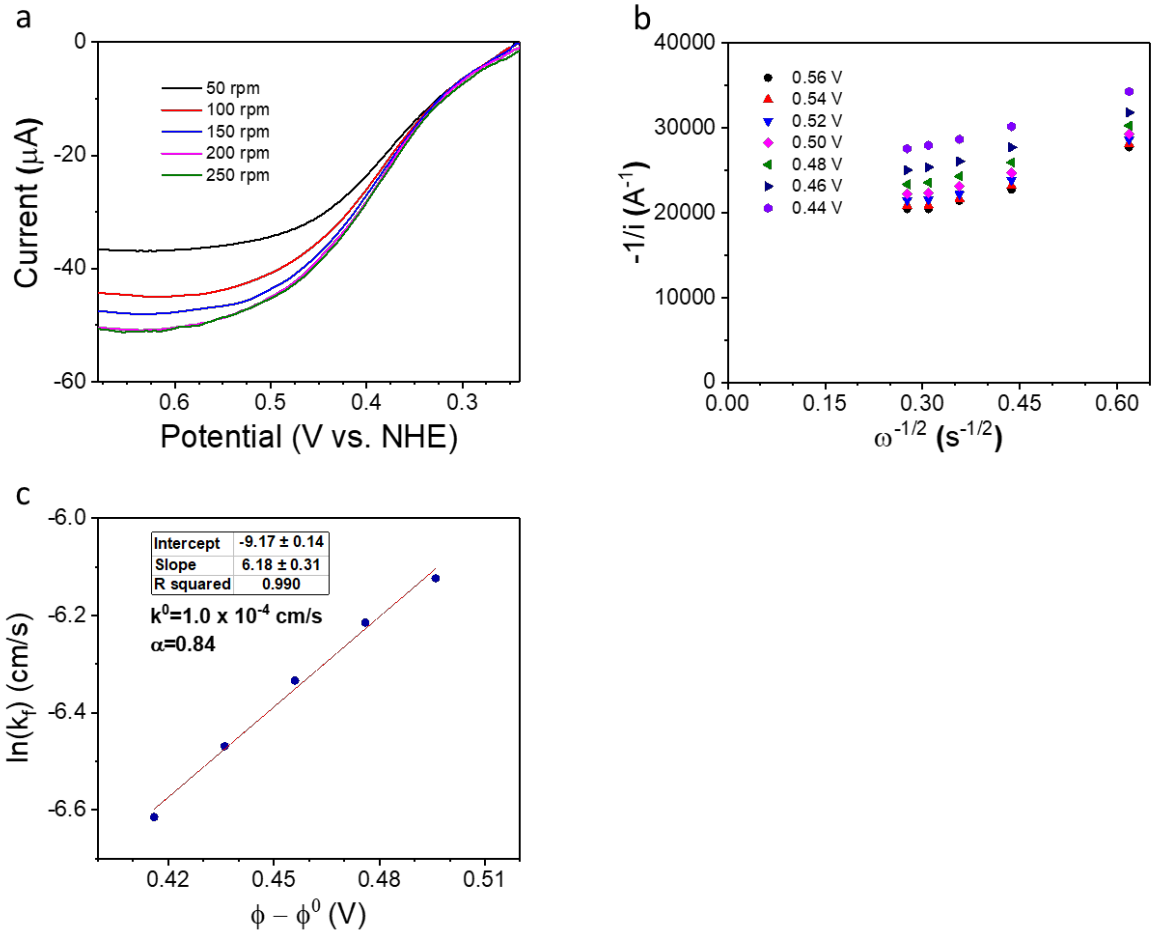

Supplementary Figure 4.39 R(R)DE, Koutecky-Levich, and Butler-Volmer analyses for $PtAu_5$/Vulcan HOR. These analyses were carried out in H_2 saturated 0.1 M $NaClO_4$.

4.11. References

(1) Goor, G.; Glenneberg, J.; Jacobi, S.: Hydrogen Peroxide. In *Ullmann's Encyclopedia of Industrial Chemistry*; Wiley-VCH Verlag GmbH & Co.: Veinheim, Germany 2007.

(2) Campos-Martin, J. M.; Blanco-Brieva, G.; Fierro, J. L. G. Hydrogen peroxide synthesis: An outlook beyond the anthraquinone process. *Angew. Chem. Int. Ed.* **2006**, *45*, 6962-6984.

(3) Clerici, M. G.; Bellussi, G.; Romano, U. Synthesis of Propyelen-Oxide from Propyelene and Hydrogen-Peroxide Catalyzed by Titanium Silicalite. *J. Catal.* **1991**, *129*, 159-167.

(4) Forde, M. M.; Armstrong, R. D.; Hammond, C.; He, Q.; Jenkins, R. L.; Kondrat, S. A.; Dimitratos, N.; Lopez-Sanchez, J. A.; Taylor, S. H.; Willock, D.; Kiely, C. J.; Hutchings, G. J. Partial Oxidation of Ethane to Oxygenates Using Fe- and Cu-Containing ZSM-5. *J. Am. Chem. Soc.* **2013**, *135*, 11087-11099.

(5) Samanta, C. Direct synthesis of hydrogen peroxide from hydrogen and oxygen: An overview of recent developments in the process. *Appl. Catal. A* **2008**, *350*, 133-149.

(6) Siahrostami, S.; Verdaguer-Casadevall, A.; Karamad, M.; Deiana, D.; Malacrida, P.; Wickman, B.; Escudero-Escribano, M.; Paoli, E. A.; Frydendal, R.; Hansen, T. W.; Chorkendorff, I.; Stephens, I. E. L.; Rossmeisl, J. Enabling direct H_2O_2 production through rational electrocatalyst design. *Nat. Mater.* **2013**, *12*, 1137-1143.

(7) Holewinski, A.; Linic, S. Elementary Mechanisms in Electrocatalysis: Revisiting the ORR Tafel Slope. *J. Electrochem. Soc.* **2012**, *159*, H864-H870.

(8) Edwin, N. N.; Edwards, J. K.; Carley, A. F.; Lopez-Sanchez, J. A.; Moulijn, J. A.; Herzing, A. A.; Kiely, C. J.; Hutchings, G. J. The role of the support in achieving high selectivity in the direct formation of hydrogen peroxide. *Green Chem.* **2008**, *10*, 1162-1169.

(9) Ford, D. C.; Nilekar, A. U.; Xu, Y.; Mavrikakis, M. Partial and complete reduction of O_2 by hydrogen on transition metal surfaces. *Surface Sci.* **2010**, *604*, 1565-1575.

(10) Rankin, R. B.; Greeley, J. Trends in Selective Hydrogen Peroxide Production on Transition Metal Surfaces from First Principles. *ACS Catal.* **2012**, *2*, 2664-2672.

(11) Wilson, N. M.; Flaherty, D. W. Mechanism for the Direct Synthesis of H_2O_2 on Pd Clusters: Heterolytic Reaction Pathways at the Liquid-Solid Interface. *J. Am. Chem. Soc.* **2016**, *138*, 574-586.

(12) Fernandez, J. L.; White, J. M.; Sun, Y. M.; Tang, W. J.; Henkelman, G.; Bard, A. J. Characterization and theory of electrocatalysts based on scanning electrochemical microscopy screening methods. *Langmuir* **2006**, *22*, 10426-10431.

(13) Bard, A. J.; Faulkner, L. R.: Electrochemical Methods: Fundamentals and Applications 2nd Edition. John Wiley & Sons Inc.: New York, 2001; pp 341-344.

(14) Fang, Y. H.; Liu, Z. P. Tafel Kinetics of Electrocatalytic Reactions: From Experiment to First-Principles. *ACS Catal.* **2014**, *4*, 4364-4376.

(15) Sheng, W. C.; Gasteiger, H. A.; Shao-Horn, Y. Hydrogen Oxidation and Evolution Reaction Kinetics on Platinum: Acid vs Alkaline Electrolytes. *J. Electrochem. Soc.* **2010**, *157*, B1529-B1536.

(16) Sheng, W. C.; Bivens, A. P.; Myint, M.; Zhuang, Z. B.; Forest, R. V.; Fang, Q. R.; Chen, J. G.; Yan, Y. S. Non-precious metal electrocatalysts with high activity for hydrogen oxidation reaction in alkaline electrolytes. *Energy Environ. Sci.* **2014**, *7*, 1719-1724.

(17) Gottesfeld, S.; Pafford, J. A New Approach to the Problem of Carbon-Monoxide Poisoning in Fuel-Cells Operating at Low-Termperatures. *J. Electrochem. Soc.* **1988**, *135*, 2651-2652.

(18) Shinagawa, T.; Garcia-Esparza, A. T.; Takanabe, K. Insight on Tafel slopes from a microkinetic analysis of aqueous electrocatalysis for energy conversion. *Sci. Reports* **2015**, *5*.

(19) Sanchez-Sanchez, C. M.; Bard, A. J. Hydrogen Peroxide Production in the Oxygen Reduction Reaction at Different Electrocatalysts as Quantified by Scanning Electrochemical Microscopy. *Anal. Chemistry* **2009**, *81*, 8094-8100.

(20) Jessop, P. G.; Ikariya, T.; Noyori, R. Homogeneous Catalytic-Hydrogenation of Supercritical Carbon-Dioxide. *Nature* **1994**, *368*, 231-233.

(21) Khusnutdinova, J. R.; Garg, J. A.; Milstein, D. Combining Low-Pressure CO_2 Capture and Hydrogenation To Form Methanol. *ACS Catal.* **2015**, *5*, 2416-2422.

(22) Zoski, C. G.; Simjee, N.; Guenat, O.; Koudelka-Hep, M. Addressable microelectrode arrays: Characterization by imaging with scanning electrochemical microscopy. *Anal. Chem.* **2004**, *76*, 62-72.

(23) Fernandez, J. L.; Mano, N.; Heller, A.; Bard, A. J. Optimization of "wired" enzyme O_2-electroreduction catalyst compositions by scanning electrochemical microscopy. *Angew. Chem. Int. Ed.* **2004**, *43*, 6355-6357.

(24) Fernandez, J. L.; Walsh, D. A.; Bard, A. J. Thermodynamic guidelines for the design of bimetallic catalysts for oxygen electroreduction and rapid screening by scanning electrochemical microscopy. M-Co (M : Pd, Ag, Au). *J. Am. Chem. Soc.* **2005**, *127*, 357-365.

Chapter 5:

Utilization of cathodic corrosion for new water splitting photoelectrochemical materials

This work was published as an original research article in *Langmuir*: Kromer, M. L.; Monzo, J.; Lawrence, M. J.; Kolodzieg, A.; Gossage, Z. T.; Simpson, B. H.; Morandi, S.; Yanson, A.; Rodríguez-López, J.; Rodríguez, P., High-Throughput Preparation of Metal Oxide Nanocrystals by Cathodic Corrosion and Their Use as Active Photocatalysts. *Langmuir*. **2017**, 33 (46), 13295–13302. This chapter was adapted with permission from the American Chemical Society, copyright 2017. DOI: 10.1021/acs.langmuir.7b02465. Javier Monzo, Matthew Lawrence, and Adam Kolodzieg were responsible for nanoparticle fabrication, and Zachary Gossage, Burton Simpson, and Sara Morandi were responsible for preliminary electrochemical characterization. All other work was accomplished by Matthew L. Kromer under the primary investigator Professor Joaquín Rodríguez-López.

5.1. Abstract

Nanoparticle metal oxide photocatalysts are attractive due to their increased reactivity and ease of processing into versatile electrode formats; however, their preparation is cumbersome. Presented here is the report on the rapid bulk synthesis of photocatalytic nanoparticles with homogeneous shape and size via the cathodic corrosion method, a simple electrochemical approach applied for the first time to the versatile preparation of complex metal oxides. Nanoparticles consisting of tungsten oxide (H_2WO_4) nanoplates, titanium oxide (TiO_2) nanowires, and symmetric star-shaped bismuth vanadate ($BiVO_4$) were prepared conveniently using tungsten, titanium, and vanadium wires as a starting material. Each of the particles were extremely rapid to produce, taking only 2-3 minutes to etch 2.5 mm of metal wire into a colloidal dispersion of photoactive materials. All crystalline H_2WO_4 and $BiVO_4$ particles and amorphous TiO_2 were photoelectrochemically active towards the water oxidation reaction. Additionally, the $BiVO_4$

particles showed enhanced photocurrent in the visible region towards the oxidation of a sacrificial sulfite reagent. This synthetic method provides an inexpensive alternative to conventional fabrication techniques and is potentially applicable to a wide variety of metal oxides, making the rapid fabrication of active photocatalysts with controlled crystallinity more efficient.

5.2. Introduction

Water splitting via semiconductor photocatalysts presents a promising means to store solar energy in the form of renewable fuels.[1-3] Additionally, as outlined in the Chapter 3 of this work, photoanode materials can prove to be quite useful in the production of H_2O_2 for industrial applications. However, implementing this technology faces important challenges in materials design, engineering, and fabrication. Among the challenges for materials scientists is identifying an inexpensive material that combines excellent visible light absorption, efficient conversion, and long-term stability. The study of the impact of structural parameters on the photocatalytic performance of nano- and microparticles creates opportunities in increasing their efficiency by decreasing charge carrier diffusion lengths and therefore decreasing recombination.[4] Furthermore, the control of surface orientation, particle shape, and particle morphology enables the exploration of emerging chemical properties.[5] The use of photoactive particles also enhances the processability of large-area photoelectrodes by means of their assembly using discrete, well-defined constituent entities.

The widespread use and commercialization of semiconductor photocatalysts requires high-throughput, robust, efficient, safe, and inexpensive fabrication procedures.[6]. To date, the most common ways to prepare photocatalysts for water oxidation are solution based methods such as solvothermal syntheses[7-10] and electrodeposition.[11,12] In the case of solvothermal methods, time consuming synthesis procedures are usually required, and low yields are common. Such methods

commonly demand the utilization of organic solvents, surfactants, or capping materials that add complexity and cost. The use of capping agents can also negatively affect the catalytic activity by blocking active sites.[13] In addition, these methods implement high temperature protocols which can result in large particle size distribution and a lack in control of the surface structure.[9] Solvothermal methods are particularly prevalent in the synthesis of various nanostructured forms of tungsten oxide and titanium dioxide. In one study, this method was employed to prepare tungstic acid hydrate nanotubes without the use of any template, [14] but the synthesis required 12 h of drying at 60ºC.[14]. The solvothermal method has been used to produce TiO_2 nanosheets with preferentially oriented surfaces.[15] This synthesis required the use of hazardous precursors (TiF_4 and HF), and took 5.5-44 h to complete, with a yield of 34.8%.[15] Conversely, electrodeposition methods while offering morphological versatility,[16] suffer from low throughput. Examples of a high degree of morphological control include the use of photolithographic patterning of Cu_2O,[17] and electrodeposition of Si nanowires followed by generation of a catalyst layer.[18] In these cases, a general strategy for applying the synthesis methods to a variety of materials is lacking. A summary of recent methods for the preparation of H_2WO_4, $BiVO_4$ and TiO_2, including synthesis time, advantages and disadvantages is shown in the Supporting Information Table S1. These examples underscore the opportunity for developing methods capable of creating complex photocatalytic materials with high throughput and in a timely manner.

Discussed in Chapter 3 was the utilization of photoelectrochemistry to facilitate the production of H_2O_2. Some of the future work in Chapter 3 outlined methodology to discovering new electrocatalysts for the production of H_2O_2. Another side still needing optimization is the light absorber that provides the electrochemical potential to drive H_2O_2 formation. It is well accepted that the current state of the art photocatalysts for driving water splitting is not in the regime of

economic relevance for carrying out industrial scale processes. It is therefore of interest to the photoelectrochemical production of H_2O_2 that the preparation of photocatalyst is as economically feasible as possible.

Here the utilization of the cathodic corrosion method[19,20] is reported for the preparation of metal oxide and mixed metal oxide photocatalysts. This method has shown the potential to prepare metal and metal alloy nanoparticles with high morphological homogeneity and well-defined composition.[19-21] Additionally, it has the capability to modulate particle size and shape by means of versatile adjustments of the potential waveform applied to the electrode. An early report demonstrated that the cathodic corrosion method can be used in the preparation of TiO_2 nanoparticles. However, these nanomaterials were used as support for Au nanocatalyst and not directly as a photoactive material.[22] Since the method does not require the utilization of organic solvents, surfactants, or capping ligands, metal nanocatalysts produced through this method have shown extraordinary catalytic activity.[21] In this report, the utility of cathodic corrosion is demonstrated as a synthetic method to prepare complex oxide nanoparticles of H_2WO_4, TiO_2, and $BiVO_4$ with unprecedented simplicity and particle size homogeneity. All of the syntheses were done on the order of minutes, making this method far superior in terms of time to any of the more commonly used synthetic methods for preparing nanoparticulate photocatalysts. In addition, the control achieved over the crystallinity of the H_2WO_4 and $BiVO_4$ nanoparticles is indicative that such control could be also achieved on other metal oxides by changing electronic parameters such as amplitude or frequency of the AC wave, or by changing chemical parameters such as concentration or nature of the cation.

5.3. Experimental

5.3.1. Synthesis and characterization of particles

The method by which these particles were synthesized is summarized in Figure 5.1. For the synthesis of H_2WO_4 particles, 2.5 mm of a tungsten wire (diameter of 0.127 mm, Rembar Co. LLC, USA) was submerged in a 1 M solution of $KHSO_4$. A square wave voltage in the range of 0 V to -10 V was applied between a W wire (working electrode) and a high surface area Pt foil (counter electrode) resulting in the instantaneous formation of the nanoparticles. The TiO_2 nanowires were prepared with a 0.2 mm diameter titanium wire that was subjected to an AC square wave in the range of 0 V to -10 V with a frequency of 100 Hz while immersed in a 10 M NaOH solution. The $BiVO_4$ nanoparticles were synthesized using a vanadium wire with diameter of 0.15 mm (99.8 % Alfa Aesar). This wire was immersed in 10 mL of a mixture (1:1 by volume) of saturated $CaCl_2$ solution and MilliQ water (Elga, 18.2 MΩ cm, 1 ppb total organic carbon), in which 750 μL of a saturated Bi_2O_3 solution was subsequently added. The synthesis was successfully achieved by applying a square wave voltage in a range of -8 V to 2 V. In each of the syntheses, current and time was monitored using a National Instruments DAQ module (NI-6211). Once synthesized, the resulting suspensions of nanoparticles were centrifuged at 3000 rpm for 20 minutes and suspended in ElgaPure water to remove the excess electrolyte. UV-vis spectroscopy was employed to elucidate species present in $KHSO_4$ solution immediately after cathodic corrosion of W wire and in the resultant supernatant solution after centrifugation at 4000 RPM for 3 minutes, using a Varian Cary 50 UV-Vis Spectrophotometer.

The crystal structures of the prepared particles were determined using a BRUKER D2 Phaser powder X-ray diffractometer operating at 30 kV, 10 mA and a Co-Kα (0.179 nm) radiation source. The X-ray diffraction (XRD) data are reported on a 2θ angle scale of a Co-Kα radiation

source for an appropriate comparison with values from the JCPDS database. The samples were prepared by depositing 25 μL of the aqueous nanoparticle suspensions on a zero background SiO (MTI) holder and dried under air atmosphere.

The particle size distribution and shape of the particles were determined by transmission electron microscopy (TEM) using a JEOL JEM 1200 EX MKI instrument and the particle thickness was determined by contact mode atomic force microscopy (AFM), obtained under ambient pressure and temperature conditions, using an AFM microscope Veeco metrology, equipped with a NanoScope IIIa controller and using a 200 μm cantilever with a pyramidal silicon nitride tip (spring constant 0.12 Nm^{-2}). Compositional analysis was determined by X-ray fluorescence (XRF) using a Bruker S8 Tiger 4 kW spectrometer under a helium atmosphere. The particle morphology and composition were confirmed by scanning electron microscopy (SEM) in a JEOL 2100 Scanning electron microscope instrument coupled with energy dispersive X-ray spectroscopy (EDX).

5.3.2. Photoelectrochemical measurements

In order to study the photoactivity of the particles, they were first integrated into a photoelectrode. The suspended particles were drop cast in volumes of 20 μL onto an indium tin oxide (ITO) cover slip (SPI Instruments 15-30 Ω). Next, 100 μL of 5 wt% Nafion® perfluorinated resin solution (Sigma Aldrich) were spun-cast onto the particles at 1200 rpm for 3 minutes to prevent the particles from detaching from the ITO when immersed in solution. Electrical connection was made to the ITO slide by using copper tape (3M Electrical Products). In the case of $BiVO_4$, particles were drop cast as 3 layers of 20 μL to increase the overall particle concentration on the surface of the ITO cover slip. The photoelectrochemical and scanning electrochemical microscopy (SECM) measurements were carried out in a custom made 3 mL Teflon cell and the potential of the

photoelectrodes was controlled via either CHI760E or 920D workstations (CHI Instruments) in a three-electrode setup. The reference electrode used was a Ag/AgCl (3 M KCl) with a $NaClO_4$ agar salt bridge and all potentials reported are versus Ag/AgCl unless otherwise stated. The counter electrode was 1 mm diameter Pt wire. All measurements were performed in 0.1 M NaOH under illumination from a 6258 Oriel Xe lamp. Incident photon-to-electron conversion efficiency (IPCE) spectra were taken by filtering this source using a Newport Oriel 1/8m Cornerstone monochromator.

5.4. Results and discussion

The reaction mechanism of the cathodic corrosion method for the formation of the nanoparticles proceeds via the formation of the metal anion stabilized by the cations, other rather than protons, present in the solution. In order to confirm this reaction mechanism in the formation of the tungsten nanoparticles via cathodic corrosion, a tungsten wire was immersed in a solution of 0.1 M H_2SO_4 and a AC wave form between 0 and -10 V with a frequency of 100 Hz was applied during 120 s. Under these conditions, only hydrogen evolution was observed (see video S1 in supporting information). In contrast, when the same AC wave form conditions were applied in a solution containing 1 M $KHSO_4$, the reaction resulted in an aqueous nanoparticle dispersion (see video S2 in supporting information). Given that the electrochemical conditions are identical and the pH in both solutions is similar, it is conclude that the presence of the metal cation is requisite for the formation of the nanoparticles and therefore the cathodic corrosion is the dominant reaction mechanism. Furthermore, it is proposed that the formation of tungsten metallic nanoparticles proceed via the formation of an anion intermediate stabilized by the cation in solution and the oxidation of this intermediates to tungsten nanoparticles. The tungsten nanoparticles are prompt to oxidation in water,[23] resulting in the formation of WO_2 and subsequently to WO_3 and H_2WO_4.[24] [2]

In a similar fashion, previous work has shown the synthesis of SnO_2 nanoparticles via two-step process involving the cathodic corrosion.[25] The formation of $BiVO_4$ nanoparticles are proposed to proceed via the formation of a multimetallic anion intermediate $(BiV)^{-n}$ on the surface of the vanadium upon the reduction of the Bi^{+3} similar to the reaction mechanism proposed for the formation of PtBi nanoparticles.[21] However, there still is the possibility that the positive potential applied during the square wave program influences in the reaction mechanism and geometry of the nanoparticles.

A freshly prepared solution was analyzed and its supernatant via UV-Vis in order to discard the presence of ionic W species. As can be seen in Figure 5.8, the spectra of the freshly prepared solution show one broad adsorption band between 200 nm and 400 nm, associated to the presence of WO_2/WO_3 colloidal nanoparticles. After the nanoparticles were centrifuged, the supernatant did not show any adsorption band. Therefore, the presence of dissolved cationic tungsten species was discarded.

5.4.1. Morphological characterization

After the synthesis of the nanoparticles of H_2WO_4 and $BiVO_4$ by cathodic corrosion, their crystal structure, composition, and particle size were studied by XRD, SEM/EDX, and TEM as shown in Figure 5.2, and by XRF as shown in Figure 5.11. XRD patterns for representative H_2WO_4 particles obtained at a frequency of 100 Hz are shown in Figure 5.2A. The 2θ angle at 14.8 indicates a preferential orientation along the (010) plane (JCPDS no. 18-1420). In the case of H_2WO_4, a colloidal suspension was always observed after cathodic corrosion, although the XRD pattern exhibited an evolution in time, as shown in Figure 5.9. The SEM/TEM images of the H_2WO_4 shows presence of H_2WO_4 nanorods/nanoplates with homogenous size and consistent shape (Figure 5.2B). The particle size distribution (Figure 5.12) was found to be 2.7 ± 0.2 μm in

length and 0.5 ± 0.1 μm in width. In addition to the particle size obtained by TEM and SEM measurement, the AFM measurements (Figure 5.13) have shown that the H_2WO_4 nanoparticles have 61±10 nm height. One of the most interesting aspects that was found for the cathodic corrosion synthesis of H_2WO_4 was its versatility for controlling the size and shape of the particles. Even though, the control on the size and shape has been probed for the synthesis of platinum nanoparticles,[26,27] the control of the size and shape of metal oxides open a new dimension of application of these materials. Until now, such control was limited by the application of high temperatures during the synthesis protocol and due to harsh conditions used to clean the capping materials and surfactants. As shown in Figure 5.3, the shape and size of the nanoparticles was tuned by simply changing the frequency of the square wave voltage. Choosing this external input allows us to change the size of the H_2WO_4 by an order of magnitude from hundreds of nanometers to few microns (Figure 5.3).

Figure 5.2C shows the X-ray pattern of the $BiVO_4$ nanoparticles which indicates the presence of (040) preferential orientation (JCPDS no. 14-0688). The SEM/TEM images show star-like shape nanoparticles with homogenous size of 1.1 ± 0.1 μm. The AFM cross section of the $BiVO_4$ nanoparticles (Figure 4.13) shows that the particles are 35±12 nm height. The composition of the $BiVO_4$ nanoparticles was confirmed by XRF and EDX analysis (Figure 5.11). Synthesis of $BiVO_4$ has demonstrated the capabilities of the cathodic corrosion method to prepare complex oxides by the addition of solution-phase components in the synthesis media. Future work will contemplate the control of the particle size, shape and composition as a function of chemical and electrochemical parameters such as amplitude and cation concentration. Although it is difficult to estimate the Faradaic yield for any of the samples prepared, the obtained powders exhibited only slight amounts of the V_2O_5 phase, displaying largely the correct crystal structure for $BiVO_4$.[28,29]

Finally, the characterization by TEM of the TiO_2 nanoparticles is presented in Figure 5.4. The size of the TiO_2 nanowires was approximately 500-800 nm in length and 4-8 nm in diameter. Despite the morphological conservation among the TiO_2 nanowires, there was no periodic crystal structure which resulted in the absence of any XRD pattern.

Under the conditions presented here the rate of formation of particles was the highest for the H_2WO_4, taking approximately 60-100 s to etch 2.5 mm of wire (Figure 5.14). The $BiVO_4$ took a similar time of 100-160 s to etch 2.5 mm of wire, and the TiO_2 took a longer time of 250-320 s to also etch the same amount of wire. The nanoparticles are collected by centrifugation as described in the experimental section after etching 5-7.5 mm of the wires and it was observed that quantities on the order of milligrams could be produced from all samples. Yields of 38±9 %, 61±7 % and 66±10 % have been achieved for H_2WO_4, $BiVO_4$ and TiO_2. Losses in mass of the nanoparticles take place during the synthesis process by attachment of the nanoparticles to the counter electrode and during the process of centrifugation and removal of the excess of electrolyte. It has been also observed that TiO_2 nanoparticles lack in stability in the NaOH solution, therefore a quick washing procedure is required to avoid major losses due to dissolution of the TiO_2 nanoparticles.

Because of the different synthesis conditions and varying sizes of the metal wires, it is difficult to draw comparisons between each of the nanoparticles. Despite the successful preparation of oxide particles from various parent metals, there are several aspects yet to be understood about the cathodic corrosion method applied to these samples, including the etching time and its relationship with the resulting particle size and crystallinity of the sample. The changes in size and shape are potentially influenced by the concentration of intermediate species (anionic and/or metallic) in solution. This intermediate species concentration is modified by changes in the frequency and amplitude of the applied waveform, as well as by the stabilizing cation

concentration in solution (here, K^+). Similar changes in size and shape were also observed during the formation of Pt, Au and Rh nanoparticles as a function of these factors.[26,27,30] Furthermore, it is plausible that the kinetics of nanoparticle oxidation ($W \rightarrow WO_x$) will be affected by the size of the particles generated after cathodic corrosion.[23] In addition, other factors such as changes in zeta potential may occur. Therefore, it is postulate that differences in nanoparticle shape and size are induced by chemical processes that take place after the electrochemical etching step, but that nonetheless are a product of the chosen cathodic corrosion parameters.

Other than the frequency of the waveform, other parameters are under investigation that govern the etching time, size, shape, and composition of the particles. Currently our groups are studying the effect of electrolyte composition and potential thresholds during cathodic corrosion on particle size and shape and this will be subject of a forthcoming publication.

5.4.2. Electrochemical characterization

Chopped light linear sweep voltammetry was used to determine the relative activation of the particles towards water oxidation and is shown in Figures 5.5A and B. Due to the relatively low surface coverage and the Nafion® partially covering some of the particles, the photocurrent density scale is fairly low for the H_2WO_4/ITO, $BiVO_4$/ITO, and TiO_2/ITO electrodes. However, as a reference point unsintered semiconductor particle films yield photocurrents on the order of □A cm^{-2}.[31] The H_2WO_4 and TiO_2 particles, prepared with a square wave function at 100 Hz, yielded photocurrent values on the same order of magnitude, and the $BiVO_4$ resulted in the lowest activity. The photocurrent shown by TiO_2 nanowires, despite having no defined crystal structure, is strongly suggestive of a mixture of photoactive crystal domains. As stated earlier, the crystallinity of nanoparticles may be dependent on the rate of corrosion, and if so, then it is hypothesized that highly crystalline TiO_2 photocatalysts can also be prepared. Despite the higher

crystallinity of the obtained samples for $BiVO_4$, its low activity toward water oxidation has been well-documented,[32,33] where the addition of Na_2SO_3 acting as a hole scavenger improved the current magnitude significantly. As shown in Figure 5.5C, the presence of Na_2SO_3 increased the photocurrent of $BiVO_4$ to be comparable to the H_2WO_4 nanoparticles and TiO_2 nanowires. This demonstrates that these photocatalysts all possess relatively similar activity so long as they are carrying out a kinetically facile reaction – sulfite oxidation in the case of $BiVO_4$. Successfully demonstrated here is the preparation of photoactive $BiVO_4$ particles through cathodic corrosion, but the challenge remains to fabricate $BiVO_4$ that is highly active toward water splitting. This will most likely be enabled through the inclusion of dopants in solution during the synthesis that are known to enhance the adsorption and interfacial charge transfer kinetics between $BiVO_4$ and H_2O to form O_2.[34,35]

Chronoamperometry of H_2WO_4 and $BiVO_4$ nanoparticles was utilized to investigate the presence of transient processes upon illumination. In the case of H_2WO_4, there is an initial decrease in current under illumination at high activation (Figure 5.6A). This decrease in current is likely due to charge recombination in the H_2WO_4 particles. This current transient is not observed for $BiVO_4$ and is likely due to the size difference between the particles. The H_2WO_4 particles are larger than the $BiVO_4$, which results in longer distances for holes to reach the surface. Since the $BiVO_4$ particles are much smaller than the H_2WO_4 particles, there is no observable charge recombination occurring. While seemingly detrimental to photocatalyst performance, this recombination is not too concerning since it only occurred at large applied biases.

The spectral response of the obtained particles was then measured. Figure 5.6C shows the chopped chronoamperometry with the $BiVO_4$ particles under illumination through a 405 nm cutoff filter. It was observed that the $BiVO_4$ retained about half of the current density when only

illuminated with visible light. Chopped chronoamperometry under visible light was also collected for the H_2WO_4 particles, but large activity was not observed (Figure 5.16) due to the relatively small amount of visible light that H_2WO_4 can be expected to absorb. It is hypothesized that cathodic corrosion could also be used to incorporate dopants for increasing the visible light response of the resulting nanoparticles. Certain dopants have already been shown in the literature to red shift the band edge of WO_3,[36-38] and could bolster the visible activity of H_2WO_4 particles.

Because crystalline $BiVO_4$ and H_2WO_4 particles absorb some portion of visible light, an IPCE spectrum was obtained for each to determine the wavelength cutoff of their band edges (Figure 5.7). A spectrum was acquired for each in the presence and absence of Na_2SO_3, which acted as a hole scavenger. The IPCE spectra for the H_2WO_4/ITO shows a cutoff around 440 nm, which is similar to what is expected for an electrodeposited film of H_2WO_4.[12,39] It also shows very slight differences in the presence of a hole scavenger, thus suggesting that interfacial charge transfer is not limiting in these particles. Additionally, the IPCE for H_2WO_4 shows a marked increase from 550 nm to 650 nm, which may be due to the presence of defects in the crystal structure.

These defects reside at an energy in between the conduction and valence band, which results in electrons occupying these states to be excited by longer wavelengths of light.[40,41] In the absence of a hole scavenger, a poor IPCE spectrum was obtained for $BiVO_4$, which is due to very slow reaction kinetics to carry out water oxidation. In contrast, upon addition of Na_2SO_3, the IPCE for the $BiVO_4$ particles showed a band edge around 510 nm, which corresponds well with what has been reported in the literature.[28,29] Altogether these measurements confirm the ability of the cathodic corrosion method to yield photoactive metal oxides with unique morphologies using a simple synthetic approach.

5.5. Single particle O_2 collection

To determine the photocatalytic activity of individual nanoparticles, SECM was utilized. These experiments were only done with the WO_3 particles because the $BiVO_4$ required the addition of sulfite for appreciable activity. This acted as an interference to O_2 detection in an SECM setup. Prior to collecting O_2 produced from a single particle, the surface was imaged to first determine the position of the particles. To acquire these images, the SECM probe (Pt UME ~800 nm radius) was held at a potential suitable to reduce O_2 (-0.5 V vs. Ag/AgCl in pH 13) and was scanned over the ITO substrate with WO_3 particles. This was done in the presence and absence of illumination to generate a background subtracted image, which is the resulting image shown in Figure 5.17. After locating the particles on the substrate, the Pt UME was positioned over the particle and poised at the same potential to reduce O_2. While this chronoamperogram was being recorded, UV-visible light was modulated to activate and deactivate the WO_3 particle. This resulted in the steady state current of the UME to become more cathodic due to a larger concentration of O_2 being produced by the particle. The resulting chronoamperograms are showing in Figure 5.18. To confirm this signal was due to the particle producing O_2, the same experiment was performed with the UME raised well above the surface (25 μm) and at no applied substrate bias. From the chronoamperogram in 5.18A, the rate of O_2 formation by the WO_3 particle can be quantified to be 104.3 ± 7.63 μmol s^{-1} m^{-2}.

5.6. Conclusion

Shown here for the first time is the application of cathodic corrosion to produce metal oxides and mixed metal oxide nanoparticles with an outstanding homogeneity of particle size and shape. All of the particles studied here were made on the order of minutes, which greatly improves upon standard photocatalyst nanoparticle synthesis procedures. Amorphous TiO_2, and crystalline

H_2WO_4 and $BiVO_4$ nanoparticles were prepared with preferential crystallographic orientation starting from the base metal as the reactant. In all cases, it was observed the successful incorporation of oxygen the lattice as confirmed via XRD and EDX. It was also illustrated for H_2WO_4 that the frequency of the excitation waveform can greatly impact the particle size. The cathodic corrosion method can be very easily modified to produce particles with a variety of sizes. In addition, the successful preparation of $BiVO_4$ underscores the exciting possibilities for the synthesis of multi-metallic oxides and the incorporation of dopants using simple solution precursors. Although the TiO_2 did not possess a high degree of crystallinity, it was nonetheless photoactive toward water oxidation. The H_2WO_4 and $BiVO_4$ both were crystalline, and H_2WO_4 carried out water oxidation under illumination. The $BiVO_4$ prepared with cathodic corrosion was not able to appreciably carry out water splitting, but displayed facile conversion of sulfite under both UV-vis and visible only illumination. This ability for $BiVO_4$ to effectively facilitate photochemical oxidation of sulfite under only visible light was displayed through chopped light chronoamperometry and the obtained IPCE spectrum. Future work will investigate alternatives to adhering particles to a surface that do not alter morphology or crystal orientation.[42,43]

The potential of the cathodic corrosion method was demonstrated for the straightforward synthesis of particles with well-defined morphology and composition. This creates opportunity in the low-cost production of large quantities of processable particles that can streamline the preparation of efficient electrodes for photocatalysis. The cathodic corrosion method is prompt for industrial scale up: the method avoids large volumes of organic solvents and the ensuing large investments in heating and cleaning treatment and safety and disposal issues. Finally, the time of synthesis of the catalyst is an important parameter to consider for further industrial applications. While other methods might require several hours or days of preparations, it is shown here the time-

effectiveness of the method to prepare particles in minutes. There is still much work to be done toward the effect that various parameters such as etching time or solution composition have on the resulting particles. Despite this, cathodic corrosion was shown here to be a facile alternative method for producing metal oxide nanoparticles.

5.7. Acknowledgements

The support from the Transatlantic Collaboration Fund and the BRIDGE program between the University of Illinois and the University of Birmingham is acknowledged. PR would like to acknowledge the University of Birmingham for the financial support through the Birmingham fellowship program. JM and AK acknowledge the University of Birmingham for the financial support through PhD scholarships at the School of Chemistry.

5.8. Figures and table

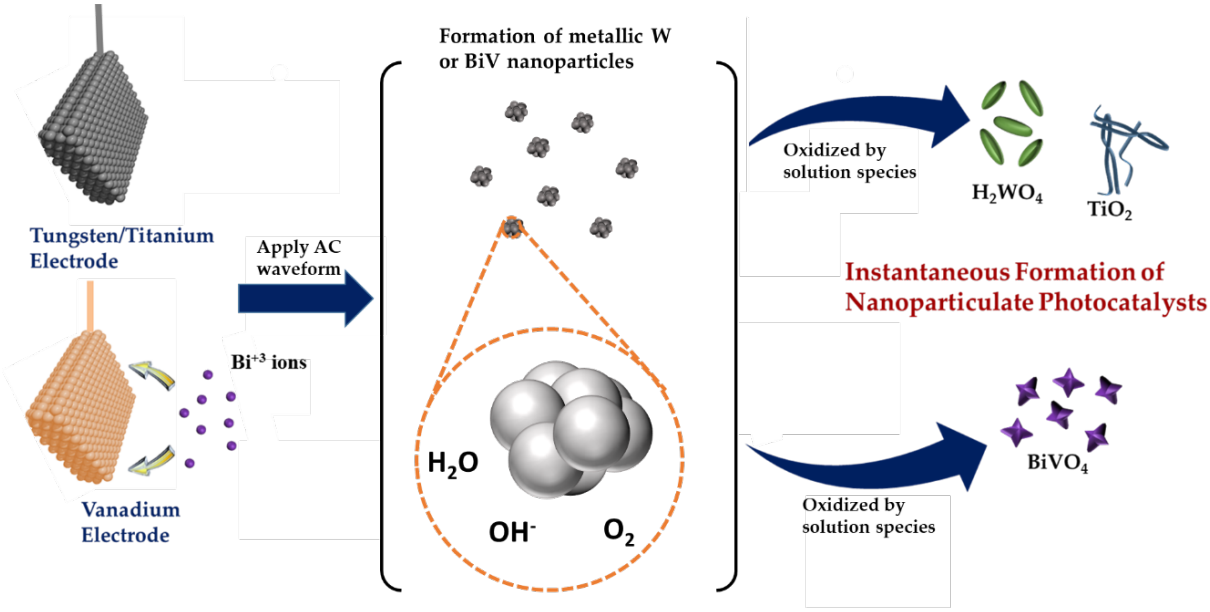

Figure 5.1 Schematic depicting how cathodic corrosion was used to prepare H_2WO_4, TiO_2, and $BiVO_4$ photocatalysts.

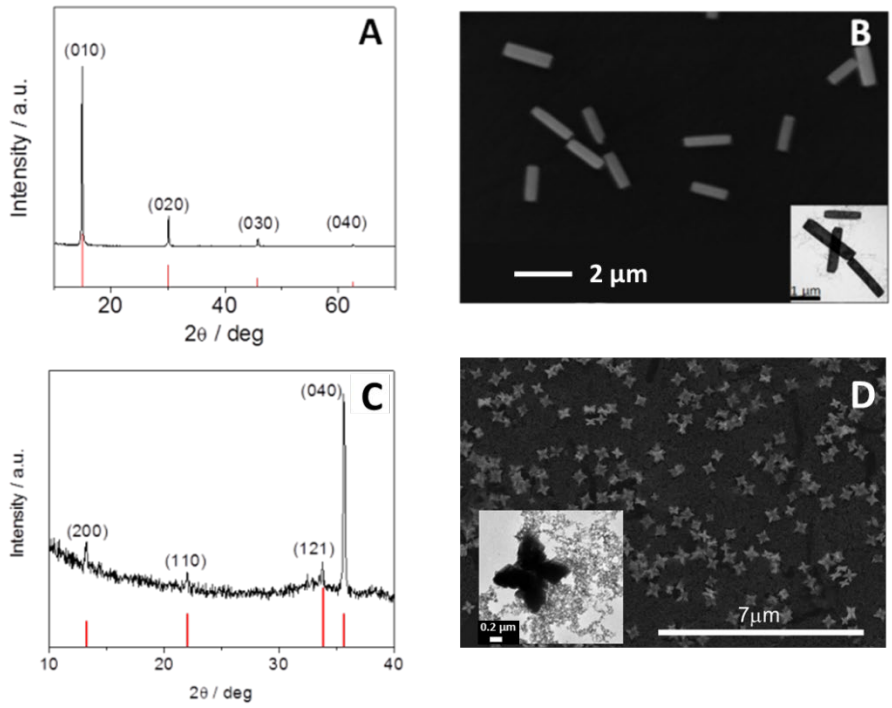

Figure 5.2 X-ray diffraction patterns and SEM images of (A, B) H_2WO_4 and (C, D) $BiVO_4$. The insets on the SEM images correspond to the HR-TEM images of the nanoparticles.

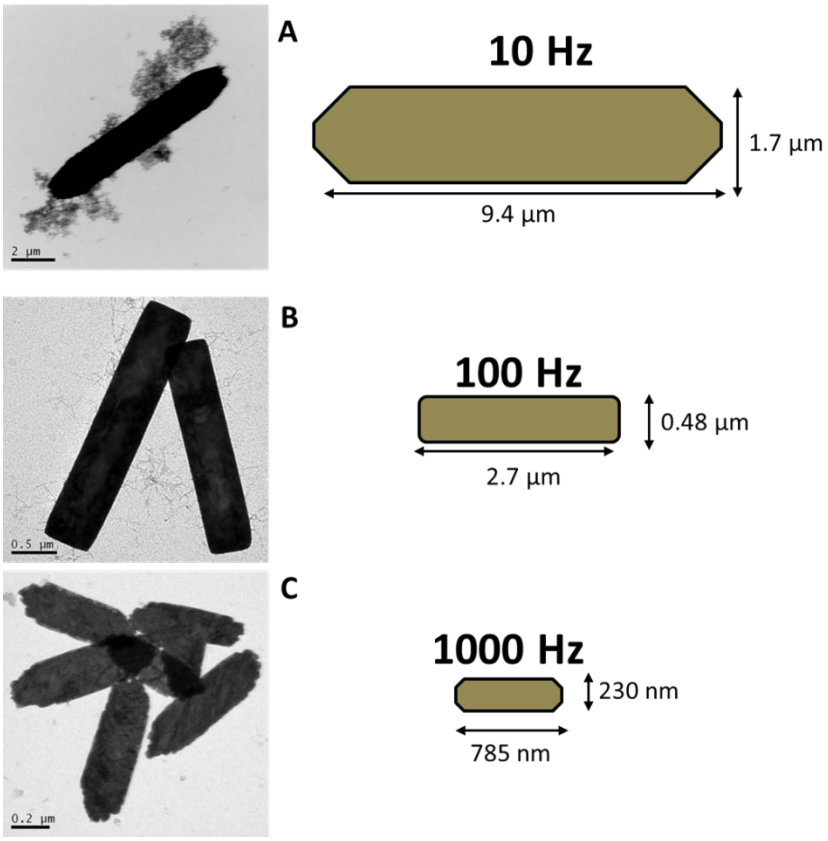

Figure 5.3 TEM images and schematic of the H_2WO_4 particles prepared by cathodic corrosion in a 1 M solution of KHSO4 with a square wave voltage between 0 V to -10 V and different frequencies (A) 10 Hz, (B) 100 Hz and (C) 1000 Hz.

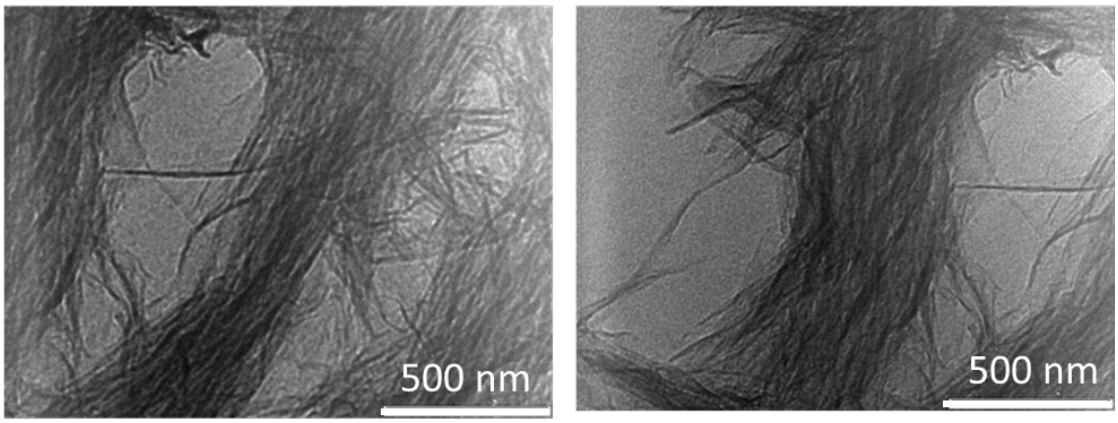

Figure 5.4 TEM of TiO_2 nanoparticles prepared by cathodic corrosion from a Ti wire in a 10 M NaOH solution using an AC square wave between -10 and 0 V with 100Hz frequency.

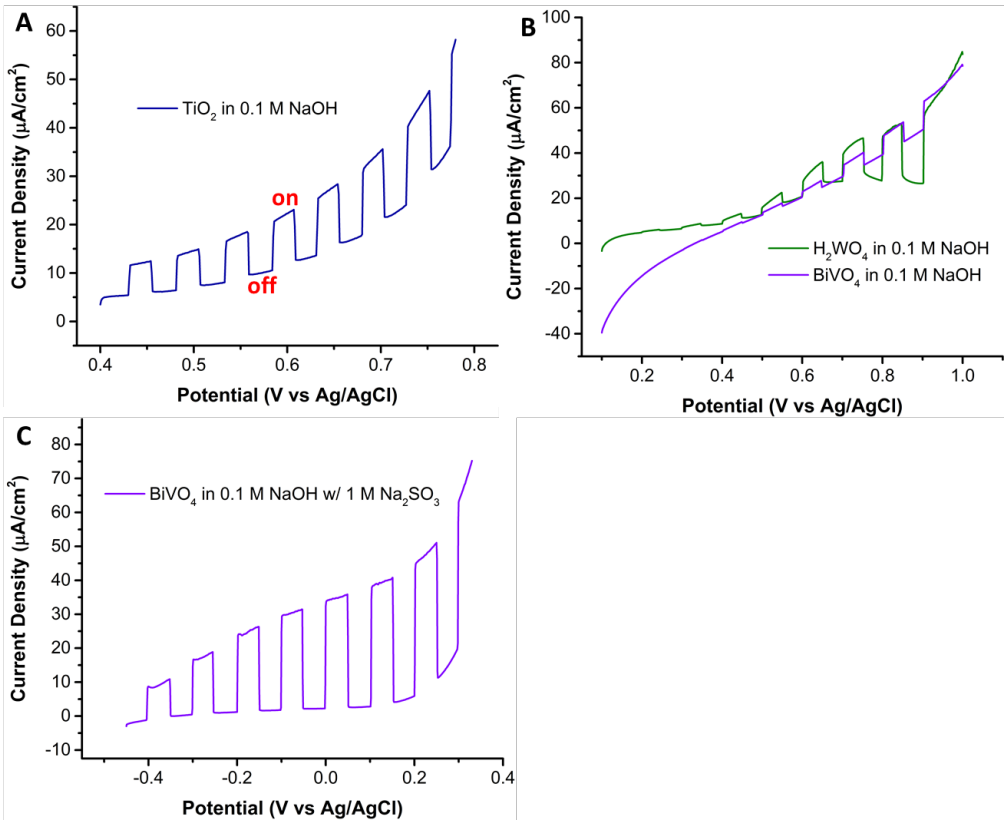

Figure 5.5 Chopped light linear sweep voltammograms of the nanoparticulate photocatalysts prepared through cathodic corrosion. A) Linear sweep voltammogram for TiO_2 in 0.1 M NaOH. B) Linear sweep voltammogram for the 100 Hz H_2WO_4 and $BiVO_4$ particles in 0.1 M NaOH. C) The same experiment shown in A repeated for $BiVO_4$ in 1 M Na_2SO_3.

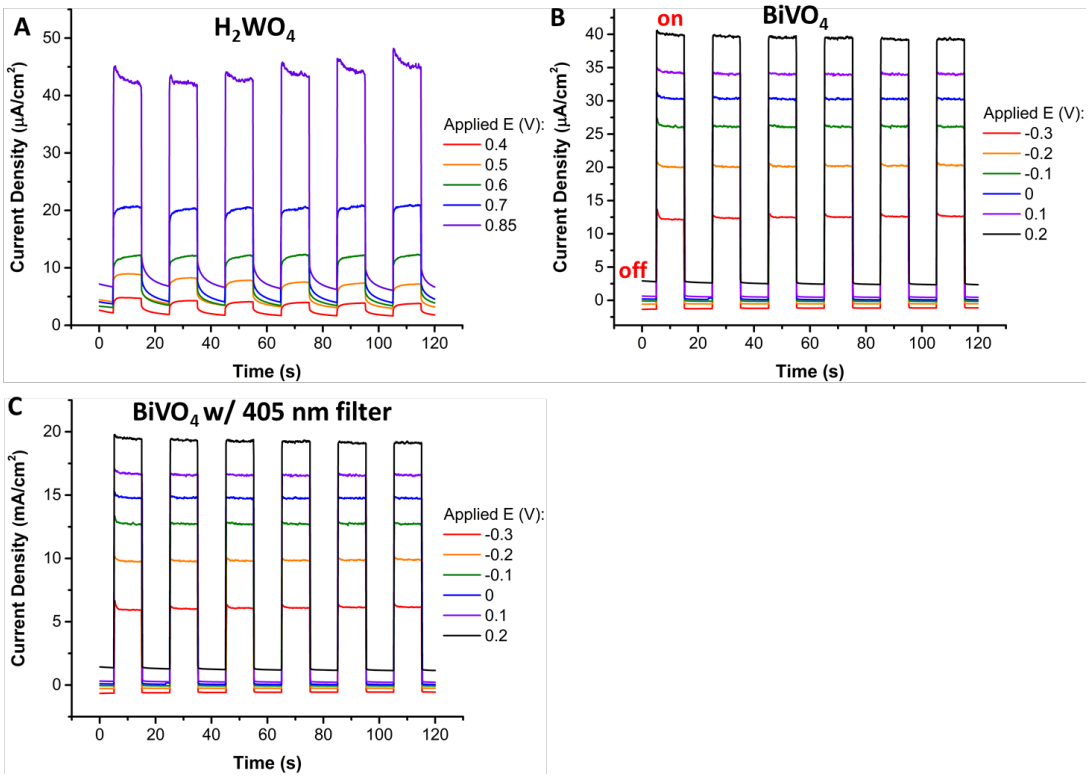

Figure 5.6 Photocurrent as a function of potential for the H_2WO_4 (A) and $BiVO_4$ (B) particles, respectively, prepared via cathodic corrosion. The chronoamperometry in (C) is the same $BiVO_4$ particles being illuminated with only visible light. Measurements were taken in 1 M Na_2SO_3 for $BiVO_4$ and 0.1 M NaOH for H_2WO_4 and both were illuminated with 60 mW/cm^2 for the chronoamperometry experiments.

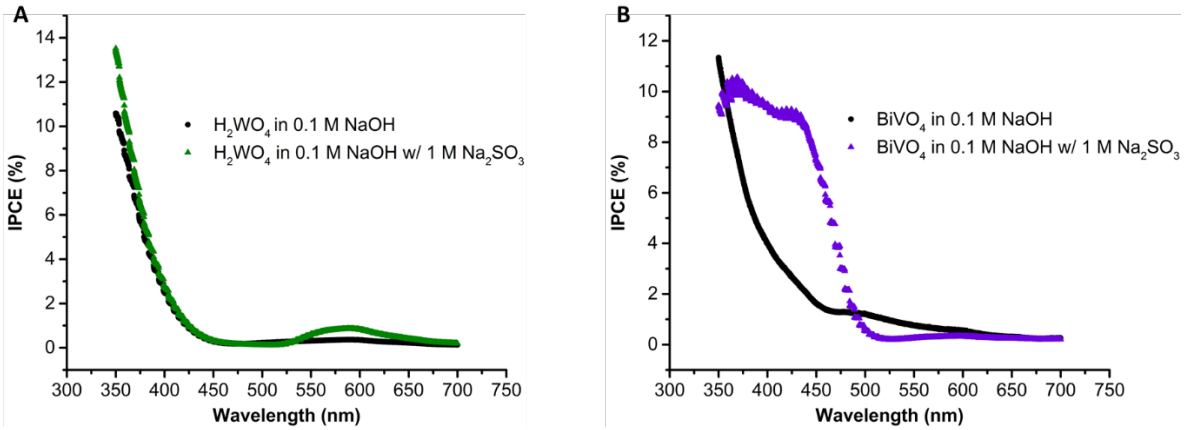

Figure 5.7 IPCE spectra for the H_2WO_4 (A) and $BiVO_4$ (B) particles depicting an appropriate band edge for each. Measurements were taken in 0.1 M NaOH with and without 1 M Na_2SO_3.

Table 5.1 Summary of the recent protocols for the synthesis of H_2WO_4, WO_3, $BiVO_4$ and TiO_2 particles.

Material	Synthetic Method	Reactants	Notes About Synthesis	Reference
H_2WO_4 nanotubes	Solvothermal	WCl_6, Urea Ethanol	12 h reaction time at 180 °C Dried at 60 °C for 12 h	44
WO_3 nanoparticles	Reverse microemulsion method	Tungsten isopropoxide Triton X-100 (surfactant) n-heptane	Aging step took 4-96 h 200-500 °C heat treatment for 2 h Post-treatment: the nanoparticles were first heated to 300 °C in air for 1 h to remove residual organics followed by a heat treatment under flowing pure H2 or a mixture of H2/N2 (1:5 v/v) at temperatures between 500 and 650 °C No morphology control	45
$BiVO_4$ thin film	Metal organic decomposition	Bismuth nitrate hexahydrate Vanadyl acetylacetonate	~10 h annealing at 500 °C, No morphology control	46
Nanoporous $BiVO_4$	Electrodeposition/ solvothermal	BiOI Vanadyl acetylacetonate	2-step Electrodeposition method Calcination process at 450 °C for 2 h, No size and morphology control	47

Table 5.1 (cont.)

TiO_2 nanorods	Solvothermal	TiF_4, 2-propanol, HF	Calcination at 180 ºC for 5.5-44 h Fluoride removal requires further heating to 600 ºC for 1.5 h 34.8% yield of anatase TiO_2	48
TiO_2 nanorods	Sol-gel	Oleic acid Oleylamine Titanium isopropoxide CTAB	~4 h reaction time at 80°C - 260 °C. Multiple purification steps including centrifugation with cyclohexane Monodisperse Very good morphology control	49
H_2WO_4	Cathodic corrosion	W wire K_2SO_4 Water	Reaction time < 2 min Room temperature Control on size and shape	*This work*
$BiVO_4$	Cathodic corrosion	V wire Bi_2O_3 $CaCl_2$ Water	Reaction time < 2min Room temperature	*This work*
TiO_2	Cathodic corrosion	Ti wire NaOH Water	Reaction time < 2min Room temperature	*This work*

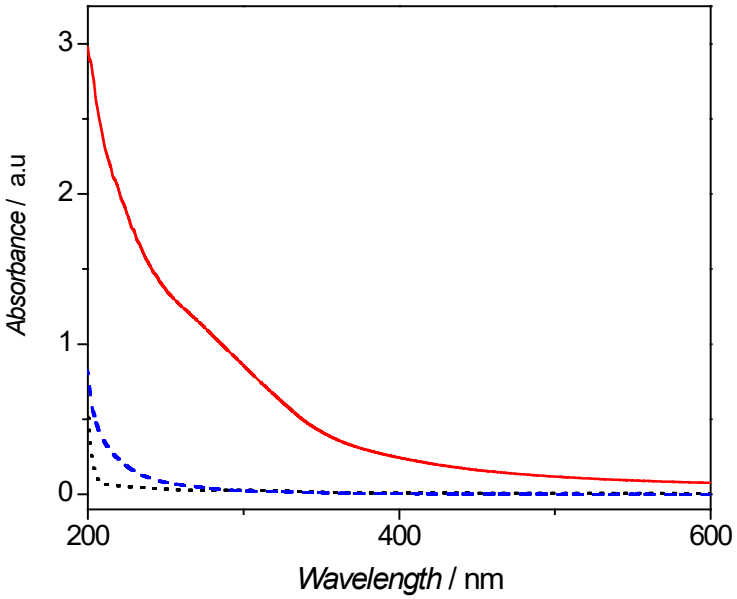

Figure 5.8 UV–Vis absorption spectra of freshly prepared WO_2/WO_3 samples in $KHSO_4$ solution (red line) and supernatant $KHSO_4$ solution after centrifugation at 4000 RPM for 3 minutes (dashed blue line). The UV-Vis adsorption spectra of the $KHSO_4$ solution has been also included (dotted black line).

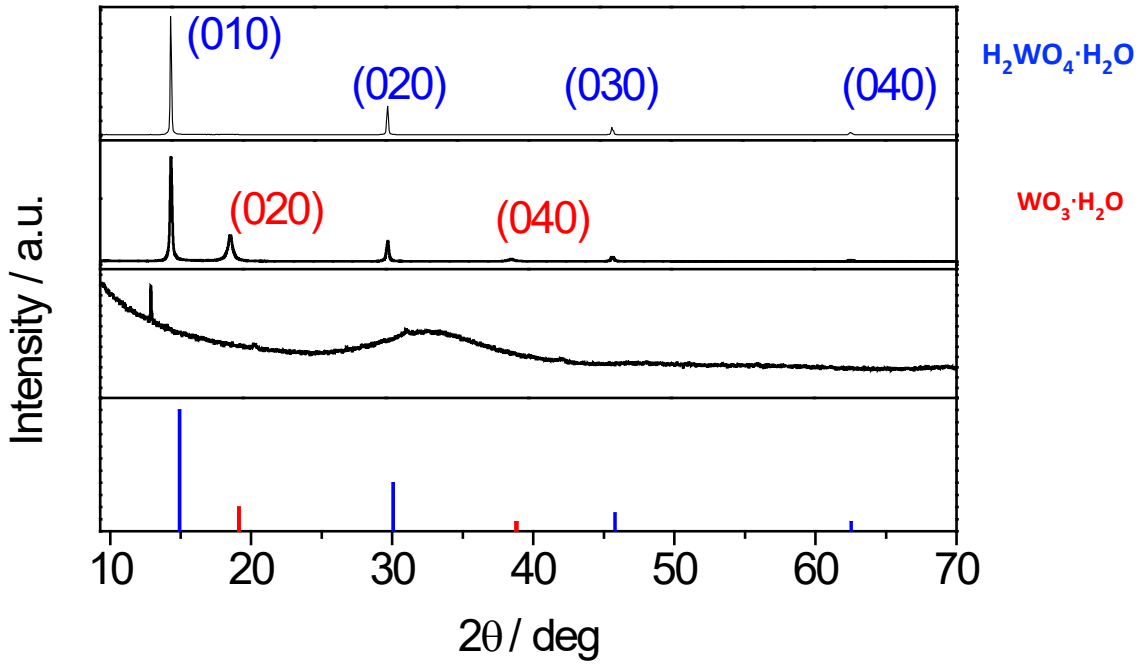

Figure 5.9 (A) XRD pattern of $H_2WO_4 \cdot H_2O$ (blue lines; JCPDS database no. 18-1420) and $WO_3 \cdot H_2O$ (red lines; JCPDS database no. 43-0679) and XRD patterns of WO_x nanoparticles as a function of the ageing time in water (B) freshly prepared (C) after 24 hours (D) after 96 hours.

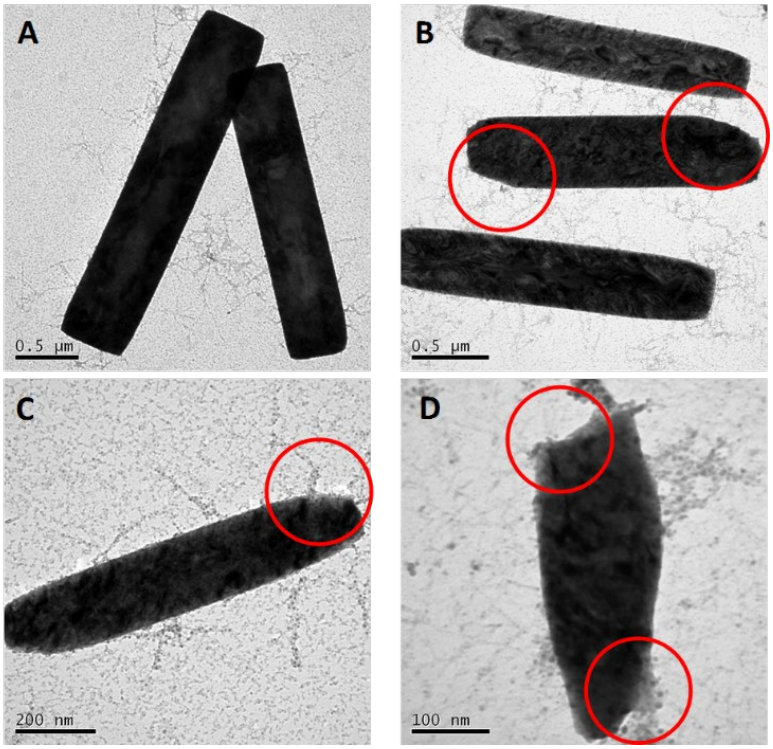

Figure 5.10 TEM images of H_2WO_4 nanoparticles prior (A) and after (B-D) ultrasonic bath treatment. The red circles indicate the areas affected by the use of the ultrasonic bath.

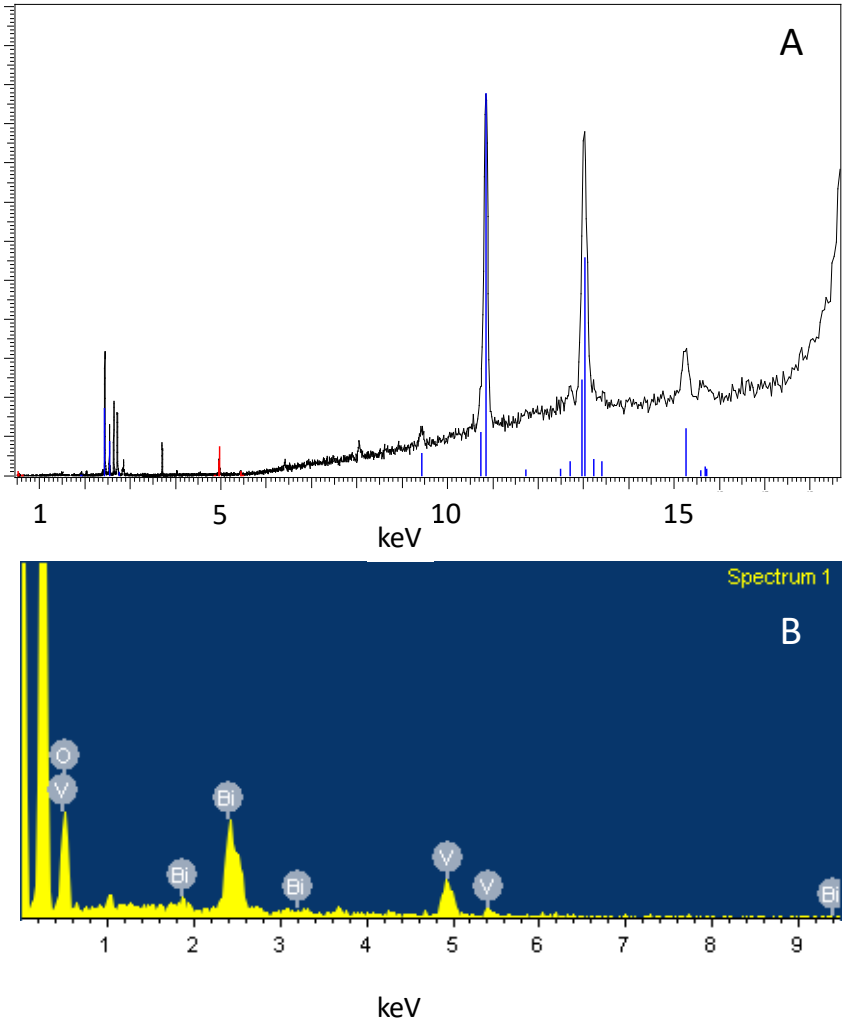

Figure 5.11 (A) XRF spectrum of $BiVO_4$ nanoparticles; red and blue lines indicate V and Bi content, respectively (B)EDX spectrum of $BiVO_4$ nanoparticles. Quantitative analysis reveals nanoparticle composition to be 56:44 (XRF) and 58:42 (EDX) for Bi:V content.

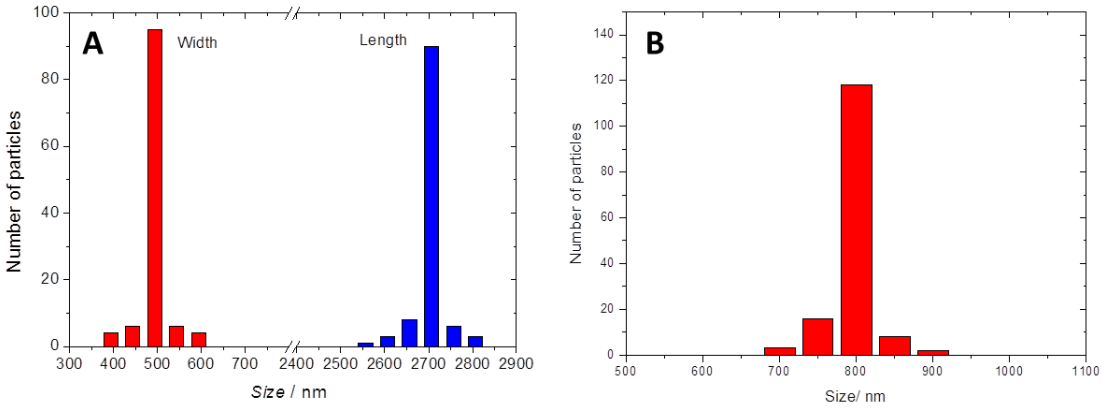

Figure 5.12 Particle size distribution of (A) H_2WO_4 and (B) $BiVO_4$ obtained from TEM measurements accordingly. The relative abundance of each particle size was calculated from a total of >150 nanoparticles.

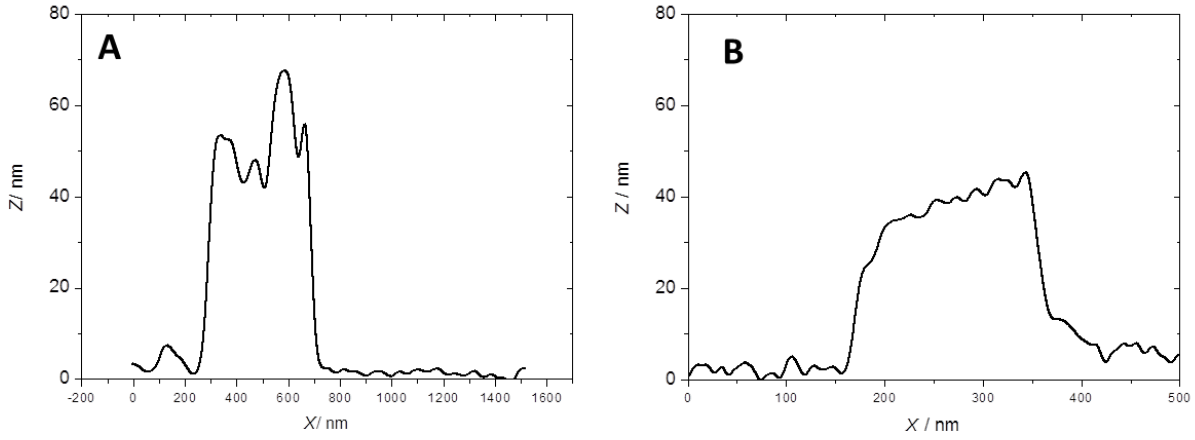

Figure 5.13 Cross section of a AFM measurement over a single (A) H_2WO_4 nanoparticle and (B)$BiVO_4$ nanoparticle.

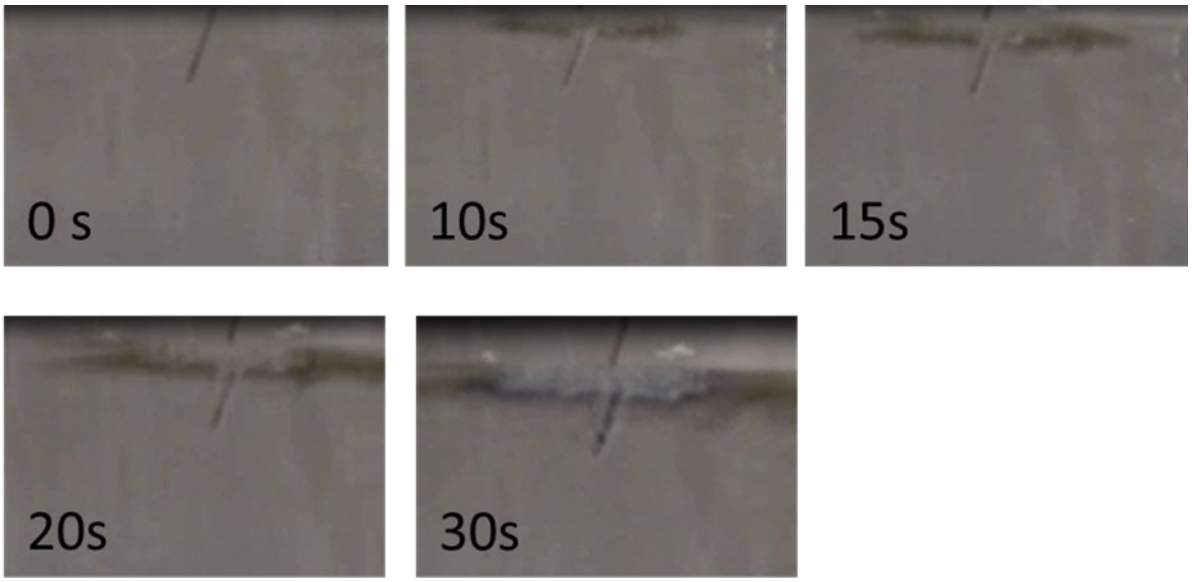

Figure 5.14 Snapshots at different timepoints during the cathodic corrosion process. As the etching proceeds, a dark cloud of colloidal nanoparticles forms in solution immediately surrounding the metal wire.

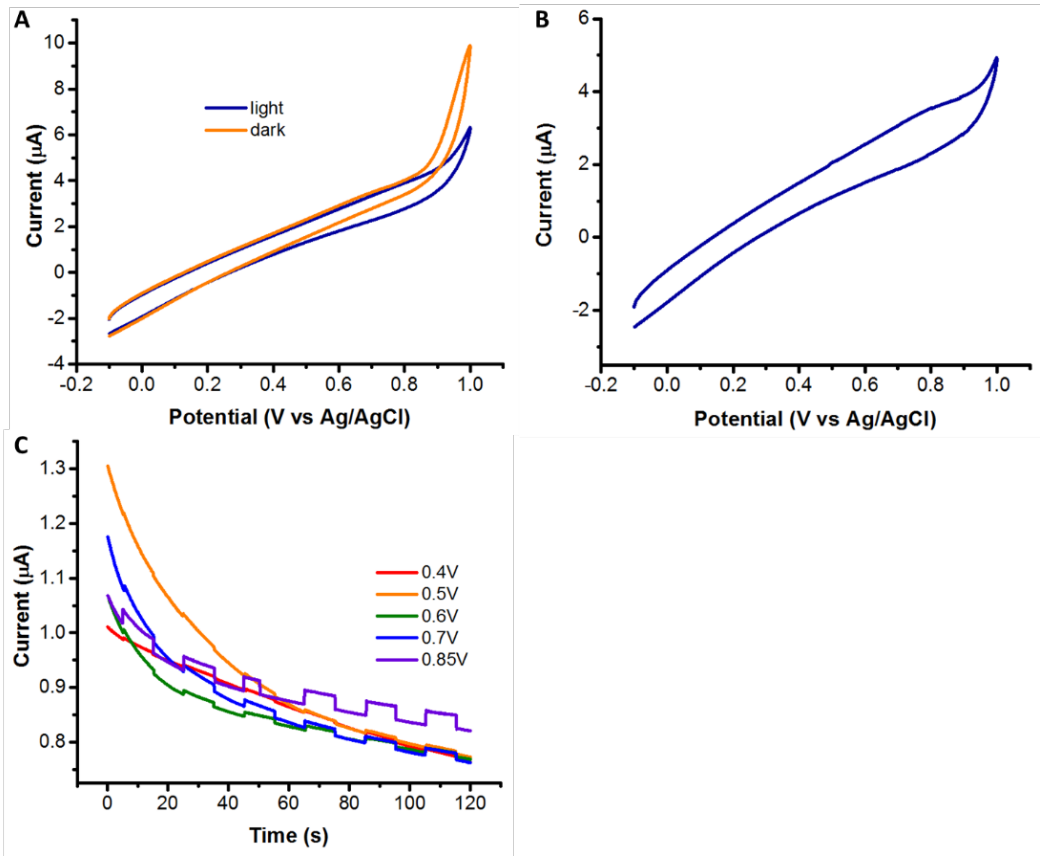

Figure 5.15 Blank measurements were taken of an ITO cover slip with a thin layer of Nafion® spin coated onto it. The data suggest some photocurrent in the absence of any photocatalyst particles, but significantly less compared to an ITO slide with photocatalytic particles on it. A) A cyclic voltammogram in dark and a cyclic voltammogram in light showing very little difference when the sample was illuminated. B) A cyclic voltammogram in which the light was chopped, which also shows very little change in current in dark compared to when illuminated. C) Chronoamperometry that clearly depicts the low values of photocurrent for the blank sample.

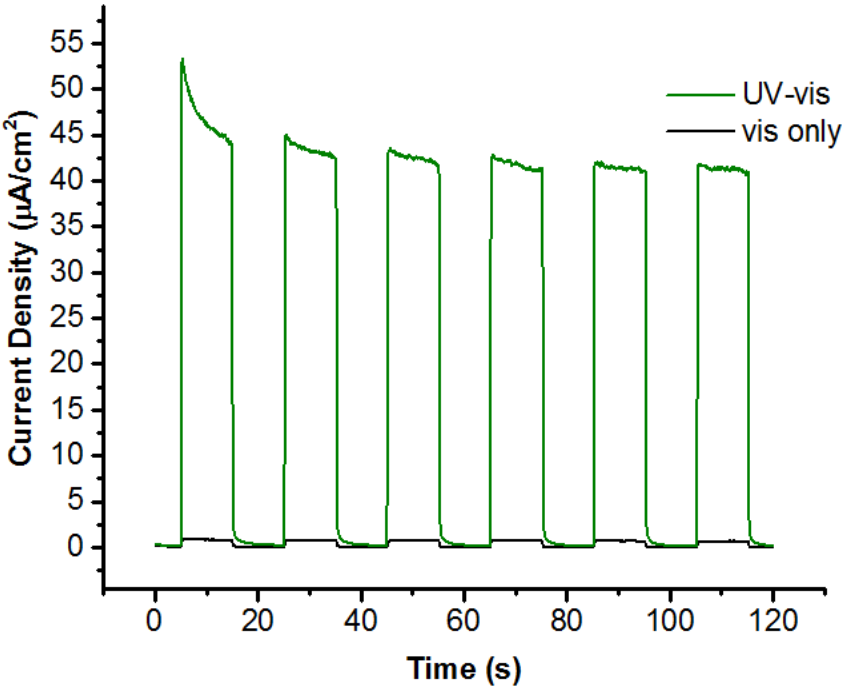

Figure 5.16 When exposed to only visible light, the H_2WO_4 displayed much lower activity. This is due to the relatively high band edge for H_2WO_4 which results in poor conversion of visible light. Sample was biased to 0.85V vs Ag/AgCl.

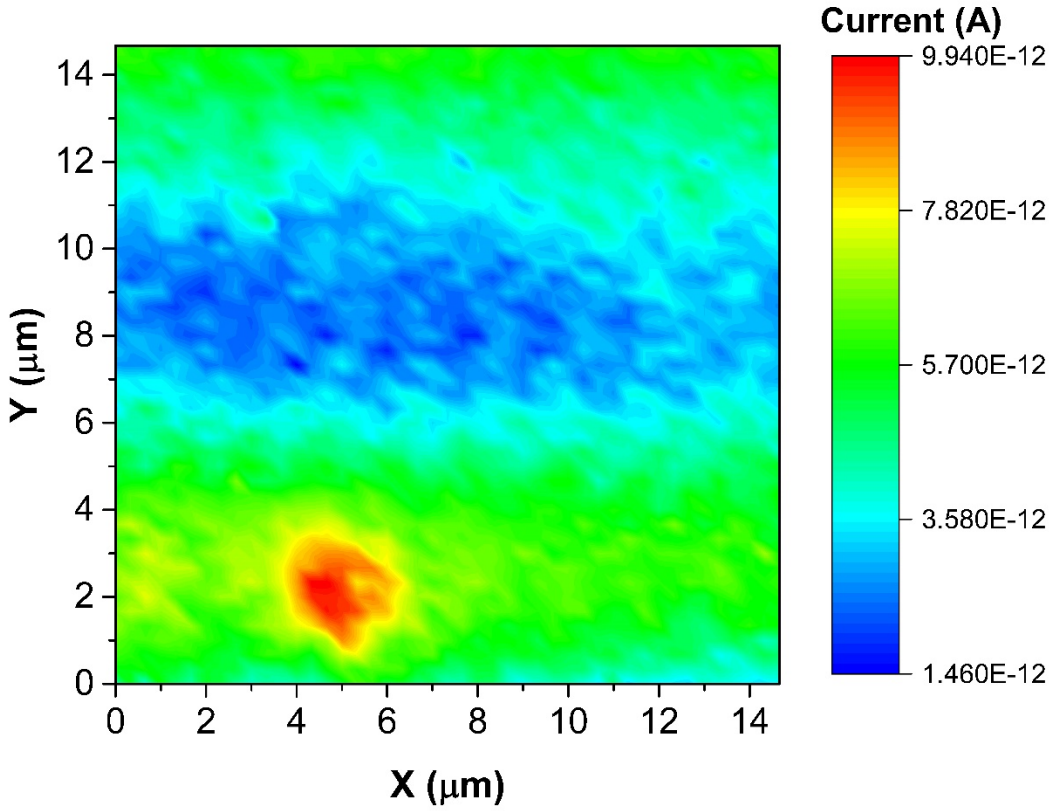

Figure 5.17 Shown here is the background subtracted SECM image used to locate the position of a WO_3 particle. This image was acquired at 0.6 V vs. Ag/AgCl (applied to the substrate) with the Pt UME held at -0.5 V vs. Ag/AgCl to reduce O_2.

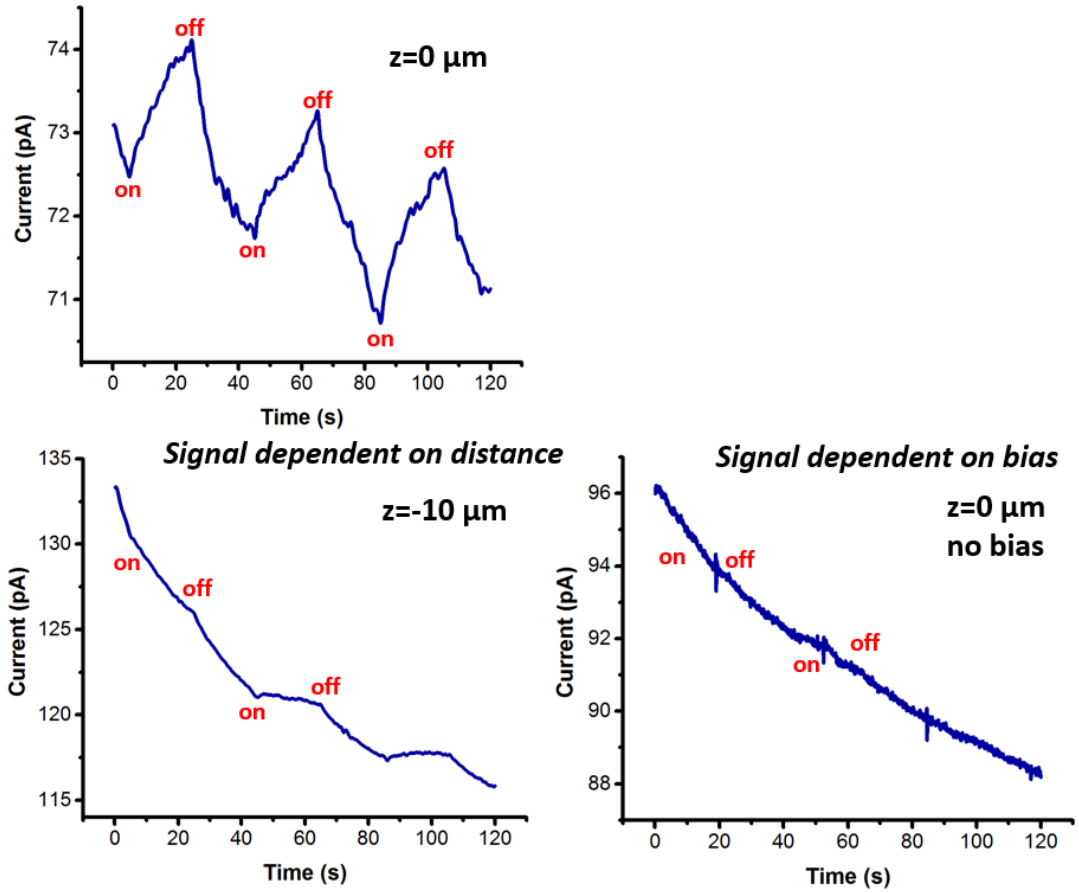

Figure 5.18 Chronoamperograms showing O_2 collection over a single WO_3 particle. Shown in (A) is the result when the particle is biased to 0.85 V vs. Ag/AgCl. When the light is turned on, the cathodic current of the UME increases due to O_2 concentration increasing**.** B) This is the resulting signal when the UME is raised above the surface, which demonstrates that the signal observed in (A) is due to the particle producing O_2. C) Shown here is the same experiment but without applying a bias to the particle, which acts as an additional control for (A) to confirm that the signal observed is due to the WO_3 producing O_2.

5.9. References

(1) Gratzel, M. Photoelectrochemical cells. *Nature* **2001**, *414*, 338-344.

(2) Bolton, J. R. Solar photoproduction of hydrogen: A review. *Sol. Energ.* **1996**, *57*, 37-50.

(3) Gust, D.; Moore, T. A.; Moore, A. L. Solar Fuels via Artificial Photosynthesis. *Acc. Chem. Res.* **2009**, *42*, 1890-1898.

(4) Memming, R. Photoinduced Charge-Transfer Processes at Semiconductor Electrodes and Particles. *Electron Transfer I* **1994**, *169*, 105-181.

(5) Li, D.; Haneda, H. Morphologies of zinc oxide particles and their effects on photocatalysis. *Chemosphere* **2003**, *51*, 129-137.

(6) Lewis, N. S. Research opportunities to advance solar energy utilization. *Science* **2016**, *351*, 1920.

(7) Choi, H. G.; Jung, Y. H.; Kim, D. K. Solvothermal synthesis of tungsten oxide nanorod/nanowire/nanosheet. *J. Am. Ceram. Soc.* **2005**, *88*, 1684-1686.

(8) Jiao, Z. H.; Wang, J. M.; Ke, L.; Sun, X. W.; Demir, H. V. Morphology-Tailored Synthesis of Tungsten Trioxide (Hydrate) Thin Films and Their Photocatalytic Properties. *ACS Appl. Mater. Interfaces* **2011**, *3*, 229-236.

(9) Waller, M. R.; Townsend, T. K.; Zhao, J.; Sabio, E. M.; Chamousis, R. L.; Browning, N. D.; Osterloh, F. E. Single-Crystal Tungsten Oxide Nanosheets: Photochemical Water Oxidation in the Quantum Confinement Regime. *Chem. Mater.* **2012**, *24*, 698-704.

(10) Lee, K.; Seo, W. S.; Park, J. T. Synthesis and optical properties of colloidal tungsten oxide nanorods. *J. Am. Chem. Soc.* **2003**, *125*, 3408-3409.

(11) Baeck, S. H.; Jaramillo, T.; Stucky, G. D.; McFarland, E. W. Controlled electrodeposition of nanoparticulate tungsten oxide. *Nano Lett.* **2002**, *2*, 831-834.

(12) Su, L. Y.; Zhang, L. G.; Fang, J. H.; Xu, M. H.; Lu, Z. H. Electrochromic and photoelectrochemical behavior of electrodeposited tungsten trioxide films. *Sol. Energ. Mat. Sol. Cells* **1999**, *58*, 133-140.

(13) Kim, C.; Lee, H. Change in the catalytic reactivity of Pt nanocubes in the presence of different surface-capping agents. *Catalysis Communications* **2009**, *10*, 1305-1309.

(14) Zhao, Z. G.; Miyauchi, M. Nanoporous-walled tungsten oxide nanotubes as highly active visible-light-driven photocatalysts. *Angew. Chem. Int. Ed.* **2008**, *47*, 7051-7055.

(15) Yang, H. G.; Liu, G.; Qiao, S. Z.; Sun, C. H.; Jin, Y. G.; Smith, S. C.; Zou, J.; Cheng, H. M.; Lu, G. Q. Solvothermal Synthesis and Photoreactivity of Anatase TiO2 Nanosheets with Dominant {001} Facets. *J. Am. Chem. Soc.* **2009**, *131*, 4078-4083.

(16) Siegfried, M. J.; Choi, K. S. Elucidating the effect of additives on the growth and stability of Cu_2O surfaces via shape transformation of pre-grown crystals. *J. Am. Chem. Soc.* **2006**, *128*, 10356-10357.

(17) Maijenburg, A. W.; Hattori, A. N.; De Respinis, M.; McShane, C. M.; Choi, K. S.; Dam, B.; Tanaka, H.; ten Elshof, J. E. Ni and p-Cu_2O Nanocubes with a Small Size Distribution by Templated Electrodeposition and Their Characterization by Photocurrent Measurement. *ACS Appl. Mater. Interfaces* **2013**, *5*, 10938-10945.

(18) Ma, L. Y.; Lee, S.; DeMuth, J.; Maldonado, S. Direct electrochemical deposition of crystalline silicon nanowires at $T \geq 60^{o}C$. *RSC Adv.* **2016**, *6*, 78818-78825.

(19) Yanson, A. I.; Rodriguez, P.; Garcia-Araez, N.; Mom, R. V.; Tichelaar, F. D.; Koper, M. T. M. Cathodic Corrosion: A Quick, Clean, and Versatile Method for the Synthesis of Metallic Nanoparticles. *Angew. Chem. Int. Ed.* **2011**, *50*, 6346-6350.

(20) Rodriguez, P.; Tichelaar, F. D.; Koper, M. T. M.; Yanson, A. I. Cathodic Corrosion as a Facile and Effective Method To Prepare Clean Metal Alloy Nanoparticles. *J. Am. Chem. Soc.* **2011**, *133*, 17626-17629.

(21) Bennett, E.; Monzo, J.; Humphrey, J.; Plana, D.; Walker, M.; McConville, C.; Fermin, D.; Yanson, A.; Rodriguez, P. A Synthetic Route for the Effective Preparation of Metal Alloy Nanoparticles and Their Use as Active Electrocatalysts. *ACS Cat.* **2016**, *6*, 1533-1539.

(22) Rodriguez, P.; Plana, D.; Fermin, D. J.; Koper, M. T. M. New insights into the catalytic activity of gold nanoparticles for CO oxidation in electrochemical media. *J. Catal.* **2014**, *311*, 182-189.

(23) Elwakkad, S. E. S.; Rizk, H. A.; Ebaid, I. G. The Electrochemical Behavior of the Tungsten Electrode and the Nature of the Different Oxides of the Metal. *J. Phys. Chem.* **1955**, *59*, 1004-1008.

(24) Elbasiouny, M. S.; Hassan, S. A.; Hefny, M. M. On the Electrochemical-Behavior of Tungsten - The Formation and Dissolution of Tungsten-Oxide in Sulfuric-Acid-Solutions. *Corros. Sci.* **1980**, *20*, 909-917.

(25) Lu, F.; Ji, X. B.; Yang, Y. C.; Deng, W. T.; Banks, C. E. Room temperature ionic liquid assisted well-dispersed core-shell tin nanoparticles through cathodic corrosion. *RSC Adv.* **2013**, *3*, 18791-18793.

(26) Yanson, A. I.; Antonov, P. V.; Rodriguez, P.; Koper, M. T. M. Influence of the electrolyte concentration on the size and shape of platinum nanoparticles synthesized by cathodic corrosion. *Electrochim. Acta* **2013**, *112*, 913-918.

(27) Duca, M.; Rodriguez, P.; Yanson, A. I.; Koper, M. T. M. Selective Electrocatalysis on Platinum Nanoparticles with Preferential (100) Orientation Prepared by Cathodic Corrosion. *Top. Catal.* **2014**, *57*, 255-264.

(28) Seabold, J. A.; Zhu, K.; Neale, N. R. Efficient solar photoelectrolysis by nanoporous Mo: $BiVO_4$ through controlled electron transport. *Phys. Chem. Chem. Phys.* **2014**, *16*, 1121-1131.

(29) Ng, Y. H.; Iwase, A.; Kudo, A.; Amal, R. Reducing Graphene Oxide on a Visible-Light $BiVO_4$ Photocatalyst for an Enhanced Photoelectrochemical Water Splitting. *J. Phys. Chem. Lett.* **2010**, *1*, 2607-2612.

(30) Hersbach, T. J. P.; Mints, V. A.; Calle-Vallejo, F.; Yanson, A. I.; Koper, M. T. M. Anisotropic etching of rhodium and gold as the onset of nanoparticle formation by cathodic corrosion. *Farad. Discuss.* **2016**, *193*, 207-222.

(31) Townsend, T. K.; Sabio, E. M.; Browning, N. D.; Osterloh, F. E. Improved Niobate Nanoscroll Photocatalysts for Partial Water Splitting. *Chemsuschem* **2011**, *4*, 185-190.

(32) Seabold, J. A.; Choi, K. S. Efficient and Stable Photo-Oxidation of Water by a Bismuth Vanadate Photoanode Coupled with an Iron Oxyhydroxide Oxygen Evolution Catalyst. *J. Am. Chem. Soc.* **2012**, *134*, 2186-2192.

(33) Zhong, D. K.; Choi, S.; Gamelin, D. R. Near-Complete Suppression of Surface Recombination in Solar Photoelectrolysis by "Co-Pi" Catalyst-Modified W:$BiVO_4$. *J. Am. Chem. Soc.* **2011**, *133*, 18370-18377.

(34) Park, H. S.; Kweon, K. E.; Ye, H.; Paek, E.; Hwang, G. S.; Bard, A. J. Factors in the Metal Doping of $BiVO_4$ for Improved Photoelectrocatalytic Activity as Studied by Scanning

Electrochemical Microscopy and First-Principles Density-Functional Calculation. *J. Phys. Chem. C* **2011**, *115*, 17870-17879.

(35) Chen, L.; Toma, F. M.; Cooper, J. K.; Lyon, A.; Lin, Y. J.; Sharp, I. D.; Ager, J. W. Mo-Doped $BiVO_4$ Photoanodes Synthesized by Reactive Sputtering. *Chemsuschem* **2015**, *8*, 1066-1071.

(36) Feng, C. X.; Wang, S. Z.; Geng, B. Y. Ti(IV) doped WO_3 nanocuboids: fabrication and enhanced visible-light-driven photocatalytic performance. *Nanoscale* **2011**, *3*, 3695-3699.

(37) Theerthagiri, J.; Senthil, R. A.; Malathi, A.; Selvi, A.; Madhavan, J.; Ashokkumar, M. Synthesis and characterization of a CuS-WO_3 composite photocatalyst for enhanced visible light photocatalytic activity. *RSC Adv.* **2015**, *5*, 52718-52725.

(38) Liew, S. L.; Zhang, Z.; Goh, T. W. G.; Subramanian, G. S.; Seng, H. L. D.; Hor, T. S. A.; Luo, H. K.; Chi, D. Z. Yb-doped WO_3 photocatalysts for water oxidation with visible light. *Int. J. Hydrogen Energy* **2014**, *39*, 4291-4298.

(39) Radecka, M.; Sobas, P.; Wimbicka, M.; Rekas, M. Photoelectrochemical properties of undoped and Ti-doped WO_3. *Physica B-Condens. Matter* **2005**, *364*, 85-92.

(40) Martyanov, I. N.; Uma, S.; Rodrigues, S.; Klabunde, K. J. Structural defects cause TiO_2-based photocatalysts to be active in visible light. *Chem. Comm.* **2004**, 2476-2477.

(41) Zhuang, J. D.; Dai, W. X.; Tian, Q. F.; Li, Z. H.; Xie, L. Y.; Wang, J. X.; Liu, P.; Shi, X. C.; Wang, D. H. Photocatalytic Degradation of RhB over TiO_2 Bilayer Films: Effect of Defects and Their Location. *Langmuir* **2010**, *26*, 9686-9694.

(42) Helms, B. A.; Williams, T. E.; Buonsanti, R.; Milliron, D. J. Colloidal Nanocrystal Frameworks. *Adv. Mater.* **2015**, *27*, 5820-5829.

(43) Singh, A.; Lindquist, B. A.; Ong, G. K.; Jadrich, R. B.; Ha, H.; Ellison, C. J.; Truskett, T. M.; Milliron, D. J. Linking Semiconductor Nanocrystals into Gel Networks through All-Inorganic Bridges. *Angew. Chem. Int. Ed.* **2015**, *54*, 14840-14844.

(44) Zhao, Z. G.; Miyauchi, M. Nanoporous-walled tungsten oxide nanotubes as highly active visible-light-driven photocatalysts. *Angew. Chem. Int. Ed.* **2008**, *47*, 7051-7055.

(45) Xiong, L. F.; He, T. Synthesis and characterization of ultrafine tungsten and tungsten oxide nanoparticles by a reverse microemulsion-mediated method. *Chem. Mater.* **2006**, *18*, 2211-2218.

(46) Zhong, D. K.; Choi, S.; Gamelin, D. R. Near-Complete Suppression of Surface Recombination in Solar Photoelectrolysis by "Co-Pi" Catalyst-Modified W:$BiVO_4$. *J. Am. Chem. Soc.* **2011**, *133*, 18370-18377.

(47) Kim, T. W.; Choi, K. S. Nanoporous $BiVO_4$ Photoanodes with Dual-Layer Oxygen Evolution Catalysts for Solar Water Splitting. *Science* **2014**, *343*, 990-994.

(48) Yang, H. G.; Liu, G.; Qiao, S. Z.; Sun, C. H.; Jin, Y. G.; Smith, S. C.; Zou, J.; Cheng, H. M.; Lu, G. Q. Solvothermal Synthesis and Photoreactivity of Anatase TiO_2 Nanosheets with Dominant {001} Facets. *J. Am. Chem. Soc.* **2009**, *131*, 4078-4083.

(49 Zhang, Z. H.; Zhong, X. H.; Liu, S. H.; Li, D. F.; Han, M. Y. Aminolysis route to monodisperse titania nanorods with tunable aspect ratio. *Angew. Chem. Int. Ed.* **2005**, *44*, 3466-3470.

Chapter 6:

Future work and outlook

6.1. Abstract

The contents of this chapter are dedicated to ongoing pursuits in the laboratory as well as future research to explore. Each section is dedicated to a different area of research to be investigated further using the work presented in previous chapters as a foundation. The results and experiments presented here represent the potential beginnings of new research studies to be pursued by interested individuals.

6.2. Utilizing SECM for catalyst discovery

The most immediate future experiments to perform is the high-throughput screening of electrocatalysts to apply to the catalytic systems studied in this dissertation. There is a large volume of work toward utilizing scanning electrochemical microscopy (SECM) to the ends of rapidly screening electrocatalysts.[1-4] This same methodology can be employed here to discover new catalysts to be scaled up for use in direct synthesis. The advantages of SECM based methods is that very small amounts catalyst materials and solvent is required to perform these high-throughput measurements. Catalyst screening via thermal catalytic methods is less attractive due to the reactors used in thermal catalyst require large quantities of both catalyst and solvents. The materials design principles outlined here can be used to guide what type of catalysts are screened with SECM. To demonstrate this technique, catalyst spot arrays were prepared by using a microdroplet dispenser (CH Instruments 1550A) to dispense droplets (60 μm jetting device, 45 V pulse amplitude, 10 ms pulse period) of catalyst precursor material. The catalyst spot array shown here was composed of PdAu, and the precursor chemicals used were $(NH_4)_2[PdCl_6]$ and H_2AuCl_4.

These chemicals were dispensed in increasing atomic ratio of Au throughout the spot array, and atomic ratio was controlled through the number of droplets used to generate the spot. The resulting droplets were first dried in a tube furnace (150°C in Ar) and then annealed (550°C in H_2) in order to reduce the precursor chemicals into their metallic form. The resulting array was screened via SECM to quantify ORR and HOR kinetics of each catalyst spot. The resulting SECM images are shown in Figure 6.1, and it is clear from these images that there is a distinct difference in each spot's ability to activate H_2.

A COMSOL Multiphysics 4.4 simulation was utilized in order to extract more quantitative information from this system. The model details are shown in Figure 6.2. The geometry was built in a 2D axis-symmetric program, in which flux boundaries were set to mimic the formation and collection of H_2O_2. The boundary for the UME was set to consume H_2O_2 (formed at the substrate) at a rate equal to the Butler-Volmer expression shown below:

$$\mathrm{Flux_{UME}} = \mathrm{k^0}\left[\mathrm{e^{-\alpha f(E-E^0)}} - \mathrm{e^{(1-\alpha)f(E-E^0)}}\right] \quad (6.1)$$

The flux boundary condition for the UME was also set to produce O_2 at a rate equal and opposite to the rate at which H_2O_2 is being consumed. The flux boundary at the catalyst spot was set to a similar Butler-Volmer expression as equation 6.1 that represented the formation of H_2O_2 from ORR. From these simulations, it is possible to extract catalyst spot selectivity toward H_2O_2 formation as well as kinetic parameters (k^0 and α) for HOR and ORR. The parameters for k^0, α, and selectivity all determine the simulation results. After completing a screening experiment, the data collected over the catalyst spots of interest can be fit this COMSOL simulation to acquire what the approximate kinetic parameters and selectivity are. The same can be performed to determine HOR kinetics at each catalyst spot. In this case, the flux boundary conditions are Butler-

Volmer expressions tailored to the HOR reaction (formation of H^+ and consumption of H_2). The increase in oxidation current as a function of increasing potential (to more positive values) can be fit with this simulation to acquire k^0 and α, as is shown in Figure 6.3.

6.3. Role of the support material in direct synthesis

The findings discussed in Chapter 4 lay the groundwork for a multitude of future studies in the area of H_2O_2 formation. Among these is the role the carbon supports play in direct synthesis of H_2O_2. It is well researched that catalysts prepared on carbon supports produce H_2O_2 at faster rates compared to the same catalysts prepared on electrochemically inactive supports (i.e. Al_2O_3, SiO_2, etc.).[5,6] This is believed to be due to a difference in acidity of the support relative to other commonly used materials. The research presented in Chapter 4 in this dissertation show a strong correlation between electrocatalysis and thermal catalysis, and it is well known that carbon is an effective electrocatalyst for forming H_2O_2 (Figure 6.4).[7,8] Carbon materials are very selective to forming H_2O_2 via the 2-electron reduction of O_2 but do so at rather high overpotentials. It is therefore likely that the carbon supports are activated to some extent in direct synthesis, but only contribute minimally to the rate of H_2O_2 formation due to small overlap in HOR and ORR activity. In fact, when deciding which carbon support to use in Chapter 4, Vulcan XC-72 was selected because it displayed very low activity. Other candidate support materials included Darco carbon, which displayed rather low overpotentials to carry out ORR, as is shown in Figure 6.5. Based on this information alone, it is not unreasonable to hypothesize that a catalyst comprised of Pt supported on Darco would display non-zero H_2O_2 selectivities. This is contrary to the well-known fact that Pt does not produce H_2O_2 with very high yields. When tested toward electrocatalysis, the Pt/Darco also exhibited fairly high ORR activity to produce H_2O_2. It is possible that the Darco is not innocent in the direct synthesis setup and is being activated to carry out ORR to form H_2O_2

while the Pt oxidizes H_2. Additionally, it has been researched that the presence of metals on carbon materials can significantly lower overpotentials to carry out catalytic reactions such as ORR.[5] Therefore, while a carbon support with no catalyst might not be active enough to form H_2O_2 in direct synthesis, the presence of another metal could render the carbon to be much more catalytically active. This is an attractive idea from an economic standpoint, because carbon materials are intrinsically very selective toward the 2-electron reduction of O_2 and are much easier to process than a precious metal catalyst.

Future research in this area could involve testing different Pt loadings and different carbon materials to utilize in direct synthesis. There are a multitude of studies in the literature regarding ORR on carbon, and there are several established strategies for lowering the overpotential for carbon to carry out ORR. Unfortunately, carbon still pales in comparison to precious metals in terms of HOR reactivity, but the addition of these metals in small weight loadings might not pose a significant economic barrier to utilizing such catalysts for direct synthesis.

A control experiment to be performed is to pack a trickle bed reactor entirely of a carbon support, (Vulcan, Darco, etc.) and quantify how effectively it forms H_2O_2. This, however, will likely result in poor H_2O_2 yields, as there is no component to activate H_2. However, the inclusion of some metal that is able to activate hydrogen will also affect the carbon's ability to activate oxygen. There is a fair amount of research in the electrocatalytic community that delves into the thermodynamic effects that metals have on carbon materials.[9] For instance, in one study, ORR kinetics were quantified for graphene where some of the graphene was either deposited onto a metal (i.e. Pt, Au) or a SiO_2. It was observed that the graphene that was deposited onto Au or Pt exhibited much faster kinetics toward ORR, which is hypothesized to be entirely due to thermodynamic effects.[9] The same effects would be present on a direct synthesis catalyst that

contained trace amounts of some H_2 activating metal on a carbon support. It is possible that catalysts such as this would produce H_2O_2 at high rates and with high selectivities. From an economic point of view, it would be of interest to utilize carbon since it is readily available and produces H_2O_2 with high yield. If this carbon-based catalyst were to be effective, there would be little reasoning behind rigorously preparing a metal alloy to produce the H_2O_2.

6.4. Compartmentalization of direct synthesis

Because direct synthesis occurs via HOR and ORR being performed in concert on a single catalyst, it is certainly possible to split the two up into half-cells. This poses an interesting solution to possibly the biggest drawback in direct synthesis which is that H_2 and O_2 need to be mixed together. To avoid the danger of forming explosive mixtures, HOR and ORR could be performed in individual half-cells, similar to a fuel cell or electrodialysis experiment.[10,11] In order to test this idea, the experimental setup discussed in Chapter 2 of this work was utilized to separate direct synthesis into half-cells (Figure 6.6). The HOR half-cell was comprised of a Pt wire in saturated H_2 solution, while the ORR half-cell was comprised of Vulcan carbon deposited onto a glassy carbon substrate. The two half-cells were electrically connected with no applied bias, and after a brief period of time, H_2O_2 was detected at a Pt UME present in the ORR half-cell. This observation gives credence to the idea that an effective direct synthesis catalyst can easily be fabricated by simply depositing minute amounts of a metal that can activate H_2 onto a carbon support. There is a great deal of research on the mechanism of H_2O_2 formation on carbons and several studies optimizing H_2O_2 formation to occur at relatively low overpotentials.[7,12] Additionally, HOR catalysis is one of the most exhaustively researched areas of electrochemistry.[13-15] This research can be used as a foundation in future work exploring the fabrication of catalysts to carry out direct synthesis in the most cost-effective way possible. Additionally, the results shown in Figure 6.4 and

6.5 show H_2O_2 formation on unaltered carbon. In direct synthesis, the H_2 activating catalyst would be supported onto the carbon, and will thermodynamically affect its ability to activate O_2, as discussed above. Ultimately, this result shows the utility in simply utilizing carbon materials as direct synthesis catalysts and can potentially eliminate the rigorous catalyst design procedures used to make traditional direct synthesis catalysts.

From an engineering point of view, the results from this work have strong implications on optimal cell design for a thermal catalytic system. The work here shows that the formation of H_2O_2 is dependent on a catalyst mediating the electron transfer between H_2 and O_2. Therefore, there is no need for the two to be mixed together in a single reactor bed, and instead, they can be separated into two individual chambers similar a fuel cell. The only difference in this case would be that a typical fuel cell seeks to suppress H_2O_2 formation, while this direct synthesis type fuel cell would seek to form it. Naturally, there would need to be some variation in cell design from a traditional fuel cell, as H_2O_2 is known to degrade most ionic membranes that separate the chambers of the cell.[16] It would be advantageous to utilize cell designs common to corrosion cells or bipolar membrane electrodialysis cells.[11,17] These cells typically involve separating two chambers with an electrocatalytic membrane. In the case of forming H_2O_2, the membrane would be constructed to have one side coated with an HOR catalyst and the other with an ORR catalyst. An example of this reactor design is shown in Figure 6.3. In this design, the HOR and ORR were split up into half-cells, where H_2 and O_2 were bubbled into their respective half-cells. A Pt wire was shorted to a Au electrode, and it was observed that H_2O_2 was formed within seconds of introducing H_2 to the HOR half-cell. The signal for H_2O_2 decreased when H_2 and O_2 were sequentially removed and the signal returned near to baseline upon removing gas flow entirely. This demonstration is a simple proof-of-concept that H_2O_2 can be formed in direct synthesis without the limitation of H_2 or O_2

concentrations. Regardless, this innovation in cell design for direct synthesis will undoubtedly lead to large improvements in its economic efficiency for producing H_2O_2, thus giving it a much larger degree of industrial relevance.

6.5. Figures

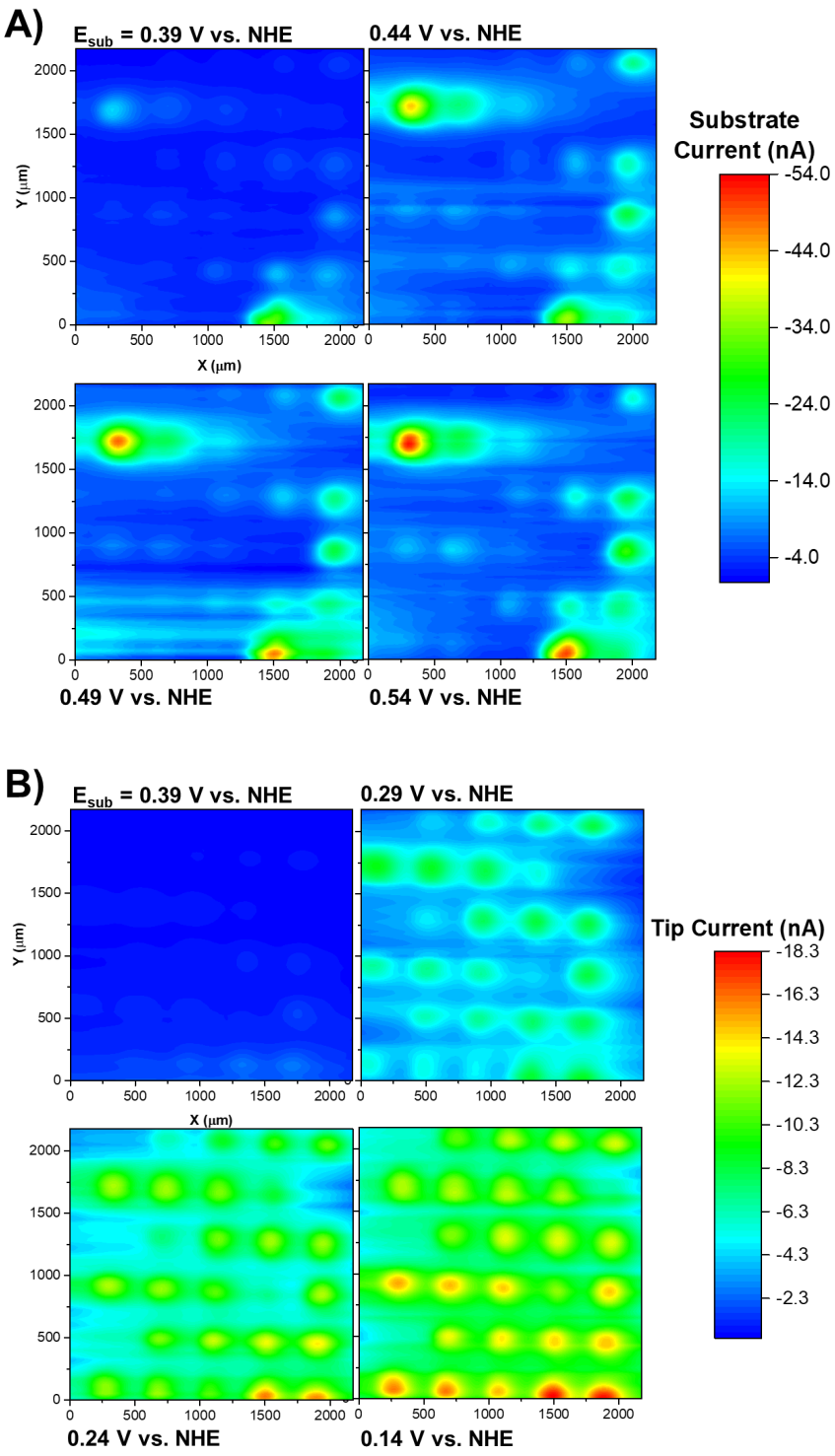

Figure 6.1 SECM images of HOR (A) and ORR (B) over a catalyst array of varying PtAu compositions. This shows the importance of catalyst composition on catalytic reactivity towards H_2 specifically.

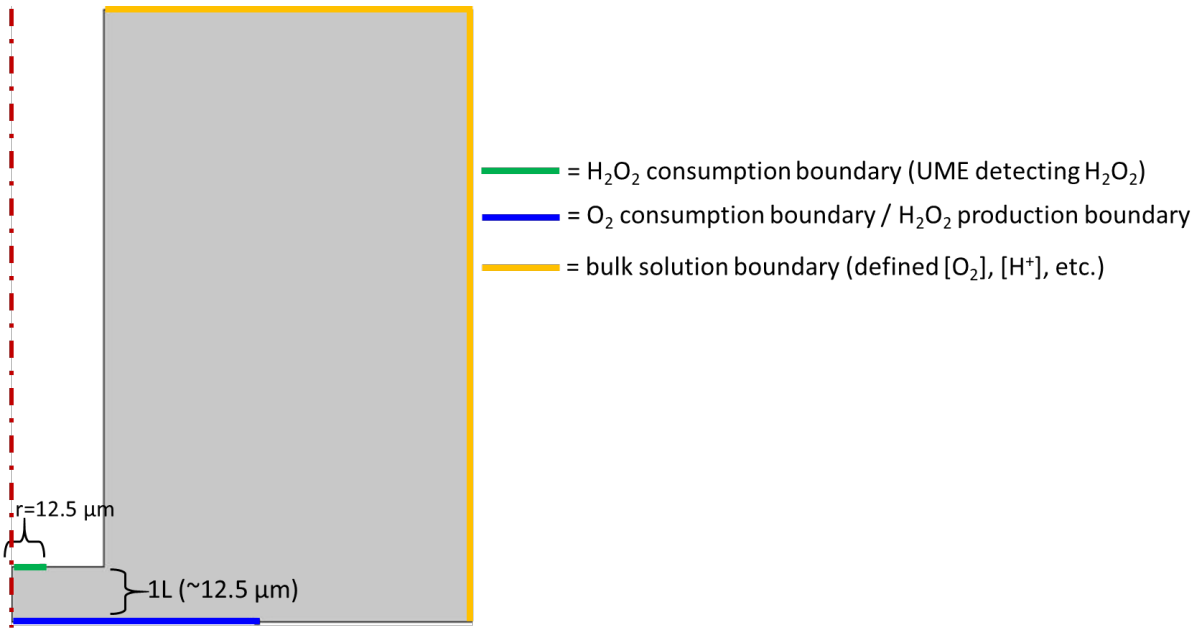

Figure 6.2 COMSOL simulation used to fit data collected from SECM images. The boundary conditions of the substrate are altered until the UME response (green boundary) matches what is acquired experimentally. This yields catalyst spot kinetic parameters (k^0, α) as well as catalyst spot H_2O_2 selectivity.

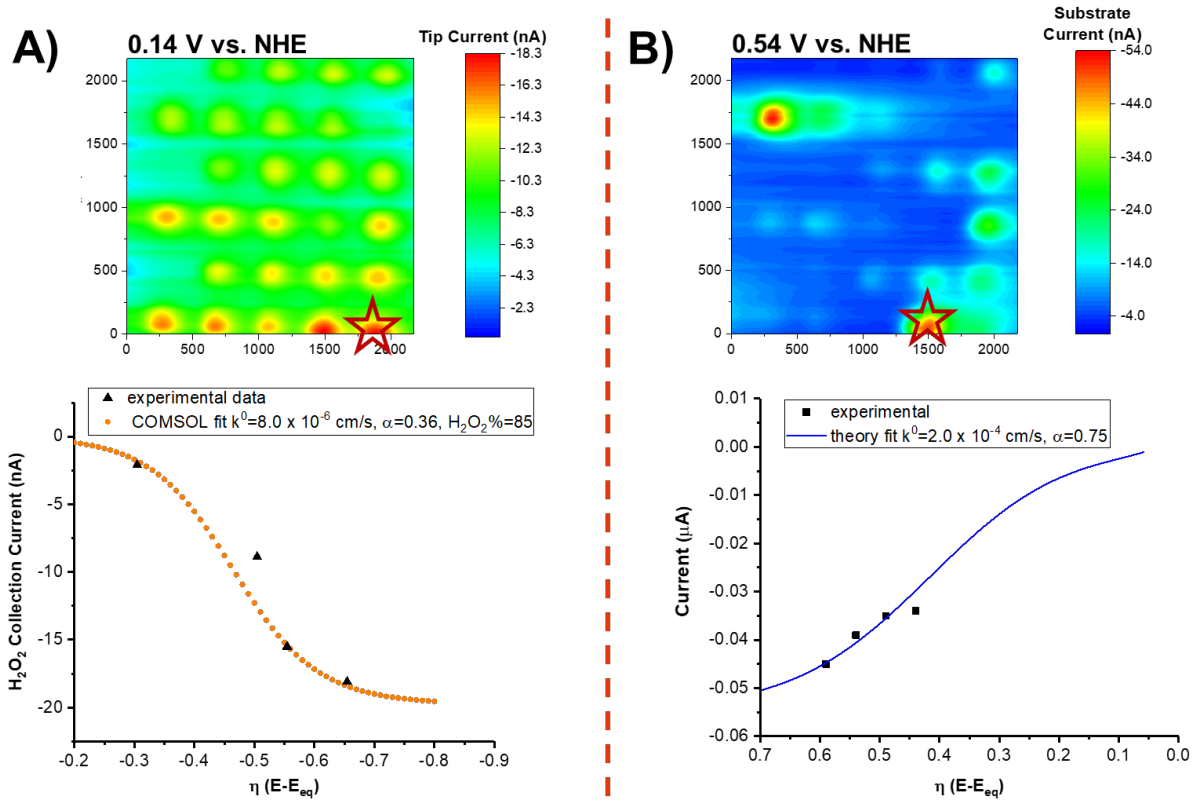

Figure 6.3 Shown here is an example of COMSOL being utilized to fit tip current collected in ORR experiments (A) as well as substrate currents measured in HOR experiments (B). By fitting these data, kinetic parameters k^0 and α as well as H_2O_2 selectivity are quantifiable (shown in legends in the plots).

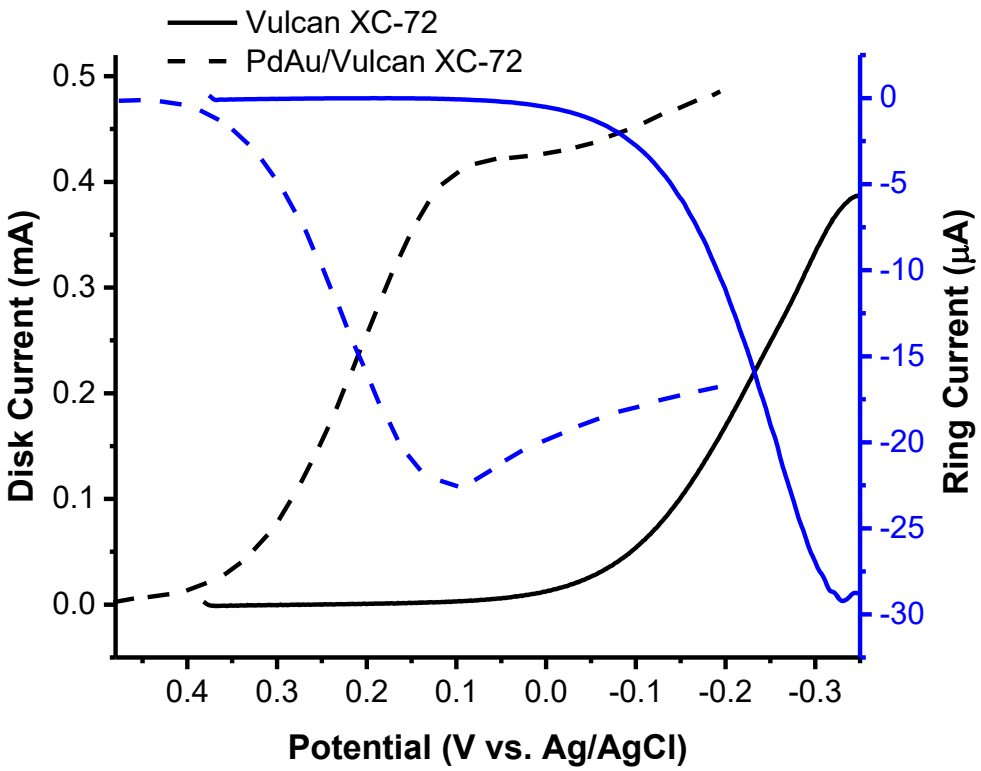

Figure 6.4 Shown here is RRDE data collected from a PdAu catalyst mounted on Vulcan and the bare Vulcan support. The nascent Vulcan support produces H_2O_2 at larger overpotentials and displays a small degree of overlap with the Vulcan support, albeit small.

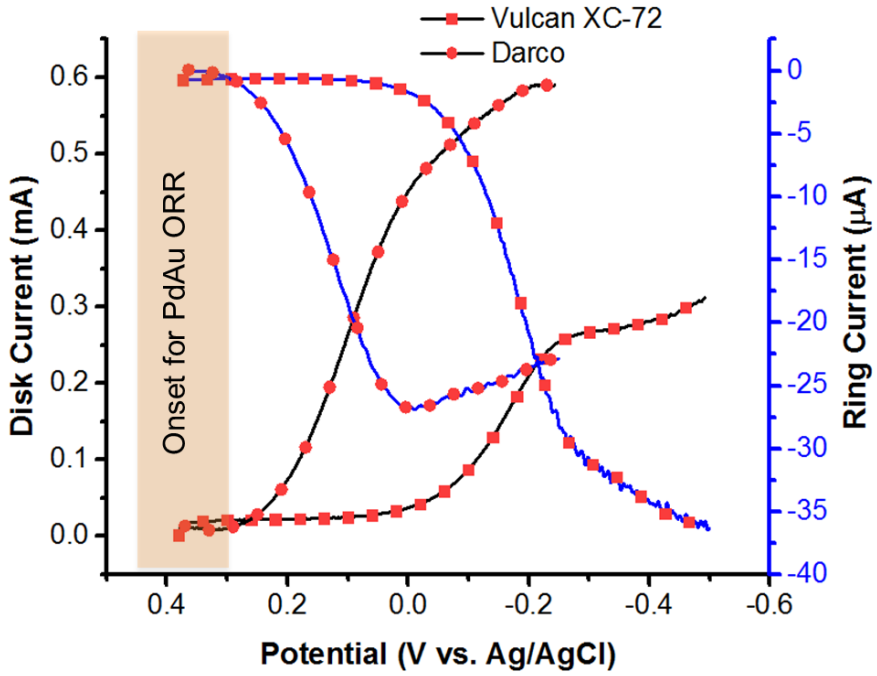

Figure 6.5 Shown here is RRDE data for various carbon supports to demonstrate its non-innocent nature in ORR electrocatalysis. The Vulcan XC-72 carbon that was used in previous work in this presentation reduces O_2 at fairly large overpotentials, but still displays some degree of overlap with the metal catalysts supported onto it.

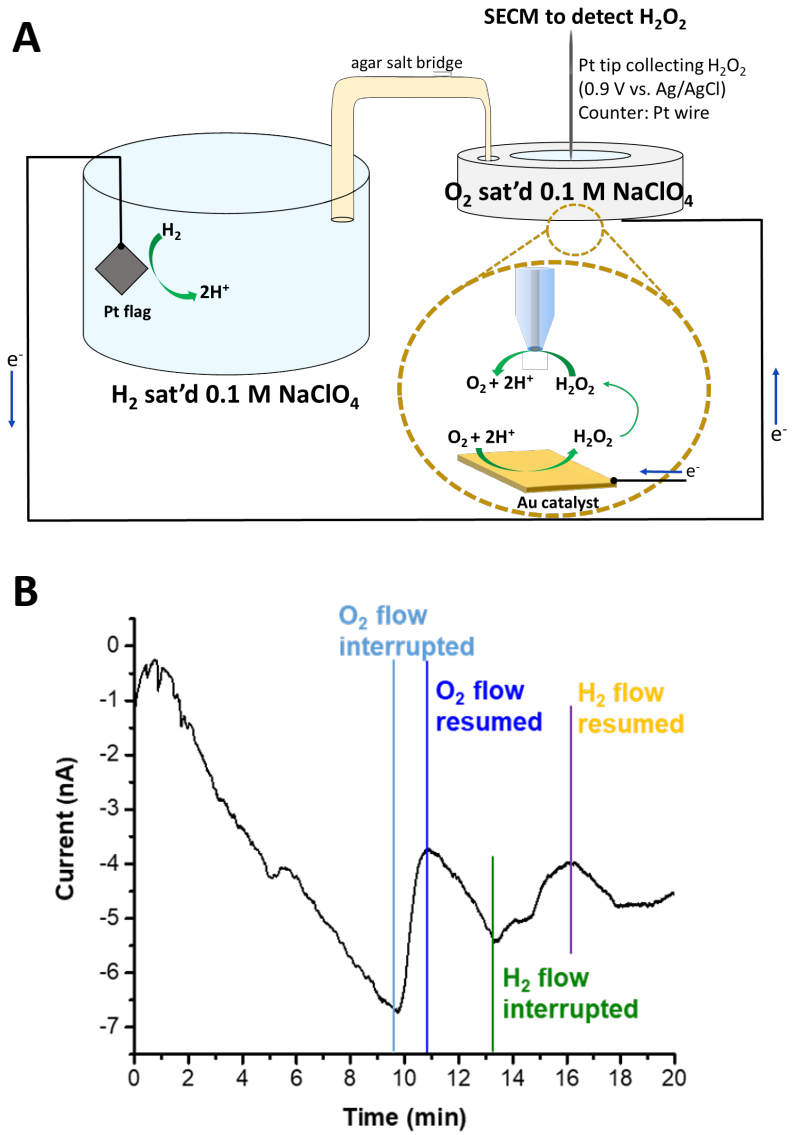

Figure 6.6 A) Shown here is the experimental setup for compartmentalizing direct synthesis into a fuel cell type system. The half-cells used were a Pt containing cell saturated with H_2 and a Au containing cell saturated with O_2. The Pt and Au electrodes were connected through an external wire to allow electron flow. In (B) is the results of the Pt UME biased to collect any H_2O_2 produced from the Au electrode. An anodic signal arises from merely connecting the Pt and Au electrodes in the presence of H_2 and O_2, respectively. This signal decreases as the gas flow of either H_2 or O_2 is halted, which gives strong support for the formation of H_2O_2.

6.6. References

(1) Zoski, C. G.; Simjee, N.; Guenat, O.; Koudelka-Hep, M. Addressable microelectrode arrays: Characterization by imaging with scanning electrochemical microscopy. *Anal. Chem.* **2004**, *76*, 62-72.

(2) Fernandez, J. L.; Mano, N.; Heller, A.; Bard, A. J. Optimization of "wired" enzyme O-2-electroreduction catalyst compositions by scanning electrochemical microscopy. *Angew. Chem. Int. Ed.* **2004**, *43*, 6355-6357.

(3) Fernandez, J. L.; Walsh, D. A.; Bard, A. J. Thermodynamic guidelines for the design of bimetallic catalysts for oxygen electroreduction and rapid screening by scanning electrochemical microscopy. M-Co (M : Pd, Ag, Au). *J. Am. Chem. Soc.* **2005**, *127*, 357-365.

(4) Fernandez, J. L.; White, J. M.; Sun, Y. M.; Tang, W. J.; Henkelman, G.; Bard, A. J. Characterization and theory of electrocatalysts based on scanning electrochemical microscopy screening methods. *Langmuir* **2006**, *22*, 10426-10431.

(5) Edwin, N. N.; Edwards, J. K.; Carley, A. F.; Lopez-Sanchez, J. A.; Moulijn, J. A.; Herzing, A. A.; Kiely, C. J.; Hutchings, G. J. The role of the support in achieving high selectivity in the direct formation of hydrogen peroxide. *Green Chem.* **2008**, *10*, 1162-1169.

(6) Samanta, C. Direct synthesis of hydrogen peroxide from hydrogen and oxygen: An overview of recent developments in the process. *Appl. Catal. A* **2008**, *350*, 133-149.

(7) Sun, Y. Y.; Sinev, I.; Ju, W.; Bergmann, A.; Dresp, S.; Kuhl, S.; Spori, C.; Schmies, H.; Wang, H.; Bernsmeier, D.; Paul, B.; Schmack, R.; Kraehnert, R.; Roldan Cuenya, B.; Strasser, P. Efficient Electrochemical Hydrogen Peroxide Production from Molecular

Oxygen on Nitrogen-Doped Mesoporous Carbon Catalysts. *ACS Catal.* **2018**, *8*, 2844-2856.

(8) Chen, Z. H.; Chen, S. C.; Siahrostami, S.; Chakthranont, P.; Hahn, C.; Nordlund, D.; Dimosthenis, S.; Norskov, J. K.; Bao, Z. N.; Jaramillo, T. F. Development of a reactor with carbon catalysts for modular-scale, low-cost electrochemical generation of H2O2. *React. Chem. Eng.* **2017**, *2*, 239-245.

(9) Hui, J. S.; Pakhira, S.; Bhargava, R.; Barton, Z. J.; Zhou, X.; Chinderle, A. J.; Mendoza-Cortes, J. L.; Rodriguez-Lopez, J. Modulating Electrocatalysis on Graphene Heterostructures: Physically Impermeable Yet Electronically Transparent Electrodes. *ACS Nano* **2018**, *12*, 2980-2990.

(10) Liu, H. S.; Song, C. J.; Zhang, L.; Zhang, J. J.; Wang, H. J.; Wilkinson, D. P. A review of anode catalysis in the direct methanol fuel cell. *J. Power Sources* **2006**, *155*, 95-110.

(11) Eisaman, M. D.; Alvarado, L.; Larner, D.; Wang, P.; Garg, B.; Littau, K. A. CO2 separation using bipolar membrane electrodialysis. *Energy Environ. Sci.* **2011**, *4*, 1319-1328.

(12) Shiraishi, Y.; Kanazawa, S.; Kofuji, Y.; Sakamoto, H.; Ichikawa, S.; Tanaka, S.; Hirai, T. Sunlight-Driven Hydrogen Peroxide Production from Water and Molecular Oxygen by Metal-Free Photocatalysts. *Angew. Chem. Int. Ed.* **2014**, *53*, 13454-13459.

(13) Santos, E.; Schmickler, W. Electrocatalysis of hydrogen oxidation-theoretical foundations. *Angew. Chem. Int. Ed.* **2007**, *46*, 8262-8265.

(14) Sheng, W. C.; Gasteiger, H. A.; Shao-Horn, Y. Hydrogen Oxidation and Evolution Reaction Kinetics on Platinum: Acid vs Alkaline Electrolytes. *J. Electrochem. Soc.* **2010**, *157*, B1529-B1536.

(15) Sheng, W. C.; Bivens, A. P.; Myint, M.; Zhuang, Z. B.; Forest, R. V.; Fang, Q. R.; Chen, J. G.; Yan, Y. S. Non-precious metal electrocatalysts with high activity for hydrogen oxidation reaction in alkaline electrolytes. *Energy Environ. Sci.* **2014**, *7*, 1719-1724.

(16) Inaba, M.; Kinumoto, T.; Kiriake, M.; Umebayashi, R.; Tasaka, A.; Ogumi, Z. Gas crossover and membrane degradation in polymer electrolyte fuel cells. *Electrochim. Acta* **2006**, *51*, 5746-5753.

(17) Yang, Y.; Gao, X. L.; Fan, A. Y.; Fu, L. L.; Gao, C. J. An innovative beneficial reuse of seawater concentrate using bipolar membrane electrodialysis. *J. Membr. Sci.* **2014**, *449*, 119-126.